

**AD-A282 833**



**INTELLIGENT PROCESSING OF FERROELECTRIC THIN FILMS**

**Annual Report**

Period: July 2, 1993 to May 31, 1994

**OFFICE OF NAVAL RESEARCH**

Contract No. N0014-91-J-1508

Principal Investigator: Gene Haertling  
Co-Investigator:

Eric Skaar  
Raj Singh

DTIC QUALITY INSPECTED 2/

Supporting Investigators: Feiling Wang  
David Dausch  
James Barrett  
Youngwoo Moon  
Jaideep Mavoori

*2/16/25*  
**94-24092**



May 31, 1994



**The Gilbert C. Robinson  
Department of Ceramic Engineering**

**College of Engineering**

**DISTRIBUTION STATEMENT A**  
Approved for Public Release  
Distribution Unlimited

## Table of Contents

- Part I ..... Introduction
- Part II ..... Intelligent Processing Implementation and Automation
- Part III ..... PLZT Powder Preparation and Characterization
- Part IV ..... Spin Coated Ferroelectric Thin Films and Bulk Ceramics
- Part V ..... Electrooptic Thin Films and Bulk Ceramics
- Part VI ..... Sputtered Thin Films and Electrooptics
- Part VII ..... Chemical Vapor Deposited Thin Films
- Part VIII ..... Publications

Accession For	
NTIS GRA&I	<input checked="" type="checkbox"/>
DTIC TAB	<input type="checkbox"/>
Unannounced	<input type="checkbox"/>
Justification	
<i>per letter</i>	
By _____	
Distribution/	
Availability Codes	
Dist	Avail and/or Special
A-1	

## SUMMARY

This report details work that was performed in the Ceramic Engineering Department of Clemson University over the period from July 2, 1993 to May 31, 1994 under ONR contract No. N0014-91-J-1508. The work described in this report covers the third year of a four-year program involving intelligent processing of ferroelectric thin films and bulk materials. It is presented in eight parts dealing with automation, powder processing, bulk materials characterization, thin film fabrication and evaluation, electrooptic behavior of thin films and published work.

In regard to process automation and intelligence, the fluid flow pattern for the batching system has been thoroughly assessed. The data show that the gravity flow of solutions through the system is sufficient for batching into a central vessel. In addition to the resistance probe, an LVDT will be linked directly to the computer through analog ports and will provide the necessary feedback to batch solutions more reliably. The software which has been chosen for the software interface segment is Visual Basic.<sup>TM</sup>

During this period, additional processing studies were carried out on various methods of producing an optimum ferroelectric powder with the acetate precursors. The results from these experiments involving coprecipitation with NH<sub>4</sub>OH and KOH showed that pH was instrumental in producing different morphologies of the powders.

An automatic spin coat reactor/analyizer was used to produce PLZT thin films from acetate precursors on Pt-coated Si wafers. The spin coater is computer controlled and fully automated for hands-off processing, thus providing a cleaner environment and more flexibility in processing parameters. The spin coating process is fully integrated with rapid thermal processing, atmosphere control and in-situ ellipsometry in one chamber. Results from the automatic spinner were compared with those of the bulk ceramics. In general, thin films on Ag or Si/Pt substrates were found to have properties comparable with those of the bulk although substrate-dependent orientation effects were noted.

Dip coated thin films on Ag foil substrates and hot pressed bulk ceramics were fabricated and compared with respect to electrical and electrooptic properties. Films approximately 0.9 um thick (24 layers) were optimally prepared by sintering at 700°C for three minutes. For a 9/65/35 composition, the bulk materials produced the usual slim hysteresis loops, but this was never completely achieved in the thin films. It is suggested that these differences may be attributed to the induced stresses built up in the thin films.

The magnetron sputtering of acetate-derived PLZT powder has produced high quality thin films in terms of dielectric and electrooptic properties. A systematic investigation of these properties have yielded some significant results.

A reflective thin film ferroelectric light modulator has been constructed on a silicon substrate. An ON/OFF ratio of twenty to one for intensity modulation and fifty

degrees for phase modulation have been achieved. Unlike transmission devices, the sandwich of the ferroelectric/electrooptic films between the air-ITO and PLZT-Pt interfaces exhibited characteristics of a Fabry-Perot etalon. Near a Fabry-Perot condition, drastically enhanced light modulation was obtained from the accumulated phase shift of the multiply-reflected light beam.

The success of depositing antiferroelectric thin films from acetate precursors has prompted a systematic study of the electrooptic effects of these thin film materials. Because of their antiferroelectric nature, these materials possess a characteristic electrooptic response different from ferroelectric materials. With the reflection differential ellipsometer, a digital birefringent response in an antiferroelectric lead zirconate thin film grown on Pt/Ti-metallized silicon substrate was observed for the first time. An important finding from the study of antiferroelectric thin films involved a photo-activated birefringent effect in PZT thin films bounded by a semiconducting ITO layer. The photo-activated birefringence is associated with a photo-assisted antiferroelectric-to-ferroelectric structural transition.

A preliminary study of the deposition of PLZT thin films via rapid isothermal processing assisted metal organic chemical vapor deposition was initiated. Initial results are encouraging, however, no conclusions regarding this technique have yet been drawn.

**Part I.**

**Introduction**

## **Part II.**

### **Intelligent Processing Implementation and Automation**

# **INTELLIGENT PROCESSING OF FERROELECTRIC THIN FILMS**

## **Annual Report**

### **Part II.**

#### **Intelligent Processing Implementation and Automation**

**Submitted by: James Barrett  
Eric Skaar**

**The Gilbert C. Robinson Department of Ceramic Engineering  
Clemson University**

## **SYNOPSIS**

This report describes efforts involved in the implementation of Intelligent Processing of Materials (IPM) for the production of PLZT acetate thin films and powders. It summarizes progress made during the three years of the program on Intelligent Processing of Ferroelectric Thin Films sponsored by the Office of Naval Research.

## **OBJECTIVES**

The objectives of this portion of the program are to develop software and hardware to implement IPM for powder production from acetate solutions:

1. Develop software to implement IPM.
2. Develop sensors for controlling solution composition and properties.
3. Design and purchase equipment for automated solution processes.

## **INTRODUCTION**

### **Intelligent Processing of Materials (IPM) for PLZT Acetate Powders:**

The purpose of IPM is to reduce the lead time between materials development and the production of those materials while at the same time increasing the quality of the product. The quality that is achieved through the IPM process is built-in during the production and not the result of post-manufactured inspection. IPM is desirable because it can improve the quality, reliability, and yield of processed materials. Quality is achieved in the IPM process by "building" it into production, and is not the result of inspection after manufacture.

IPM combines the expertise of the process engineer and the knowledge of the materials scientist through the use of an expert system. The expert system is an application of artificial intelligence that utilizes efficient and effective data handling and retrieval to analyze and predict processing events so that corrections and/or compensations can instantaneously be made in the process to achieve a high quality product. This system monitors all processing steps from raw material characteristics to the final product during manufacturing so that changes can be made in each step and in future steps to attain the highest quality product. Process models and real-time sensors are heavily relied upon in the IPM strategy so that higher levels of control and awareness can be attained than in conventional processing. In-situ sensors can monitor complex characteristics such as microstructures in real time and combine this data with conventionally sensed data, such as temperature or viscosity and the resulting

combination is used by the expert system to make process judgements to compensate for process and raw material variability.

To implement IPM in the production of powders from PLZT acetate solutions, a production process that is compatible with the requirements of an automated process is needed. The process must be completely defined. The entire process for this system includes: the making of PLZT acetate solutions, the precipitation of a solid, the separation of the solid from the liquid, and the processing of the solid into a powder. As the process is defined, process variables are defined and assessed. These variables must be isolated and treated in a manner that is consistent with the IPM process. It is also important that the equipment that makes up the system be compatible so that it can be linked efficiently and effectively. The hardware, such as mixing equipment, valves, and sensors must be linked to the software (computer) that runs the system. The hardware and software are the two major components of any IPM system, and each has its own purpose.

The hardware needed to initiate and implement IPM to the batching component of manufacturing PLZT acetate powders has been purchased or fabricated from existing parts and adapted to perform specific tasks. A computer has been purchased and is currently in use in controlling the batching equipment. The software that has been acquired is conducive to self-learning processing algorithms and capable of correcting errors in manufacture. Other software has been written to enable the communication between the computer and the process equipment, as well as enabling the use of the purchased software in this system. The unique requirements of IPM make it necessary that the software be developed for the specific tasks and functions at hand.

Sensors are the link between the process and the computer that drives the process. In order to select or design sensors, it is necessary to establish the parameters that affect the product properties that are important. One type of sensor, for fluid level control in the raw material reservoirs, has been installed in the batching system. Another type of sensor has been designed and tested for the PLZT fluid system to measure the fluid resistivity under alternating current. All process variables and their limits must be assessed, then the methods and conditions under which they are monitored must be considered.

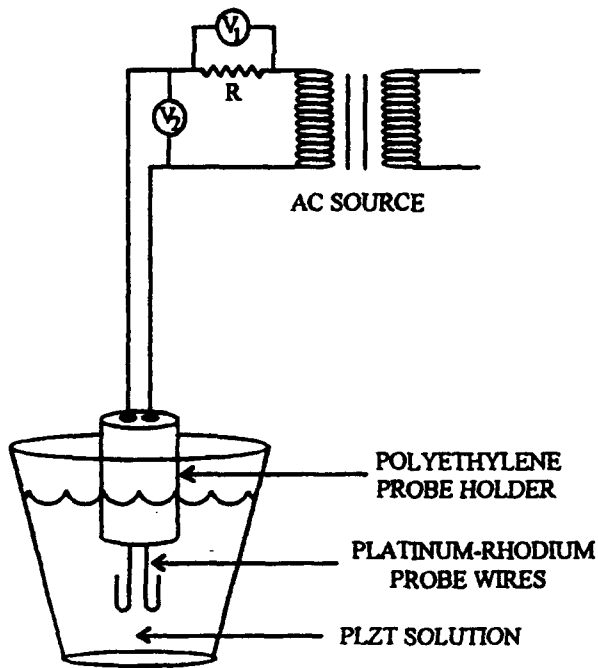
Traditional programming is not designed to apply experience to control. An alternative software scheme is neural networking software. Another requirement for software is that it be compatible with the computers that are available at present, in this case, an MS-DOS machine. A software package called NeuroWindows™ was purchased to partially fulfill these requirements. The software is not geared specifically for control, so it was necessary to write device drivers that will work concurrently with NeuroWindows™ to complete the software needs in linking the computer to the other hardware. To implement IPM in the

production of powders from PLZT acetate solutions, a production process that is compatible with the requirements of an automated process is needed. The production process must be completely defined. The entire process includes the making of solutions, the precipitation of a solid, and the separation of the solid from the liquid. The major variables need to be isolated and treated in a manner that is amenable and consistent with the IPM process. In addition, the hardware, software, and sensors must be set up as a system.

## EXPERIMENTAL

### I. Hardware:

As stated, sensing is the key component in linking hardware and software in an IPM process. The sensors for fluid levels in the batching system have been built from stainless steel rods and installed in the batch reservoirs. Included in each reservoir are a low-level sensor and a high-level sensor. The AC resistivity sensor that was described in the first annual report can be used in conjunction with the level sensor to assess raw material properties within the reservoirs using the same hardware, but separate electronic hookups. A schematic of the AC resistivity sensor used can be found in Figure 1.



$$R_{\text{fluid}} = \frac{V_2}{I}$$

Figure 1. Method of measuring resistance of PLZT solutions using alternating current.

The materials chosen for the batch system and sensors have been evaluated for corrosion. The stainless steel rods used for level sensing were checked by immersion and storage in a container of each batch constituent, at an ordinary concentration. The samples were examined on an approximately daily basis for six weeks. No apparent signs of any corrosion were present. The same test was applied to the thread tape that was used to seal the valves and reservoir connections, with similar results. The compatibility of the polyethylene reservoirs with the batch constituents has already been established.

The entire automated process for the production of PLZT acetate powders has many parts that need to be both optimized and automated. The section of the process that received the greatest attention initially in the development of the total process is the batching system itself. The automated process hardware for the batching of PLZT acetate solutions has been assembled and the equipment has been constructed, tested, and is operating properly. The system utilizes manually filled reservoirs containing the liquefied constituents of the PLZT acetate system that supply smaller, computer-controlled reservoirs that are used to dispense batch amounts. Solenoid valves have been installed beneath each reservoir, to permit control of dispensation. Polyethylene containers, which are used as reservoirs, and tubing connecting the valves and reservoirs has been set up on a custom built chemical rack. The level sensors mentioned previously are a part of a switch system that is used to control the filling of the computer-controlled reservoirs from the manually-controlled reservoirs, as well as being a low-liquid-level alarm. When the valve for the manually controlled reservoirs is opened, the fluid will flow until the liquid completes the circuit between the common rod and the high-level rod. The computer detects the signal through an input board that links the valve to the computer. Then, the computer can send a signal to the output board that links the valves and the computer, and the valve can be closed to stop fluid flow. The low-level sensor is useful in determining when the valves from the manually-filled reservoirs need to be opened to replenish the computer-controlled reservoirs, or to signal the need to refill the manually-filled reservoirs. An IBM 433DX/S has been joined to the batch system through the I/O relay boards that are connected to the solenoid valves and level sensors. Again, the stainless steel level sensors are in place in the solution reservoirs and are connected to the input relay board for automatic switching. The computer currently controls and times the switching of valves on and off, through the output board and the device drivers that were written. In addition, all ten valves can be operated manually via a switch panel, and indicator lights for each open valve operate whether the system is under automatic or manual control. A main power switch separates computer control and manual control, such that manual control can be used to override the computer control, if necessary. A diagram of the equipment setup is shown in Figure 2.

SOLUTION RESERVOIRS (MANUAL CONTROL)

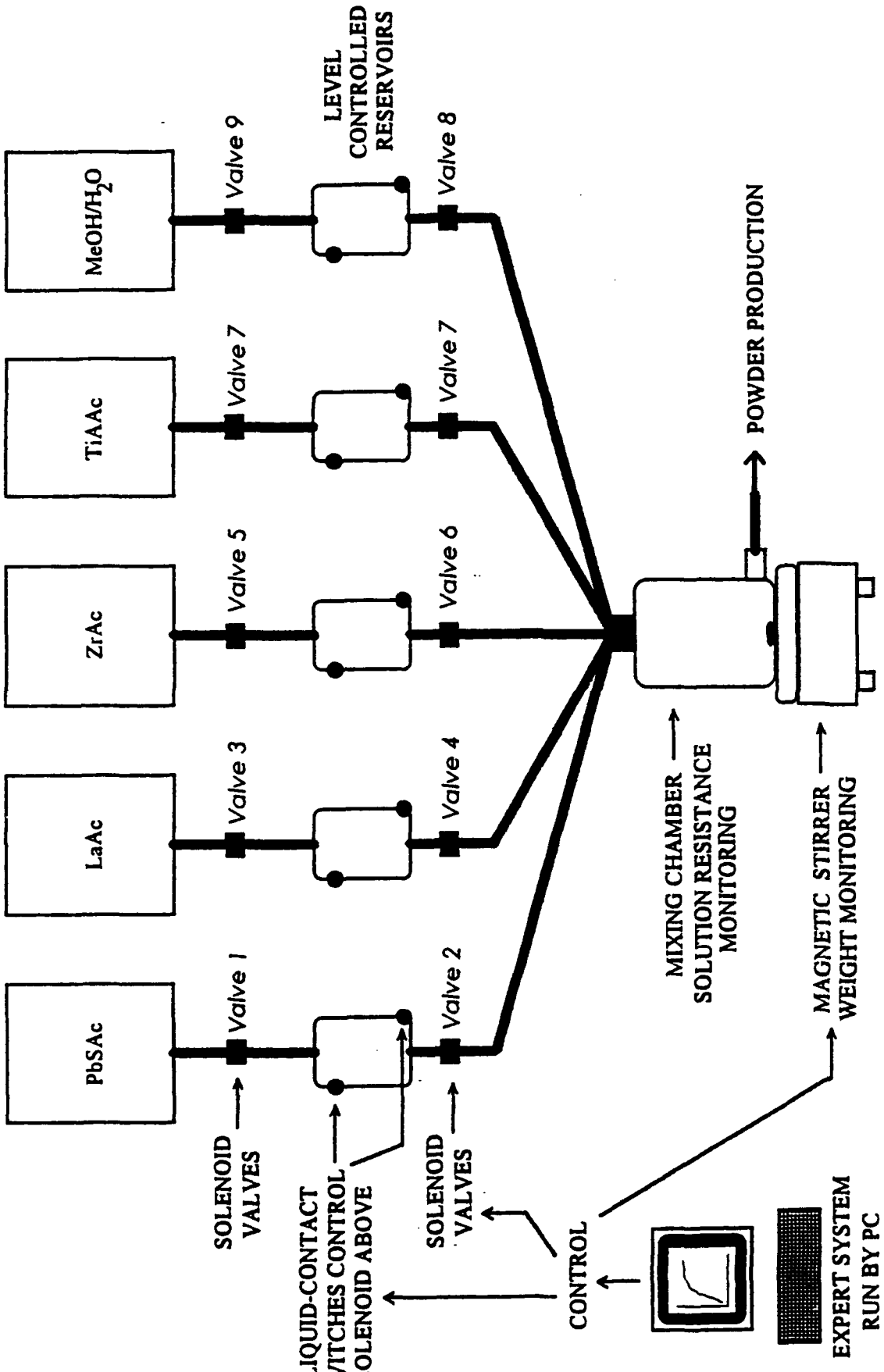


Figure 2. Automated solution batching system controlled by IBM PC.

The input and output boards used to interface the computer and batch equipment are Advantech PCL-812 electronic cards. They are high speed, multi-function data acquisition cards and are compatible with many types of software and hardware. The key applications include: process control, automatic testing, data acquisition, and process automation. A schematic of the features and layout of the boards is shown in Figure 3.

## II. Software and Programming of Batch System Elements:

The device drivers needed to link the computer and its neural network, NeuroWindows™, with the batch system hardware were designed for the MS-DOS platform. The drivers permit the use of the input and output boards to control communication and execution between the computer and batch equipment. The software operates under the Microsoft Windows system, which greatly enhances its compatibility with any other software packages that may be necessary.

The control algorithm for the automated batching process is a two part algorithm. The first part is a normal weighing or batching algorithm. This part is responsible for the communications between the computer and the batching equipment. It utilizes the device drivers and the input and output boards to link the batching requirements to "mechanical" action. It also contains the timing control for the opening and closing of individual valves, as well as an "Emergency Stop" manual override and a manual override for maintenance and replenishment of the batch system. The screen panel for these functions can be seen in Figure 4. The final task for the control algorithm section is to also contain a database of recipes for the solutions required to make powders of various compositions. As long as the process does not vary, and all the settings remain constant, the process is capable of running with this section of the algorithm alone. The second part of the algorithm is designed to sense problems and makes corrections to the process.

This second section is an artificially intelligent program based on a neural network. It is designed to sense "out of control" conditions and make appropriate corrections to the weighing or batching algorithm.

Neural networks excel at pattern recognition, diagnosis, and decision making. The idea behind this section of the algorithm is to recognize an assignable problem as it develops, and compensate. In a sense, the computer is programmed to utilize statistical process control.

For example, suppose the metering mechanism for one of the constituents became partially clogged. The result would be a variance from normal with respect to the weight and the resistance measurements for the batch. The pattern of these measurements would change. The neural network would be taught to recognize this pattern, and effect the appropriate

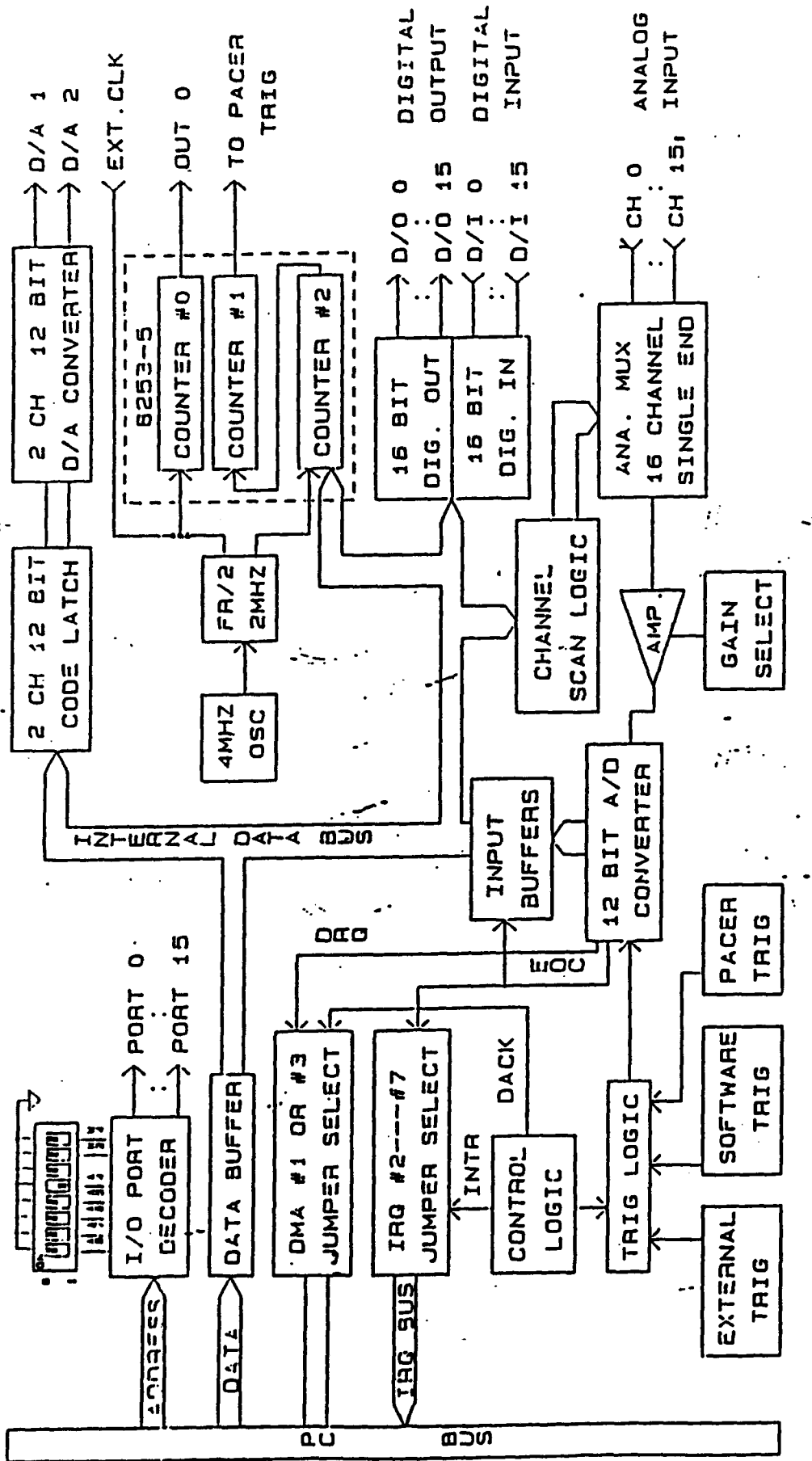


Figure 3. Schematic of the Advantech PCL-812 PC-LabCard™ used for input and output.

compensation. Other types of assignable problems would also present their unique patterns that the neural network would be taught to recognize.

The unique beauty of using neural network technology for this application is that the teaching of the network is not a function of programming, but rather simulation. For the network to function, it has to be taught the patterns that specific problems create. This task is accomplished by actually simulating the problem in the process. The network is programmed to learn and recognize the resulting sensor patterns. Once the network recognizes the pattern, it is programmed to compensate for the deficiency. A properly designed network, therefore, does not depend upon an exhaustive database of every problem. Rather, as experience is gained with a process, the problems and solutions can be taught to the network. The algorithm improves with operating experience and thus the process can proceed toward optimization.

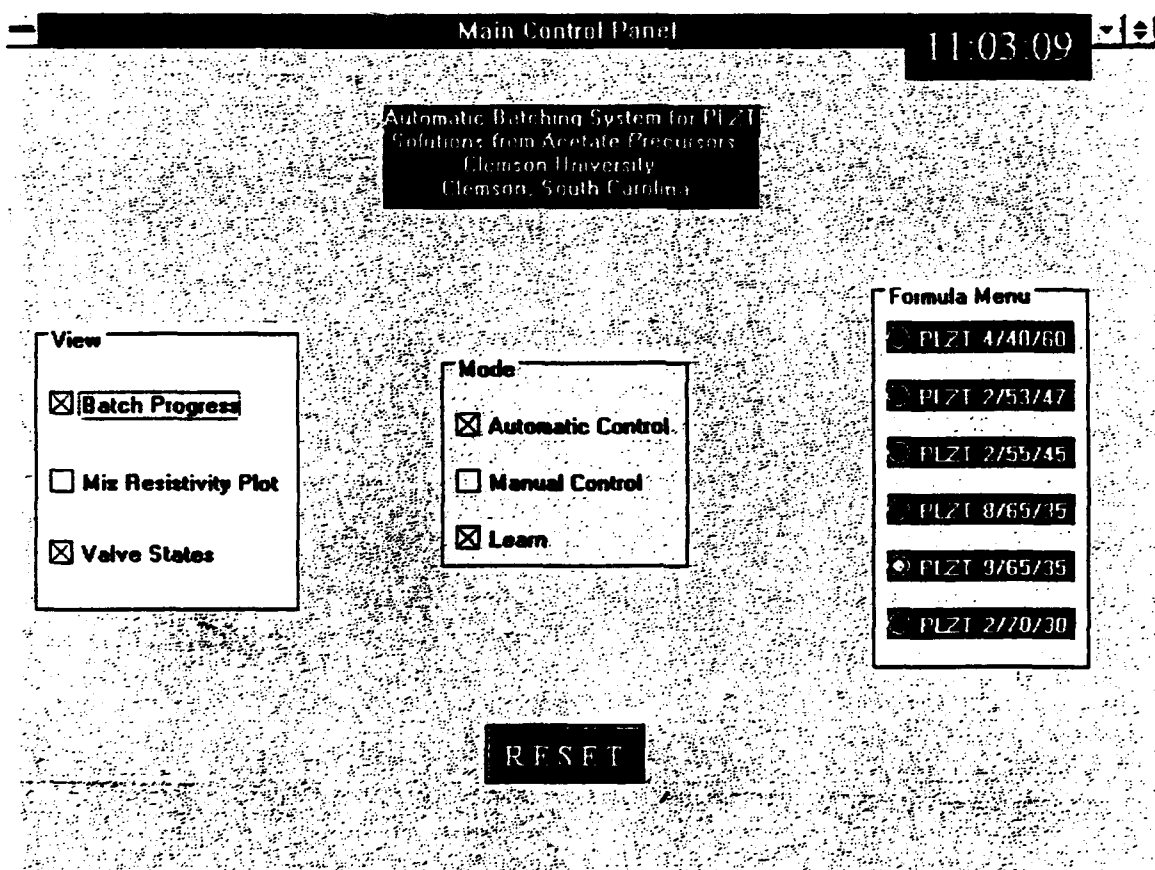


Figure 4. Main Control Panel for automated batch system, the human interface.

## RESULTS

### I. Hardware:

The two-conductor AC resistance probe that was constructed has been tested for reading stability and response time. Both requirements for this resistivity measurement tool were easily met by the probe, as the response time for a change in resistance was two to five seconds and the resulting readings were stable for days. No probe maintenance occurred during these tests, as it was used continuously, as required by the IPM process. The application of the AC resistivity sensor will be in the mixing vessel of the batch system. A newer, more rugged version of the probe was constructed to reduce the possibility that it be damaged. The new probe was constructed of Pyrex™ glass and platinum wire. The new probe also is easier to configure with the mixture reservoir. The input driver for the probe has been completed and it has been linked to the computer.

In order to utilize the neural networking software, it is necessary to have input from the hardware (the total batch system) to the software (the computer and its algorithms). The resistivity probe is one avenue of providing input from the batch system for data measurement and control. Another tool that can be used that is more established is a total liquid volume level sensor. An LVDT with a float for measuring the total volume of the batch mixture has been ordered, but not received. The LVDT will be linked directly to the computer through its analog ports and will provide the necessary feedback to batch solutions confidently. The schematic of the total batch reservoir with LVDT and resistivity probe can be seen in Figure 5. The main purpose of the resistivity sensor is to provide data that can be used to detect

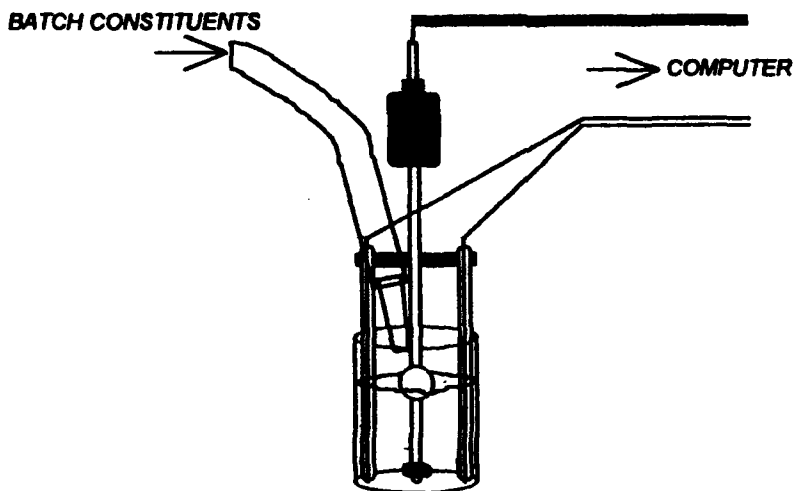


Figure 5. Schematic of batch constituents, resistivity sensing, and liquid level sensing.

other process variations, such as raw material quality.

The AC resistance probe has been tested in a simulated batching experiment. The batch constituents for a 9/65/35 PLZT acetate solution were added, one at a time, and the changes in resistance of the total solution were tabulated and plotted, as can be seen in Figure 6. An order of addition of constituents was chosen to best suit the homogeneity of the batch. Generally, the resistance of the total batch increased as each constituent was added. This result shows that this tool is amenable for use in an IPM process. The constituent that shows a possible exception for the upward trend is lead subacetate, for which the resistance decreased after a point. However, the neural network that runs the system can be "trained" to compensate for this result. The probe can be used to help the expert system "learn" the characteristics and properties of the batching process, from one constituent to the next, while the LVDT provides feedback relating the total batched volume of constituents. The process model for the batching procedure must be available to the network, and it can be referenced by the process algorithm as a guide and a check. The neural network should be able to take the resulting "batch pattern" and use it to develop a process model to assist in the preparation of solutions through the automated batch system.

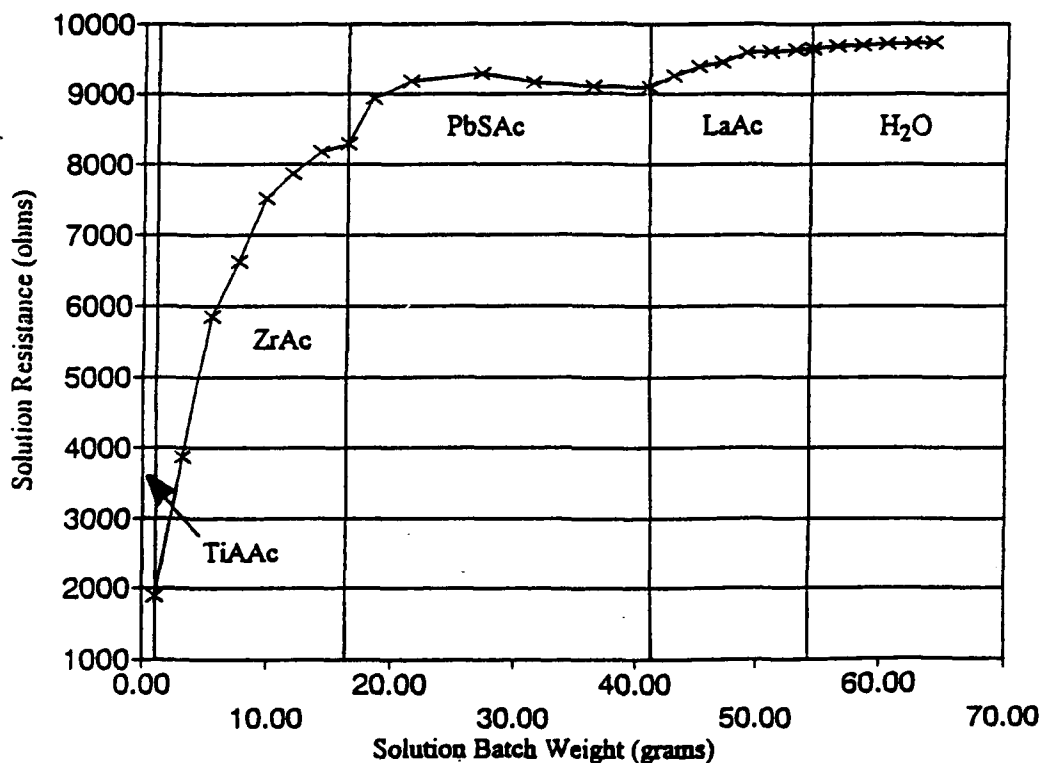


Figure 6. Solution resistance (AC measurement) for the total PLZT acetate batch as constituents were added.

The fluid-flow pattern for the batch system has been thoroughly assessed. The data shows that the gravity-flow of solutions through the system should be sufficient for batching into a central mixing vessel. A sample time of three seconds was used to check the flow volumes through each valve. The computer controlled and timed the valve openings automatically for these tests. The fluid from the open valve was collected and measured, through ten trials per lower valve (one valve per solution constituent). The valve numbers can be referenced in Figure 2. The fluid used for the preliminary tests was water, one of the batch constituents. The flow data for each valve can be seen in Figures 7 through 17. The results indicate that there is a need to prime the batching lines before attempting to batch. The results were much more consistent after the lines from the valves to the collecting vessel were "primed" by the removal of air bubbles from the lines, while establishing an amount of fluid in each line that remains constant. This consideration need only apply when the system is being run for the first time, or after maintenance to the batch lines has occurred. Also, since the capacity for each constituent is greater than 3.5 liters (including the upper reservoirs for each material), many batches could be run before the lines empty. Also, the length of the tubing from each valve to the central mixing area affected the results. Valve numbers 2 and 10 have the same length batch lines, as well as 4 and 8. The flow data for these pairs of lines varied similarly. The line for valve 6 is the shortest, and also showed the most variability. The stability of the dispensed volume appears to be inversely proportional to the length of the line. A *trial* was defined as one run of fluid (approximately 1.5 liters) from a lower reservoir of the batch system from full to empty. An *event* was defined as a single opening of the valve for the constituent for a period of exactly three seconds, as timed by the computer. The consistency of each reading from one event to another has shown that there is a steady decrease in the amount of fluid dispensed as the reservoir is emptied. This result positively reinforced the preliminary data that showed that the effect of gravity on the mechanical batching apparatus was predictable and conducive for use in automated production. The consistency from one trial to another showed that the system is reliable from one refill of the reservoirs to the next. Figures 7 through 17 show the flow data for each valve; the first plot for each valve shows all of the trial runs for comparison, while the second shows the average of all runs versus the predicted values for each valve based on linear regression analysis of the data. The last plot, Figure 17, shows a different perspective of the data that helps illustrate the general trends more obviously.

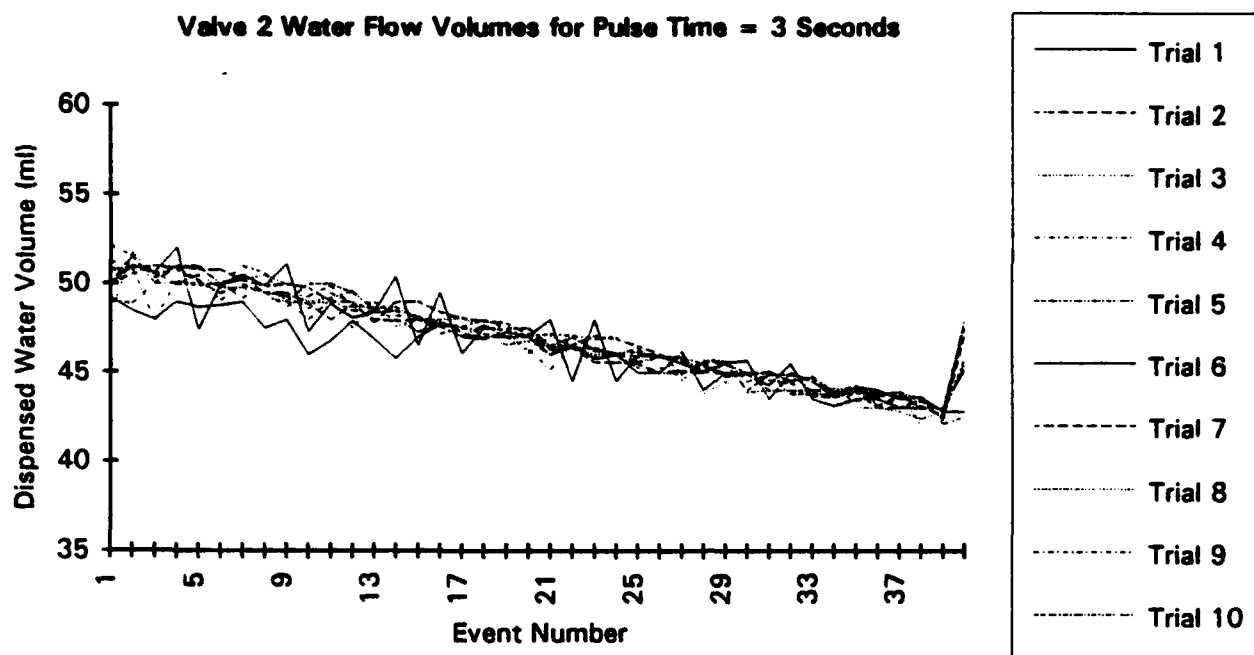


Figure 7. Trial runs for Valve 2 with an open time of three seconds each run.

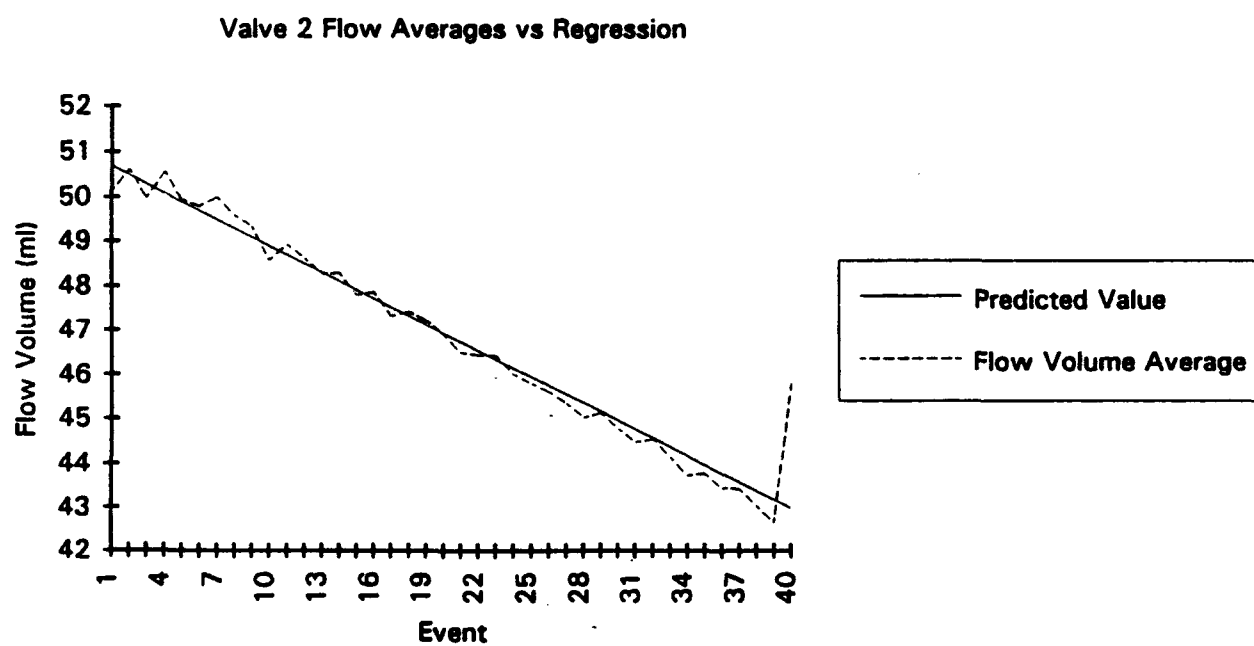
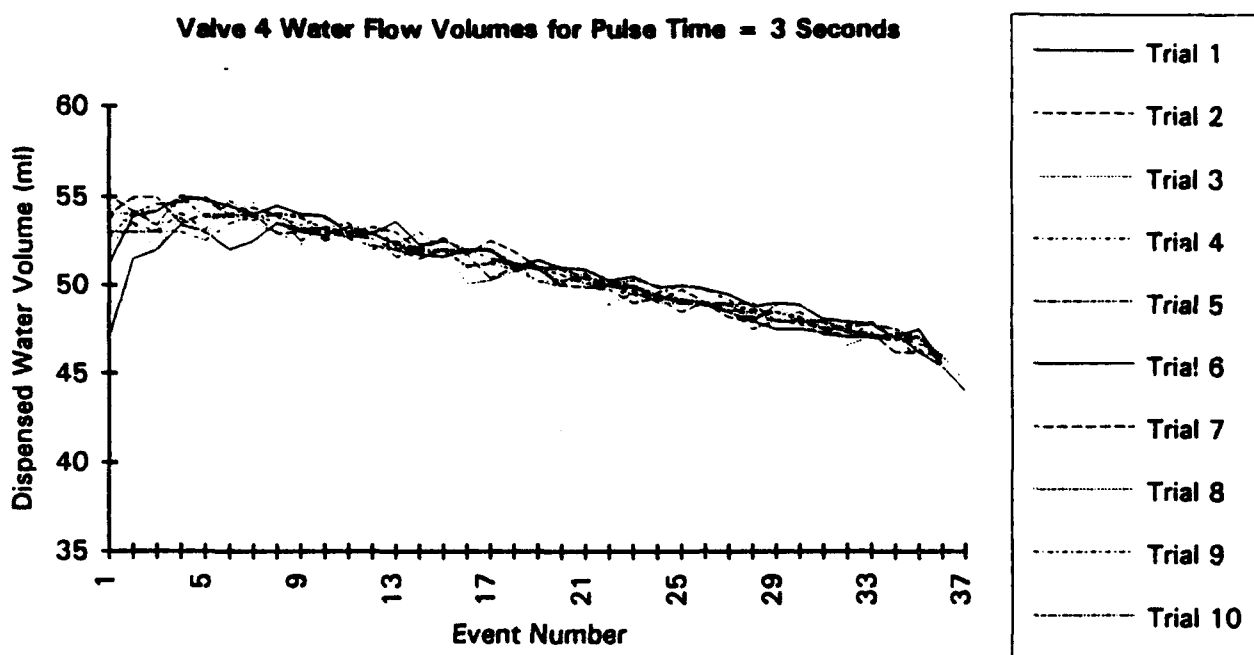
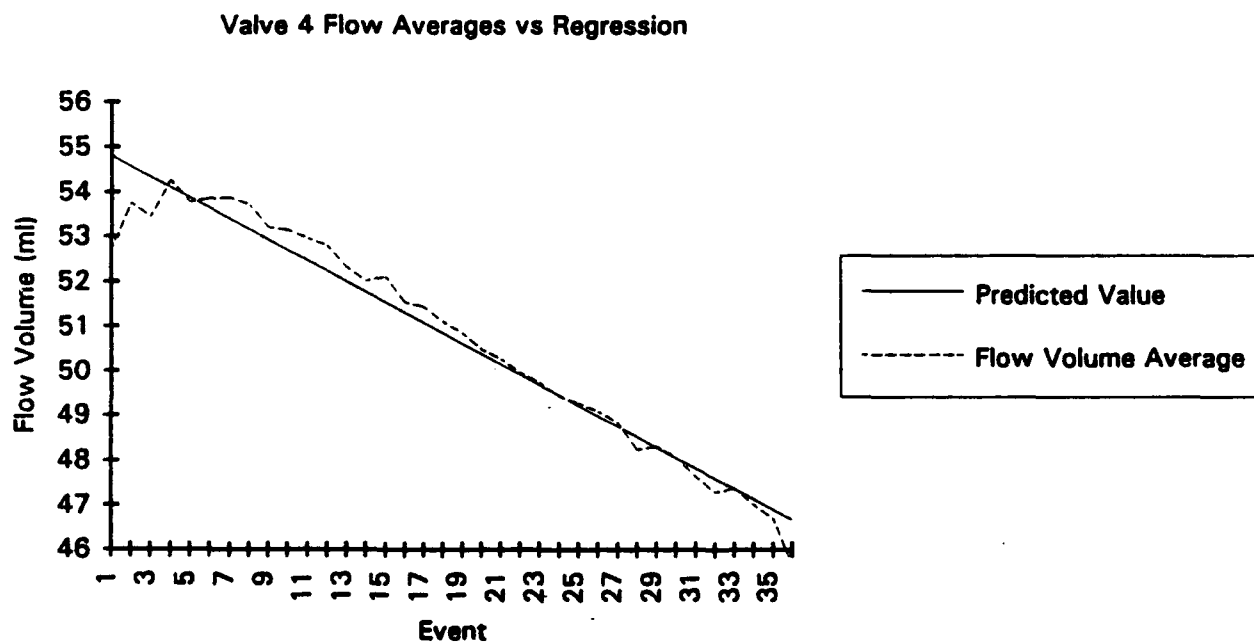


Figure 8. Average flow values for Valve 2 versus Predicted Values.



**Figure 9.** Trial runs for Valve 4 with an open time of three seconds each run.



**Figure 10.** Average flow values for Valve 4 versus Predicted Values.

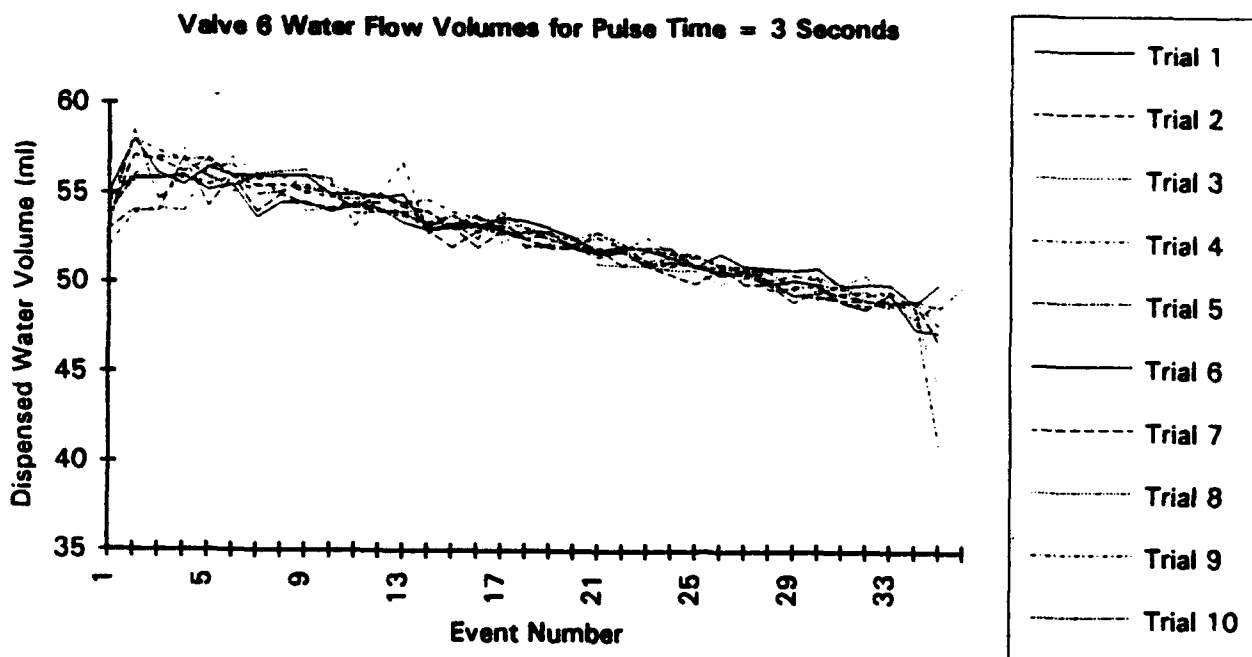


Figure 11. Trial runs for Valve 6 with an open time of three seconds each run.

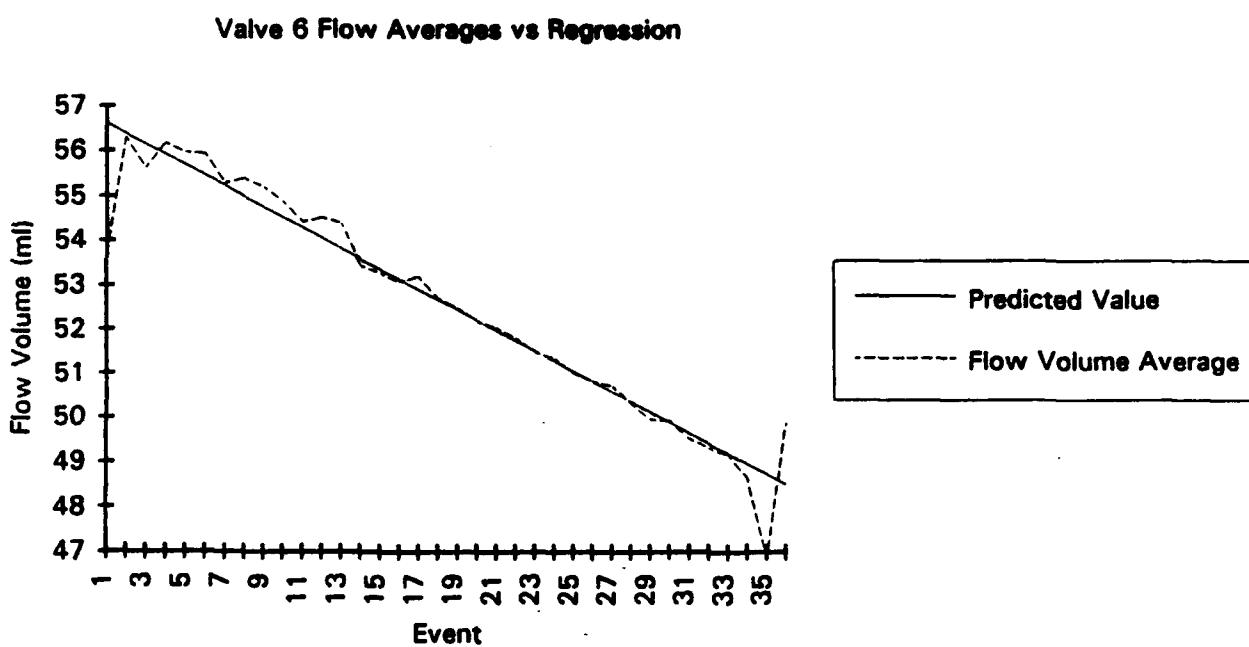
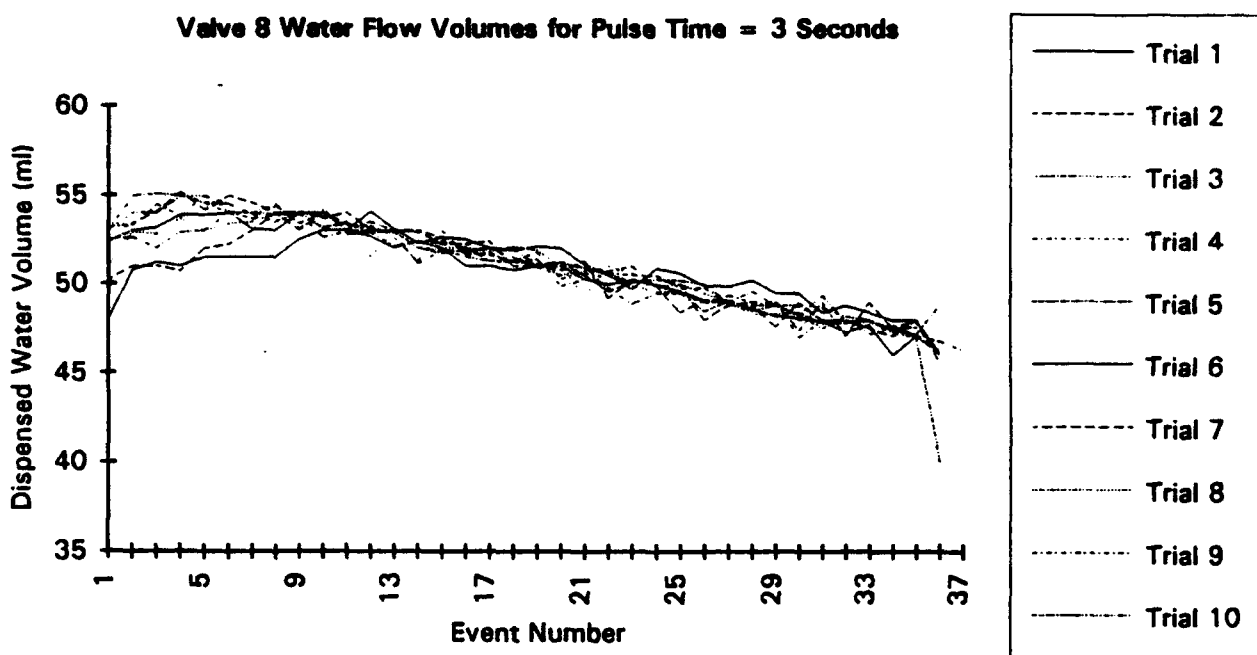
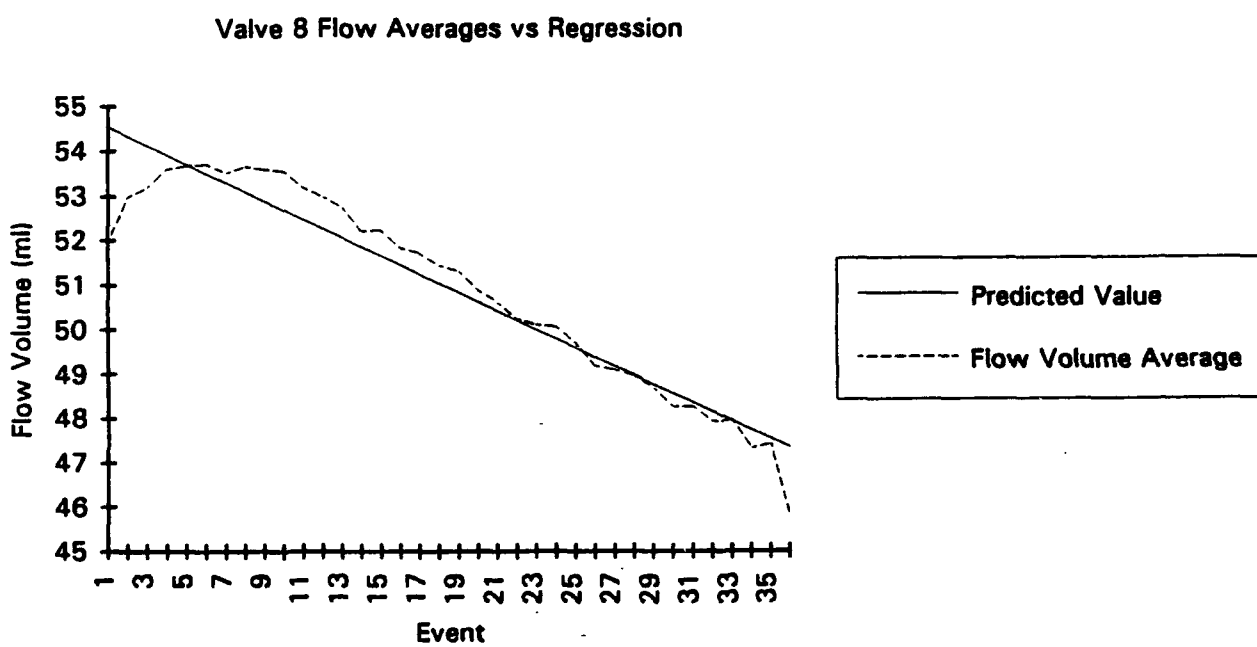


Figure 12. Average flow values for Valve 6 versus Predicted Values.



**Figure 13.** Trial runs for Valve 8 with an open time of three seconds each run.



**Figure 14.** Average flow values for Valve 8 versus Predicted Values.

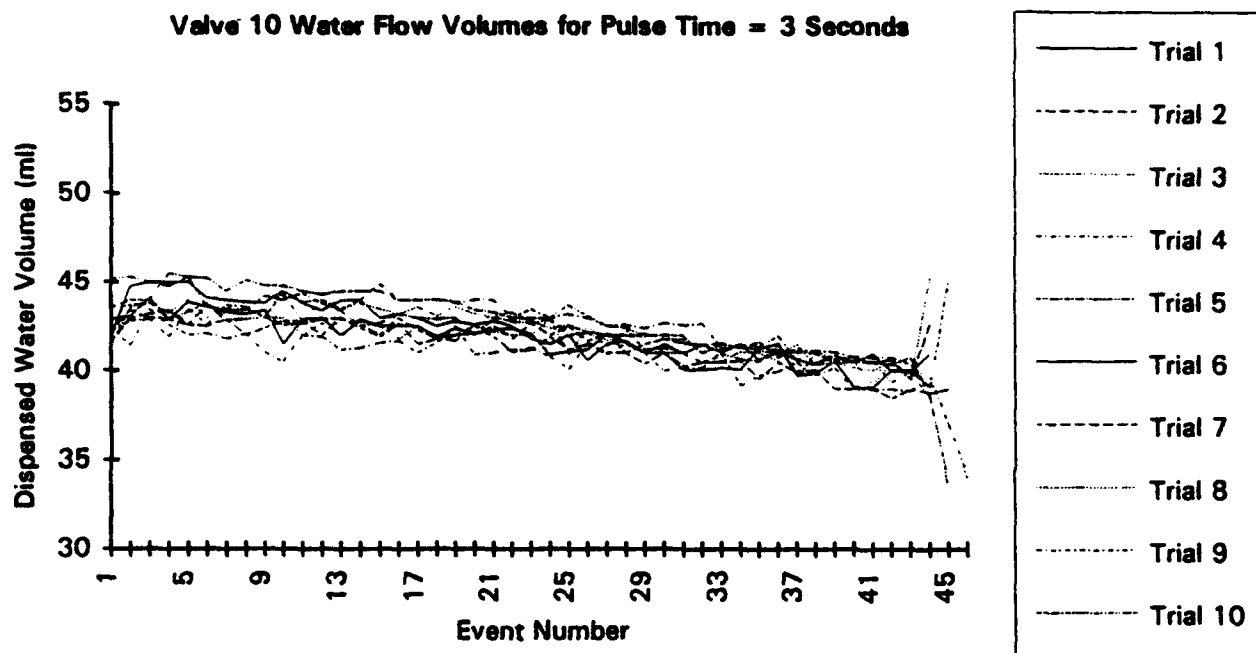


**Figure 15.** Trial runs for Valve 10 with an open time of three seconds each run.

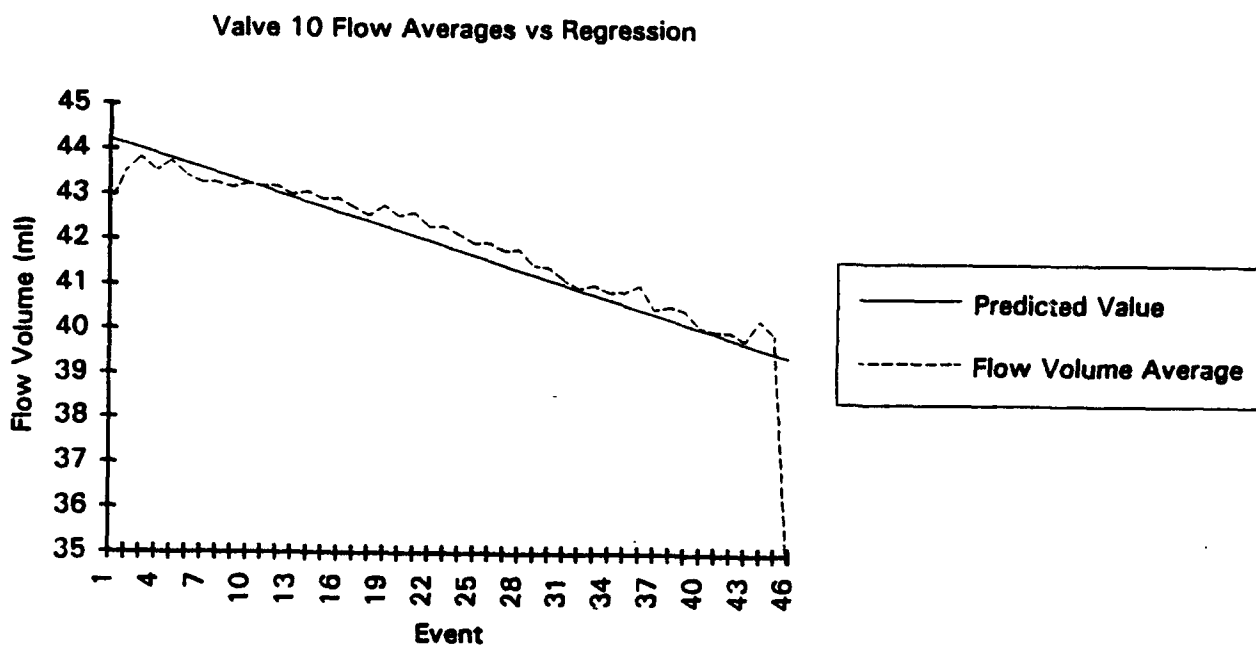


**Figure 16.** Average flow values for Valve 10 versus Predicted Values.

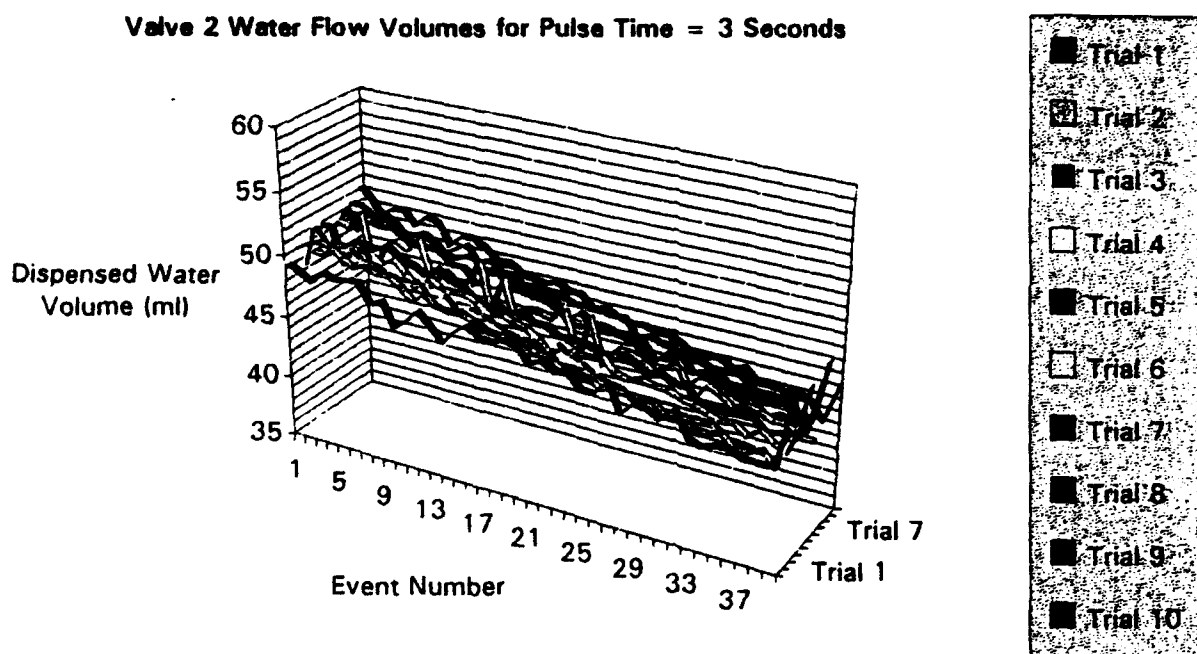


**Figure 17.** Three Dimensional view of trial runs for Valve 2.

## **II. Software and Programming of Batch System Elements:**

The programming uses the modular design. Using this approach code can be written and "debugged" in segments, rather than developed and debugged as a complete program. This minimizes development time, and greatly facilitates software maintenance.

Basically, the program consists of 4 main segments, as shown in Figure 18. They are: the neural network, the software interface, the primitive hardware interface output, and the primitive hardware interface input.

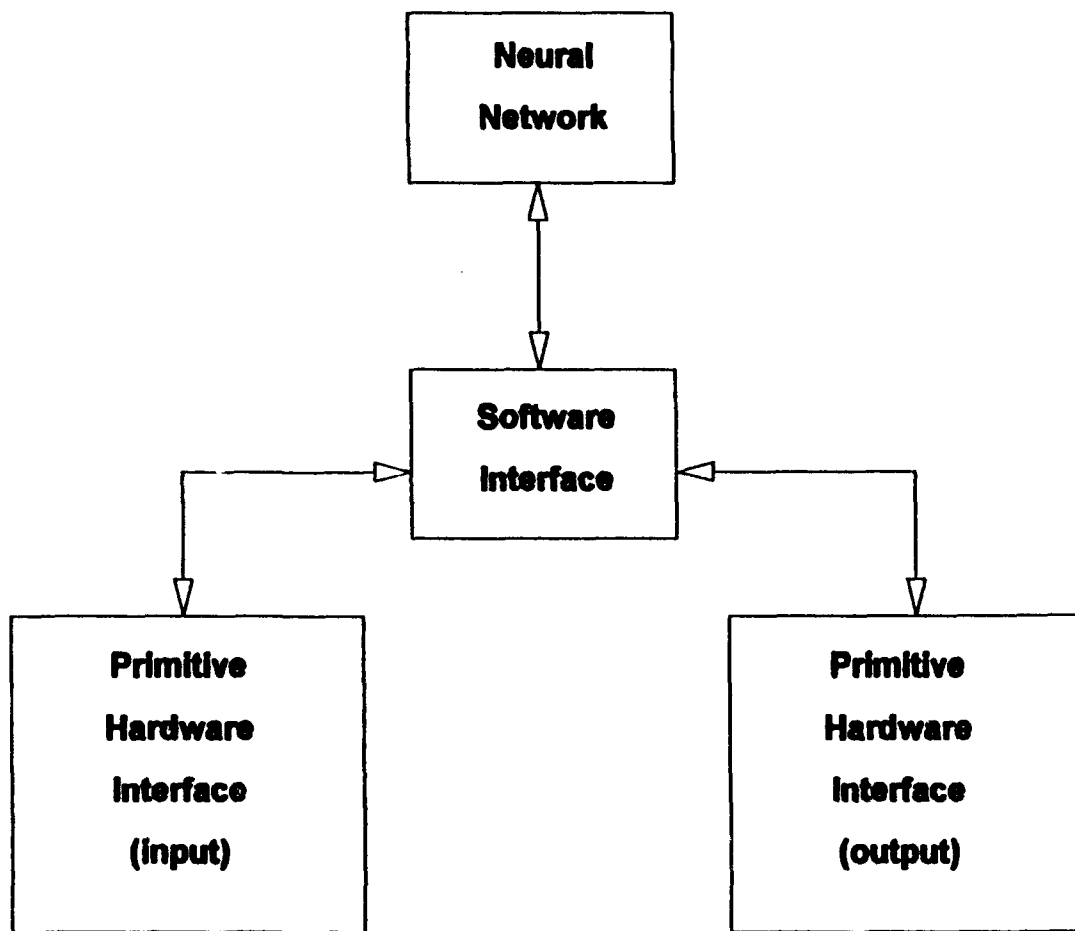


**Figure 18. Elements of the Batch System Program.**

The two primitive hardware interfaces control the hardware directly by writing and reading from memory mapped addresses. These primitives were designed as device drivers, because this provided the most flexibility in the other segments.

The software interface is the "spinal column" of the program. This segment of the program contains three main sections, according to Figure 19. These are the human interface,

neural network interface, and the primitive software interface.

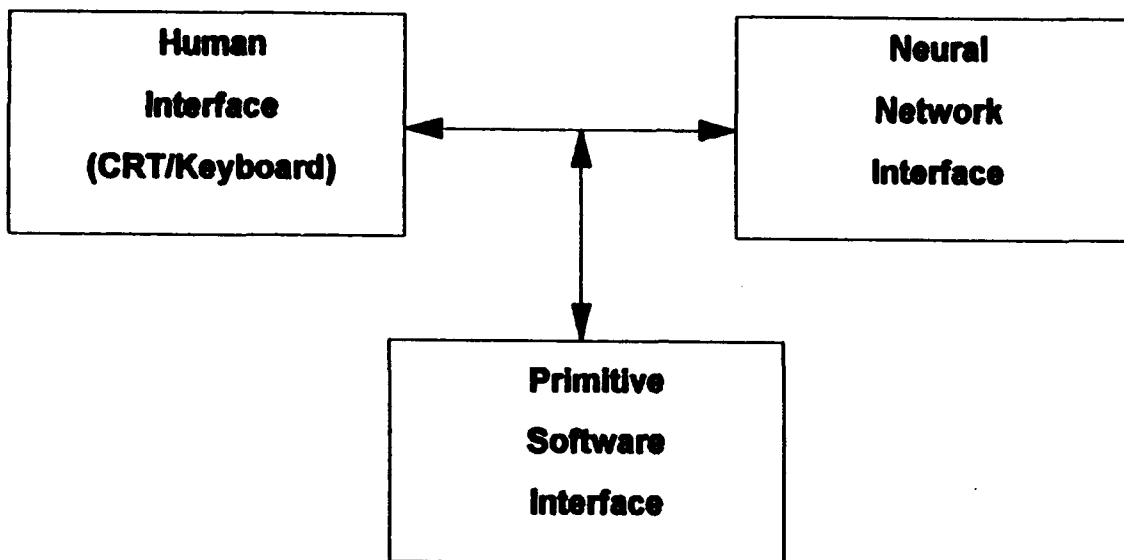


**Figure 19.** Schematic of the Control System.

The human interface section of the program reports progress, accepts input, and selects program functions. This section allows the operator to teach the neural network new sensor patterns. This section allows the operator to use manual control where applicable. This section allows the use of automatic control. In each case the human interface section displays the progress of the process. This section also allows the operator to select various recipes to make under automatic control.

The neural network interface section is the section of the program which takes the primitive data and massages it to input to the neural network. For example the raw data coming off the resistivity sensor is in arbitrary data units. For measurement of the AC resistance of the solution, two raw data measurements have to be combined and fed to the network. This section of the program accomplishes that task. This section of the program also translates the output from the neural network into commands suitable for the other sections of the program to utilize to control the hardware.

The final section of the software interface segment is the primitive software section. Basically, this section interfaces with the two primitive hardware interfaces. This section contains the filling algorithms and input algorithms to pass along the primitive input data to the rest of the program.

The last main segment is the neural network. This is the "brains of the program." This segment, developed with NeuroWindows™, can recognize patterns which it is taught. This

segment will store data patterns for all materials taught, for both well functioning and faulty runs. This segment will be able to diagnose problems, and develop a corrective action.

The primitive hardware interface segments must be written in assembly language. The other two segments can be written in a higher level language. The preferred software that has been chosen for the software interface segment is Visual Basic™ because it has facilities to design a sophisticated human interface, and interfaces with NeuroWindows.™ The initial human interface that has been constructed using Visual Basic™ is shown in Figure 8, and serves as the main user control panel for the final automated batching system. It includes a "Mode" section for the selection of automatic or manual operating states, as well as the option to initiate a "learning session" through either automatic or manual operation. Also, a list of formulations is included. Of course, each formulation will have to be evaluated and formatted for the computer before it can be placed on an activation menu. There is a "View" section that provides the operator with different options to track the process, such as the opening and closing of valves. The final element of the Main Control Panel is a "RESET" button to automatically stop the process and switch ~~all~~ control to manual at one time, in the event that the process needs to be stopped.

The first programming module written utilized the output drivers and was used to control the valves either individually, together, or in the "upper" and "lower" groups. It also includes an "Emergency Stop" function. This module has been used the most and it is the main means by which manual control can be exerted upon the batch system. It has been made into a stand-alone program to run in Windows™, but it does not require Visual Basic™ to be installed. It has its own Windows™ icon, and can be run as any other application. The screen output for this module can be seen in Figure 20.

The second programming module written was a valve timing program to automatically time the opening and closing of valves in any combination, order, or interval. The valve timing panel, as shown in Figure 21, also has its own icon in Windows™, as it is also now a stand-alone program.

The two preceding modules were combined to create a master panel for the mechanical workings of the batch system. All of the elements of each module were included in the combination, but now they work together to give the user a full knowledge of the states of the process with respect to the opening, closing, and timing of process valves. The Timed Valve Control Panel is shown in Figure 22.

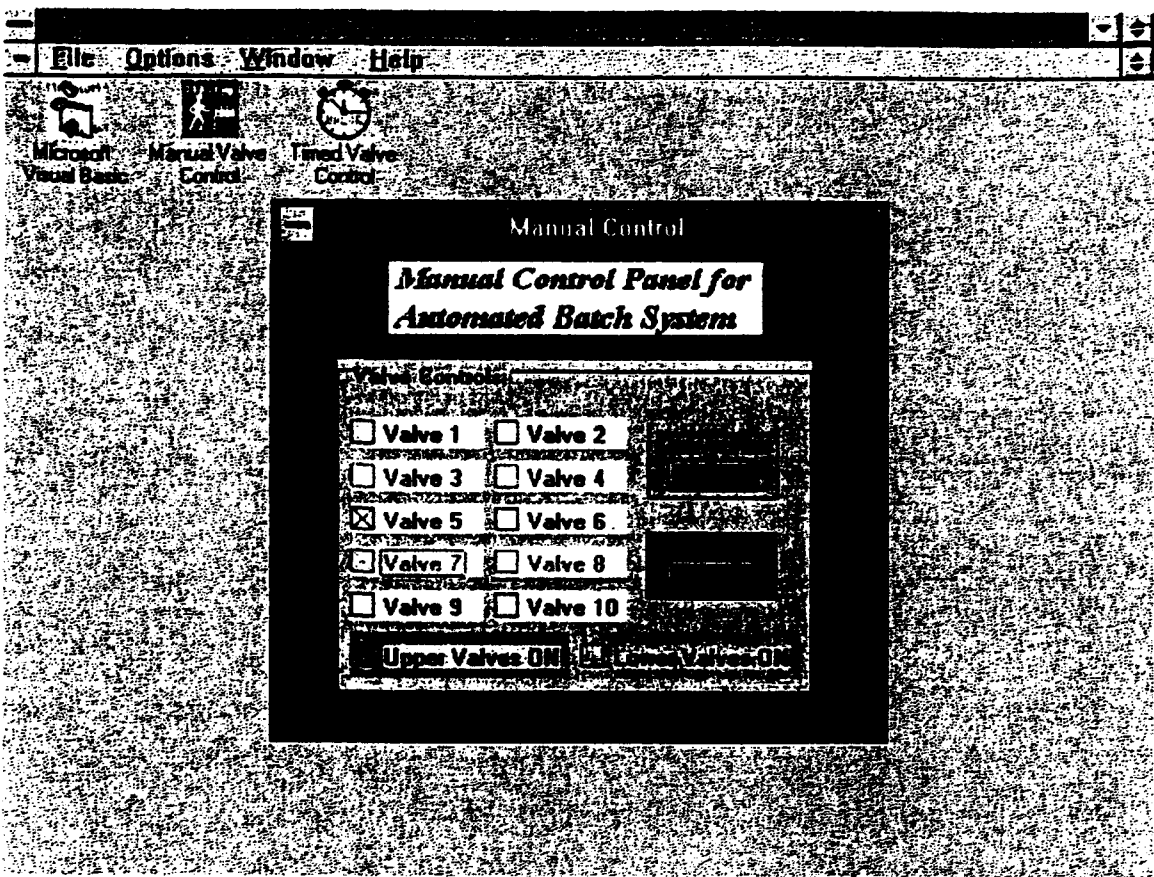


**Figure 20.** Manual Control Panel for Automated Batch System as a stand-alone.

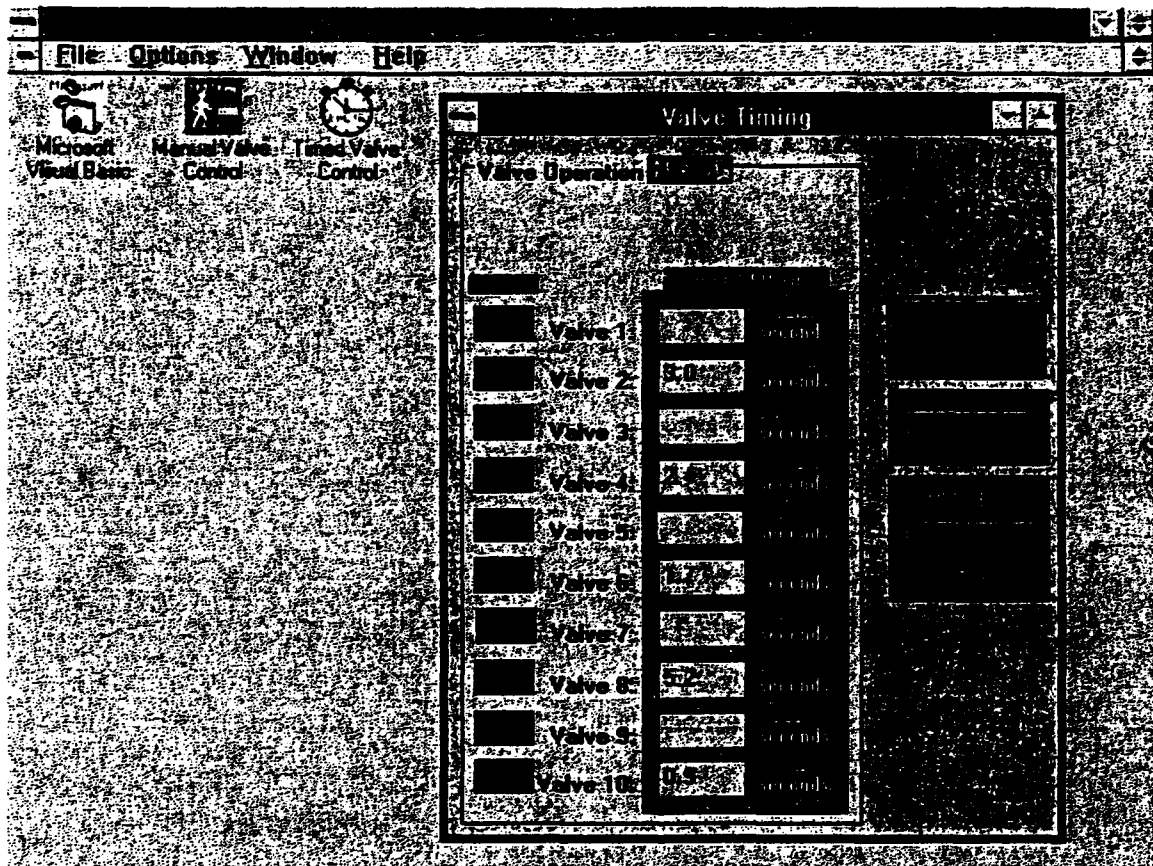


**Figure 21.** Valve Timing Control Panel for Automated Batch System as a stand-alone.

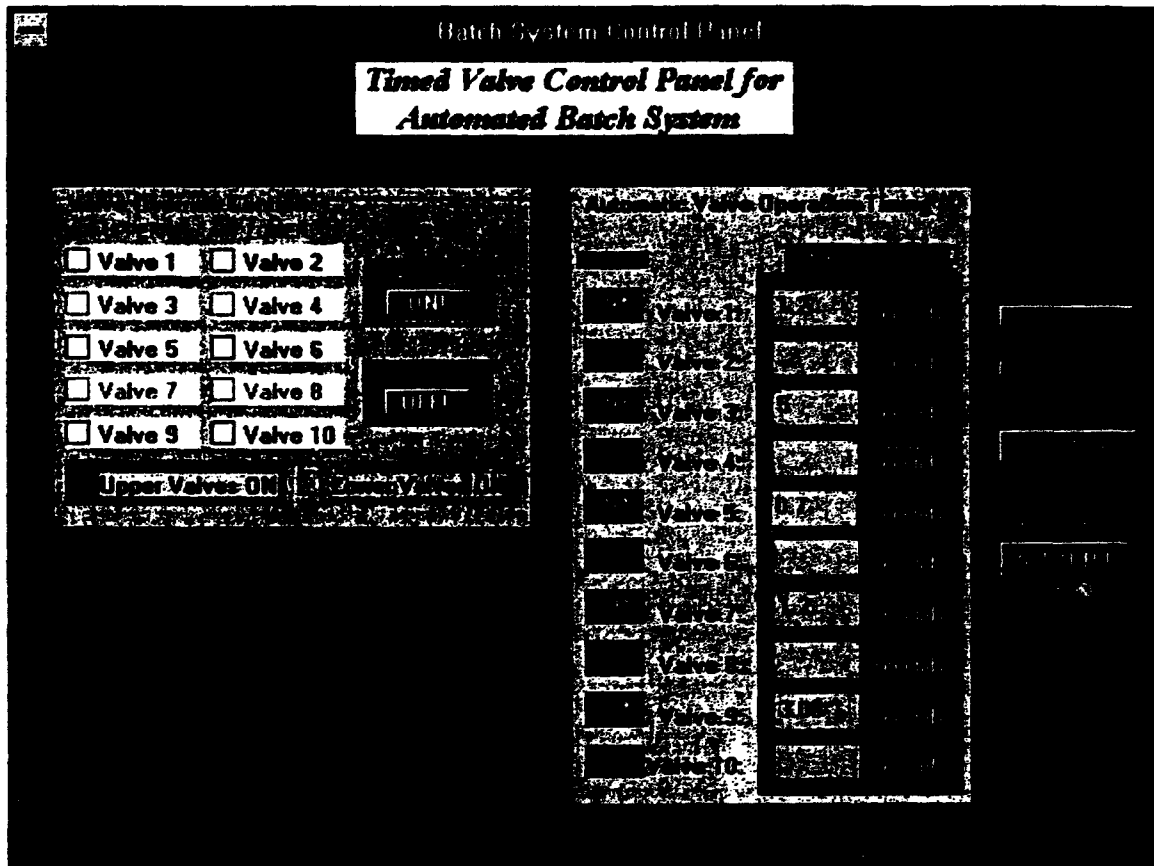


**Figure 22.** Integrated Timed Valve Control Panel for Automated Batch System as an independent program.

**Part III.**

**PLZT Powder Preparation and Characterization**

# **INTELLIGENT PROCESSING OF FERROELECTRIC THIN FILMS**

## **Annual Report**

### **Part III.**

#### **PLZT Powder Preparation and Characterization**

**Submitted by: Youngwoo Moon  
Gene Haertling**

**The Gilbert C. Robinson Department of Ceramic Engineering  
Clemson University**

## **Introduction**

The importance of PLZT ferroelectric ceramics has been grown up as an electrooptic material. Consequently, a great deal of effort has been expended to the development of processing which is responsible to the properties of PLZT ceramics. Chemical homogeneity, physical uniformity, and excellent reactivity have been recognized as the required conditions of advanced ceramic powder. To achieve the purpose, chemical methods such as coprecipitation method, sol - gel process, and hydrothermal process was researched intensively.

The coprecipitation method which is based on the chemical reaction of precursors in an aqueous solution has been studied widely as one of the promising nonconventional methods. However, as a chemical process, the results of coprecipitation are greatly influenced by experimental conditions.

In this study, the effect of pH value was investigated and combined with different precipitating agents. Acetate solutions corresponding to the PLZT system were used as starting materials. To induce metal hydroxide type precipitant, NH<sub>4</sub>OH and KOH were employed. The results were analyzed using FTIR, SEM, and XRD.

## **Experimental Procedure**

The coprecipitation method was used to fabricate PLZT powders. As starting materials, acetate solutions corresponding to the PLZT system were used. They are lead subacetate, lanthanum acetate, zirconium acetate, and titanium acetylacetate. After precipitation, the precipitant powder thus obtained was washed to remove excess ions and then calcined. Fig. 1 represents the experimental procedure. FTIR, SEM, and XRD technique were employed to analyze both precipitant powder and calcined powder.

In view of its chemistry, the precipitation process can be affected by many experimental factors. As a consequence, the characteristics of the fabricated powder are also changed. During the chemical precipitation reaction, the ion activity is greatly influenced by the pH value to change the nature of precipitated powder.

To investigate the effect of pH value on the precipitation of metal hydroxide, NH<sub>4</sub>OH and KOH were used at pH 11 and pH 13.5.

#### **A. Precipitation Process**

The acetate solution corresponding 8/65/35 PLZT system was premixed. The precipitation was performed at room temperature by drop by drop of the mixture into the prepared NH<sub>4</sub>OH solution whose pH value was maintained at 11 and 13.5. In order to keep the pH constant, NH<sub>4</sub>OH solution was added during the precipitation procedure. After precipitation, the centrifuge method was employed to wash the obtained powder. The powder was dried using a conventional drying oven and then calcined at 750 °C for 4hrs to obtain the PLZT powder.

In case of KOH, instead of NH<sub>4</sub>OH, KOH solution was used at the same conditions(i.e. pH 11 and pH13.5). However, the washing was performed more carefully to remove K<sup>+</sup> ion which is harmful for sintering of PLZT ceramics.

#### **B. Characterization Methods**

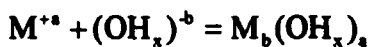
According to the precipitation condition (i.e. pH, concentration, ion type, etc.), the nature of the precipitated metal hydroxide can be varied. To investigate the nature of the precipitated metal hydroxides, FTIR technique was used. To make the FTIR specimen, the dried precipitated powder was mixed with KBr and pressed to make a thin pellet.

The characterization of both precipitated and calcined powder was performed using SEM and X-ray diffraction. Using SEM, the difference of powder morphology was investigated as a function of fabrication conditions. The identification of the crystal phases was performed employing the X-ray diffraction method.

## Results and Discussion

### (1) Precipitation of metal hydroxide

In general, the metal cation ( $M^{+}$ ) can be precipitated in an appropriate condition by making a chemical bond with a hydroxide-type anion in aqueous solution. This chemical reaction is described as :



In the hydroxide ion system, it is known that three kind of ligands are related to the reaction : aquo ligand ( $OH_2$ ), hydroxo ligand (-OH), and oxo ligand (=O). In a different pH value, the existing ions have different activities. Consequently, the variation of the nature of the precipitated powder arises as a function of the pH value while the precipitation process goes on. For example, it is reported that the existence of complex types of metal hydroxides such as  $TiO(OH_2)^{+2}$ ,  $Ti(OH)(OH_2)^{+3}$ ,  $Zr(OH)(OH_2)^{+3}$ ,  $Zr(OH_2)^{+4}$ , and so on. Fig. 2 represents the "charge - pH diagram" which summarize the nature of metal hydroxide as a function of the formal charge  $z$  of the cation  $M^{+z}$  and the pH value of the aqueous solution.

## **(2) Characteristics of precipitant powder.**

The bonding type of precipitant was investigated using FTIR for the powder precipitated at pH 11 in NH<sub>4</sub>OH and at pH 13.5 in KOH. Fig. 3 (a) and (b) show the variation of FTIR spectra, respectively. In case of (a), the extra absorption bands were observed. This means that, when the precipitation proceeded in NH<sub>4</sub>OH solution, more ligands participated in precipitation so as to make the system more complex.

Fig. 4 (a) and (b) show the variation of morphology of the precipitant powders prepared with different precipitating agents. The powder precipitated in NH<sub>4</sub>OH shows spherical shape. The size distribution was in the range of 0.2μm-0.5μm. However, when the precipitation was performed in KOH solution, the powder size was decreased (0.1μm-0.3μm). The morphology cannot easily be distinguished due to strong agglomeration. This can be explained by the difference of the nucleation rate. In case of KOH, the nucleation rate is expected to be faster because of the strong dissociation tendency of KOH.

Fig. 5 shows the SEM micrography of the precipitated powder at pH 13.5 in NH<sub>4</sub>OH. From the comparison of Fig. 5 with Fig. 4 (a), a decrease of particle size and morphology change was observed. It is also considered that the increased nucleation contributed to the change of morphology. The results are summarized in Table 1.

**Table 1** The size distribution and morphology of coprecipitated PLZT powders at different conditions.

	<u>Morphology</u>	<u>Size Distribution</u>
pH 11 in NH <sub>4</sub> OH	spherical	0.2 μm - 0.5 μm
pH 13.5 in NH <sub>4</sub> OH	soft gel	0.1 μm - 0.3 μm
pH 11 in KOH	soft gel	0.1 μm - 0.3 μm

### **(3) Characterization of calcined powder**

After drying the precipitated powder was fabricated, calcination was performed at 750 °C for 4 hrs. Fig. 6 (a), (b), and (c) show the X-ray diffraction patterns of the PLZT powder obtained at different conditions. According to the results of Fig. 6 (a), a significant amount of pyrochlore phase was detected from the powder fabricated in NH<sub>4</sub>OH at pH 11. However, by using KOH or increasing pH value, the pyrochlore phase was decreased significantly. In addition, the crystallinity was enhanced as well. It is considered that the result is related to the nature of the precipitant powder which was analyzed using the FTIR technique.

The morphology of the calcined powders were observed using SEM. Fig. 7 (a) and (b) show the difference of morphology of calcined powder according to the precipitation agent. When the precipitation was performed using KOH, spherical powder was obtained. The particle size was distributed in the range of 0.5μm-2μm. The result is summarized in Table 2.

**Table 2 The size distribution and morphology of calcined PLZT powders precipitated at different conditions.**

	<u>Morphology</u>	<u>Size distribution</u>	<u>Extra Phases</u>
pH 11 at NH <sub>4</sub> OH	irregular	0.3 μm - 2.0 μm	pyrochlore phase
pH 11 at KOH	spherical	0.5 μm - 1.5 μm	none

## **Summary**

The coprecipitation method was studied as a process for fabrication of PLZT powders. PLZT powders were fabricated successfully from the acetate solution by inducing metal hydroxide type coprecipitation using the NH<sub>4</sub>OH and KOH solutions. However, the characteristics of the PLZT powder was changed as a function of coprecipitation condition ( i.e. pH value, precipitation agent). When the precipitation was performed in KOH at pH 11 or in NH<sub>4</sub>OH at pH 13.5, the size of the precipitated powder was decreased and the pyrochlore phase was decreased significantly. Careful washing was required for the powder precipitated in the KOH solution to remove K<sup>+</sup> ion which is harmful for sintering of PLZT ceramics.

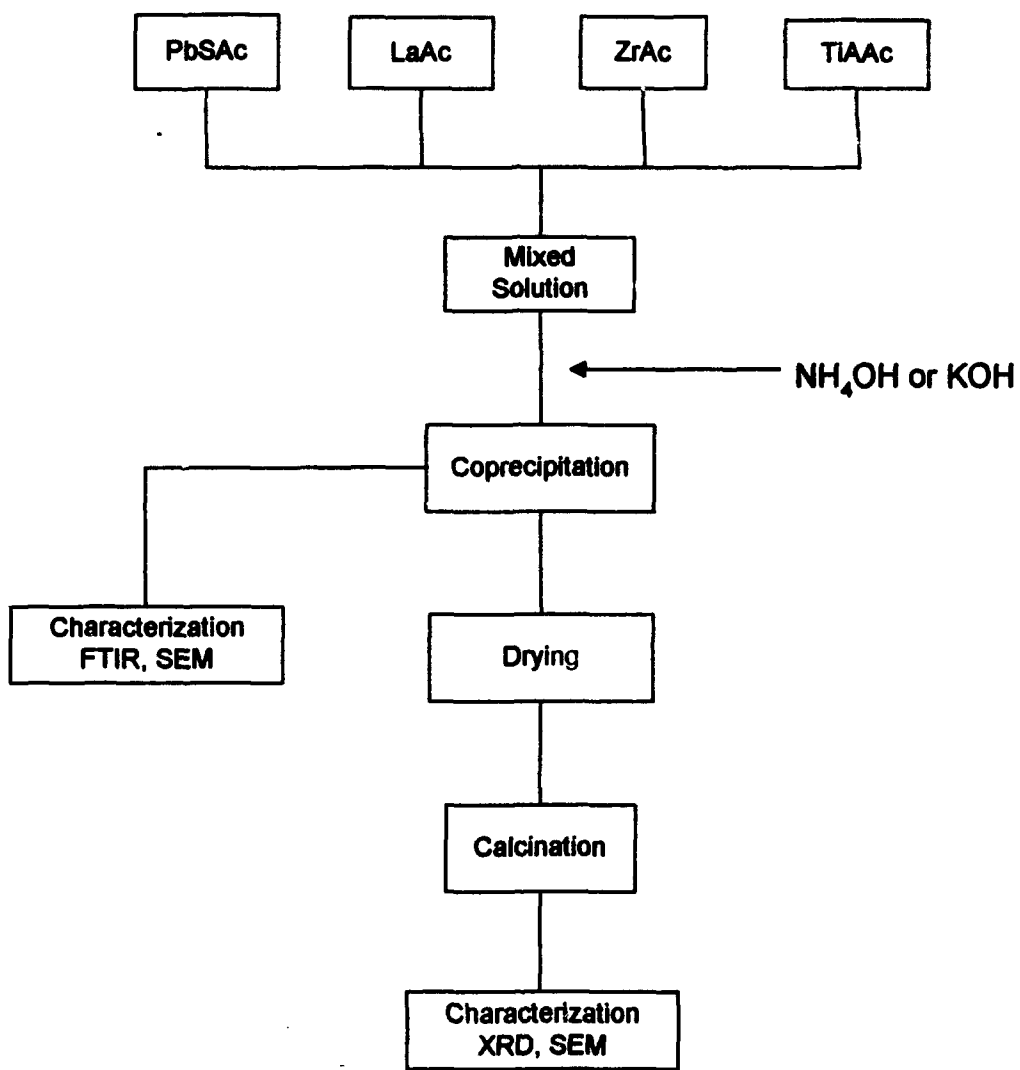


Fig.1 Experimental Procedure of Coprecipitation Method

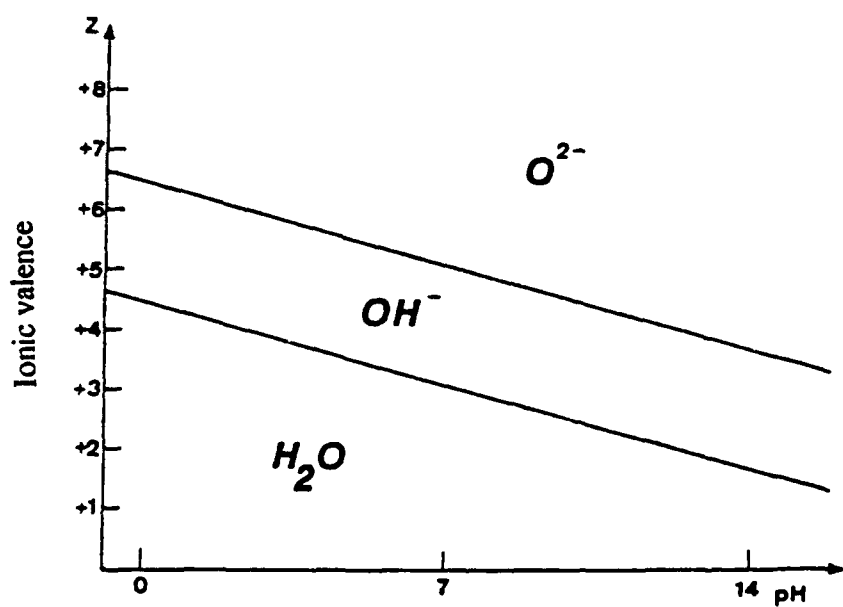
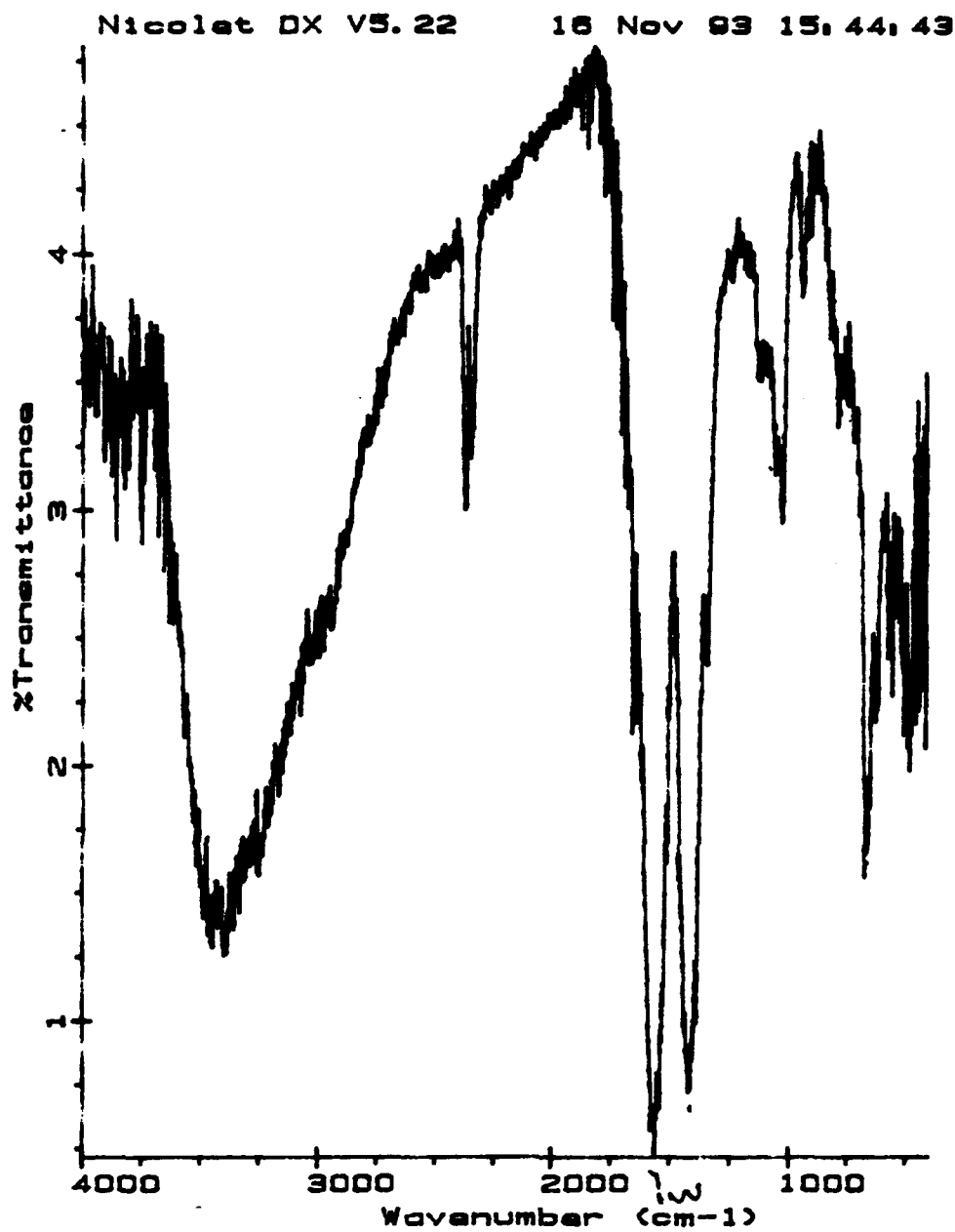
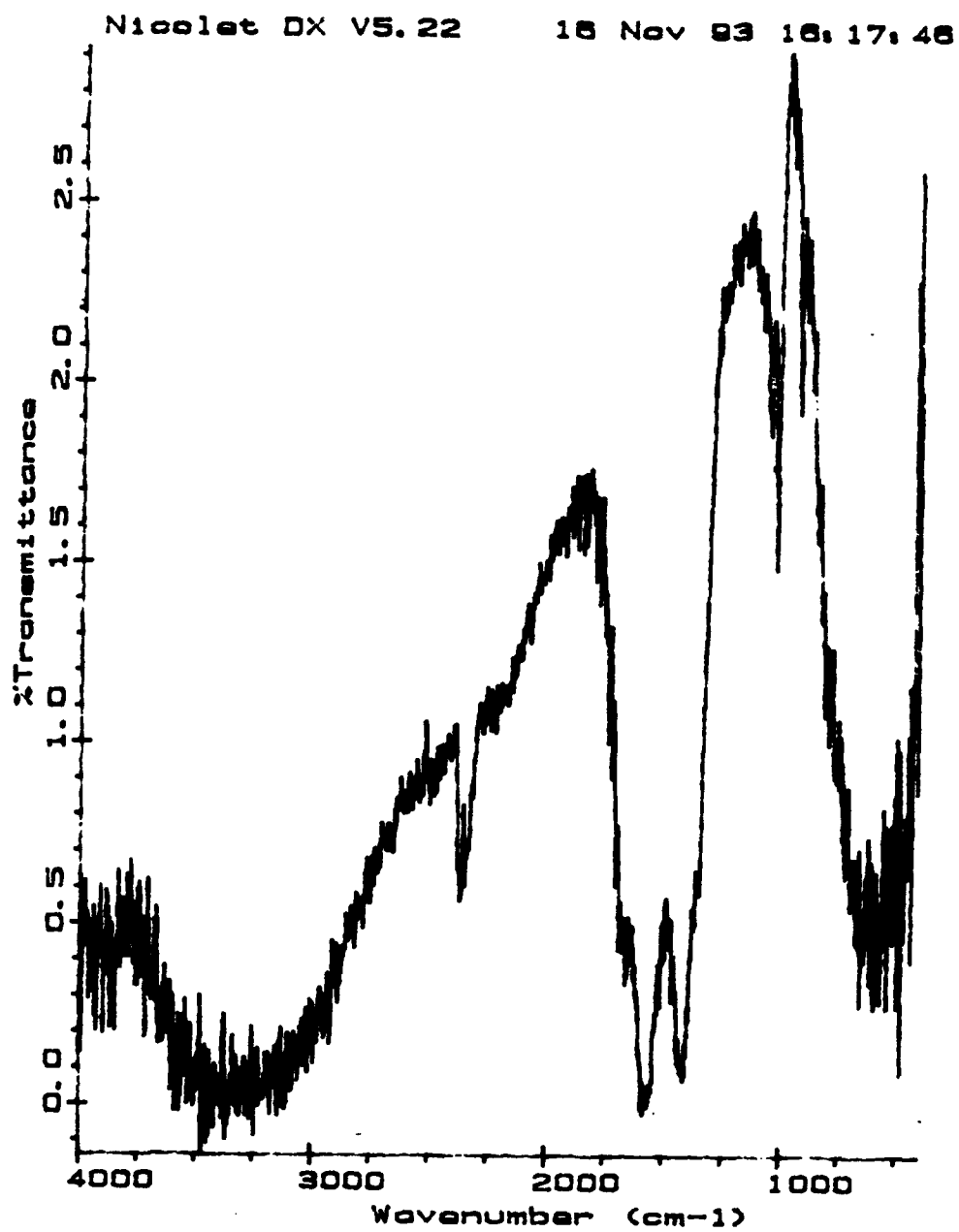


Fig. 2 The stability of metal hydroxides of different ionic valence as a function of pH value.



(a) in  $\text{NH}_4\text{OH}$  at pH 11

Fig. 3 Change in FTIR Spectra of Precipitated Powders at Different Condition.



(b) in KOH at pH 14

Fig. 3 Continued



(a)



(b)

**Fig. 4 Scanning Electron Micrograph of PLZT Powders Precipitated**

(a) in  $\text{NH}_4\text{OH}$  at pH 11

(b) in  $\text{KOH}$  at pH 11

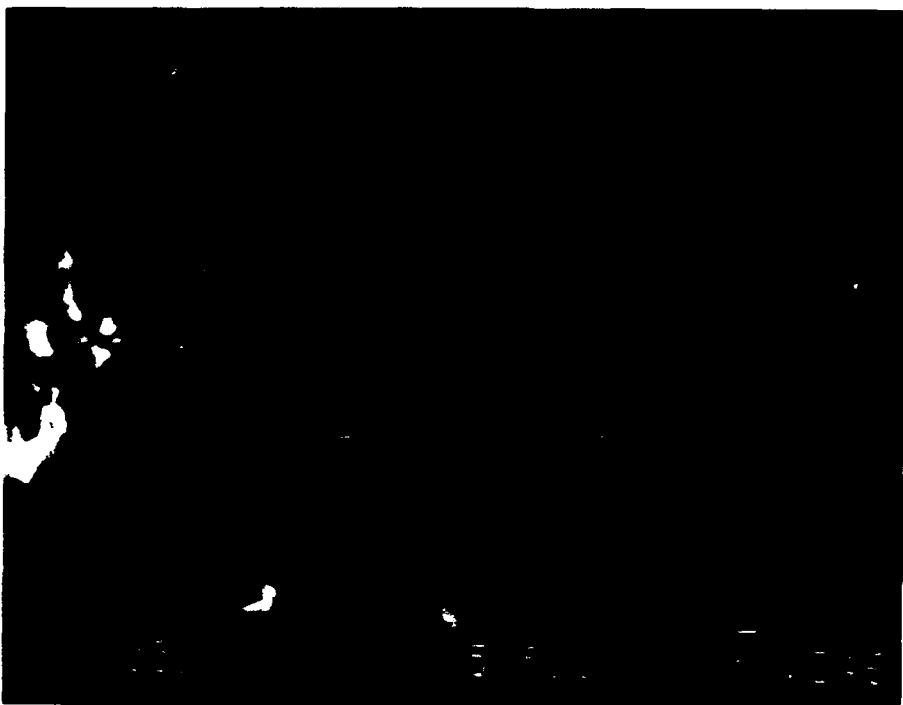
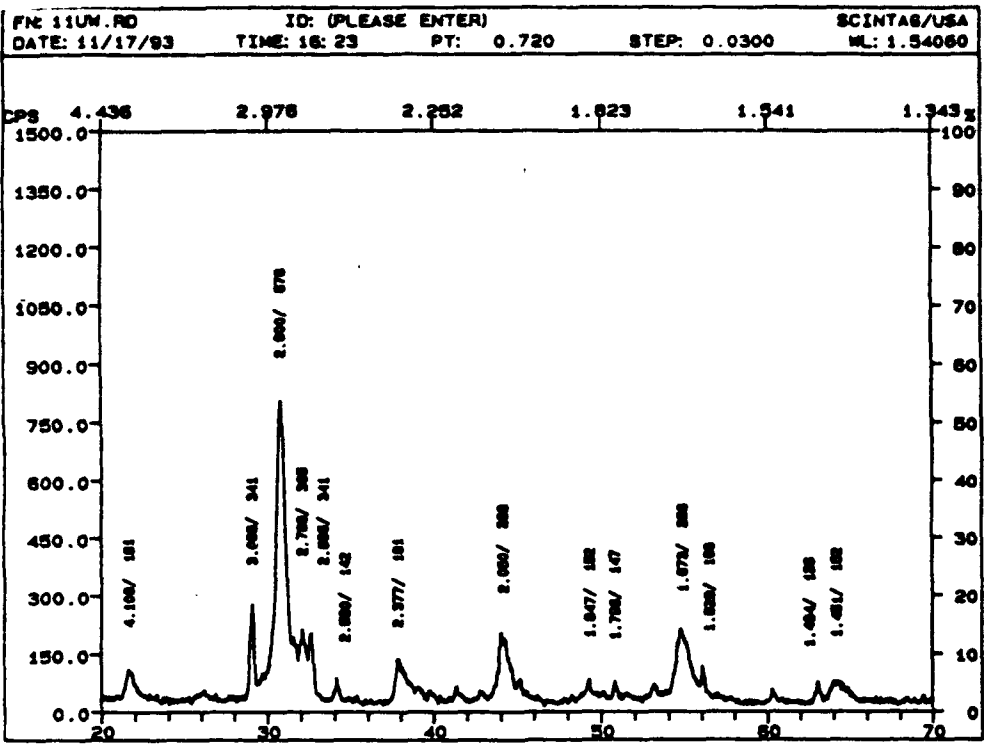
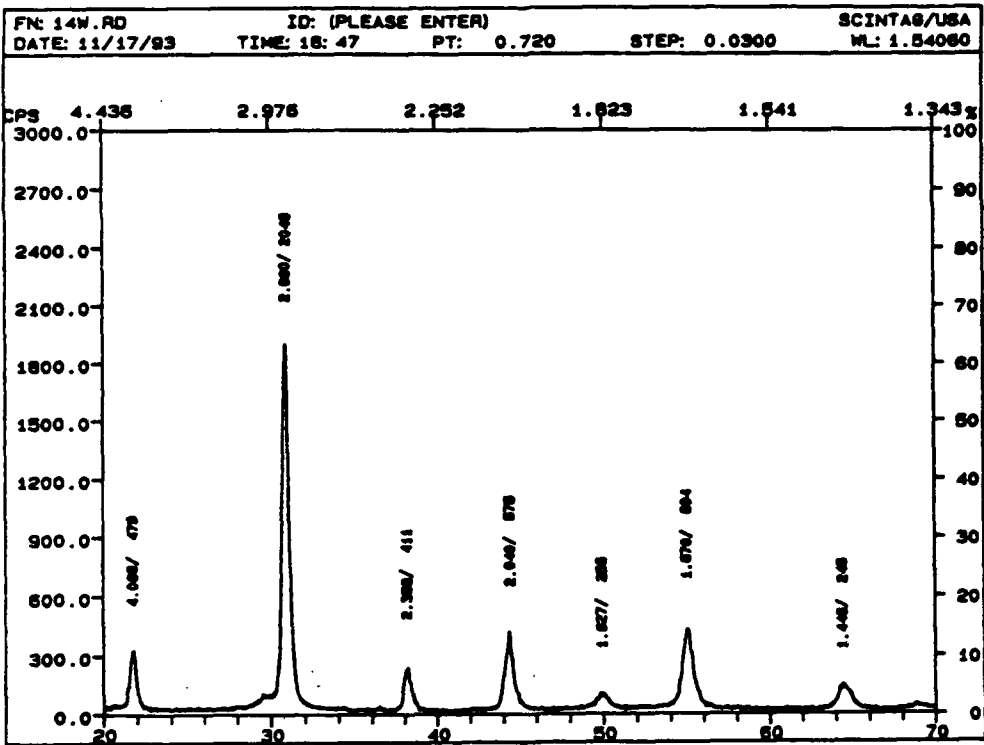


**Fig. 5 Scanning Electron Micrograph of PLZT Powders Precipitated at pH 13.5 in  
 $\text{NH}_4\text{OH}$ .**



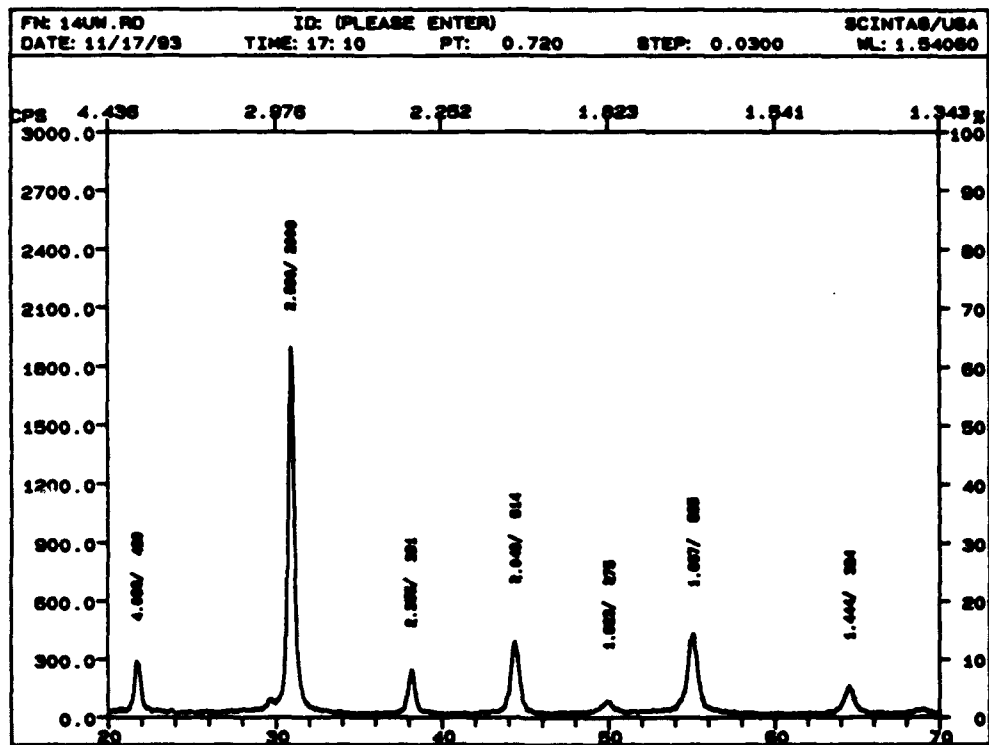
(a)



(b)

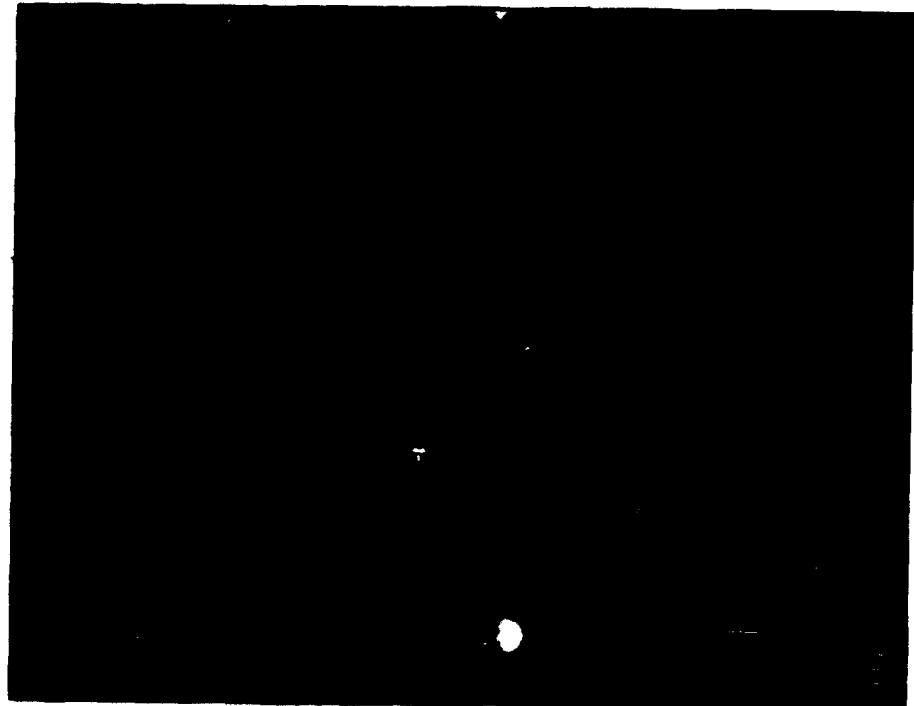
Fig. 6 X-ray Diffraction Patterns of Calcined PLZT Powders Precipitated at Different Condition

(a)  $\text{NH}_4\text{OH}$  at pH 11 (b) KOH at pH 11 (c)  $\text{NH}_4\text{OH}$  at pH 13.5



(c)

Fig. 6 (continued)



(a)



(b)

Fig. 7 Scanning Electron Micrography of calcined PLZT powder at 750 °C for 4hrs.

(a) precipitated in  $\text{NH}_4\text{OH}$  at pH 11

(b) precipitated in  $\text{KOH}$  at pH 13.5

**Part IV.**

**Spin Coated Ferroelectric Thin Films and Bulk Ceramics**

# **INTELLIGENT PROCESSING OF FERROELECTRIC THIN FILMS**

**Annual Report**

**Part IV.**

## **Spin Coated Ferroelectric Thin Films and Bulk Ceramics**

**Submitted by: David Dausch  
Gene Haertling**

**The Gilbert C. Robinson Department of Ceramic Engineering  
Clemson University**

## I. INTRODUCTION

The wide range of applications of PLZT ferroelectric materials, including piezoelectric, dielectric, pyroelectric, ferroelectric, electrostrictive and electrooptic devices, has led to useful bulk electronic ceramic devices such as piezoelectric actuators, multi-layer capacitors and pyroelectric sensors,<sup>1</sup> while newer thin film technology has yielded optical storage devices and ferroelectric memories for integrated circuits.<sup>2</sup> Ferroelectric materials have traditionally been fabricated by a variety of processes including thin film physical (i.e. sputtering, evaporation, laser ablation) and chemical (CVD, sol-gel, MOD) deposition processes as well as bulk ceramic processing techniques (i.e. cold press, tape cast, sintering, hot press); however, the properties of these materials can vary widely due to sample geometry, size and type of deposition process. For instance, thin film devices have extended the applicability of PZT; however, the ferroelectric properties of bulk ceramics normally surpass those of thin films. Diminished thin film properties such as lower dielectric constant ( $K$ ) and remanent polarization ( $P_R$ ) and higher coercive field ( $E_C$ ) and dielectric loss ( $\tan \delta$ ) can be attributed to effects such as smaller grain size of thin film materials, film-substrate or film-electrode interactions and mechanical clamping or stress from the underlying substrate.<sup>3</sup> In some instances, however, thin films possess advantages over bulk ceramics which make them more desirable for many devices and broaden the range of applications for ferroelectric materials. Lower operating voltage, higher speed, easier integration with silicon technology and lower cost are among the advantages favoring thin film ferroelectrics. One goal of "Intelligent Processing of Ferroelectric Thin films" was to fabricate and characterize PLZT thin films produced by new wet chemical techniques and investigate similarities and differences in material properties between these films, traditional vacuum deposited films and chemically prepared bulk ceramic materials.

In order to more fully understand and optimize the behavior of these chemically prepared thin films, a comparison was necessary to more traditional bulk ceramics and vacuum deposited films. Direct correlation between the bulk and thin film materials is typically difficult since the precursors and processing techniques of each are usually so dissimilar; however, a study is presented here that diminishes this disparity. In the same way, thin film chemical and vacuum deposition techniques generally present similar barriers. This research focused on the fabrication and characterization of PLZT thin films and bulk ceramics produced from the same acetate precursor solutions. It is believed that this process allowed for a close comparison of PLZT thin film and bulk ferroelectrics by minimizing or eliminating differences in the processing of these

materials induced by batching variations, precursor impurities and differences in mixing, reactivity and chemical composition of the precursor materials. A study of several PLZT compositions was completed to explore similarities and differences in the behavior of hot pressed bulk ceramics produced from chemically coprecipitated powders and spin coated thin films produced by a metallorganic decomposition (MOD) process. In addition, thin films spin coated from acetate precursors were related to radio-frequency (RF) magnetron sputtered films produced from the coprecipitated powders.

Further optimization of the chemically prepared films involved investigation of different thermal processing techniques and firing schedules. Films were pyrolyzed using rapid thermal processing (RTP) and compared to films pyrolyzed by conventional furnace pyrolysis (CFP). RTP has become an increasingly more popular technique for the fabrication of ferroelectric thin films. The growing interest in utilizing these films as integrated circuit devices<sup>4</sup> has led to the search for a processing technique which is compatible with semiconductor integrated circuits. RTP has been used for many applications in semiconductor IC processing, and this technique possesses advantages over conventional furnace pyrolysis (CFP) that have justified its use for the processing of ferroelectric thin films.<sup>5-8</sup> Such advantages include reduction in the thermal budget or decrease in the temperature and time required to produce the same results, increased heating rate which promotes the formation of the desired crystalline phase and reduced annealing time which minimizes film/substrate reaction, evaporation and electrode degradation.

The properties of PZT and PLZT metallorganic decomposition (MOD) processed thin films fabricated by spin coating have been widely studied.<sup>8-14</sup> These processes typically include a heat treatment and/or post-anneal performed in a conventional box furnace for removal of residual organics and crystallization. CFP, however, is not ideal for the production of actual ferroelectric thin film devices, especially IC devices. Since IC device applications require shorter annealing times and lower annealing temperatures, RTP has been investigated of late as a candidate not only for increasing process compatibility with Si IC technology, but also for improving the properties of PZT and PLZT thin films.<sup>5,7-9,14-16</sup>

Typically, RTP is performed in a separate reaction chamber; however, the ideal situation for IC processing is a single multi-process reactor utilizing RTP.<sup>6</sup> This multi-process reactor would decrease cost and increase flexibility in IC fabrication by incorporating several processes into one automated system. In addition, a cleaner environment would more easily be controlled in a single chamber since many processing steps could be completed without exposure of the wafer to contamination sources outside

of the chamber. Because of the characteristics of RTP which include faster heating rate, shorter annealing times and lower temperatures, RTP enhances the properties of ferroelectric thin films typically produced by CFP.<sup>8,9,14,15,17</sup> The increased heating rate of RTP inhibits the sluggish formation of the undesirable pyrochlore phase and favors the development of the ferroelectric perovskite phase which leads to improved crystallinity. Other improvements include higher dielectric constants, higher remanent polarizations ( $P_R$ ), lower coercive fields ( $E_C$ ), reduced Pb loss due to shorter annealing times and smoother surfaces due to smaller grain size. Optimization of firing schedules included investigation of various firing temperatures and times. More desirable firing schedules resulting in thermal budget reduction were possible with RTP.

In this study, a computer controlled multi-process reactor has been utilized for spin coating and rapid thermal processing of thin films from liquid precursors. This automatic spin coat reactor/analyzer was used to produce PLZT thin films by spinning an acetate precursor solution onto Pt-coated Si substrates and crystallizing the films by RTP. Computer control provides hands-off fabrication and flexibility in processing of the films, while laser ellipsometry, used to perform film thickness analysis within the reaction chamber, provides in-situ analysis of the films. PLZT thin films were produced on 3" diameter and 5/8" square Si substrates with the automatic spin coater. The larger sample was fabricated for a study of thickness uniformity yielded by the spin coating process, and the smaller samples were measured for electrical properties and compared to films spun manually using a photoresist spin technique and pyrolyzed by CFP. Additionally, the thickness uniformity of these films was related to that of RF magnetron sputtered films. This study of PLZT thin films and bulk ceramics derived from the same chemical precursors but fabricated by different processes has provided an accurate comparison of processing techniques by minimization of batching variation between materials and has led to a greater understanding of ferroelectric thin film behavior.

## **II. EXPERIMENTAL PROCEDURE**

### **II.1. Materials Preparation**

A combined batching system was developed to produce chemically prepared PLZT hot pressed ceramics and spin coated thin films using the same batch of water soluble acetate precursors.<sup>3</sup> As shown in the process flow chart in Figure 1, this combined batching produced spin coating solution as well as coprecipitated powder for

bulk ceramics and magnetron sputtering targets from the same acetate formulation. The acetate precursors were chosen primarily for their chemical stability, insensitivity to moisture and low cost. The starting precursors included lead subacetate (PbAc) powder, lanthanum acetate (LaAc), zirconium acetate (ZrAc) and titanium acetyl acetonate (TiAAC) solutions. For processing simplicity and accuracy, PbAc was mixed into solution by the addition of acetic acid and methanol so that all of the acetate precursors were in liquid form. This ensured that the beginning acetate formulation was readily and completely mixed into solution. Incomplete mixing would produce compositional fluctuations between the powder and spin coating solutions. The chemical batching process has reduced the possibility of batching variations between bulk and thin film materials so that similarities and differences in their properties were not a result of these variations.

After initial acetate formulation, the solution was separated into powder and spin coating portions. The powder portion was coprecipitated in a high speed blender with oxalic acid and methanol and then vacuum dried at 70°C to produce a solid, friable cake. The cake was crushed, calcined at 500°C for 8 hours and milled in trichloroethylene for 6 hours to produce a PLZT oxide powder. Typically, 100g of powder was produced for hot pressing, and 50g of powder was used for sputtering targets. Hot pressing conditions were 1200°C for 4 hours at 14 MPa. To prepare samples for electrical measurement, the hot pressed parts were sliced on a diamond saw and lapped to 0.5 mm (20 mil) thickness. Electroless nickel electrodes were plated onto the samples. Excess PbO powder was added to the coprecipitated PLZT powder for sputtering targets in order to compensate for PbO volatilization during sputtering. Films were sputtered onto Pt-coated Si substrates at temperatures of approximately 350°C, total pressure of 10 microns (40% O<sub>2</sub>) and RF power of 50 watts. Film thickness ranged from 0.4 to 0.8 μm. Post-annealing was performed in a conventional Thermolyne furnace at 600-700°C for 40 minutes. Evaporated Cu electrodes were deposited on the films for measurement of electrical properties.

PLZT thin films were also produced on Pt-coated Si wafers with the automatic spin coater which is discussed in the next section. The film deposition cycle was repeated for 5-10 layers yielding a final thickness of 0.4 to 0.8 μm. Films were spun automatically at 2000 rpm for 30 seconds, dried for 3 minutes before RTP, heated at 700°C and cooled to room temperature for 20-30 minutes between layers. Samples used for comparison with manually spun films were heated at 700°C for a total of 15 minutes which was divided into the firing schedules listed in Table I. Typically, rapid thermal annealing is employed as a post-anneal heat treatment in the fabrication of thin films;

however, for this comparison, RTP was used as the sole thermal processing technique for automatically spun films. After the deposition and spinning of 5 individual layers, a rapid thermal heat treatment was performed for 15 seconds to 3 minutes. To ensure good ferroelectric properties in the films, the succession of 5 deposited layers was followed by a rapid thermal post-anneal which provided a combined firing time of 15 minutes. Rapid thermal post-anneals were divided into several shorter segments, no longer than 5 minutes each, to reduce excessive heating of the spin coater chamber. The 15 minute total firing time was chosen for RTP and CFP thin films in order to attribute contrasting film properties to thermal processing technique, or more specifically heating rate, instead of firing time. A rapid thermal post-anneal was used for these films. Films spun automatically for comparison with sputtered films were rapid thermally processed at 600 and 700°C for 1 minute per layer with a 10 minute rapid thermal post-anneal. The temperature controlling thermocouple, which reached 700°C in 2 to 3 seconds, was positioned directly above the sample surface. Actual sample temperature and heating rate, however, were calibrated by contacting an additional measuring thermocouple to the reverse side of the sample. It was found that the back of the substrate reached 700°C in 10 seconds; consequently, the film on the surface of the sample presumably heated at a rate greater than 70°C per second.

For thin film production via manual spin coating, a small portion (usually 5g) of solution was decanted from the acetate formulation and diluted with methanol at a 2:1 ratio by weight. The solution was spun onto Ag foil for comparison with bulk ceramics using a photoresist spinner at 2000 rpm for 15 seconds. After drying for 15 seconds, the spun layer was pyrolyzed at 700°C for 4 minutes in the conventional furnace. Repeating this process for 10 layers produced a PLZT thin film approximately 0.9 μm thick. For measurement of electrical properties, Cu electrodes were applied to the surface of the films via vacuum evaporation. Manually spun films were also produced on Pt-coated Si for comparison with the automatically spun and sputtered films. Conventional furnace pyrolysis was performed at 700°C in the Thermolyne furnace using firing schedules 1-3 in Table I with conventional furnace post-anneals. These post-anneals were also segmented to match the firing conditions of RTP. One initial effect of thermal processing technique should be noted here in that the last two firing schedules in Table I for CFP produced electrically unstable films which readily shorted. RTP permitted individual layer firing times of less than 1 minute. Manually spun films for comparison with sputtered films were pyrolyzed at 700°C for 1 minute per layer for 8 layers with a 32 minute post-anneal for 40 total minutes of heat treatment. The thickness and total firing time of these films was approximately the same as sputtered films annealed at 700°C. A

thermocouple placed above the sample indicated that the furnace reached 700°C in approximately 20 seconds. This implied that the CFP samples heated to the firing temperature at a rate no more than 35°C per second. Hence, the heating rate for RTP thin films was at least twice that for the CFP samples.

## **II.2. Automatic Spin Coater Design**

The automatic spin coat reactor/analyzer, produced by Digital Controls, Inc. in Rolla, MO, utilizes the four basic systems diagrammed in Figures 2-5: fluid dispense system, rapid thermal processing unit, atmosphere control system and in-situ laser ellipsometer. The systems are controlled by an IBM compatible, 80386DX computer with software to operate the ellipsometer and set parameters for deposition, spinning, atmospheric gas control, heating and cooling. Multiple layers can be deposited onto one film with different parameters for each layer, if desired. Samples may be prepared and analyzed without exposure to the external environment. Although described here, the atmosphere control system was not used for this study.

The fluid dispense system has the capability of depositing one of three precursor solutions onto 1/2" to 4" diameter substrates. The fluid, stored in one of the three fluid reservoirs, is pumped by diaphragm-operated resist pumps through a dispense arm onto the substrate. A vacuum pump in conjunction with the resist pumps provides a "suck-back" feature which prevents the fluid from dripping onto the substrate while the sample is spinning. A nitrogen dusting step can also be inserted through the dispense arm before fluid deposition. Located on the left side of the chamber, the dispense arm is moved over the sample chuck for deposition and is returned after spinning. Spinning is executed with an ac brushless servo motor and controller with programmable time, speed and acceleration.

Six water-cooled parabolic strip heaters with infrared quartz lamps containing tungsten filaments comprise the rapid thermal processing unit. Positioned in the rear of the chamber during deposition, the heater assembly is moved forward over the sample stage for heating. The temperature is controlled by a thermocouple placed directly above the sample surface and was calibrated by observing the temperature recorded from a thermocouple located under the sample. This RTP unit allows the sample to be heated to 700°C within 5 to 10 seconds by direct radiation from the parabolic strip heaters.

Variable atmospheric gases (N<sub>2</sub>, O<sub>2</sub>, Ar) and low pressures as well as vacuum capability are possible in the atmosphere control system. The gas or vacuum pressure is

displayed by the computer during atmosphere control before deposition. Oxygen content in the atmospheric gas is monitored by a ZrO<sub>2</sub> oxygen probe and is also displayed.

In-situ thickness measurements are taken before and after heating by a Gaertner Scientific laser ellipsometer ( $\lambda = 6328$  angstroms). The ellipsometer is moved across the surface of the wafer in order to obtain thickness measurements for various locations on the film. An ellipsometer software program calculates the thickness of the film. The laser is passed through the reactor chamber via optical ports at an angle of incidence of 70° from the sample surface normal.

### **II.3. Thin Film and Bulk Ceramic Analysis**

Bulk and thin film samples were analyzed using several electrical and physical measurement techniques. Poled and virgin dielectric constants ( $K_{pol}$  and  $K_{vir}$ ) and dissipation factors ( $\tan \delta$ ) were measured on a Leader LCR meter at 1 kHz. The Curie temperature of bulk samples was determined for several PLZT compositions. Bulk samples were placed in a stirred oil bath and heated while taking capacitance and loss tangent measurements at 5°C increments. Curie temperatures were indicated by maxima in the measured capacitance. Polarization (P) vs. electric field (E) hysteresis loops were also measured for both materials. The bulk samples were measured using a Sawyer-Tower circuit with a dc applied voltage of  $\pm 1400$  V. The hysteresis loops were plotted with a Goerz Metrawatt X-Y plotter. Hysteresis loops of the thin film samples were customarily measured at 1 kHz using a Sawyer-Tower circuit and an oscilloscope readout; however, in order to more accurately compare measurement of bulk and film hysteresis loops, some of the thin film samples were also measured using a low voltage ( $\pm 30\text{-}50$  V) dc looper. Resistivity measurement, obtained in approximately 60 seconds with a 1 V measuring signal, was performed using a Keithley electrometer. X-ray diffraction patterns of thin films and bulk ceramics, produced using a Scintag XDS 2000 diffractometer with Cu K $\alpha$  radiation, and SEM micrographs of spin coated thin films, obtained by a Jeol JSM-IC 848 microscope, were also observed.

A 3" diameter automatic spin coated sample and a 1"x2" rectangular sputtered film were measured for thickness uniformity with the laser ellipsometer. Both films were pyrolyzed at 700°C to form the perovskite phase. The index of refraction for the films was fixed at 2.45 (PLZT for red light), and the index of refraction of the substrate used was 2.33 for Pt. A 775 angstrom standard SiO<sub>2</sub> film on Si was used to calibrate the ellipsometer. Measurements were taken starting from the center of the automatically spun film and again at 1/4" intervals to the edge of the wafer. Another series of

measurements was taken after a 90° rotation of the sample. After completing four of these series of measurements, the data was grouped in order to display two sequences across perpendicular diameters of the wafer. These measurements produced two thickness profiles of the film. Because of heater size restrictions in the sputterer, the sputtered film for thickness uniformity measurements was somewhat smaller than the spin coated film, and only a portion of this film was directly contacted to the heater and could be used for measurement. Non-uniform heating during sputtering can lead to variations in deposition rate. Thickness measurements for the sputtered film initiated near the center of the entire film and traversed the surface of the measurable portion of the film in 1/4" intervals. Three thickness profiles, two across the center and one across the edge of the film, were obtained across the 1 1/2" usable portion of the rectangular film. Ellipsometry, which was also used to determine the thickness of the smaller spin coated and sputtered samples on Si substrates, yielded results consistent with measurements from a Tencor profilometer and laser prism coupler. Because of substrate surface roughness, the thickness of films on Ag foil could not be measured by these techniques and was estimated as approximately the thickness of similar films on Si wafers.

### **III. RESULTS AND DISCUSSION**

Thin films and bulk ceramics derived from the same acetate precursors have been fabricated by several techniques and compared to discover similarities and differences in the properties of these materials. Bulk ceramics hot pressed from chemically coprecipitated powder were compared to thin films manually spin coated on Ag substrates from acetate precursors in order to correlate bulk ceramic devices with thin films. Manually spun films pyrolyzed by CFP were compared with automatically spun films pyrolyzed by RTP in order to investigate the effect of thermal processing technique. Finally, spin coated thin films were compared to RF magnetron sputtered films to relate wet chemical deposition with traditional vacuum deposition of thin films. These topics will be discussed in the following sections.

#### **III.1. Spin Coated Thin Films and Hot Pressed Bulk Ceramics**

Several compositions were chosen for study near phase boundaries in the PLZT system. The morphotropic phase boundary compositions consisted of 2/55/45, 2/53/47

and 2/51/49 which regularly exhibit ferroelectric memory behavior. Compositions approaching and entering the paraelectric phase region with 65/35 Zr/Ti ratios included those with 6, 7, 8, 9, 9.5 and 10% La. These materials typically are memory materials at 6% La and range toward slim-loop ferroelectric materials in the 9 to 10% La range. Hot pressed bulk ceramics and spin coated thin films on Ag foil substrates were fabricated, and a comparison of properties was established.

### III.1.1. DIELECTRIC PROPERTIES

Dielectric and ferroelectric properties are listed for bulk and thin film samples in Table II including virgin and poled dielectric constants and dissipation factors for each. As expected, thin film dielectric constants were generally lower than their bulk ceramic counterparts. These effects have previously been reported to be due to several effects caused by the obvious differences between bulk and thin film configurations including small grain size of the thin films, mechanical clamping effects and voltage sensitivity of the dielectric measurement due to the high electric field applied to a  $<1 \mu\text{m}$  thin film.<sup>3</sup> The difference in dielectric properties found in the present results, however, was not as significant as that reported earlier.

In comparing bulk 2% La samples to thin films, some similarities and differences were noted. Unsurprisingly, both bulk and thin film data showed maxima in  $K_{vir}$  and  $K_{pol}$  at the 2/53/47 composition indicating the existence of the morphotropic phase boundary near this composition; however, the position of the boundary for the thin films seemed to be slightly different than that of the bulk samples.  $K_{pol}$  and  $K_{vir}$  for 2/51/49 thin films was essentially equal to that of 2/55/45 films, while bulk 2/51/49 had a much greater poled dielectric constant than bulk 2/55/45. This result suggested that thin films and bulk ceramics did not behave equivalently near the morphotropic phase boundary since the dielectric constant was expected to peak at this boundary. A comparable result occurred for  $x/65/35$  compositions when the paraelectric phase boundary was encountered. The dielectric constant was expected to reach a maximum at this phase boundary which was previously reported at the 9/65/35 composition for mixed oxide processes.<sup>18</sup> Though both bulk and thin film samples seemed to have maximum dielectric constants at the 9.5/65/35 compositions, the 9/65/35 thin films were closer to 9.5/65/35 than the bulk. Note the occurrence of the high  $K_{pol}$  for the 8/65/35 bulk sample despite the lower  $K_{vir}$  shown by this sample. The bulk ceramics demonstrated a larger difference in dielectric constants between the 9 and 9.5/65/35 compositions. Additionally, the thin film 6/65/35 composition revealed a higher dielectric constant than

the bulk 6/65/35. These results would suggest that bulk and thin film samples showed dissimilar behavior also near the paraelectric phase boundary. Despite the differences in behavior near phase boundaries, the dielectric properties of thin film and bulk samples seemed to have reasonable agreement.

As mentioned above, the expected maximum dielectric constant for x/65/35 bulk ceramics produced via mixed oxide processes was 9/65/35; however, the results in Table II for the chemical process generally indicate a maximum at the 9.5/65/35 composition. Furthermore, the dielectric constants for all of these compositions were higher than values reported for mixed oxide processes.<sup>18</sup> These results could possibly be explained by realizing the type of process used in this study for fabricating bulk ceramics and thin films; i.e., thoroughly mixed acetate precursor solutions to produce chemically derived powders and thin films. This process may provide improved mixing of components which could slightly alter stoichiometry in the bulk and thin film samples-- especially Zr/Ti ratio and dispersion of the La dopant in PLZT. This could have produced higher dielectric constants and shifted the maximum in dielectric constants of these materials to 9.5% La. In order to explore this supposition, Curie temperatures of bulk x/65/35 samples were measured and are shown in Table III and Figure 6. The Curie temperatures measured were consistently 10°C lower than previously reported for bulk samples produced by a mixed oxide process.<sup>18</sup> This result further emphasizes the possibility that the stoichiometries of the chemically prepared materials presented here were slightly different than the mixed oxide materials.

### III.1.2. CRYSTALLINITY AND MICROSTRUCTURE

X-ray diffraction patterns of thin film 8/65/35 and bulk 8/65/35 samples are shown in Figures 7a and 7b, respectively, and the d-spacings for the PLZT peaks are labeled. Due to their greater intensities, the three Ag substrate peaks labeled on the thin film pattern masked three PLZT film peaks expected at the same angles. The thin film sample produced lower intensity PLZT peaks than the corresponding bulk sample. This could have been a result of the thin film having either a lower degree of crystallinity than the bulk sample or simply a smaller quantity of material being analyzed by the diffractometer. In analyzing the lattice spacings of the materials, it was found that the thin film d-spacings were slightly larger than in the bulk material. Watanabe et al.<sup>19</sup> proposed that mechanical stress present in PZT thin films caused by lattice or thermal expansion mismatch between the film and the substrate can cause differences in lattice constant between bulk and thin film materials. Compressive stress caused by thermal

expansion mismatch between Ag and PLZT was the likely cause of the difference in d-spacing observed here. The increase in d-spacing for the thin films was quite small—approximately 0.6 to 1% between the bulk and thin film samples. An absence of larger differences in d-spacings could be attributed to the ductility of the Ag substrates which may have allowed the films to be relatively stress free compared to films fabricated on more rigid substrates (i.e. Si, sapphire, MgO).

Both the film and bulk ceramic yielded similar [110] preferred crystallographic orientation. This was apparent from the high relative intensity diffracted by the (110) plane at a d-spacing near 2.9 angstroms for both the thin film and bulk materials. SEM and optical micrographs of 2/55/45 thin film and bulk ceramic samples, respectively, are shown in Figure 8. As expected, the thin film sample with grain size of less than 0.5  $\mu\text{m}$  exhibited a much finer microstructure than the bulk ceramic which possessed a grain size of approximately 2.5  $\mu\text{m}$ . This phenomenon may in part be responsible for some differences in properties such as lower film dielectric constant and higher film coercive field.

### III.1.3. FERROELECTRIC PROPERTIES

The ferroelectric properties calculated in Table II were taken from the P vs. E hysteresis loops shown in Figure 9. As stated above in the discussion of dielectric properties, both bulk and thin film materials indicated a transition across the morphotropic phase boundary. This transition was also evident in the hysteresis loops of the materials. In the bulk materials, the transition was obvious with a widening of the hysteresis loop signaling the emergence of the tetragonal phase in the 2/51/49 material. This phenomenon, however, did not occur in the thin film samples. The tetragonal phase was evident in the dc hysteresis loops of the thin films by a slightly more square hysteresis loop for 2/51/49 than for the rhombohedral 2/55/45 film. The phase transition was apparent in both ac and dc hysteresis loops of the films by a rise in remanent polarization in the 2/53/47 film. Previous work mentioned that thin films have a lower  $P_R$  and higher  $E_C$  than bulk materials for reasons similar to differences in dielectric properties mentioned above (grain size, clamping, voltage sensitivity).<sup>3</sup> Although the thin films presented here with 2% La had a higher  $E_C$ , the  $P_R$  of these films was not necessarily lower than for bulk materials. In fact, 2/53/47 and 2/51/49 films had a higher  $P_R$  than bulk samples of the same composition. Again, as with dielectric properties, the ferroelectric properties of the thin films seemed to be different across the phase boundary than the bulk ceramics. This was also the case for x/65/35 materials.

In PLZT bulk x/65/35 samples, the hysteresis loops obtained were similar to those expected for these compositions. The remanent polarizations and coercive fields calculated were lower than reported mixed oxide values,<sup>18</sup> and this can possibly be attributed to the difference in processing between the coprecipitation and mixed oxide processes as discussed above. As anticipated, the 6, 7 and 8% La materials were memory materials, and the 9, 9.5 and 10% La materials were slim-loop materials. For the memory materials,  $E_C$  was higher and  $P_R$  was lower for thin films than for bulk materials which was similar to previously reported results.<sup>3</sup> Although both bulk and thin film memory materials experienced narrowing of their hysteresis loops with increasing %La, the bulk materials transformed to slim-loop materials at 9% La, while the thin films maintained ferroelectric memory hysteresis loops beyond 9% La. Research by Gu et al.<sup>20</sup> on quenched PLZT 9.5/65/35 ceramics showed that internal stresses induced in quenched samples can enhance polar region ordering and produce a more ferroelectric-like response. This produced higher remanent polarizations in quenched samples than in annealed samples. These findings could explain the memory behavior observed in the 9, 9.5 and 10/65/35 thin films in this study. Residual stresses in the thin films which could have produced the differences in d-spacings discussed above may have caused these films to retain ferroelectric memory hysteresis loops that were not observed in the bulk materials of the same compositions. As with the dielectric properties, some differences in behavior near phase boundaries was evident between the thin film and bulk materials; however, the thin films in this study had ferroelectric properties comparable with the bulk ceramic materials produced.

### **III.2. Thin Films Pyrolyzed by RTP and CFP**

As discussed earlier, thin films of composition 2/55/45 were produced by automatic and manual spin coating with the application of rapid thermal processing (RTP) and conventional furnace pyrolysis (CFP), respectively. Different thermal processing techniques have yielded differences in thin film properties, and this study reveals some of these effects.

#### **III.2.1. PHYSICAL PROPERTIES**

Previous investigators have found that because of much higher heating rates, the perovskite phase forms more readily with RTP than with CFP.<sup>9,15</sup> In addition, sharper, more intense x-ray peaks have been observed in rapid thermally processed films

indicating improved crystallinity.<sup>8,14</sup> X-ray diffraction patterns of the rapid thermally processed thin films for this study are displayed in Figure 10. The films seemed to show some preferential orientation in the [110] and [111] directions. Upon comparison of these films to the conventional furnace pyrolyzed films in Figure 11, the CFP films were generally oriented in the [100] direction. The (110), (111) and (211) peaks of the RTP films were more intense than the corresponding peaks in the CFP films. Similarly, the (100) and (200) peaks of the CFP films were more intense than those of the RTP films. It is interesting to note that the 2/55/45 composition is a rhombohedral phase, and rhombohedral distortion from the cubic unit cell is along the [111] direction; furthermore, the polarization direction of the rhombohedral unit cell is the [111] direction. Consequently, it can be inferred that a [111] or [110] orientation would be more beneficial for this composition than [100] since the dipoles will more easily align in the polarization direction. Another general observation from the diffraction patterns of the entire group of films related to the firing schedule. For both processes, the crystallinity improved as the firing time per layer decreased and the post-anneal time increased. In addition, more peak splitting was observed in the (111) and (211) peaks of the films fired longer per layer with less post-anneal for both types of films. All of the films in this study were found to be perovskite phase with no pyrochlore detected by x-ray diffraction.

SEM micrographs of chemically etched rapid thermally processed and conventional furnace pyrolyzed thin films are shown in Figures 12 and 13, respectively. As with x-ray diffraction, these micrographs indicated a single phase material where any difference in brightness denoted height in the samples caused by etching. As expected, the grain sizes of the RTP films were smaller than for the CFP films. The finer microstructure becomes particularly apparent when comparing Figures 12a and 13a which display films from the two different processes with equivalent firing schedules. Many finer grains were revealed in the RTP film which were not seen in the CFP film. Previous investigators have observed smaller grain size for RTP films due to faster heating rate which reduces the time for grain growth.<sup>8</sup> A more substantial difference in morphology was observed with changes in firing schedule. For both RTP and CFP, the grain size of the film fired for less time per layer with longer post-anneal was much finer, approximately 0.1 to 0.2  $\mu\text{m}$ , than the grain size of the film fired 3 minutes per layer, roughly 0.3 to 0.5  $\mu\text{m}$ . Since longer dwell times have been found to enhance grain growth in rapid thermally annealed thin films,<sup>5</sup> the coarse grain structures exhibited in Figures 12a and 13a are attributed to longer individual layer firing times.

### III.2.2. ELECTRICAL PROPERTIES

The dielectric and ferroelectric properties of the automatically spun and manually spun films are shown in Tables IV and V, respectively. With respect to firing schedule, it was observed that the properties improved as the firing time per layer decreased and the post-anneal time increased. Dielectric constants increased, coercive fields decreased and remanent polarizations showed some increase with shorter firing time per layer and longer post-anneal; however, the dissipation factors also increased with these parameters which may have indicated some conduction. A high measuring field of approximately 20 kV/cm caused by the 1 V ac signal of the LCR meter across a 0.5  $\mu\text{m}$  film may also explain the high dissipation factors and lead to somewhat higher dielectric constants. The resistivity of all of the films was on the order of  $10^{11} \Omega\text{-cm}$ .

Automatically spun films with RTP also exhibited improved properties compared to manually spun films with CFP. Dielectric constants were higher and coercive fields were lower for RTP thin films. Remanent polarizations, however, did not seem to increase with RTP. One possible reason for this improvement in properties was the difference in orientation between these films. The dipoles of the RTP films have switched easier and aligned better with the [111] polarization direction of the rhombohedral phase in the measuring direction of the films. Another advantage of the automatically spun films was the capability of rapid thermally processing for less than 1 minute per layer. As discussed previously, the manually spun films were electrically unstable and did not yield well-developed hysteresis loops under these heating conditions. The possibility of processing for only 15 to 30 seconds per layer with RTP is promising for IC device production; however, some post-annealing is still necessary. Automatically spun films with 30 second individual layer firing times and no post-anneals possessed dielectric constants less than 300 and poorly developed hysteresis loops.

Film thickness, measured by the ellipsometer, is also listed in Tables IV and V. The thickness of the automatically spun films, roughly 0.5  $\mu\text{m}$ , was somewhat higher than the manually spun films, approximately 0.4  $\mu\text{m}$ , even though all of the films were 5 layers thick. Thickness differences likely occurred because solution for manual spinning was dispensed sparingly by hand, and the fluid pumps of the automatic spin coater could only release larger amounts of solution onto the substrate. In addition, there was a slightly longer pause between the fluid dispense and spin stages in automatic spinning as the computer processed information for the next stage.

Figure 14 displays the P vs. E hysteresis loops of the 2/55/45 thin films. RTP yielded films with slimmer, better-saturated hysteresis loops. The maximum voltage applied to the films was approximately  $\pm 25$  V; however, the film spun manually with CFP for 1 minute per layer could only withstand  $\pm 15$  V without electrically shorting. More asymmetry was observed in the hysteresis loops of the RTP films compared to the CFP films. This observation is not yet understood; however, possible factors inducing this asymmetry include interaction between the PLZT and bottom Pt electrode, the presence of a barrier or porous layer at this interface, differences in behavior between the Cu and Pt electrode interfaces and differences in the crystallinity or stress caused by rapid heating effects.

### **III.3. Automatic Spin Coated and Magnetron Sputtered Thin Films**

This comparison investigates the properties of 2/55/45 films produced by two different processes-- traditional vacuum deposition and newer wet chemical deposition. Batching variations have been minimized as with the comparison of bulk ceramics and thin films by deriving coprecipitated powder for sputtering targets and acetate solution for spin coating from the same acetate formulation. In order to emulate typical automatic spin coating and sputtering processes, conventional furnace post-anneals of 40 minutes were used for sputtered films while much shorter rapid thermal post-anneals were available for spin coated films. Manually spun films were also produced with longer conventional furnace post-anneals to eliminate thermal processing technique as a variable and attribute differences in film properties to deposition technique.

#### **III.3.1. THICKNESS UNIFORMITY**

An important property when considering IC device manufacture and reliability is thickness uniformity of the ferroelectric film across the surface of the Si wafer substrate. Variation in thickness could mean variation in properties and performance; hence, uniform thickness is a critical factor in producing a wafer with the maximum possible yield of consistent devices. A PLZT film on a 3" diameter Si wafer produced by the automatic spin coat reactor/analyizer was analyzed using the laser ellipsometer. Figure 15 displays the thickness profiles obtained for this film. The thickness of the film was determined to be  $4291 \pm 151$  angstroms for the first profile and  $4293 \pm 120$  angstroms for the second profile revealing a maximum thickness variations of 7 and 5.6%, respectively. Upon closer examination, however, it appeared that most of this variation

occurred on the outer portion of the film. This could have been caused by greater stresses on the outer portion of the film causing larger thickness variation, or the variation could have been a result of the nature of the spinning process which builds up more solution on outward regions of the wafer. In addition, the film had some discolored areas on its outer section corresponding to cavities in the sample chuck. The thickness variation corresponded to these areas which may have cooled more quickly or been at a slightly lower temperature than the rest of the film. When neglecting the outer two measurements on each side of the profiles or, in other words, when only considering the inner 1.5" diameter of the wafer, the thickness was even more uniform. As shown in Figure 16, the maximum variation in this case was 1.5 to 2% with an average thickness of 4317 and 4297 angstroms. Considering these results, the automatic spin coater appeared to produce uniform films with most of the variation in thickness occurring on the outer portion of the 3" coated wafer.

Thickness profiles of the 1"x2" sputtered film are plotted in Figure 17. This film had rings of discoloration which corresponded to an initial decrease in thickness on outer portions of the film. Mean thicknesses ranged from 6552 and 6479 angstroms in the center to 6149 angstroms on the edge profile with variations of 12.6 and 15.4% in the center to 13.5% on the edge of the film. As with the spin coated film, most of the thickness variation occurred on outer portions of the film. As shown in Figure 18, the first 1/2" in the center of the film yields much less thickness variations of 0.8, 1.8 and 3.8%. Mean thickness values are 6732 and 6755 angstroms in the center and 6110 angstroms on the edge. Both processes produced to some extent quite uniform thicknesses in the center of the films; however, with the available equipment, spin coating produced a slightly more uniform film center and over a larger area than did sputtering. In addition, vacuum deposition by sputtering produced twice as much thickness variation over the entire film area as wet chemical spinning.

### III.3.2. CRYSTALLINITY

Figures 19 and 20 display x-ray diffraction patterns of automatically spin coated and sputtered films heat treated at 700 and 600°C, respectively. As in section III.2.1, a slight difference in preferred crystallographic orientation was observed in the spin coated film rapid thermally processed at 700°C compared to the conventional furnace pyrolyzed sputtered film; however, the sputtered film had a much higher degree of crystallinity due to the much longer post-anneal of 40 minutes compared with 10 minutes of the spin coated film. More intense (100) and (111) peaks were observed in the sputtered film,

while (110) and (111) peaks were the most intense of the spin coated film. The films heat treated at 600°C had the same preferred orientations, i.e. both had (100) and (111) as the strongest peaks, but the sputtered film again exhibited a higher degree of crystallinity. It is also interesting to note that bulk ceramics, as in Figure 7, exhibited [110] orientation with only minor (111) peaks, while these spin coated and sputtered films on Si exhibited strong [111] orientation with either strong (110) or (100) peaks in addition.

### III.3.3. ELECTRICAL PROPERTIES

Table VI displays the dielectric and ferroelectric properties of sputtered and spin coated films. The first two films for spin coating were spun automatically with 10 minute rapid thermal post-anneals. Films with 32 and 40 minute post-anneals were produced by CFP. Higher dielectric constants were obtained for sputtered films with long post-anneals; in fact, these values were nearly double the 2/55/45 bulk ceramic values. This rise in dielectric constant may be attributed to the strong [111] preferred orientation of the rhombohedral sputtered films compared to the [110] orientation of the bulk ceramics or to the high 20 kV/cm measuring field of the LCR meter (1 V signal). These dielectric constants were also higher than those of the automatically spun films with shorter rapid thermal post-anneals; however, dielectric properties comparable with bulk ceramics were obtained by RTP with much shorter annealing times. A manually spun film with 40 total minutes of CFP also yielded higher dielectric constants than the automatically spun films indicating some influence of the longer post-anneal.

Typical hysteresis loops of the films are shown in Figure 21. Both automatic spinning and sputtering produced highly square, well-developed hysteresis loops for films on Si substrates. The sputtered film annealed at 700°C obtained higher  $P_R$ , and the 600°C annealed film possessed lower  $E_C$  than the automatically spun film which may have been indications of the higher degree of crystallinity in the [111] rhombohedral polarization direction. Because of this crystallinity, polarization switching seemed to occur more readily in these sputtered films.

## IV. CONCLUSIONS

PLZT thin films and bulk ceramics were fabricated from the same acetate precursor solutions in order to minimize batching variations and accurately compare

properties between thin film samples produced by various deposition techniques and bulk ceramics. A combined batching system provided acetate solution for automatic and manual spinning and coprecipitated powder for RF magnetron sputtering targets and hot pressed bulk ceramics. It is believed that this process provided complete mixing of precursors and accurate batching of materials by minimizing batching differences that could cause serious variations in composition and properties of bulk and thin film PLZT ferroelectrics. In order to characterize and optimize thin films produced by wet chemical deposition or MOD processing techniques, a comparison of thin films spin coated from acetate precursors to traditional vacuum deposited (sputtered) thin films and bulk ceramics (hot pressed) was completed.

Thin films spun on Ag substrates were observed to have comparable properties with bulk ceramic materials; however, there were some differences in behavior. It was found that materials near the morphotropic phase boundary with 2% La differed in behavior. Maximum dielectric constants were found at 2/53/47 for both materials; however, the bulk 2/51/49 had a proportionally higher dielectric constant than the thin film when compared to their respective 2/55/45 samples. The hysteresis loops of the bulk samples indicated a transition to a tetragonal phase with a widening of hysteresis loops (increased  $E_C$ , decreased  $P_R$ ). Thin films also indicated a transition but with a maximum in  $P_R$  for the 2/53/47 composition. Bulk x/65/35 materials behaved as expected with the exception of slightly lower Curie temperatures, coercive fields and remanent polarizations and slightly higher dielectric constants than previously reported for mixed oxide processes. The 6, 7 and 8/65/35 materials produced memory hysteresis loops, and the 9, 9.5 and 10/65/35 materials produced slim hysteresis loops. The thin film memory loops were somewhat slimmer than the bulk memory loops, and continual narrowing of the loops occurred toward the paraelectric phase boundary; however, slim-loop ferroelectrics were never completely achieved in the thin film materials. X-ray diffraction analysis showed that thin film lattice spacings were slightly greater than the corresponding bulk spacings, and both materials exhibited preferred orientation in the [110] crystallographic direction. Thin films, with grain size of less than 0.5  $\mu\text{m}$ , also exhibited much finer grain structures than bulk ceramics with grain size of 2.5  $\mu\text{m}$ .

Spin coated thin films on Si substrates pyrolyzed by RTP were also found to have comparable dielectric properties with bulk ceramics. Sputtered films exhibited improved dielectric properties; however, much longer post-anneals were required to attain these levels. Films produced by both deposition techniques produced well-saturated hysteresis loops. A higher degree of crystallinity was obtained in sputtered films compared to spin coated films; however, films from both processes revealed preferred orientations in the

[111] rhombohedral polarization direction. Although both deposition processes yielded films with only small thickness variation in the central region of the films, spin coating produced films with 5-7% variation over the entire film while sputtering produced variations of 12-15% over the entire film surface.

One major advancement in the processing compatibility of thin films with IC manufacture was the utilization of a unique automatic spin coat reactor/analyser. This computer controlled automatic spin coater combines deposition, rapid thermal processing and in-situ thickness analysis for thin film production without removal of the sample from the reaction chamber. Since RTP enhances the properties of the films as well as improves the compatibility of their fabrication with IC manufacture, rapid thermal processing has become a valuable technique for the processing of PLZT thin films. In order to investigate the effects of thermal processing technique on thin film processing, automatically spun films with RTP were compared with manually spun films with CFP. It was discovered that the RTP thin films experienced heating rates at least twice that of the CFP films.

Thin films crystallized by RTP were found to have preferred orientations different from those of thin films processed by CFP. Rapid thermal processing enhanced the [110] and [111] orientations, while conventional furnace pyrolysis generally produced the [100] orientation. In this respect, RTP presumably has allowed the rhombohedral PLZT 2/55/45 films to more easily align in the polarization direction. Crystallinity was also found to improve with shorter individual layer firing and longer post-anneal. The morphology of the films was greatly affected by firing schedule. Films fired for less time per layer with longer post-anneals had much finer grain structures than the films fired 3 minutes per layer. Additionally, the rapid thermally processed films consisted of smaller grains than their conventional furnace pyrolyzed counterparts. The electrical properties of the films produced by RTP were improved over CFP films. Dielectric constants were higher, coercive fields were lower and hysteresis loops were better saturated. Electrical properties also improved with shorter individual layer firing and longer post-anneal. Somewhat high dissipation factors and hysteresis loop asymmetry was also discovered. Nevertheless, the automatic spin coater with the application of rapid thermal processing demonstrated improvements in the properties and processing of PLZT thin films.

From these studies, a greater understanding of ferroelectric thin film behavior has been achieved. Good correlation of dielectric properties was observed between bulk ceramics and manually spin coated films on Ag substrates and automatically spun films on Si substrates. Substrate effects such as thermal expansion mismatch resulted in shifted thin film lattice spacings and the absence of slim-loop behavior in thin films.

Thermal processing also produced substantial variations in properties such as high dielectric constants in sputtered films resulting from a high degree of crystallinity in the [111] direction. Because of increased heating rates, RTP significantly improved thin film properties compared to CFP and allowed shorter annealing times and lower temperatures. It is essential to investigate these types of phenomena in order to optimize ferroelectric thin film performance for actual device application; furthermore, it is believed that this research has created the foundation for future research in this area.

## V. REFERENCES

1. G. H. Haertling, "Piezoelectric and Electrooptic Ceramics," in Ceramic Materials for Electronics, ed. R. C. Buchanan, Marcel-Dekker, Inc., New York, 139 (1986).
2. L. M. Sheppard, *Am. Cer. Soc. Bull.*, **71**, 85 (1992).
3. G. H. Haertling, *Proc. IEEE 7th International Symposium on Applications of Ferroelectrics*, 292 (1990).
4. Y. Xu and J. D. MacKenzie, *Integrated Ferroelectrics*, **1**, 17 (1992).
5. J. Chen, K. R. Udayakumar, K. G. Brooks and L. E. Cross, *J. Appl. Phys.*, **71**, 4465 (1992).
6. F. Roozeboom and N. Parekh, *J. Vac. Sci. Technol. B*, **8**, 1249 (1990).
7. M. Sayer, *Proc. 3rd International Symposium on Integrated Ferroelectrics*, 1 (1991).
8. L. Shi, S. B. Krupanidhi and G. H. Haertling, *Integrated Ferroelectrics*, **1**, 111 (1992).
9. B. A. Tuttle, R. W. Schwartz, D. H. Doughty, J. A. Voigt and A. H. Carim, *Mat. Res. Soc. Symp. Proc.*, Vol. **200**: "Ferroelectric Thin Films," (eds. E. R. Myers and A. I. Kingon), 159 (1990).
10. R. A. Lipeles and D. J. Coleman, *Ultrastructure Proc. of Adv. Ceram.*, (eds. J. D. MacKenzie and D. R. Ulrich), John Wiley & Sons, New York, 919, 1987.

11. R. W. Vest and J. Xu, *Ferroelectrics*, **93**, 21 (1989).
12. A. H. Carim, B. A. Tuttle, D. H. Doughty and S. L. Martinez, *J. Am. Ceram. Soc.*, **74**, 1455 (1991).
13. G. H. Haertling, *Ferroelectrics*, **116**, 51 (1991).
14. H. Hu, L. Shi, V. Kumar and S. B. Krupanidhi, *Ceramic Transactions*, Vol. **25**: "Ferroelectric Films," (eds. A. S. Bhalla and K. M. Nair), 113 (1992).
15. H. Hu, C. J. Peng and S. B. Krupanidhi, *Thin Solid Films*, **223**, 327 (1993).
16. C. V. R. Vasant Kumar, R. Pascual and M. Sayer, *J. Appl. Phys.*, **71**, 864 (1992).
17. S. B. Krupanidhi, *Proc. 3rd International Symposium on Integrated Ferroelectrics*, 23 (1991).
18. G. H. Haertling, Engineered Materials Handbook, vol. **4** (Ceramics and Glasses), ASM International, 1124 (1991).
19. H. Watanabe, T. Mihara and C. A. Paz De Araujo, *Proc. 3rd International Symposium on Integrated Ferroelectrics*, 139 (1991).
20. W. Y. Gu, E. Furman, A. Bhalla and L. E. Cross, *Ferroelectrics*, **89**, 221 (1989).

**TABLE I.** Firing schedules for automatically (RTP) and manually (CFP) spun thin films. The total firing time was 15 minutes. All films consisted of 5 deposited layers.

	time per layer (X5 layers)	post-anneal*
1)	3 minutes	None
2)	2 minutes	5 minutes
3)	1 minute	10 minutes
4)	30 seconds**	12.5 minutes
5)	15 seconds**	13.75 minutes

\* Rapid thermal or conventional furnace anneal

\*\* Only possible with RTP

TABLE II. Dielectric and ferroelectric properties of PZT hot pressed bulk ceramics and manually spin coated thin films.

BULK CERAMICS							THIN FILMS		
Kpol	tan δ(pol)	Kvir	tan δ(vir)	EC (dc) [kV/cm]	PR (dc) [uC/cm <sup>2</sup> ]	EC (ac) [kV/cm]	PR (ac) [uC/cm <sup>2</sup> ]		
2/55/45	1328	.029	1293	.033	8	46	--	--	
2/53/47	1885	.025	1391	.028	10	40	--	--	
2/51/49	1630	.024	1234	.034	16	33	--	--	
6/65/35	1355	.036	1774	.056	6	33	--	--	
7/65/35	2712	.033	2479	.036	5	31	--	--	
8/65/35	5700	.055	4692	.050	3	20	--	--	
9/65/35	5147	.054	5007	.050	0	0	--	--	
9.5/65/35	5658	.048	5603	.046	0	0	--	--	
10/65/35	5548	.036	5538	.033	0	0	--	--	
2/55/45	997	.122	1228	.133	27	34	43	32	
2/53/47	1265	.132	1619	.160	28	47	44	45	
2/51/49	972	.122	1237	.146	28	38	46	37	
6/65/35	1871	.142	1995	.141	14	21	28	25	
7/65/35	2499	.170	2460	.145	14	18	27	21	
8/65/35	3211	.194	3172	.176	11	15	22	19	
9/65/35	4221	.195	4001	.172	9	11	22	17	
9.5/65/35	4234	.190	4092	.164	7	8	19	18	
10/65/35	4157	.193	4157	.209	7	10	18	16	

**TABLE III.** Curie temperatures of PLZT x/65/35 bulk ceramics.

Composition	T <sub>c</sub>
7/65/35	140
8/65/35	100
9/65/35	70
9.5/65/35	65
10/65/35	60

**TABLE IV.** Electrical properties of automatically spin coated, rapid thermally processed thin films.

temp/time (anneal) [min]	Kpol	tan δ	Kvir	tan δ	E <sub>C</sub> [kV/cm]	P <sub>R</sub> [μC/cm <sup>2</sup> ]	t [μm]
700/3	715	.085	811	.111	64	10	.48
700/2 (5)	952	.125	985	.150	43	12	.52
700/1 (10)	1090	.147	1190	.155	47	12	.47
700/0.5 (12.5)	1704	.217	2013	.229	41	17	.50
700/0.25 (13.75)	1628	.193	2079	.221	34	10	.49

**TABLE V.** Electrical properties of manually spin coated, conventional furnace pyrolyzed thin films.

temp/time (anneal) [min]	Kpol	tan δ	Kvir	tan δ	$E_C$ [kV/cm]	$P_R$ [μC/cm <sup>2</sup> ]	t [μm]
700/3	597	.090	640	.130	104	11	.41
700/2 (5)	638	.088	814	.156	78	10	.40
700/1 (10)	740	.120	1061	.305	63	13	.41

**TABLE VI.** Electrical properties of automatically spin coated and magnetron sputtered 2.55/45 thin films.

Automatic spin coating							
temp/ time (anneal)	Kpol	tan δ	Kvir	tan δ	Ec kV/cm	PR uC/cm <sup>2</sup>	t(μm)
600/1 (10)	1160	.103	1189	.088	45	15	.76
700/1 (10)	1090	.147	1190	.155	47	12	.47
700/1 (32)	1437	.140	1371	.113	47	18	.63

Magnetron Sputtering							
temp/ anneal	Kpol	tan δ	Kvir	tan δ	Ec kV/cm	PR uC/cm <sup>2</sup>	t(μm)
600/40	2193	.136	2027	.070	25	15	.82
700/40	2290	.139	1972	.081	40	24	.65

PbAc. HAc. MeOH

PbSAC

LaAc

ZrAc

TiAAc

H<sub>2</sub>O

ACETATE FORMULATION

DILUTE

MIX

- Oxalic Acid

- Methanol

MANUAL SPIN COAT  
AUTO SPIN COAT  
DIP COAT

DRY

DRY

CALCINE

PYROLYZE

PLZT OXIDE POWDER

MILL

SINTERED LAYER

HOT PRESS

ADD EXCESS PbO

PLZT THIN FILM

PLZT BULK CERAMIC

R.F. SPUTTER

ELECTRODE

MACHINE

POST-ANNEAL

ELECTRODE

PLZT THIN FILM

ELECTRODE

Figure 1. Combined batching system for the fabrication of acetate solution and coprecipitated powder from the same stock acetate formulation.

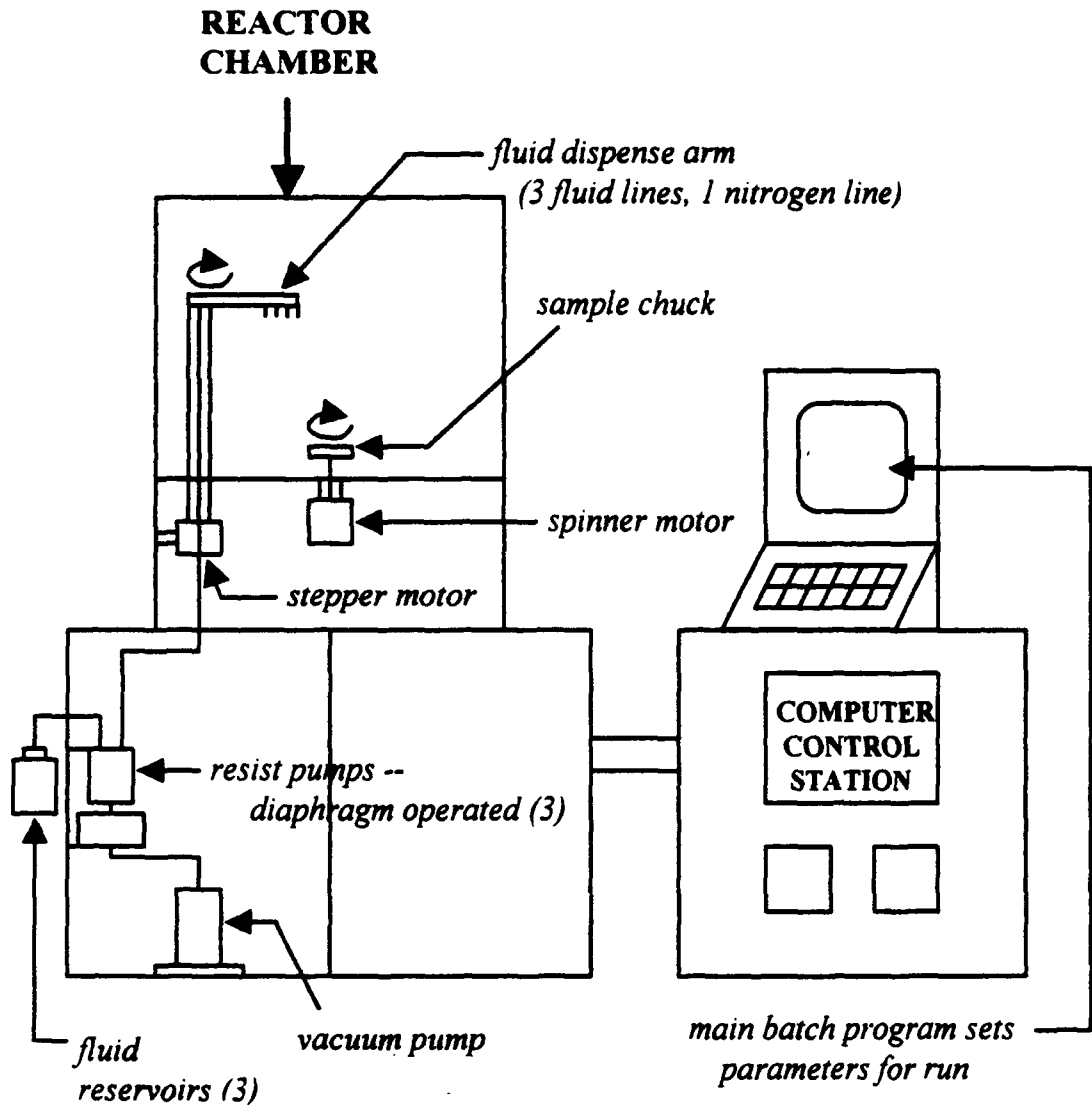


**Figure 2.** Fluid dispense system of the automatic spin coater.

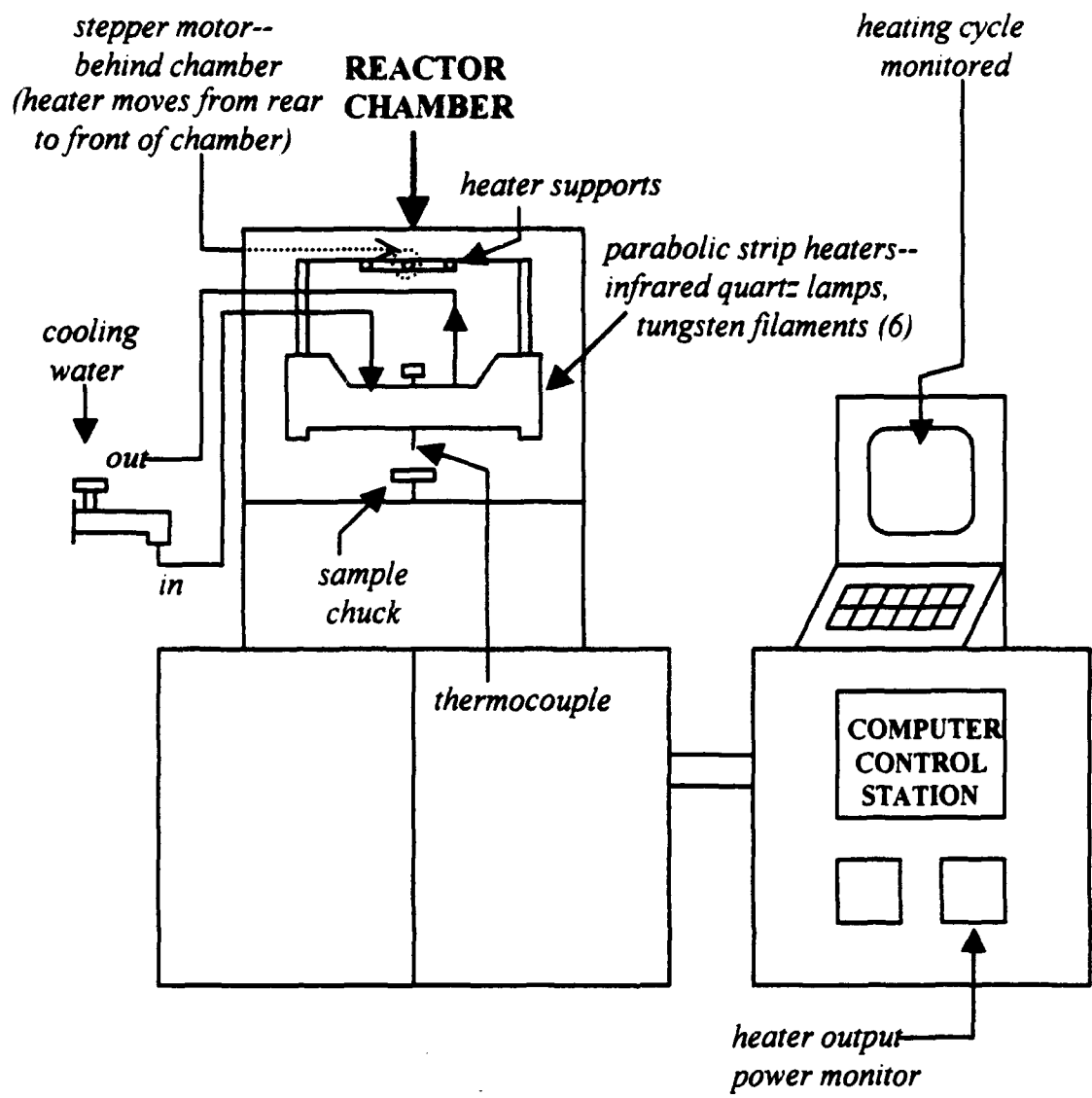


**Figure 3.** Rapid thermal processing unit of the automatic spin coater.

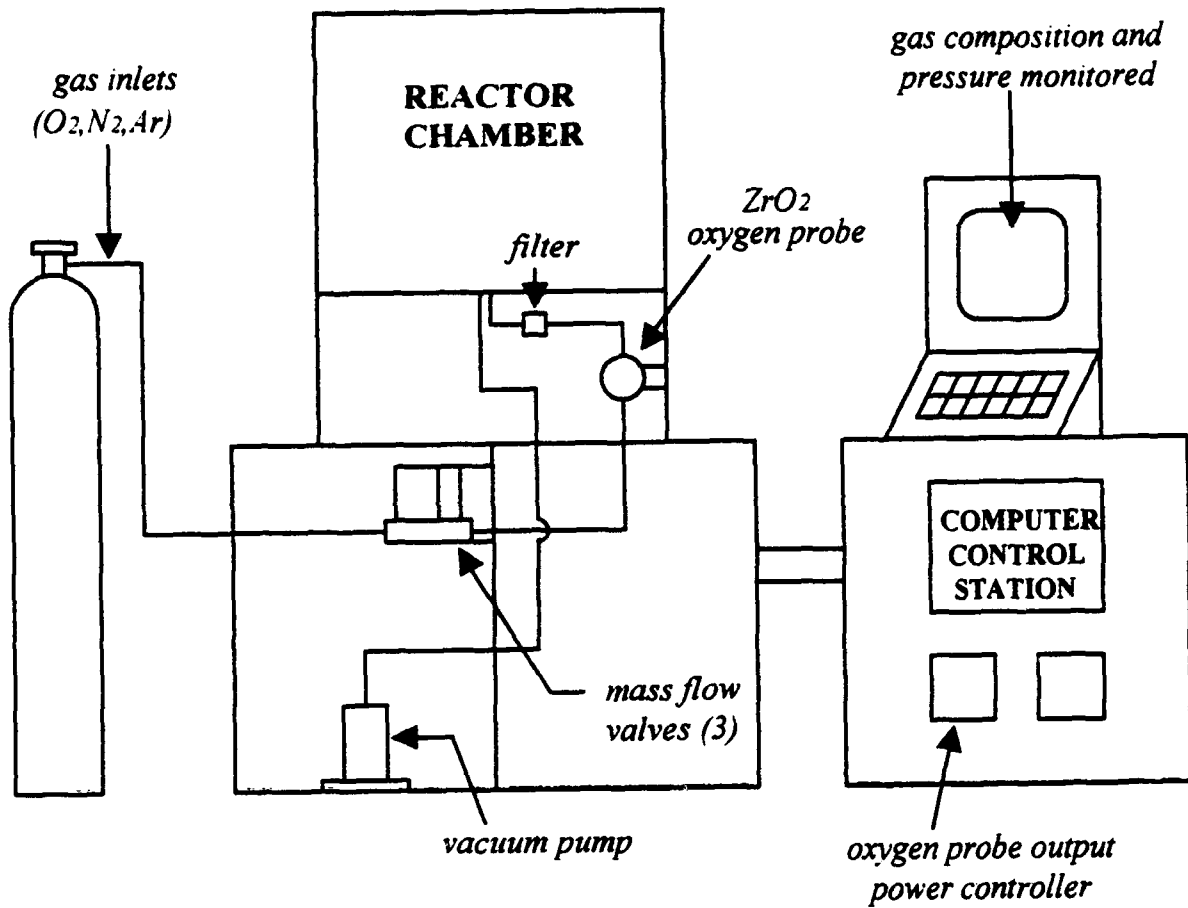


**Figure 4.** Atmosphere control system of the automatic spin coater.

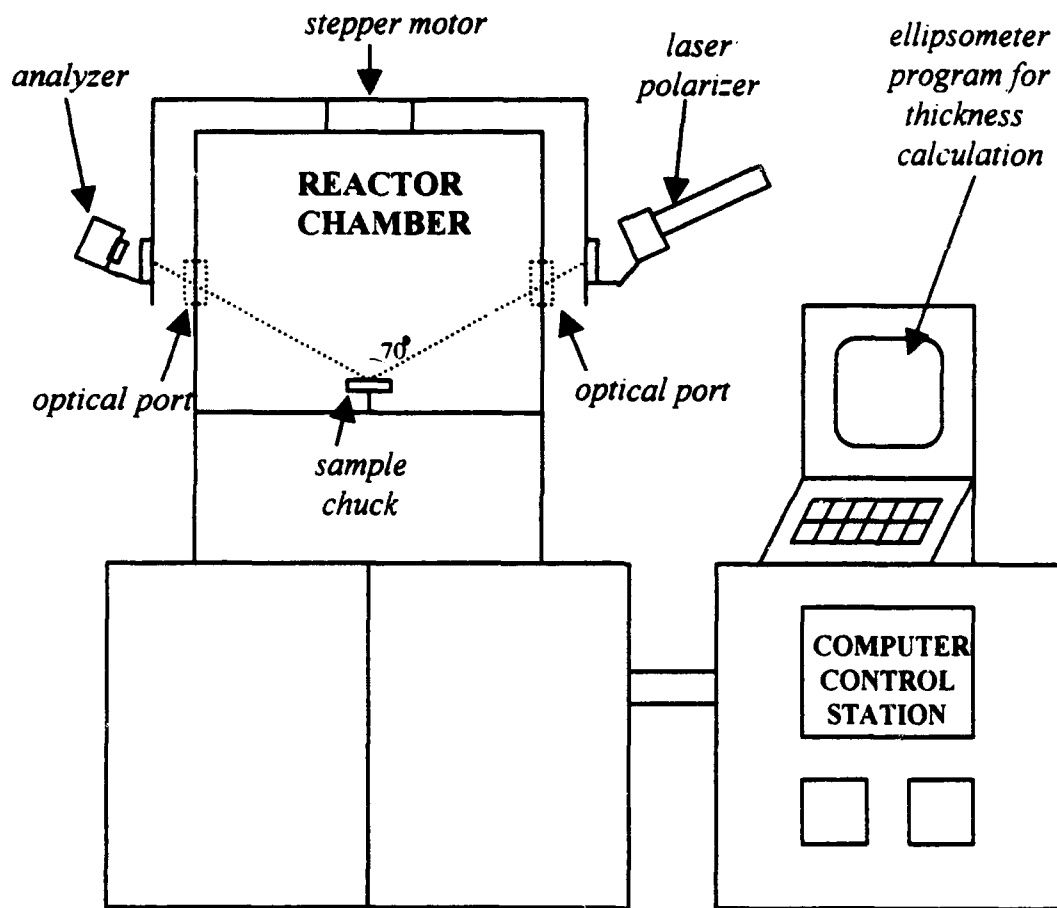


**Figure 5.** In-situ ellipsometer system of the automatic spin coater.

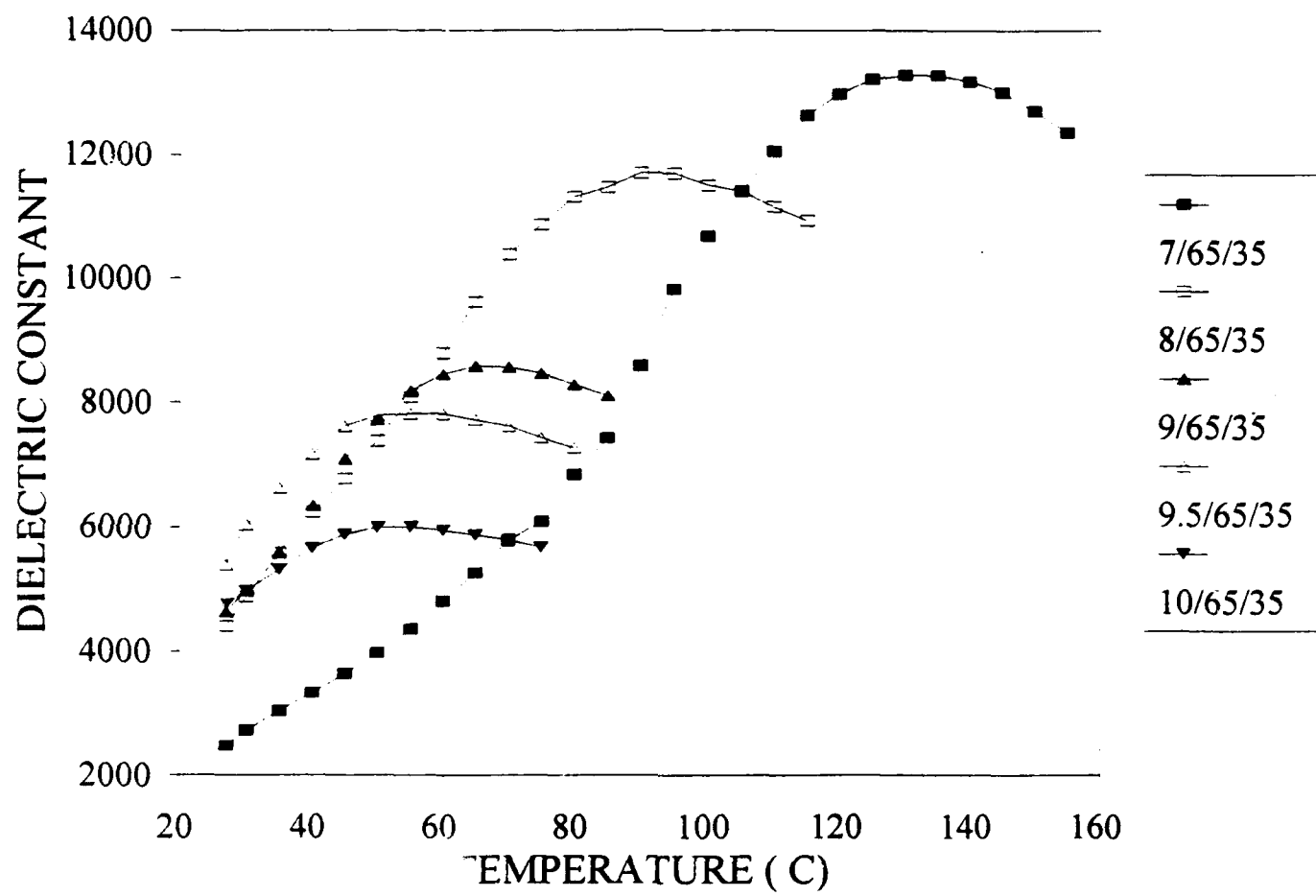


**Figure 6.** Curie temperature measurements of PLZT x/65/35 bulk ceramics hot pressed from chemically coprecipitated powder.

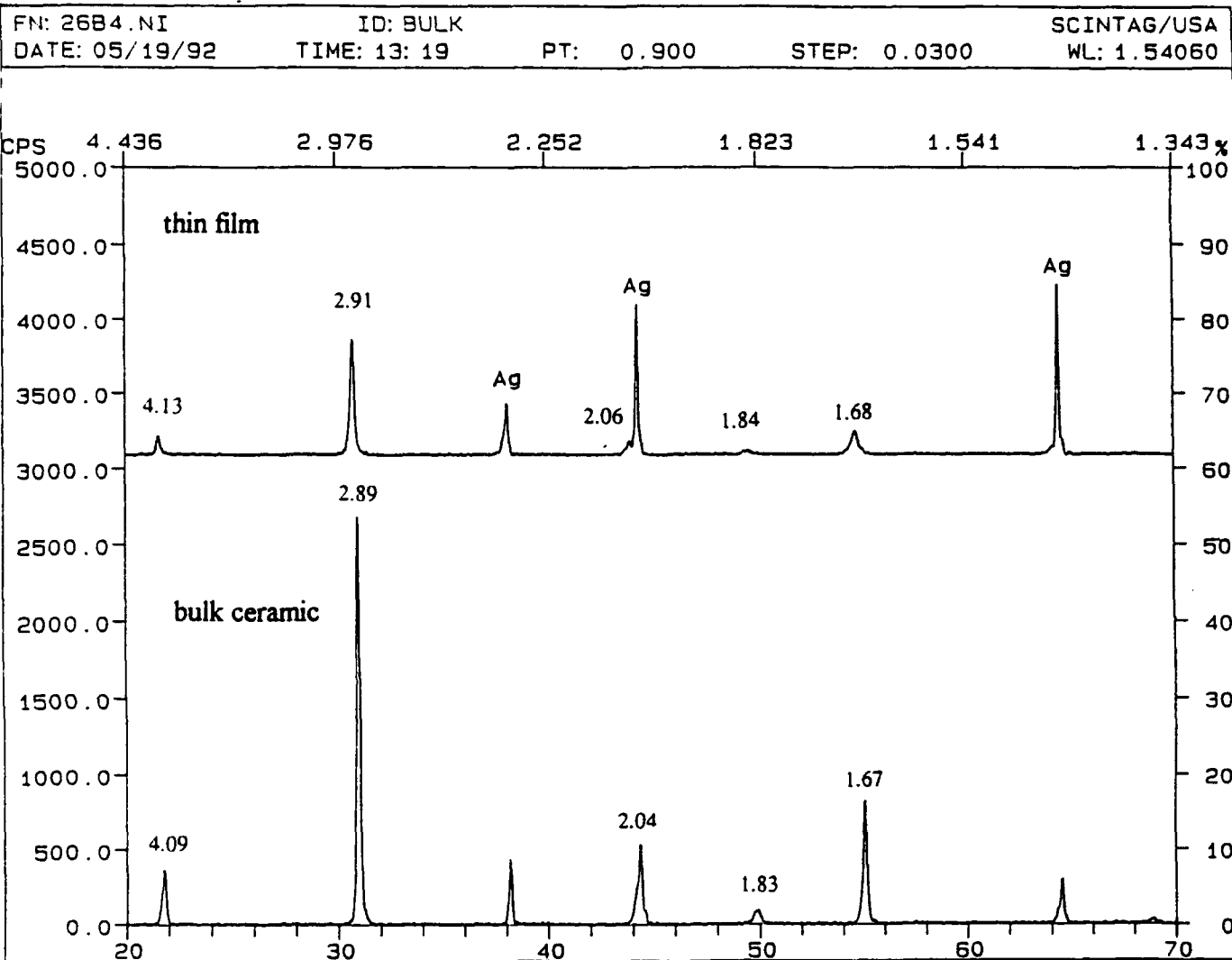
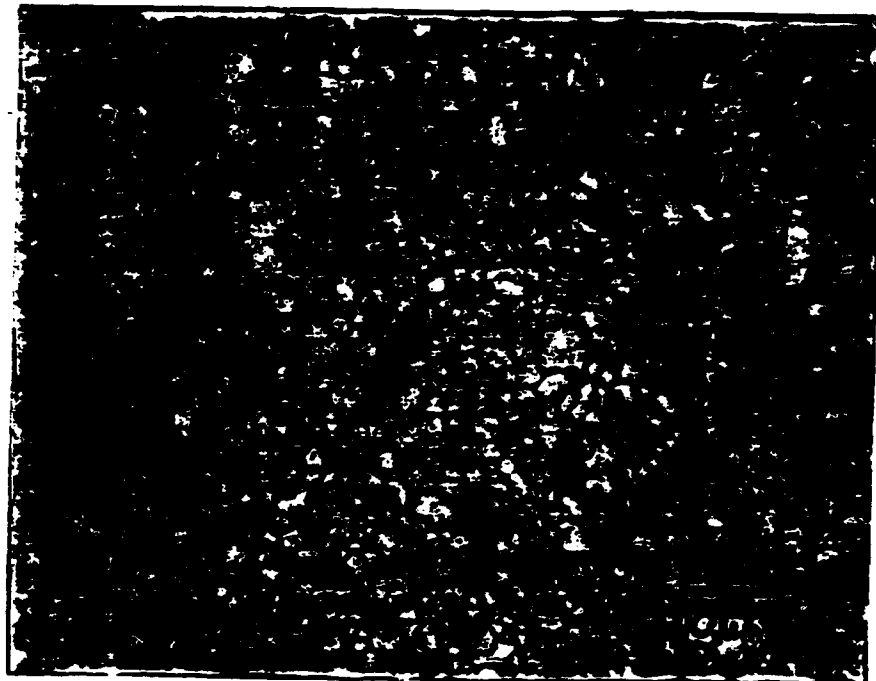


**Figure 7.** X-ray diffraction patterns of a PLZT 8/65/35 thin film and bulk ceramic.

A)



B)

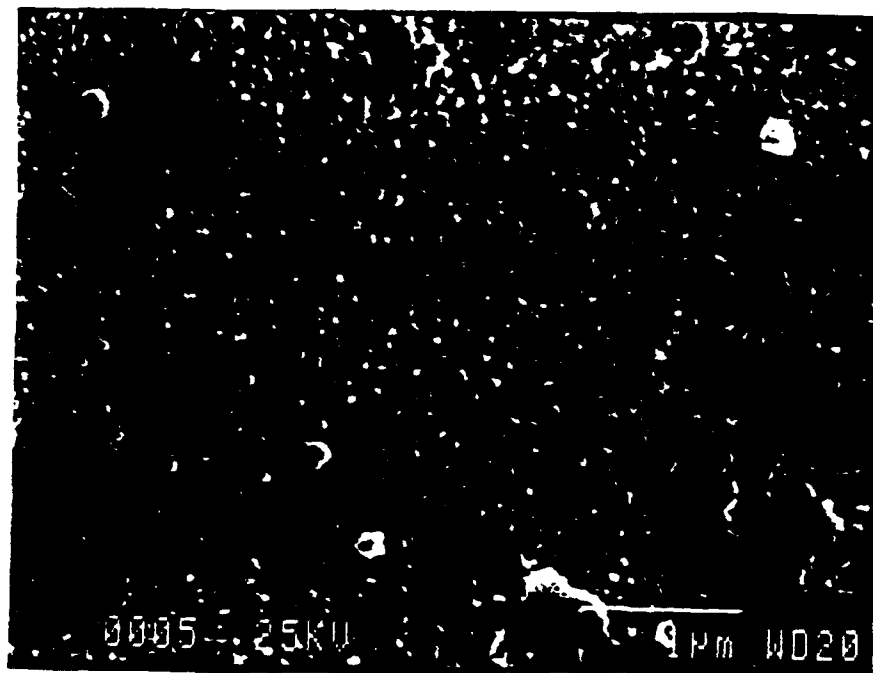
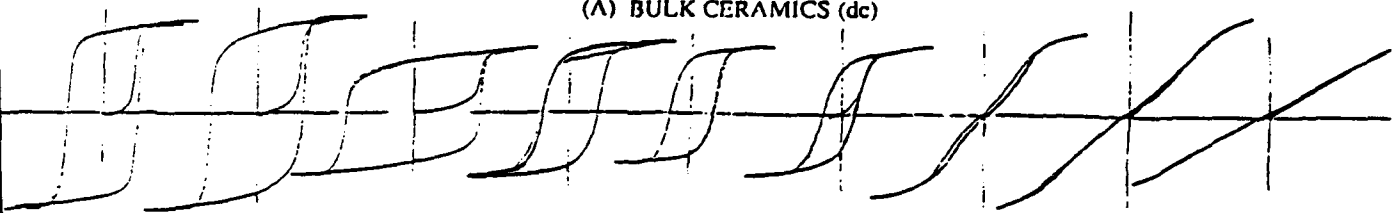


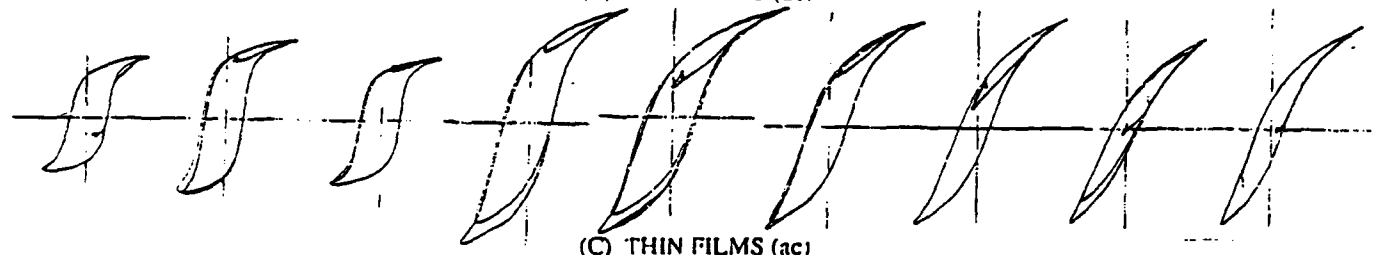
**Figure 8.** Microstructures of a) 2/55/45 hot pressed bulk ceramic (optical microscope) and b) 2/55/45 spin coated thin film on Si substrate (SEM).

2/55/45      2/53/47      2/51/49      6/65/35      7/65/35      8/65/35      9/65/35      9.5/65/35      10/65/35

(A) BULK CERAMICS (dc)



(B) THIN FILMS (dc)



(C) THIN FILMS (ac)

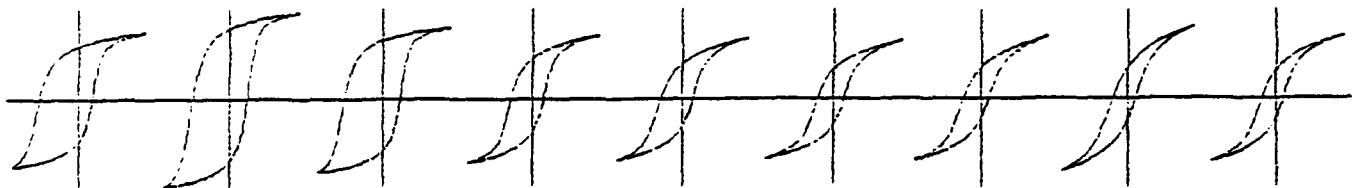


**Figure 9.** Polarization vs. electric field hysteresis loops of PLZT bulk ceramics and thin films.

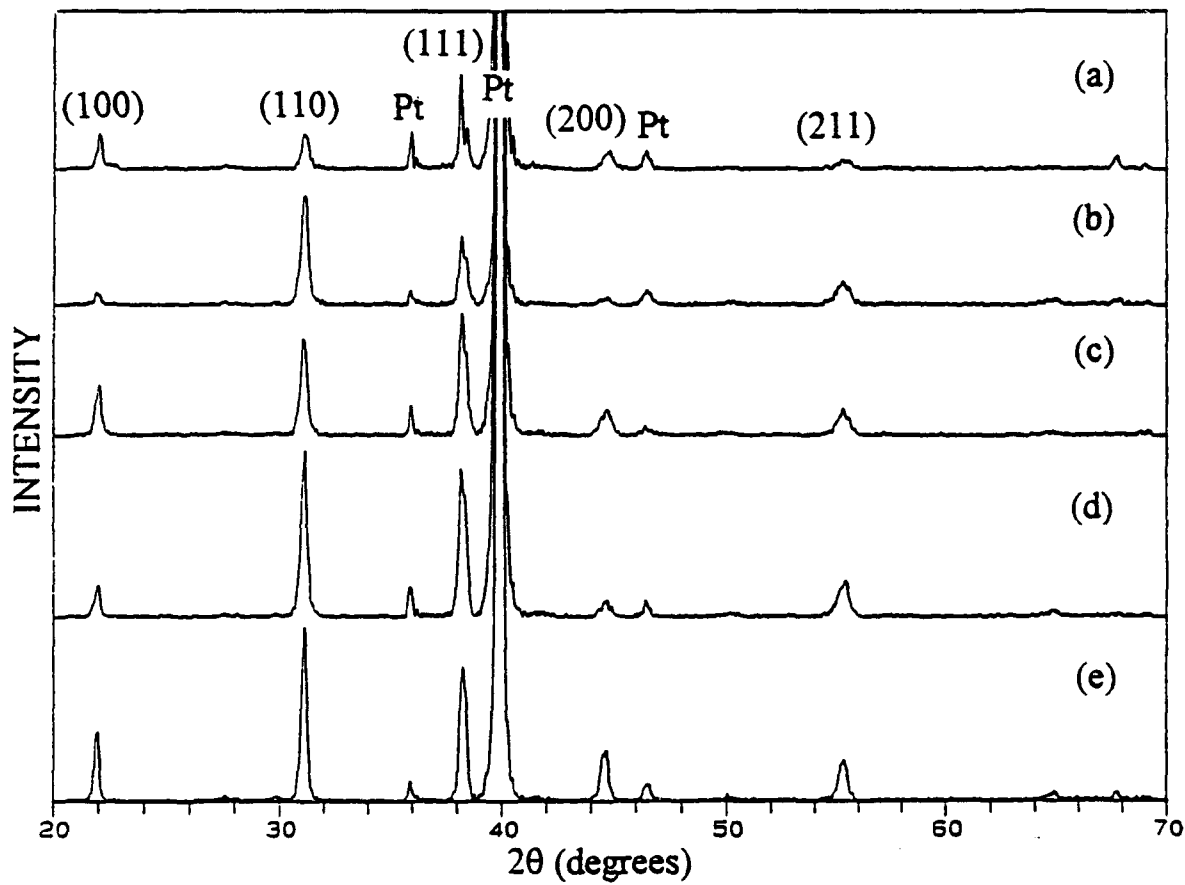


**Figure 10.** X-ray diffraction patterns of rapid thermally processed PLZT thin films. The firing schedules for the films were (in minutes): a) 700/3, b) 700/2(5), c) 700/1(10), d) 700/0.5(12.5) and e) 700/0.25(13.75).

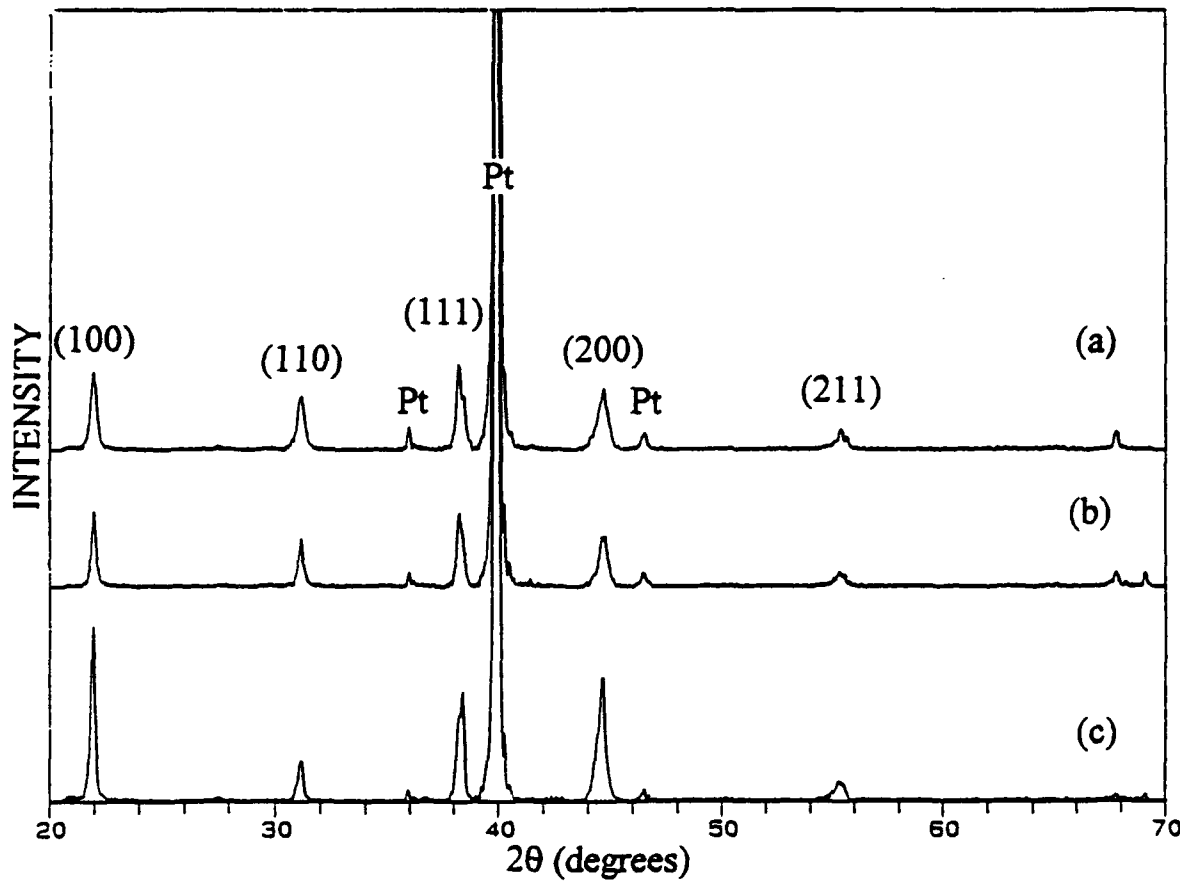


**Figure 11.** X-ray diffraction patterns of conventional furnace pyrolyzed PLZT thin films. The firing schedules for the films were (in minutes): a) 700/3, b) 700/2(5) and c) 700/1(10).

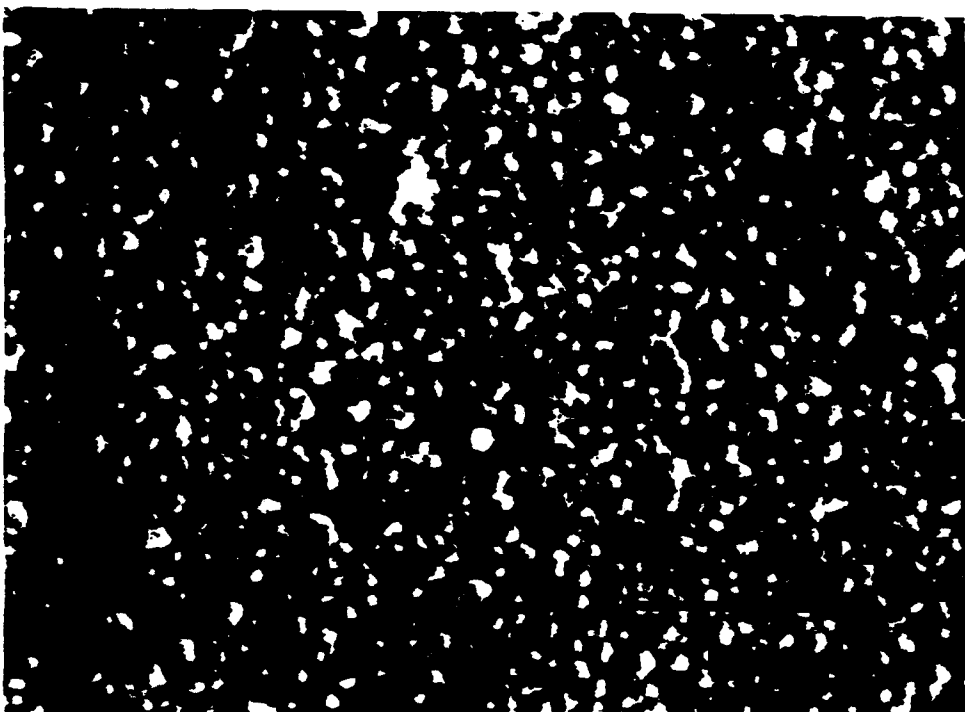
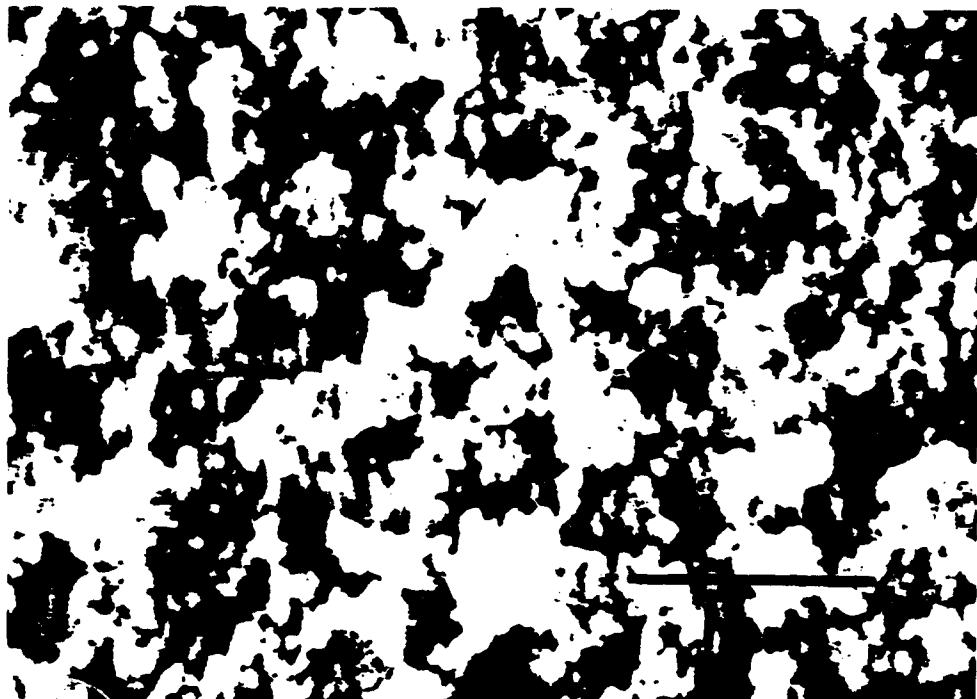


**Figure 12.** SEM micrographs of rapid thermally processed PLZT thin films. The firing schedules for the films were (in minutes): a) 700/3 and b) 700/0.25(13.75).

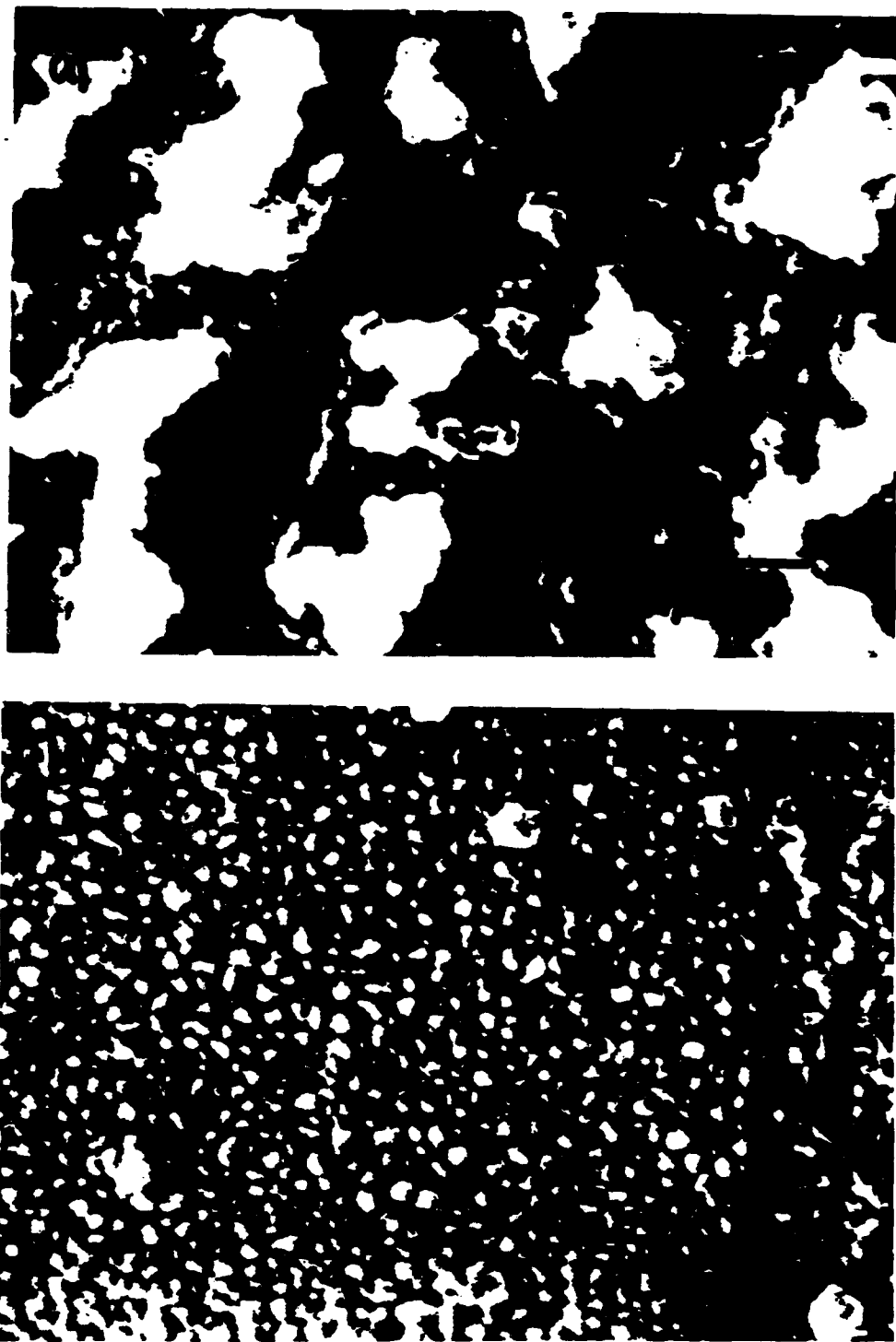


**Figure 13.** SEM micrographs of conventional furnace pyrolyzed PLZT thin films. The firing schedules for the films were (in minutes): a) 700/3 and b) 700/1(10).

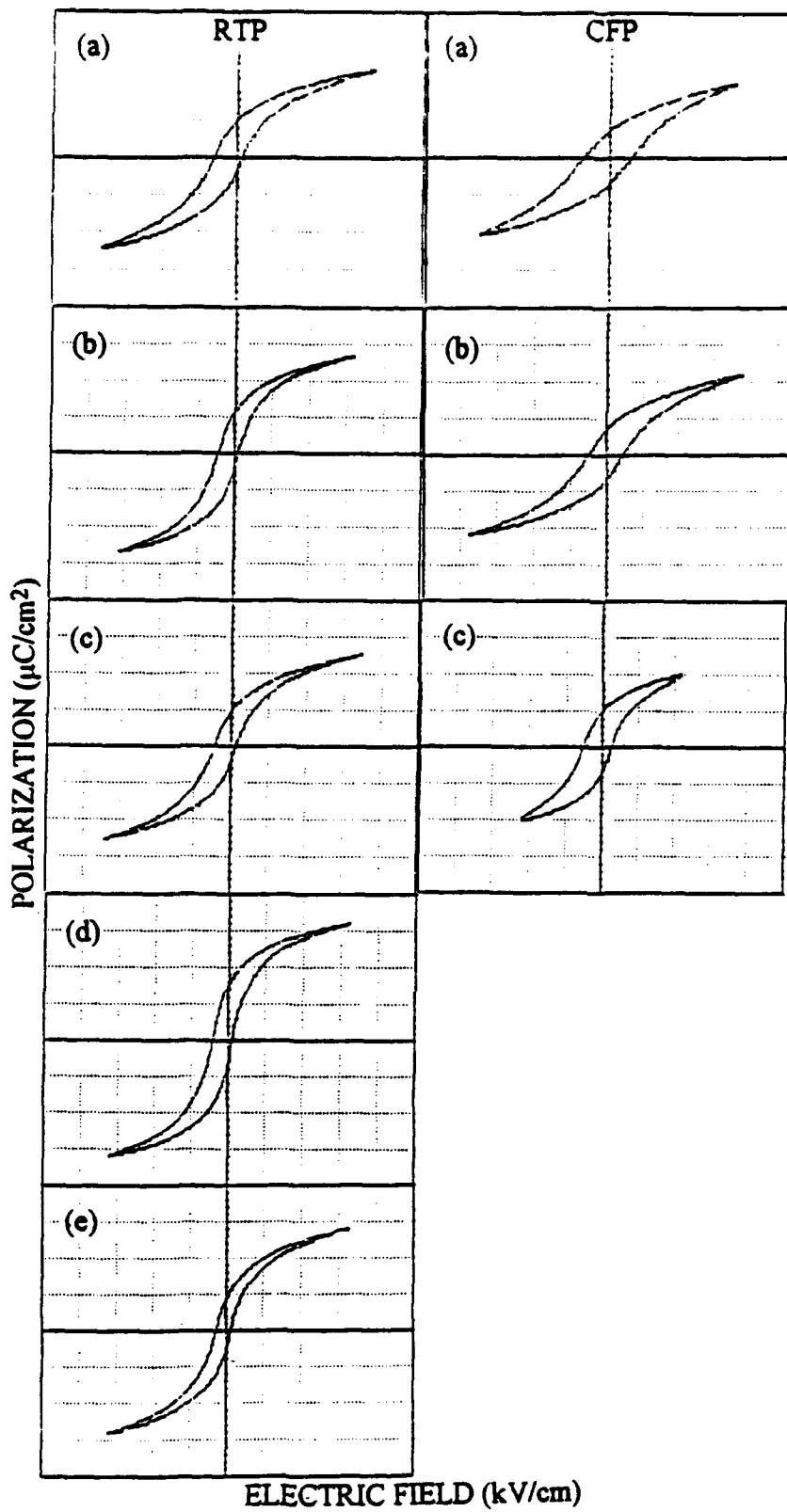


**Figure 14.** Hysteresis loops of rapid thermally processed (RTP) and conventional furnace pyrolyzed (CFP) PLZT thin films. The firing schedules for the films were (in minutes): a) 700/3, b) 700/2(5), c) 700/1(10), d) 700/0.5(12.5) and e) 700/0.25(13.75). The scale for the y-axis (polarization) is  $15 \mu\text{C}/\text{cm}^2$  per division, and the x-axis (electric field) is  $160 \text{kV}/\text{cm}$  per division.

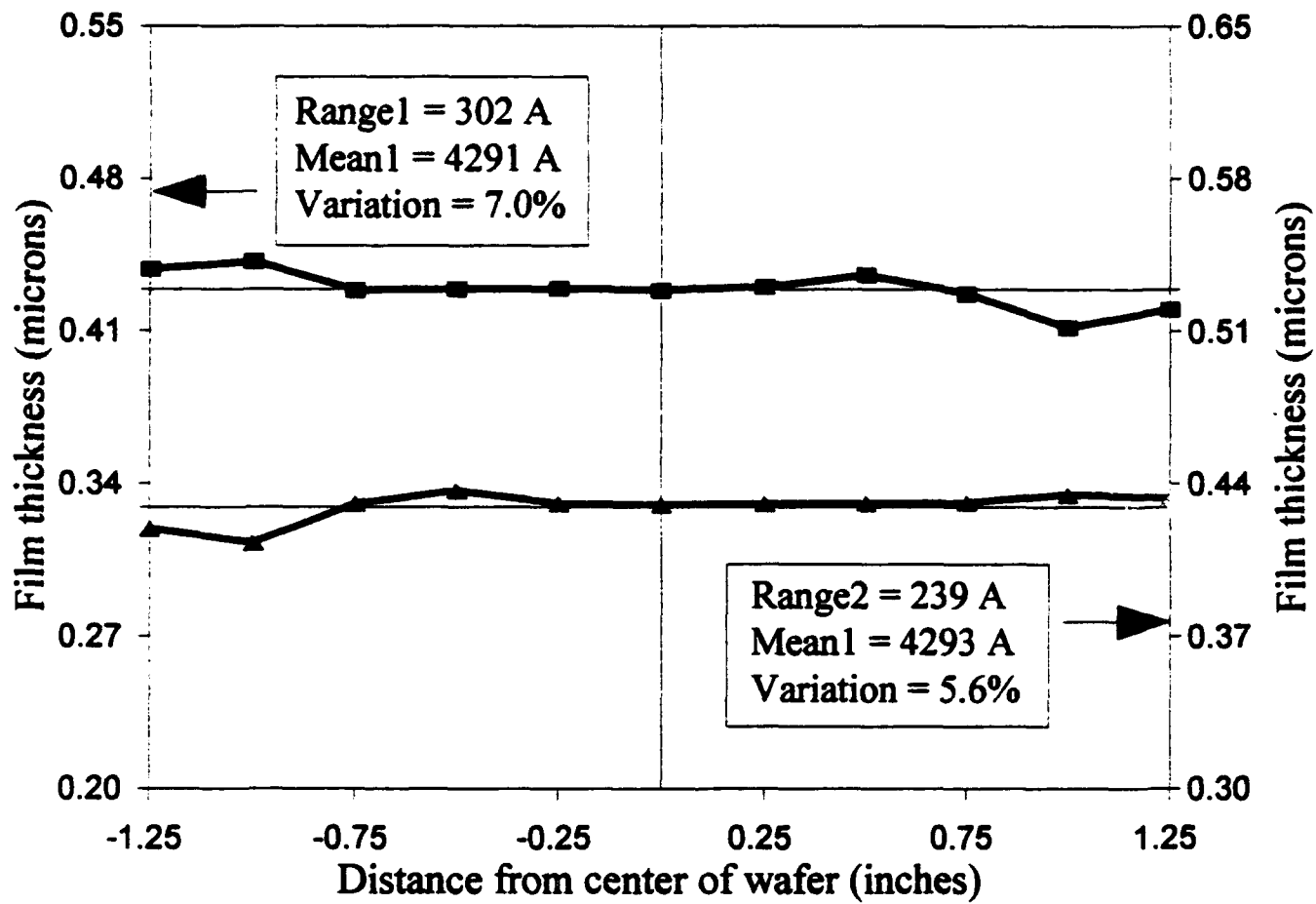


**Figure 15.** Thickness uniformity of a 3" diameter PLZT film spin coated on Si substrate.

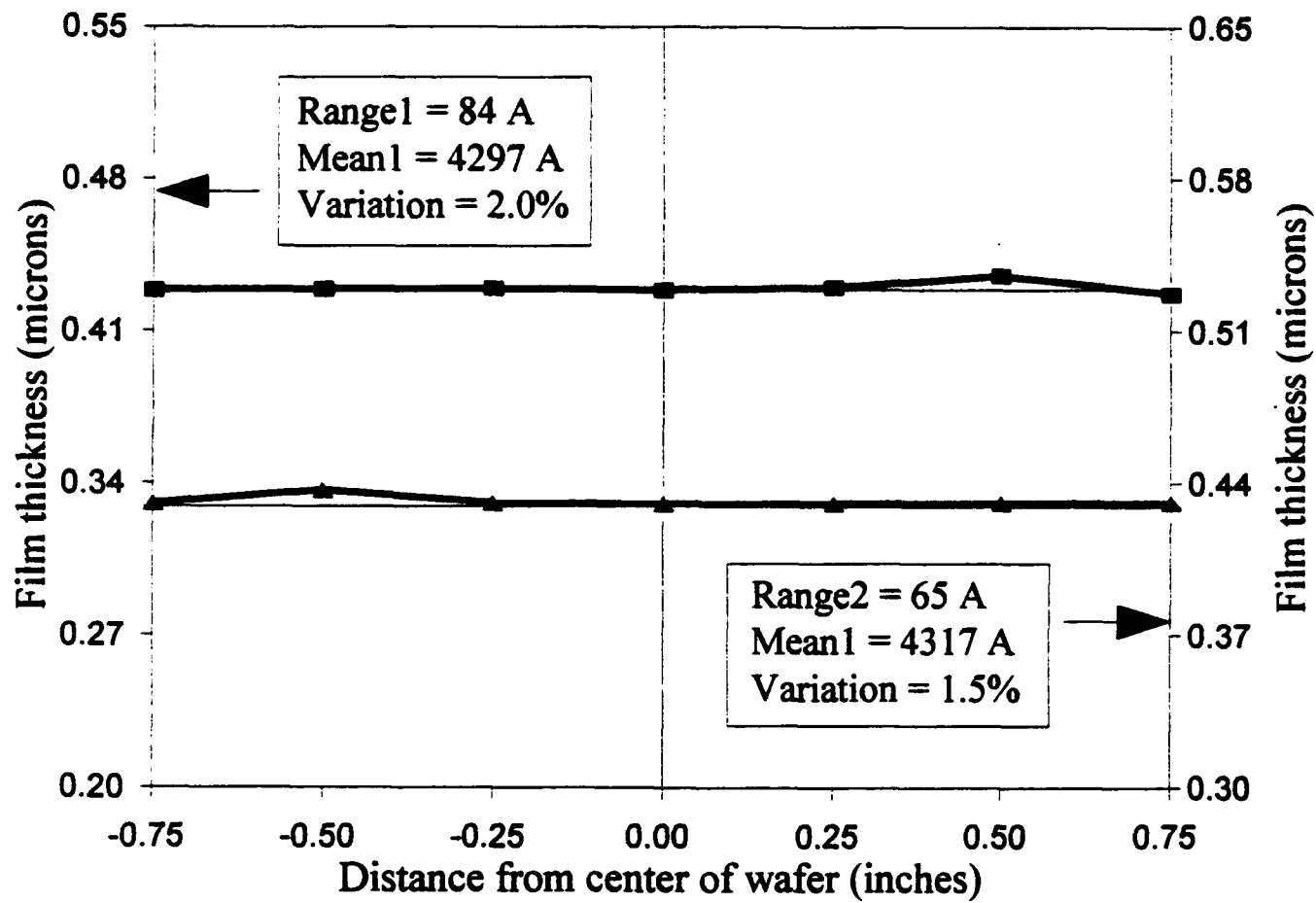


**Figure 16.** Thickness uniformity of the inner 1 1/2" diameter area of a 3" diameter PLZT film spin coated on Si substrate.

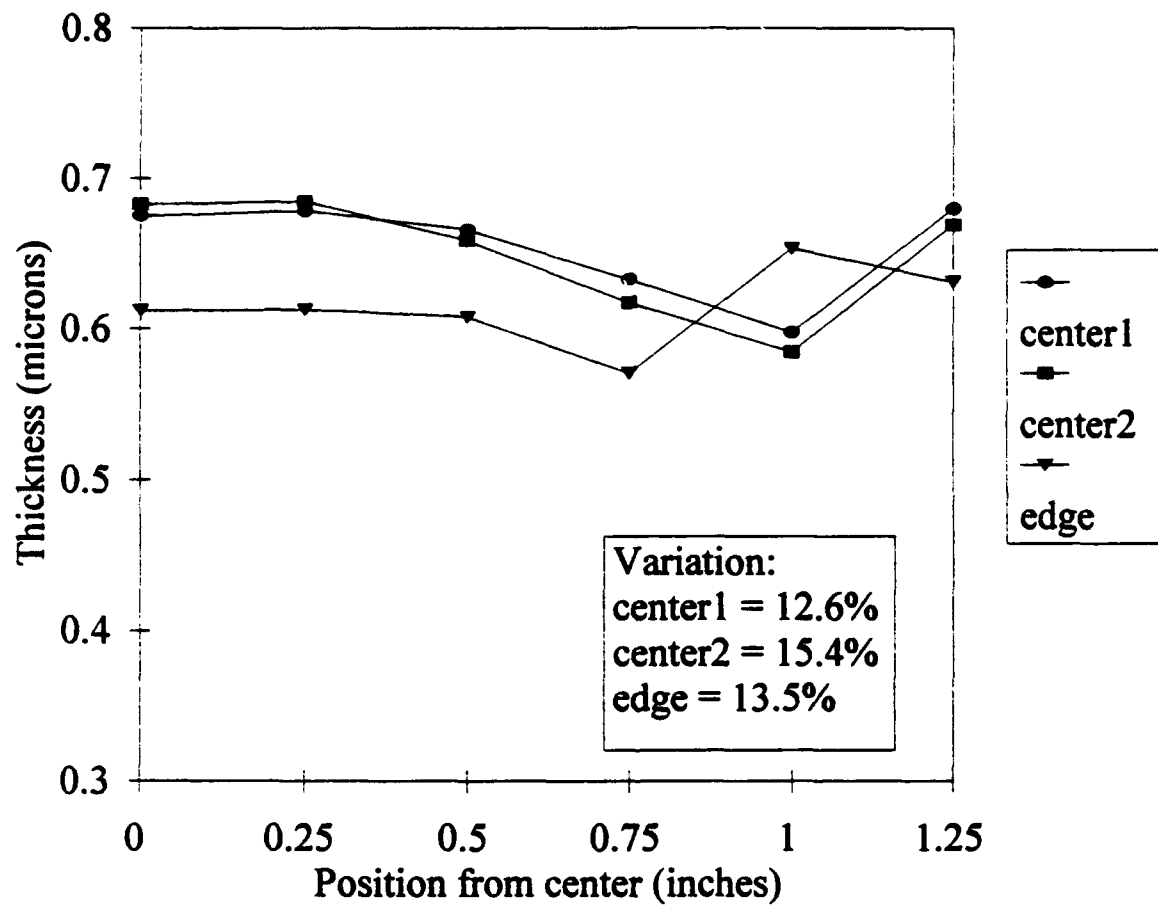


**Figure 17.** Thickness uniformity of a 1"x2" PLZT film sputtered on Si substrate.

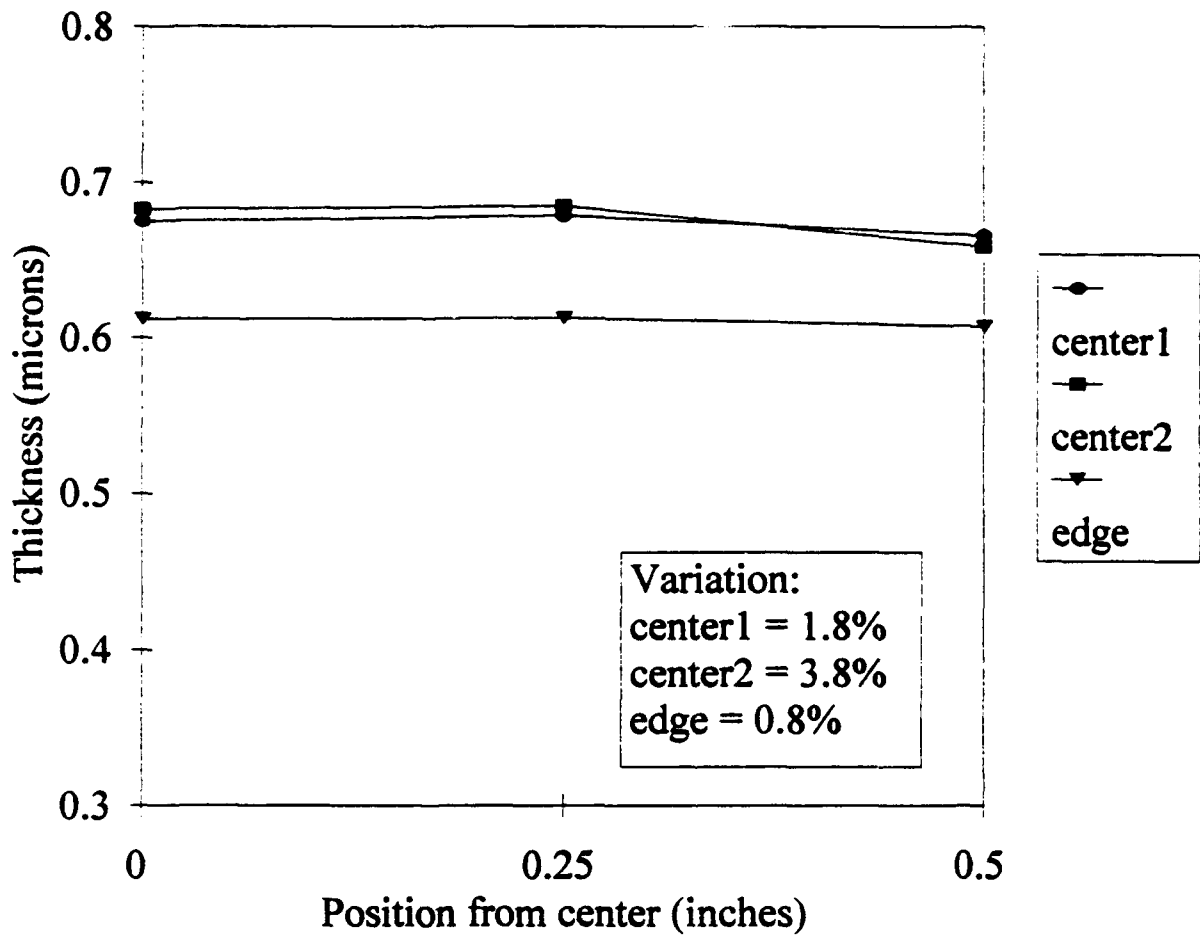


**Figure 18.** Thickness uniformity of the inner i/2" portion of a 1"x2" PLZT film sputtered on Si substrate.

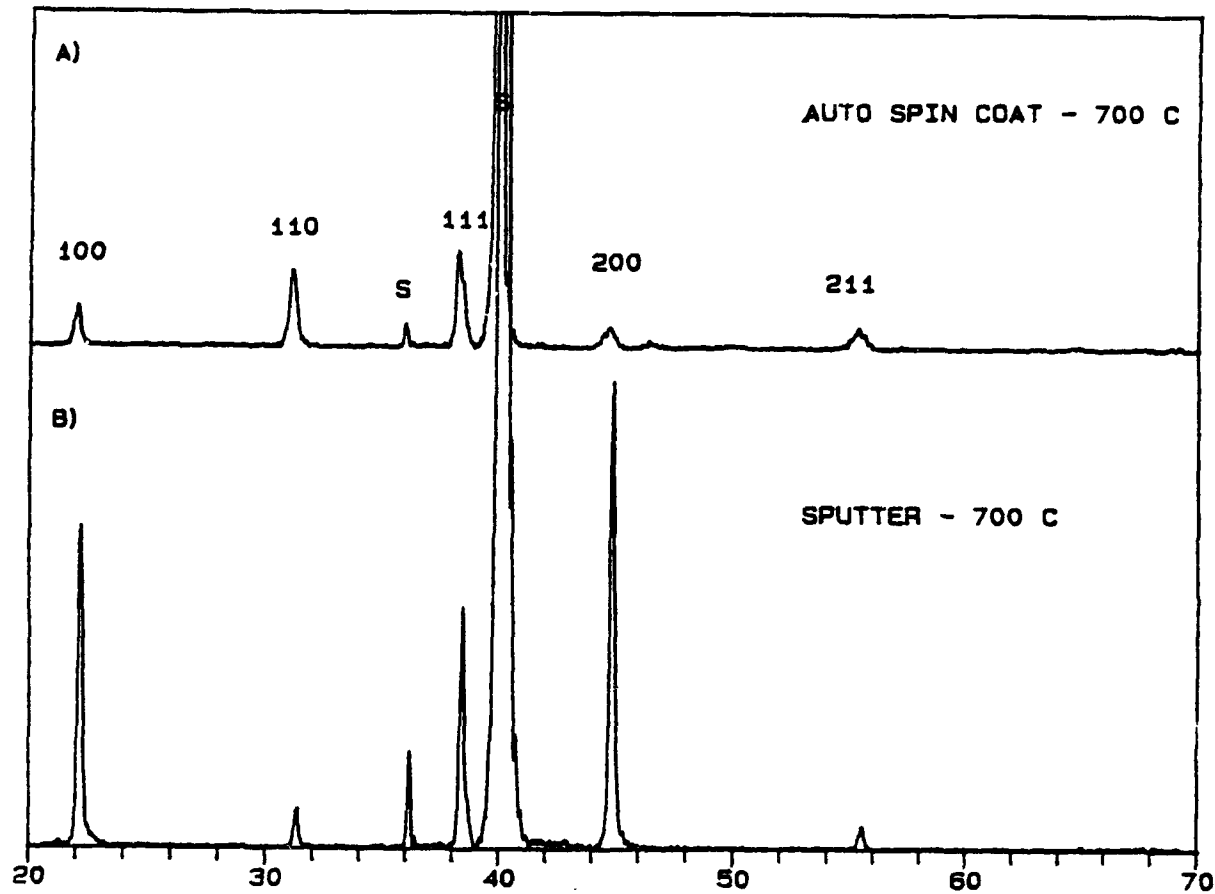


**Figure 19.** X-ray diffraction patterns of PLZT 2/55/45 automatic spin coated and RF magnetron sputtered thin films heat treated at 700°C.

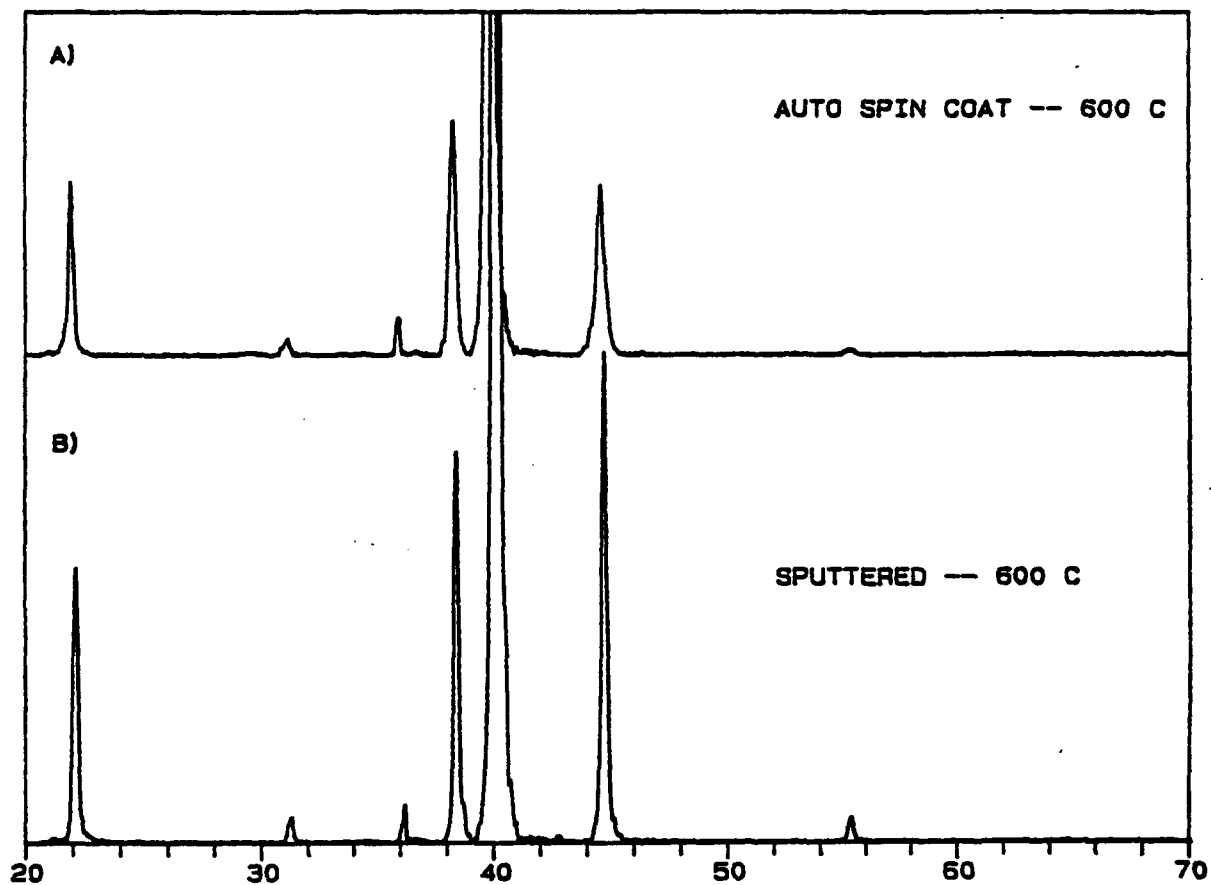
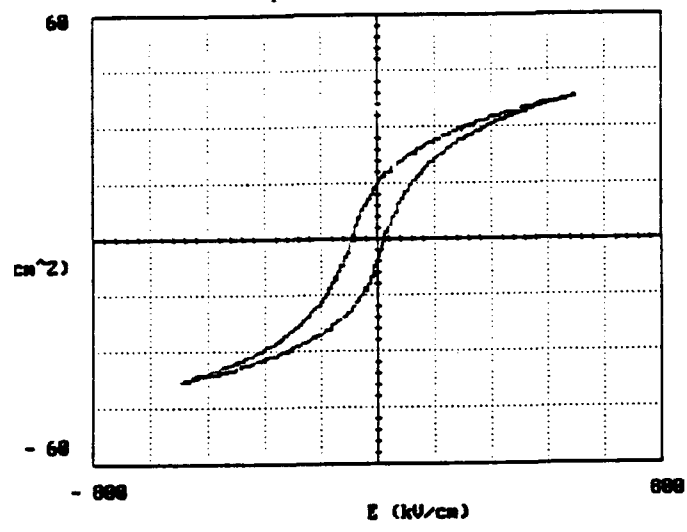
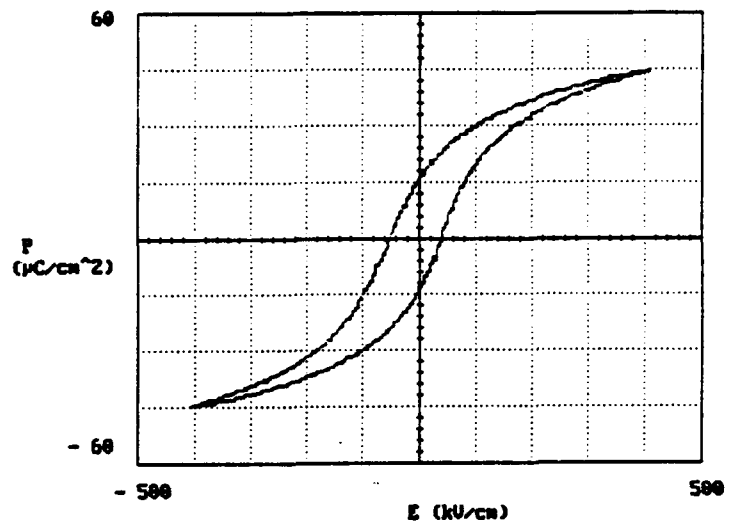


**Figure 20.** X-ray diffraction patterns of PLZT 2/55/45 automatic spin coated and RF magnetron sputtered thin films heat treated at 600°C.

## Automatic Spin Coating

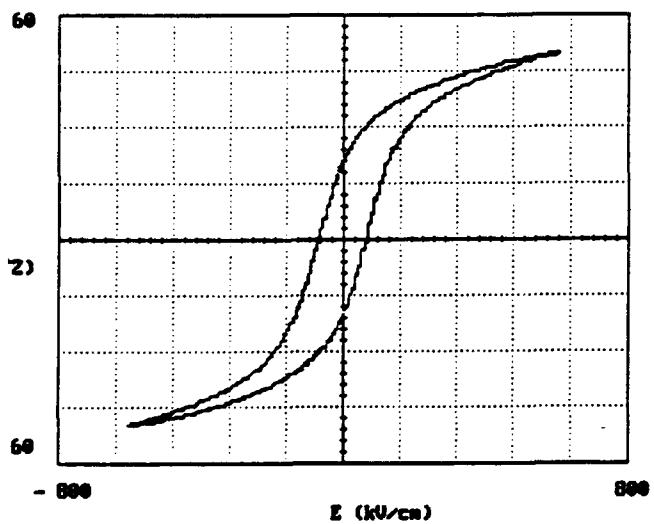


700/1(10)

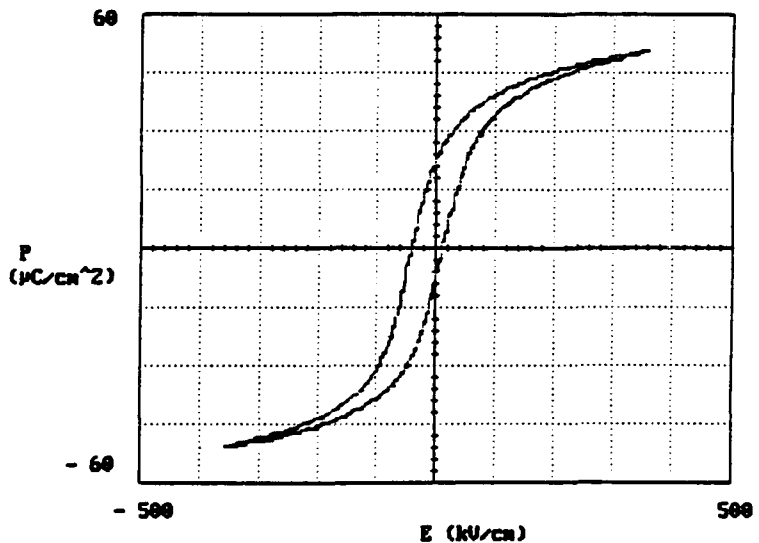


600/1(10)

## Magnetron Sputtering



700/40



600/40

**Figure 21.**  $P$  vs.  $E$  hysteresis loops of automatic spin coated and RF magnetron sputtered 2/55/45 thin films heat treated at 600 and 700°C. Spin coated films were rapid thermally processed and sputtered films were conventional furnace annealed.

**Part V.**

**Electrooptic Thin Films and Bulk Ceramics**

# **INTELLIGENT PROCESSING OF FERROELECTRIC THIN FILMS**

## **Annual Report**

### **Part V.**

#### **Electrooptic Thin Films and Bulk Ceramics (EPSCOR)**

**Submitted by: William Paradise  
Gene Haertling**

**The Gilbert C. Robinson Department of Ceramic Engineering  
Clemson University**

## **ABSTRACT**

Electrooptic ceramics have properties that can vary widely due to thickness, shape and processing method. These materials have conventionally been produced by a variety of deposition processes. These processes include the bulk ceramic techniques (sintering, hot pressing and tape casting) along with chemical (sol-gel, CVD and MOD) and physical (evaporation, sputtering and laser ablation) processes used in producing thin films.<sup>1</sup> The goals of the ONR program on "Intelligent Processing of Electrooptic Thin Films" are to determine the similarities and differences in material properties produced by various processes. Parts of these goals are carried out by producing electrooptic thin films and bulk ceramics from the same acetate precursors and then characterizing the chemical, electrical, physical and electrooptic properties of these materials. It is desirable that a processing method compatible with both thin films and bulk ceramics be used in order to better compare their respective properties. An acetate precursor system was employed to produce both acetate solutions for spin and dip coated thin films as well as coprecipitated powders for bulk ceramics. The principal interests now under examination are the electrooptic properties of the thin films and how stresses acting on and within these films can effect their properties. The automated spin coat reactor/analyizer has been brought on line and will soon be in use for producing electrooptic films.

## **INTRODUCTION**

Electrooptic thin films have been a topic of interest due to the unique properties they possess. The importance of electrooptic thin films is evident in their many applications ranging from sensors to light modulators.<sup>1</sup> These thin film uses come from the electrooptic bulk ceramics developed over the years. Thin films possess advantages over bulk ceramics such as lower operating voltage, higher speed, easier integration with silicon technology and lower cost which make them more desirable for many devices. It is believed that through the study of the processing technique used, an optimization of properties can be achieved.

In order to understand and optimize thin film electrooptic behavior, a comparison is necessary to bulk electrooptic ceramics. Direct correlation between the bulk and thin film materials is difficult since the precursors and processing techniques of each are typically so dissimilar. Within this research this problem was eliminated by using the same acetate precursor solutions in the manufacturing of the PLZT bulk ceramics and thin films. It is believed that this process allows for a close comparison of PLZT bulk and thin film

electrooptics by minimizing or eliminating differences in the processing of these materials induced by precursor impurities, batching variations and differences in mixing of the precursor materials. This allows us to characterize similarities and differences in the properties of bulk ceramics produced from chemically coprecipitated powders and dip coated thin films produced by a metallorganic decomposition process without having variations in starting materials as a factor.

## PROCESSING

PLZT bulk ceramics and dip coated thin films were produced using a water soluble acetate precursor method.<sup>2</sup> The chemical coprecipitation process which was used to produce PLZT powder from acetate precursors is shown in Figure 1. This processing method produces bulk and thin film samples from the same batches. This allowed for a unique comparison of properties between bulk ceramics and thin films since it reduced or removed any variations between batches and precursor histories. The acetate precursors were chosen primarily for their low cost, insensitivity to moisture, and chemical stability. The starting precursors were titanium acetyl acetonate, zirconium acetate, lanthanum acetate and lead subacetate powder. The lead subacetate was mixed into solution by the addition of acetic acid and methanol so that all of the acetate precursors were in a liquid form in order to promote a more homogeneous and intimate mixing. Incomplete mixing would produce compositional fluctuations between bulk and thin film solutions. A portion of this solution was then taken off to be used for the thin film productions.

The bulk portion was coprecipitated in a high speed blender. Oxalic acid and methanol were then added to this solution to bring about precipitation of the PLZT powder. As stated earlier this process produces a more homogeneous mixture of precursors and therefore produces a more intimately mixed PLZT powder with a smaller particle size than the mixed oxide process. This powder was then vacuum dried at 70°C to produce a cake. The cake was crushed, calcined at 500°C for 8 hours and milled in trichloroethylene for 6 hours to produce a PLZT oxide powder. The powder was then either pressed into disks at 3000 psi and sintered at 1250°C in a lead-rich atmosphere for 4-6 hours or hot pressed for 4-6 hours at 1250°C and 2000 psi. Typically, 110g of powder was produced for hot pressing. The sintered and hot pressed parts were sliced on a diamond saw and lapped to 20 mils thickness. Electroless nickel electrodes were plated onto the ceramics through a series of chemical baths. The samples were electrode for measurement of their dielectric and hysteresis loop properties.

Thin films were produced manually by the dip coating process shown in Figure 2. These films were produced to determine if the firing temperature could be reduced without affecting the films' properties. For thin film production, the small portion (usually 5g) of the acetate solution decanted was diluted with methanol at a 4:1 ratio by weight. The films were dipped onto silver foil substrates, allowed to dry for 30 seconds and pyrolyzed at 500°C or 700°C for 3 minutes. Some of the films had their firing temperature changed after the first and/or before the last layer was applied. Therefore a "575" film had the first layer fired on at 500°C, the middle 22 layers fired on at 700°C and the remaining layer fired on at 500°C. All the films had 24 layers and were approximately 0.9 µm thick. The films were electroded by vacuum evaporation of copper and measured for dielectric constants, resistivities and hysteresis loops.

## MEASUREMENTS

Bulk and thin film samples were measured for resistance, capacitance, dissipation and hysteresis loops. The capacitance and dissipation factor were measured on bulk and thin film samples using a Leader LCR meter at a measuring frequency of 1 kHz. Resistance was measured using a Keithley electrometer. Hysteresis loops were also measured for both materials to determine their polarization versus an electric field. The bulk samples were measured using a Sawyer-Tower circuit with a dc applied voltage of  $\pm 1400$  V and the hysteresis loops were plotted with a Goerz Metrawatt X-Y plotter. Hysteresis loops of the thin film samples were measured at 1 kHz using a Sawyer-Tower circuit with an oscilloscope readout.

## RESULTS AND DISCUSSION

Hot pressed bulk ceramics and dip coated thin films on Ag foil substrates were fabricated, and a comparison of properties was established. Sintered and hot pressed ceramics along with dip coated thin films (on silver foil) for the 9/65/35 composition were compared as shown in Table 1. These values showed that the hot pressed ceramics had very little remanent polarization and reached a lower saturation level than the other two; while the thin films had a large amount of remanent polarization with a lower dielectric constant than either of the bulk ceramics. These effects have been reported to be due to differences between bulk and thin film configurations.<sup>2</sup> The fact that the thin film dielectric constants were generally lower could be attributed to the small grain size of the thin films, mechanical clamping effects or, due to the high electric field applied to the thin

films, the voltage sensitivity of the measurement. This could imply that the hot pressed ceramics had better properties due to larger grain growth and fewer defects, which would be expected with hot pressed materials. These differences could also be seen when comparing the hysteresis loops as in Figure 3. Research on quenched PLZT 9.5/65/35 ceramics showed that internal stresses induced in samples can enhance polar region ordering.<sup>3</sup> This would produce a more ferroelectric-like response by the material. This response would produce higher remanent polarizations in quenched samples than in annealed samples. These findings could explain the memory behavior found in the thin films used in this experiment. Residual stresses may have caused these films to retain ferroelectric memory hysteresis loops that were not observed in the bulk materials. More batches are being produced and analyzed in an attempt to further explain differences and similarities in properties between the bulk and thin film electrooptics.

The coercive fields and remanent polarizations were calculated for all the films in the temperature dependence test and are listed along with dielectric constants and dissipation factors in Table 2. The highest poled dielectric constants were found to be in the "777" thin film. In comparison to the "777" sample, the hysteresis loop of the "555" sample was more conductive and electrically shorted more readily. The ac loop of the "777" sample reached much better saturation and looked similar to a bulk hysteresis loop. The ac hysteresis loops are shown in Figure 4. The hysteresis loops also became slimmer as the temperature used increased. All this indicated that films fired at higher temperatures had better nucleation and grain growth. As anticipated, the properties of the thin films were found to be highly dependent on firing schedule. Graphs of the improvements in properties with firing temperatures are shown in Figures 5 and 6. These graphs clearly show the increase in dielectric constant and remanent polarization as the firing temperature is increased from 500°C to 700°C.

## SUMMARY

Sintered and hot pressed ceramics along with dip coated thin films (on silver foil) for the 9/65/35 composition were compared. PLZT bulk ceramics and thin films were fabricated from the same acetate precursor solutions in order to minimize batching variations and accurately compare properties between bulk and thin film samples of the same compositions. The bulk materials produced slim hysteresis loops, but this was never completely achieved in the thin films. It has been suggested that these differences may be attributed to the induced stresses built up within the thin films. This comparison of bulk and thin film electrooptics is believed to be an accurate comparison of properties caused

only by the differences in processing. Therefore, the only variables between the bulk ceramics and thin films were their physical differences. It is believed that the complete mixing of precursors and accurate batching of materials which was used for both bulk and thin film production provided a minimization of differences that could cause serious variations in their composition and properties. It is believed this process provided a true correlation between these materials.

The temperature experiment proved that the properties of the thin films were found to be highly dependent on firing schedule. It is believed that at higher firing temperatures the films had better nucleation and grain growth which would account for the increase in measured properties.

## AUTOMATIC SPIN COATING

Thin films will be produced by an automatic spin coat reactor/analyser which is shown in Figure 7. The automatic spin coat reactor/analyser, produced by Digital Controls, Inc. in Rolla, MO, is controlled by an IBM compatible, 80386DX computer with software to operate the ellipsometer and set parameters for atmospheric gas control, deposition, spinning, heating and cooling. It will be utilized for spin coating and rapid thermal processing of thin films from liquid precursors. Computer control provides hands-off fabrication and flexibility in processing of the films. Samples may be prepared without exposure to the outside environment.

The fluid dispense system has the capability of depositing one of three precursor solutions onto 1/2" to 4" diameter substrates. A nitrogen dusting step can also be inserted through the dispense arm before fluid deposition. Spinning is executed with an ac brushless servo motor and controller with programmable time, speed and acceleration. Six water-cooled parabolic strip heaters with infrared quartz lamps containing tungsten filaments comprise the rapid thermal processing unit. This RTP unit allows the sample to be heated to 700°C within 5 to 10 seconds. Variable atmospheric gases (N<sub>2</sub>, O<sub>2</sub>, Ar) and low pressures as well as vacuum capability are possible in the atmosphere control system. In-situ thickness measurements are taken before and after heating by a Gaertner Scientific laser ellipsometer. A typical run would proceed as follows:

1. Chamber was pumped down to vacuum pressures
2. Chamber was vented with set gas mixture and pressure
3. Dispense arm moved over substrate, blew off surface  
with nitrogen gas and fluid injected onto substrate
4. Sample stage spin initiated

5. Dispense arm moved back and heater (water cooled quartz infrared lamps) moved forward over sample stage
6. Heater ramped and soaked at set parameters using a rapid thermal annealing process
7. Heater moved back and laser ellipsometer used to measure film thickness

This cycle can be repeated for any number of layers or with a change in composition of layers. A cooling stage is placed in between layers to allow the film to cool before the next deposit of solution. The electrooptic thin films produced by the automatic spin coater and the dip coater will be analyzed for birefringence in transmission and reflective modes. These measurements along with the measurements already obtained should help us understand the differences and similarities that exist between bulk materials and thin films.

## **FUTURE WORK**

As stated earlier, there maybe a strong correlation between the amount of stress a film has placed upon it and the properties the film exhibits. This correlation will be researched further to determine if the properties within a film can be optimized or enhanced. The electrooptic response of thin films will be manipulated by varying the stresses placed upon the films. Selected films in the PLZT system will be produced by using the dip-coating process and applying various stresses and electric fields. Comparisons will be made between mechanically applied stresses and stresses from thermal expansion mismatch between the substrate and the film. The effects of these variables on the physical, electrical and electrooptic properties of the films will be analyzed.

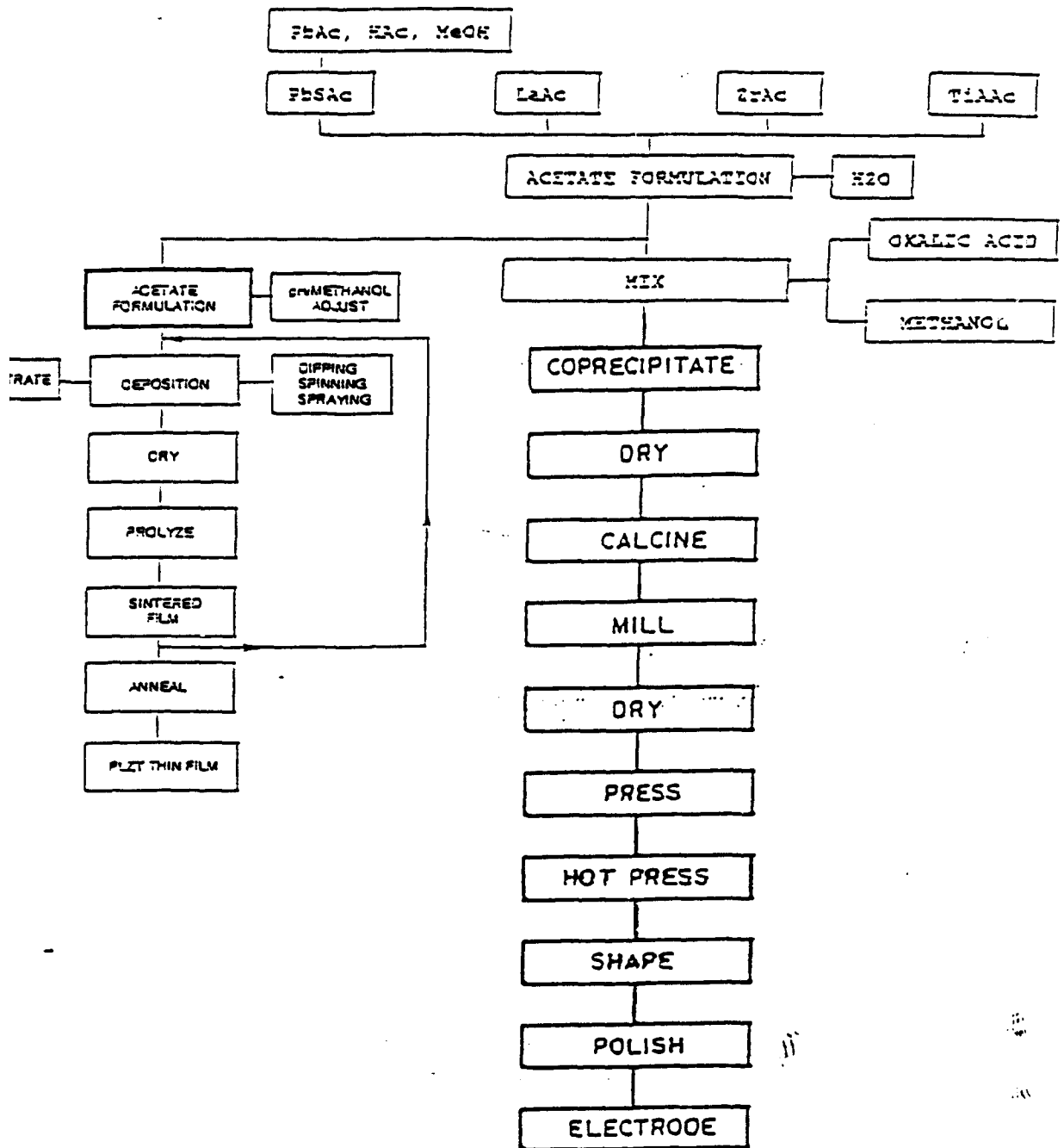


**Figure 1.** Acetate precursor coprecipitation process for producing PLZT thin film solutions and bulk powders.

**Automatic dip coating apparatus (designed by  
Kewen Li, Clemson University)**

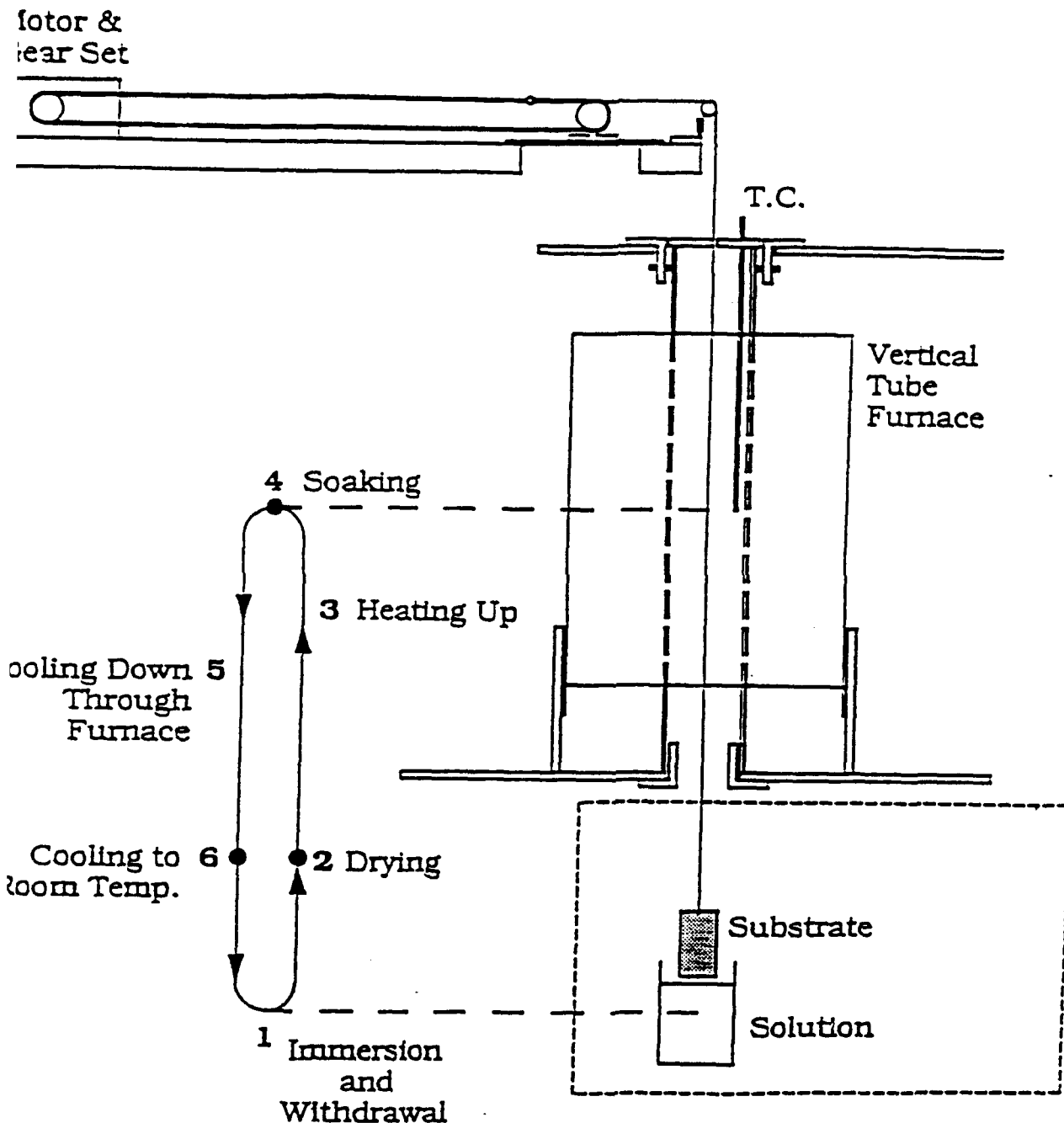


**Figure 2.** Dip coating apparatus.

**Table 1.** Electrical properties of sintered, hot pressed and dip coated PLZT (9/65/35) thin films.

	$\tan \delta$ (pol)	K (pol)	$E_C$ [kV/cm]	$P_R$ [ $\mu\text{C}/\text{cm}^2$ ]	$P_{10}$ [ $\mu\text{C}/\text{cm}^2$ ]	$P_{20}$ [ $\mu\text{C}/\text{cm}^2$ ]
<b>Sintered</b>	.035	4205	1.77	3.27	26.2	29.6
<b>Hot pressed</b>	.033	4317	.958	1.45	20.57	27.13
<b>Thin film</b>	.151	3194	23	19.7	-----	-----



**Figure 3.** Hysteresis loops for sintered and hot pressed bulk materials and dip coated thin films (PLZT 9/65/35).

**Table 2.** Electrical properties of PLZT (9/65/35) thin films with various firing schedules.

	P <sub>R</sub> [μC/cm <sup>2</sup> ]	E <sub>C</sub> [kV/cm]	tan δ (pol)	K (pol)
<b>555</b>	----	----	.035	----
<b>755</b>	----	----	.034	----
<b>575</b>	14.1	38	.094	1174
<b>775</b>	15.4	24	.116	2014
<b>557</b>	9	19	.119	1833
<b>757</b>	14.1	21	.162	2414
<b>577</b>	11.8	23	.138	1901
<b>777</b>	19.7	23	.151	3194

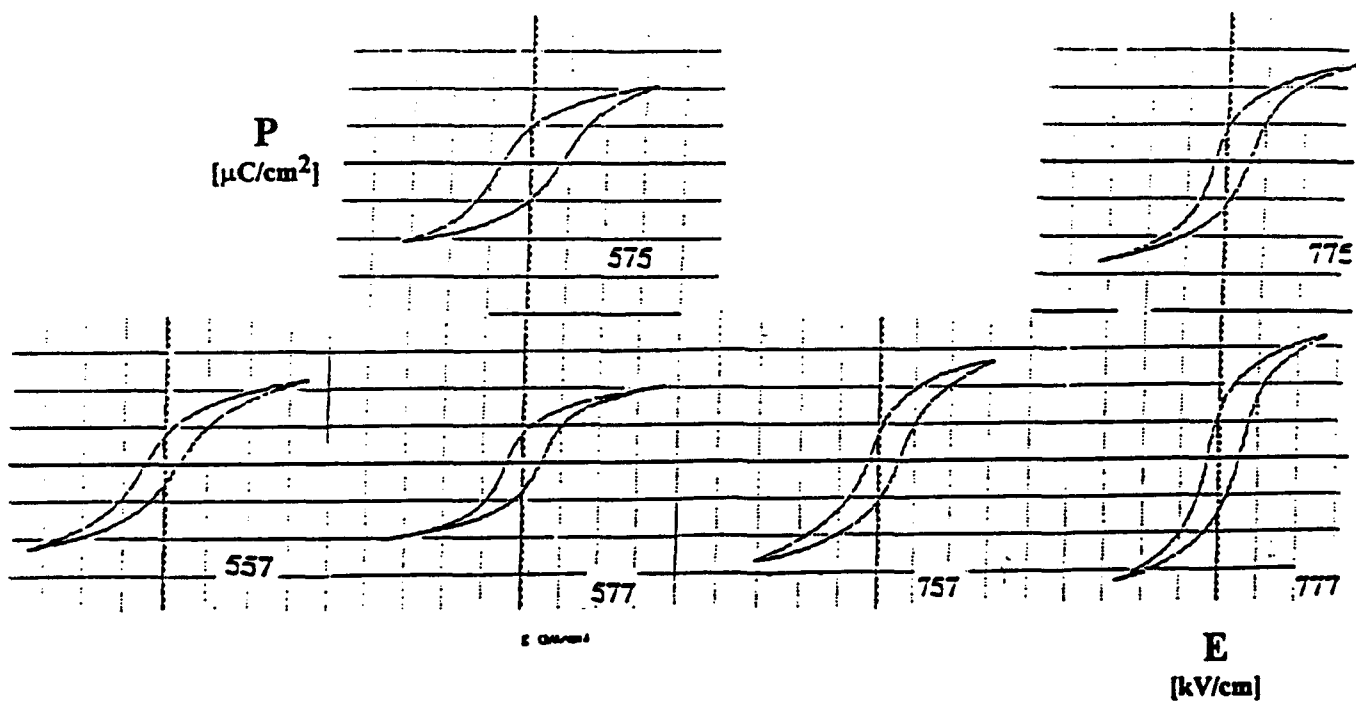


**Figure 4.** Ac hysteresis loops of PLZT 9/65/35 thin films with various firing schedules.  
Vertical scale =  $15 \mu\text{C}/\text{cm}^2$  per div. Horizontal scale =  $50 \text{kV}/\text{cm}$  per div.

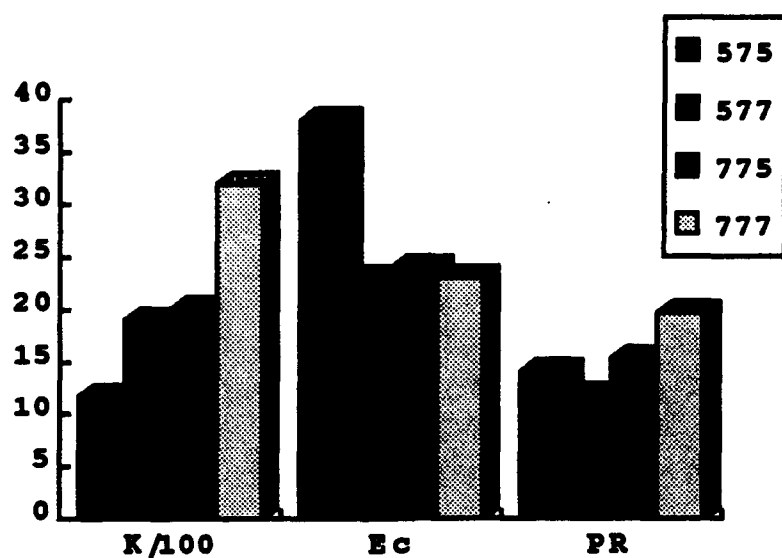


**Figure 5.** Thin film electrical measurements arranged according to increasing temperature within firing schedule.

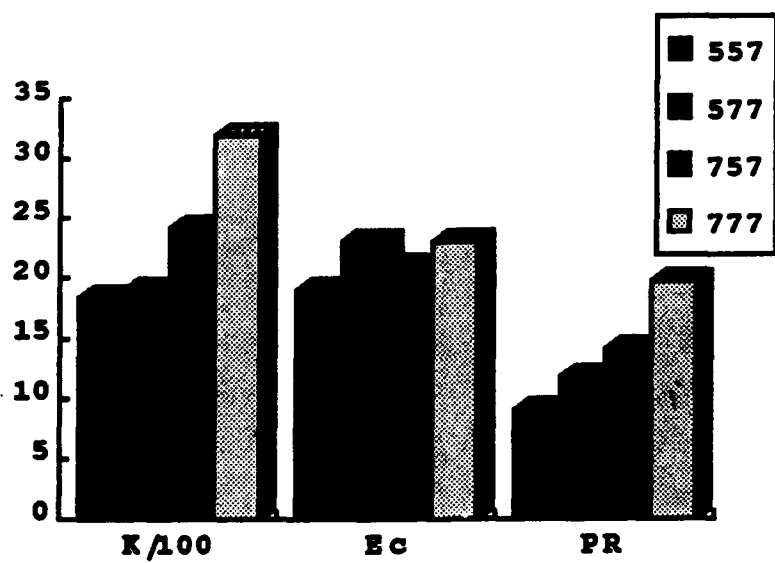


**Figure 6.** Thin film electrical measurements arranged according to increasing temperature within firing schedule.

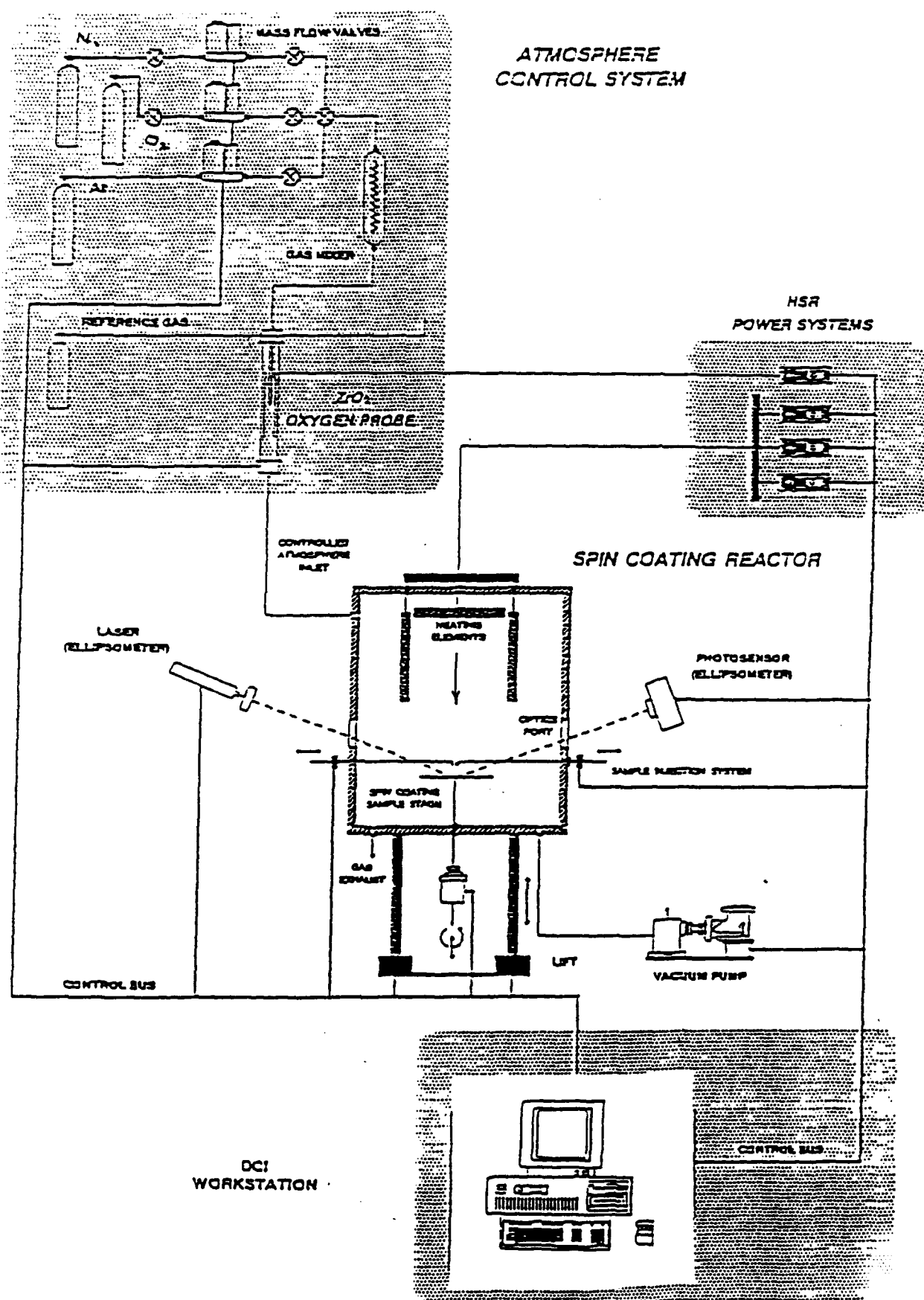


Figure 7. Automatic spin coat reactor/analyzer.

## **REFERENCES**

- [1] G. H. Haertling, Engineered Materials Handbook, 1124-1130 vol. 4 (Ceramics and Glasses), ASM International, (1991).
- [2] G. H. Haertling, *Proc. IEEE 7th International Symposium on Applications of Electrooptics*, 292 (1990).
- [3] W. Y. Gu, E. Furman, A. Bhalla and L. E. Cross, *Electrooptics*, 89, 221 (1989).

**Part VI.**

**Sputtered Thin Films and Electrooptics**

# **INTELLIGENT PROCESSING OF FERROELECTRIC THIN FILMS**

**Annual Report**

**Part VI.**

## **Sputtered Thin Films and Electrooptics**

**Submitted by: Feiling Wang  
Gene Haertling**

**The Gilbert C. Robinson Department of Ceramic Engineering  
Clemson University**

## **INTRODUCTION**

This report summarizes the main findings and conclusions of the electrooptic portion of the ONR project "Intelligent Processing of Ferroelectric Thin Films", marking the completion of the third year of this research program. Topics covered in this report include sputtered thin films and electrooptics with the following sub-topics:

- Fabrication of Ferroelectric Thin Films Using Sputter Deposition**
- Techniques for Electrooptic Characterization of Ferroelectric Thin Films**
- Novel Electrooptic Properties of Ferroelectric Thin Films**
- Light Modulations with Ferroelectric Thin Films in Fabry-Perot Etalon**
- Electrooptic Properties of Antiferroelectric Thin Film Materials**
- Photo-Activated Birefringence in Antiferroelectric Thin Films**
- Prototype PLZT Thin Film Light Modulator**

This document is organized in such a way that the detailed description of the findings and conclusions of each sub-topic is contained in one or more sections. The remainder of this introduction highlights some of the main findings and conclusions and guides the reader to the corresponding sections.

Fabrication of ferroelectric thin films by means of magnetron sputtering, alongside the other film-deposition techniques being studied in this project, has proven to be able to produce high quality PLZT thin films in terms of their dielectric and electrooptic properties (Section 1, 3 and 5). With conscious choices of boundary materials, i.e., substrates and electrodes, novel properties of the thin film materials can be obtained. Such manipulation of the thin film properties is through mechanical stress (Section 1) and the electric contact behavior between films and their electrodes (Section 3 and 10).

An advanced electrooptic characterization technique has been developed to study the birefringent electrooptic property of thin film materials. The technique involves a differential ellipsometric measurement that provides the direct detection of the field-induced optical phase retardation (Section 2). The measuring technique is applicable to thin films grown on either opaque or transparent substrates. The modeling of the differential ellipsometry by taking into account multiple reflections has resulted in a more

sophisticated and reliable measuring technique. The measuring method can also be utilized to measure the respective field-induced change for ordinary and extraordinary indices in thin film materials.

A phenomenon of birefringent bistability has been observed in ferroelectric thin film materials in a metal/ferroelectric/semiconductor (MFS) thin film structure (Section 3). The bistability is associated with the contact behavior existing between the ferroelectric and the semiconductor materials. A nonvolatile electrooptic switching has been realized by applying bipolar electric pulses to the MFS structure. Such birefringent bistability provides a mechanism for optical switching and storage in waveguide or free-space digital optics.

An optical phase modulator has been made from a PLZT material derived from acetate precursors (Section 4). Making use of the electrooptic saturation behavior, the modulator may be operated in either a linear or a quadratic mode by choosing the dc bias. The modulator therefore is capable of analog modulation.

A reflective thin film ferroelectric light modulator has been constructed on a silicon substrate (Section 5). An on/off ratio of twenty for intensity modulation and fifty degrees for phase modulation have been achieved. A thin film structure of ITO/PLZT/Pt was adopted. Unlike transmission devices, the sandwich of the ferroelectric/electrooptic films between the air-ITO and PLZT-Pt interfaces exhibited characteristics of a Fabry-Perot etalon (Section 2 and 5). The light modulation was detected in a laser beam reflected from the thin film structure when a voltage signal was applied to the ITO and Pt electrodes. Near a Fabry-Perot, drastically enhanced light modulation was obtained from the accumulated phase shift of the multiply reflected light beams.

The success of depositing antiferroelectric thin film materials from acetate precursors has prompted a systematic study of the electrooptic effects of these thin film materials (Section 6, 7 and 8). Because of the antiferroelectric nature, the materials possess a characteristic electrooptic response different from ferroelectric materials. With the reflection differential ellipsometer (Section 2), a digital birefringent response in an antiferroelectric lead zirconate thin film material grown on Pt/Ti-metallized silicon substrate was observed for the first time (Section 9). Such digital response stemmed from an electric field-induced antiferroelectric-ferroelectric phase transition. With a bias, the

**thin film material exhibited a birefringent bistability that may possess significant value in optical switching and storage.**

As an important finding from the study of antiferroelectric thin film materials, a photo-activated birefringent effect in PZT thin films bounded by a semiconducting ITO layer has been observed (Section 10). The photo-activated birefringence is associated with a photo-assisted antiferroelectric-to-ferroelectric structural transition. A low intensity soft-ultraviolet light is found to be effective in producing this effect. This newly observed phenomenon may have great implications for the usage of the antiferroelectric thin film materials for all-optical switching or storage.

Features and advantages of the prototype reflective thin film light modulator are described in Section 11, complementing the general description provided in Section 5.

## **TABLE OF CONTENTS**

### **I. Introduction**

### **II. Sections**

- 1. Transverse Electrooptic Properties of Magnetron Sputtered PLZT Thin Films, by F. Wang and G. H. Haertling**
- 2. Electrooptic Measurement of Thin Films by Means of Reflection Differential Ellipsometry, by F. Wang, G. H. Haertling and E. Furman**
- 3. Birefringent Bistability in  $(\text{Pb},\text{La})(\text{Zr},\text{Ti})\text{O}_3$  Thin Films with a Ferroelectric-Semiconductor Interface, by F. Wang and G. H. Haertling**
- 4. A PLZT Optical Phase Modulator and Its Applications, by F. Wang and G. H. Haertling**
- 5. Thin Film Ferroelectric Reflection Spatial Light Modulator with Fabry-Perot Etalon, by F. Wang and G. H. Haertling**
- 6. Transverse Electrooptic Effects of Antiferroelectric Lead Zirconate Thin Films, by F. Wang, K. K. Li and G. H. Haertling**
- 7. Antiferroelectric Lead Zirconate Thin Films Derived from Acetate Precursor Systems, by K. K. Li, F. Wang and G. H. Haertling**
- 8. Transverse Electrooptic Properties of Antiferroelectric Lead Containing Thin Films, by F. Wang, K. K. Li and G. H. Haertling**
- 9. Discrete Electrooptic Response in Lead Zirconate Thin Films from a Field-Induced Phase Transition, by F. Wang, K. K. Li, E. Furman and G. H. Haertling**
- 10. Photo-Activated Birefringence in Antiferroelectric Thin Films via a Structural Phase Transition, by F. Wang, G. H. Haertling and K. K. Li**
- 11. Reflective PLZT Thin Film Light Modulator — A Prototype Device**

## **SECTION 1**

## **TRANSVERSE ELECTROOPTIC PROPERTIES OF MAGNETRON SPUTTERED PLZT THIN FILMS**

**F. WANG and G.H. HAERTLING**  
Department of Ceramic Engineering,  
Clemson University,  
Clemson, SC 29634 , USA

**ABSTRACT.** Ferroelectric thin films of  $(\text{Pb},\text{La})(\text{Zr},\text{Ti})\text{O}_3$  ceramics were deposited on various substrates by magnetron sputtering. With the use of a phase-detection technique, the transverse electrooptic properties of the films were characterized. It was found that the electrooptic response of the films is strongly dependent on the grain orientation of the thin film materials.

### **1. Introduction**

Lead lanthanum zirconate titanate (PLZT) thin films have been deposited onto various substrates by means of solution coating techniques using acetate precursors [1-3]. In search of the optimum coating technique for producing high quality PLZT thin films for various applications, PLZT powders derived from the acetate precursors have been used as target materials in a radio-frequency (RF) magnetron sputter deposition technique designed to complement the solution coating methods.

Recently, increasing attention has been paid to the choice of substrates in obtaining thin films of desired properties [2]. It was reported that the thermal expansion mismatch between a ferroelectric thin film and its substrate significantly influences the orientational preference of ferroelectric domains, thus their dielectric properties. This paper is mainly concerned with the observed divergence of the transverse electrooptic properties in PLZT thin films deposited on various substrates by the RF magnetron sputtering.

### **2. Experimental Method**

A high vacuum RF magnetron sputter unit was used to deposit PLZT thin films. The target material was a PLZT powder of composition 2/55/45 (La/Zr/Ti) produced by a coprecipitation method from a water soluble acetate precursor [1]. A post-deposition annealing process was utilized to obtain perovskite PLZT films. Typical deposition and annealing parameters are listed below:

RF power:	70 watt	Annealing temperature:	650°C
Total pressure:	10 micron	Annealing time:	40 min.
Oxygen percentage:	40%		
Substrate temperature:	350°C		
Deposition rate:	250 nm/hour		

Thin films were deposited onto three types of substrates, i.e. Pt/Ti-coated silicon, randomly oriented sapphire and fused silica substrates.

The transverse electrooptic properties of the PLZT thin films on sapphire and fused silica substrates were measured by a phase-detection technique [4] in a transmission mode using a He-Ne laser as the light source. Planar copper electrodes with a gap width of 50 nm were fabricated on top of the thin film by a photolithography process.

### 3. Results and Discussion

#### 3.1 GRAIN ORIENTATION

With the identical deposition and annealing processes mentioned previously, the thin films deposited on the three types of substrates exhibited significant differences in grain orientation as revealed by x-ray diffraction patterns.

By comparing to the diffraction pattern of the powder, it was found that peak heights for (100) and (110) orientations in thin films on Pt/Ti-coated silicon were reversed, as shown in Figure 1(a). In contrast to the films on Pt/Ti-coated silicon, films on sapphire substrates, shown in Figure 1(b), exhibit a strengthening of the (110) peak, indicating a preferred (110) grain orientation. The most drastic preferential orientation of crystal grains was observed in the thin films deposited on fused silica substrate with (100) being the dominant orientation, as shown in Figure 1(c). Summarized in Table 1 are the types of preferential grain orientation for 2/55/45 PLZT thin films deposited on the three different substrate along with their thermal expansion coefficients.

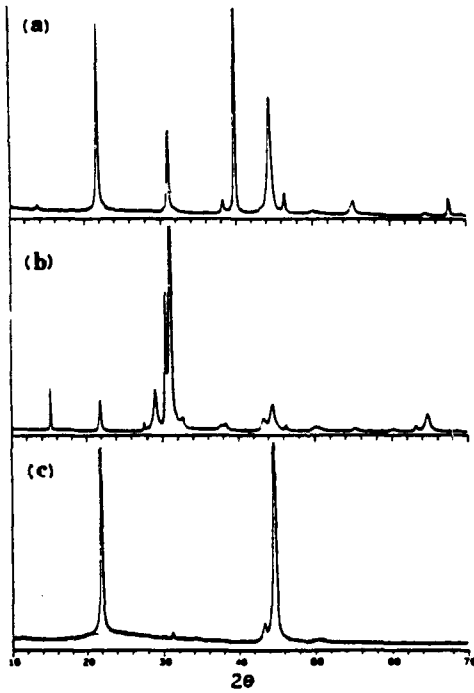


Figure 1. X-ray diffraction patterns for 2/55/45 PLZT thin films deposited on (a) Pt/Ti-coated silicon, (b) sapphire and (c) fused silica substrates.

TABLE 1. Orientation of 2/55/45 PLZT thin films

Substrate	thermal expansion coef. (ppm/ $^{\circ}$ C)	film orientation
fused silica	0.5	dominant (100)
silicon	2.5	preferred (100)
sapphire	8.0	preferred (110)

Noticing that the thermal expansion coefficient of PLZT materials (approximately 5 ppm/ $^{\circ}$ C) is intermediate between those of silicon and sapphire, the results strongly suggest that there is a correlation between the grain orientation and the thermal expansion property of the substrates in sputter deposited thin films. As shown in Table 1, thin films deposited on substrates with smaller thermal expansion coefficients exhibited dominant or preferred (100) orientation while thin films deposited on substrate with larger expansion coefficient exhibits preferred (110) grain orientation. It is not clear at present whether the preferred grain orientations are formed during the low temperature deposition or during the annealing procedure.

### 3.2. ELECTROOPTIC PROPERTIES

The field-induced birefringence of soft ferroelectric materials generally exhibit butterfly loops. In order to quantitatively describe this hysteretic electrooptic effect, three quantities are proposed to characterize a butterfly loop in the following discussion. These quantities are: the optical coercive field  $E_{oc}$  where two birefringence minima occur, the birefringence at the crossover point of a loop  $\Delta n_c$  (measured from the bottom of a curve) and the birefringence at the tip of a loop  $\Delta n_t$ . The value of  $\Delta n_t$  is meaningful only when the corresponding electric field at the tip  $E_t$  is given.

A series of butterfly loops for the electrooptic effect of a sputtered 2/55/45 PLZT film on a sapphire substrate is shown in Figure 2, created by a series field scans from a small range to a large range. Compared to the films on sapphire substrate, the 2/55/45 PLZT thin films deposited on the fused silica substrate exhibit much poorer electrooptic response as shown in Figure 3. The  $\Delta n_t$  for the film on fused silica is approximately one fourth of that for the film on sapphire substrate, taken under the same  $E_t$ . Table 2 lists the three characteristic quantities for films on both sapphire and fused silica substrates.

TABLE 2. Electrooptic properties of 2/55/45 PLZT thin films

Substrate	Thickness (nm)	$E_{oc}$ (kV/mm)	$\Delta n_t \cdot 10^{-3}$	$\Delta n_c \cdot 10^{-3}$
f. silica	620	2.0	1.5	0.2
sapphire	620	1.6	6.2	1.3

$\Delta n_t$  values were taken at  $E_t=8$  kV/mm for both samples.

Being a rhombohedral material, the polar direction of a 2/55/45 PLZT crystal grain is along a three-fold direction of a oxygen-octahedra, i.e. a (111) crystal direction. When the external electric field is parallel to the substrate surface in the phase-detection measurement in the transmission mode, there is virtually no chance for the external field to encounter the (111) crystal direction of the grains in films on fused silica with (100) dominant orientation. Films of this type of orientation, therefore, are unfavorable for utilizing the transverse electrooptic effect of the films in the transmission mode.

In contrast to the films on fused silica, sputtered films on sapphire substrate possess (110) preferred grain orientation, which enhances the possibility for the external electric field to encounter the (111) crystal direction. This preferred grain orientation, therefore,

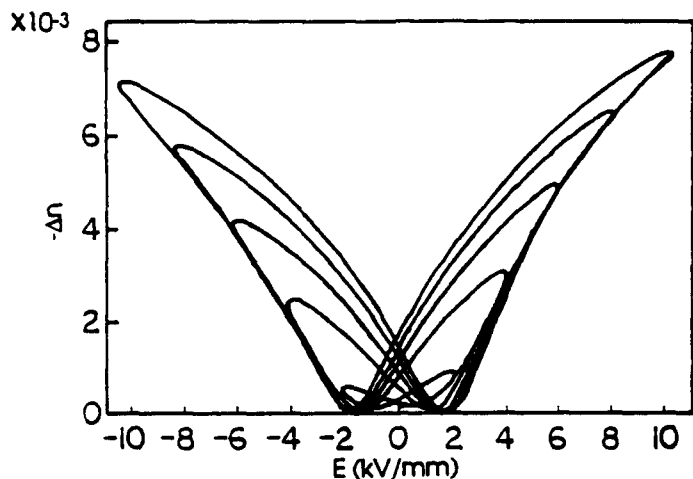


Figure 2. The evolution of the electrooptic response from a small to a large field scan range for a 2/55/45 PLZT film of thickness of  $0.62 \mu\text{m}$  on a sapphire substrate.

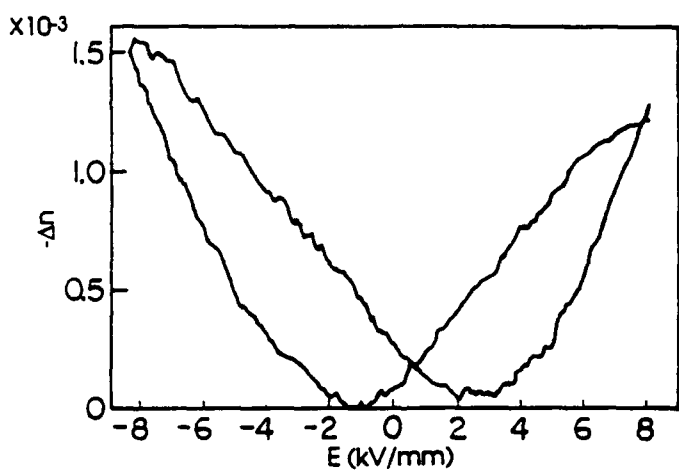


Figure 3. The electrooptic response of a 2/55/45 PLZT film of  $0.62 \mu\text{m}$  thickness on a fused silica substrate.

favors the polarization, which in turn produces a large field-induced birefringence in the materials. As shown in Table 2, films deposited on sapphire substrates with preferred (110) grain orientation indeed exhibited superior electrooptic response.

#### 4. Conclusions

PLZT thin films of composition 2/55/45 were deposited on various substrate with a RF magnetron sputtering technique using powders derived from an acetate precursor.

The electrooptic characterization shows that the films on sapphire with preferred (110) orientation exhibits superior electrooptic response over the films on fused silica with dominant (100) grain orientation. The difference is attributed to the fact that (110) orientation favors the polarization in rhombohedral thin film materials when the external electric field is along a planar direction.

#### 5. Acknowledgements

This research was supported by the Office of Naval Research under contract No. N00014-91-J-508.

#### 6. References

1. G.H. Haertling, *Ferroelectrics* **116** (1991) 51.
2. K.D. Preston and G.H. Haertling, *Appl. Phys. Lett.* **60** (1992) 2831.
3. K.K. Li, G.H. Haertling and W.Y. Howng, *Integrated Ferroelectrics* vol.3, No.1 (in print, 1992)
4. F. Wang, C.B. Juang, C. Bustamante, and A.Y. Wu, in Proc. of 4th International SAMPE Electronic Conference, Albuquerque, New Mexico, June 12-14, 1990, p.712.

## **SECTION 2**

## **ELECTROOPTIC MEASUREMENTS OF THIN FILMS BY MEANS OF REFLECTION DIFFERENTIAL ELLIPSOMETRY**

Feiling Wang, Gene H. Haertling and Eugene Furman

Department of Ceramic Engineering

Clemson University

Clemson, SC 29634-0907

A reflection differential ellipsometry has been developed for the electrooptic characterizations of thin films grown on opaque substrates. The scheme of the measurement involves a phase-sensitive detection of the field-induced phase shift in a probing light beam reflected from thin film samples. With this measuring method the field-induced birefringence may be directly plotted against a low frequency cycling voltage. The incoherent scattering of the probing light by the thin films causes negligible error in the electrooptic evaluations. To accurately calibrate the field-induced index changes or birefringence, however, it is essential to model the multiple reflection of the light in the thin film structure, which causes the "amplification" or the "reduction" of the field-induced index changes due to the interference of the reflected partial waves. The modeling reveals that the calibration coefficients for the extraordinary index change and ordinary index change, as functions of the incident angle, possess different functional forms. By measuring the field-induced phase shift of a thin film sample at different incident angles, therefore, the field-induced change of ordinary index and extraordinary index of the material may be determined separately. Detailed descriptions of the measuring technique and the modeling work are presented in the paper. Examples of the applications of this detection method are also given.

## I. Introduction

The primary role of electrooptic thin film materials in integrated optical and optoelectronic devices is to modulate guided light waves with respect to their optical phase or amplitude. Such modulations are achieved by means of the electric-field-controlled indices of refraction in the thin film materials via their birefringent electrooptic property. The characterization of the electrooptic properties of the thin film materials is, therefore, of obvious importance. In order to obtain single-mode propagation, the thickness of the electrooptic thin films, as waveguiding media, is usually less than the wavelength of the light. Accurate and reliable detection of the birefringent electrooptic effects in these thin films has remained a difficult and sometimes a challenging task. In terms of the configuration of the electrodes and the light propagation, the reported detection methods may be summarized under the following three categories: 1) the transmission method for thin films grown on transparent substrates<sup>1-5</sup>; 2) the reflection-mode detection for thin films grown on opaque substrates<sup>6-9</sup> and 3) waveguide-mode method<sup>10</sup>. Under the first two categories, either intensity-sensitive or phase-sensitive detection scheme can be adopted for the electrooptic characterization.

The transmission method of category 1 with either intensity- or phase-sensitive detection is the most widely used technique where planar electrode pairs are fabricated on thin films. Despite its advantage of simplicity, a major limitation of this method is that it is only applicable to thin films deposited on transparent substrates while many integrated devices are fabricated on substrates which are opaque to the light wavelength of concern. Because of the planar structure of the electrodes in method 1, the electric-field distribution in the gap may be significantly nonuniform<sup>11</sup>; and thus the accuracy of the measurements is unsatisfactory. To detect the electrooptic effects of thin films deposited on opaque substrates a waveguide refractometry of category 3 was reported. An advantage of the waveguide refractometry is its capability of resolving the change in ordinary index from the change in the extraordinary index. Some successes were obtained in detecting the electrooptic properties of thin films by using reflection-mode detection of category 2 with an intensity-detection approach. In these measurements because the detected signal is, under small phase shift limitaion, approximately proportional to the square of the field-induced birefringence, direct

plot of the birefringence vs. electric-field or polarization may not be obtained. Incoherent scattering may also limit the sensitivity and the accuracy of the detection, a problem suffered by all intensity-detection approaches. On the other hand, a reflection-mode detection in conjugation with a phase-detection scheme has recently been used to characterize the electrooptic effects of various thin films grown on opaque substrates. The principle of this detection method is a reflection differential ellipsometry. In addition to the advantages associated with the phase-detection scheme, recent experiments and modeling work has shown that the reflection differential ellipsometry may also be used to separate the field-induced changes in ordinary index and the extraordinary index in thin film materials.

In this paper the reflection differential ellipsometry is discussed in detail. Emphasis is placed upon the effects of multiple reflections on the accuracy of the measurements - a topic which has rarely been addressed in electrooptic measurements; but nevertheless, is important to all reflection-mode and transmission-mode methods. We intend to show how multiple reflection significantly complicates the interpretation of the measured signal thus leads to necessary corrections to the calibration method. We will also demonstrate how the interference from the multiple reflections may be utilized to separate the contribution of the extraordinary index from that of the ordinary index of the field-induced birefringence.

## **II. The Principles of the Measurement**

### **1. Single-Reflection Model**

In the reflection differential ellipsometry the field-induced change in the ellipticity of the reflected light is measured. A parallel electrode configuration is employed as shown in Figure 1. An electrooptic thin film is sandwiched between a transparent or semi-transparent top electrode and a bottom electrode during the measurement. When an electric signal is applied to the electrodes, the sandwiched thin film becomes optically uniaxial with its c axis parallel the normal of the surface as a result of the birefringent electrooptic effect. It is desirable to measure the field-induced changes in extraordinary index  $\Delta n_e$  and in ordinary index  $\Delta n_o$ , or the field-induced birefringence  $\Delta n = \Delta n_e - \Delta n_o$ . The optical arrangement of the

reflection differential ellipsometer is depicted in Figure 2. Two polarizers are inclined  $45^\circ$  with respect to the incident plane clockwise and anticlockwise, respectively. The polarization state of the probing laser beam is modulated in a periodic manner by means of an optical phase modulator, M. The purpose of the inserted optical compensator, C, is to adjust the phase angle of the probe beam and to calibrate the detected signal.

In order to discuss the mechanism of the detection technique in a progressive way we first make a single reflection approximation by neglecting the multiple reflection of the thin film structure. At first we calculate the change of the indices along the two principal axes for the probing light propagating along the diffraction direction defined by  $\theta_2$ . We designate the light component polarized in the incident plane (defined by the incident beam the normal of the film surface) as the p-polarization and the component polarized perpendicularly to the incident plane as the s-polarization. In the following calculation, whenever p or s appears as a subscript the referred quantity is associated with p- or s-polarization respectively. In an uniaxial material the index of refraction for the p-polarized light propagating along  $\theta_2$ ,  $n_p(\theta_2)$ , is given by<sup>12</sup>

$$\frac{1}{n_p^2(\theta_2)} = \frac{\cos^2 \theta_2}{n_o^2} + \frac{\sin^2 \theta_2}{n_s^2} . \quad (1)$$

For small field-induced changes in  $n_s$  and  $n_o$  we have

$$\Delta n_p(\theta_2) = \sin^2 \theta_2 \Delta n_s + \cos^2 \theta_2 \Delta n_o ; \quad (2)$$

$$\Delta n_s = \Delta n_o$$

Therefore, after a single reflection, the field-induced phase shift of the p-component with respect to the s-component is given by

$$\Delta\Gamma = \frac{4\pi d}{\lambda} \frac{\sin^2 \theta_2}{\cos \theta_2} (\Delta n_s - \Delta n_o) , \quad (3)$$

where  $d$  is the thickness of the electrooptic thin film and  $\lambda$  is the wavelength of the light beam. Because in the materials of our concern  $n_s \approx n_o$ , the difference in the diffraction angles between the two polarized component has been neglected in the above equation.

Assuming the phase modulation provided by the optical phase modulator is given by a modulating function  $R(t)$  exerted upon the p-component, the complex amplitudes for the two components (both of unity amplitude) of the incident beam may be written as

$$\begin{aligned} E_s &= 1 \\ E_p &= e^{-j[R(t)+\Gamma_c]} \end{aligned} \quad (4)$$

where  $\Delta\Gamma_c$  is the phase shift of the inserted optical compensator. After a single reflection the p-component picks up a phase shift  $\Gamma_p$ ; and the s-component picks up a phase shift  $\Gamma_s$ . The amplitudes of the reflected light then become

$$\begin{aligned} E_s &= R_s e^{-j\Gamma_s} \\ E_p &= R_p e^{-j[R(t)+\Gamma_c+\Gamma_p]} \end{aligned} \quad (5)$$

where  $R_s$  and  $R_p$  are the reflection coefficients of the thin film sample for s-component and p-component, respectively. Passing the second polarizer, the amplitude of the light that arrives at the photodetector is given by

$$E_A = \frac{I}{\sqrt{2}} \left\{ R_p e^{-j[R(t)+\Gamma_c+\Gamma_p]} - R_s e^{-j\Gamma_s} \right\}. \quad (6)$$

The detected intensity of the reflected light beam, therefore, takes the following form

$$I = -R_p R_s \cos [R(t) + \Gamma_c + \Gamma_p - \Gamma_s] + \frac{1}{2} (R_p^2 + R_s^2) . \quad (7)$$

The phase shift  $\Gamma_p$  consists of a zero-field part  $\Gamma_p(0)$  and a field-induced part  $\Delta\Gamma_p$ , (the same applies to  $\Gamma_s$ ):

$$\begin{aligned} \Gamma_p &= \Gamma_p(0) + \Delta\Gamma_p, \\ \Gamma_s &= \Gamma_s(0) + \Delta\Gamma_s . \end{aligned} \quad (8)$$

If one adjusts the optical compensator so that  $\Gamma_c + \Gamma_p(0) + \Gamma_s(0) = 0$ , the intensity of the detected light may be rewritten as

$$I = -R_p R_s \cos(M \cos \Omega t + \Delta\Gamma_p - \Delta\Gamma_s) + \frac{1}{2} (R_p^2 + R_s^2) \quad (9)$$

In the above expression the modulation function  $R(t)$  has been replaced by a sinusoid function of amplitude  $M$  and frequency  $\Omega$ , as provided by many commercially available phase modulating devices.

By setting the reference signal of the lock-in amplifier as  $\cos \Omega t$ , the output signal of the lock-in amplifier,  $S$ , is proportional to the Fourier amplitude of the light intensity associated with  $\cos \Omega t$ , which is given by

$$S = C \int_0^T I \cos \Omega t dt = C J_1(M) \sin(\Delta\Gamma_p - \Delta\Gamma_s) . \quad (10)$$

Under single reflection approximation, the difference in the field-induced phase shifts for the two polarization components,  $\Delta\Gamma_p - \Delta\Gamma_s$ , is given by Equation (3). In most practical cases where the phase shift  $\Delta\Gamma$  is very small, the output of the lock-in amplifier may be rewritten as

$$S = C(\Delta n_e - \Delta n_o) . \quad (11)$$

The proportional constant  $C$  in the above equation or Equation (11) can be calibrated using the adjustable optical compensator by reading the output signal,  $S$ , associated with a known phase change,  $\Delta\Gamma_c$ , of the compensator.

In this phase detection scheme, incoherent scattering of the light beam does not contribute to the measured phase shift. This can be easily seen from Equation 7, where incoherent scattering may be represented by an additional constant term. Such constant term does not alter the output signal of the lock-in amplifier given by Equation 10. On the other hand, field-induced scattering of the light may cause errors in the calibration of the detected signal. However, such situation only happens when very severe field-induced scattering causes the amplitude of the reflected light to become substantially field dependent. In the electrooptic measurement of thin film materials, these situations are very rare.

## 2. Multiple-Reflection Model

As has been mentioned previously, the single-reflection model is only a simplification of the real world situation where multiple reflection of the light beam occurs in the parallel thin film structure. In the presence of multiple reflections the amplitude for both p- and s-component arriving at the photodetector is the coherent summation of each partial amplitude. In this situation, Equation (10) remains valid. However, the measured phase difference,  $\Delta\Gamma = \Delta\Gamma_p - \Delta\Gamma_s$ , is no longer, in general, proportional to the field-induced birefringence  $\Delta n = \Delta n_e - \Delta n_o$ , as given by Equation (4).

To find the relationship between the detected phase difference  $\Delta\Gamma$  and the field-induced changes of refractive index,  $\Delta n$ , and  $\Delta n_o$ , first we need to derive the complex reflectance of the thin film structure by coherently summing the partial reflected waves for each component with given indices and thickness of thin film samples. The problem of concern here is the overall reflectance of two thin films sandwiched between semi-infinite ambient and substrate. We may now borrow the results developed for the theory of ellipsometry. It is found that in such

stratified structure the complex reflectance,  $\tilde{R}$ , for both polarization components is given by:

$$\tilde{R} = Re^{-j\Gamma} = \frac{(r_{01} + r_{12}e^{-j2\beta_1}) + (r_{01}r_{12} + e^{-j2\beta_1})r_{23}e^{-2j\beta_2}}{(1 + r_{01}r_{12}e^{-j2\beta_1}) + (r_{01} + r_{12}e^{-j2\beta_1})r_{23}e^{-2j\beta_2}}, \quad (12)$$

where  $r_{01}$ ,  $r_{12}$  and  $r_{23}$  are the individual Fresnel reflection coefficients for boundaries between media {0,1}, {1,2} and {2,3}, respectively;  $\beta_1$  and  $\beta_2$  are the phase thickness of layer 1 and layer 2 respectively. Because the above equation applies to both polarizations the subscripts associated with all the quantities have been omitted. It is important to note, however, that since the Fresnel reflection coefficients are different for the two polarization components, the above equation represents two different functional forms of the incident-angle dependence for the p- and s-polarizations.

All the Fresnel reflection coefficients and phase thicknesses involved in Equation (12) can be expressed in terms of the thickness of the films, the indices of all the media and the incident angle. The overall reflection coefficient,  $\tilde{R}$ , in turn, may be expressed by the incident angle and these material parameters. For our main concern, in particular, the overall phase angles,  $\Gamma_p$  and  $\Gamma_s$ , may be written in the following form:

$$\begin{aligned}\Gamma_p &= f_p(n_1, n_2, n_3, d_1, d_2, \theta_0) \\ \Gamma_s &= f_s(n_1, n_2, n_3, d_1, d_2, \theta_0)\end{aligned} \quad (13)$$

The differentiation of the above functions with respect to  $n_2$  gives the change rate of the measured phase shifts  $\Delta\Gamma_p$  and  $\Delta\Gamma_s$  caused by small field-induced index changes,  $\Delta n_p$  and  $\Delta n_s$ . Formally, these derivatives can be written as:

$$\begin{aligned} \left. \frac{df_p}{dn_2} \right|_{n_2(0)} &= w_p(n_1, n_2, n_3, d_1, d_2, \theta_0); \\ \left. \frac{df_s}{dn_2} \right|_{n_2(0)} &= w_s(n_1, n_2, n_3, d_1, d_2, \theta_0), \end{aligned} \quad (14)$$

where  $n_2(0)$  is the index of the electrooptic film under zero external field. With the help of Equation. (2), the detected phase shift is found to be given by

$$\Delta\Gamma \equiv \Delta\Gamma_p - \Delta\Gamma_s = w_p \sin^2 \theta_2 \Delta n_e - (w_s - w_p \cos^2 \theta_2) \Delta n_o . \quad (15)$$

The above equation shows that the contributions of the extraordinary index change and ordinary index change to the detected phase shift are weighted by  $w_p$ ,  $w_s$  as well as the incident angle of the probing light. It can be seen that unless  $w_s$  and  $w_p$  happen to have the same value at certain incident angles the measured phase shift  $\Delta\Gamma$  is not proportional to the field-induced birefringence  $\Delta n = \Delta n_e - \Delta n_o$ .

The explicit functional forms of  $w_p$  and  $w_s$  can be derived from Equation (12). The derivations are straightforward, however, leads to lengthy expressions. To evaluate the field-induced index changes,  $\Delta n_e$  and  $\Delta n_o$  of a sample from the measured quantity  $\Delta\Gamma$ , it is necessary to calculate the values of  $w_p$  and  $w_s$  for the sample. These calculations may be performed with the help of a computer. In general, because of the changing phase relation between the adjacent partial waves, the detected phase shift oscillates as the incident angle or the thickness of the film changes. As an example,  $w_s$  and  $w_p$  are computed for the case of a typical perovskite thin film grown on a platinum bottom electrode with an indium-tin oxide (ITO) top electrode. The thicknesses of the electrooptic layer and the top electrode are assumed to be unity wavelength and 0.2 wavelength, respectively; the indices of the electrooptic layer and top electrode are assumed to be 2.5 and 2.0, respectively. The calculated  $w_s$  and  $w_p$  are plotted against the incident angle in Figure 3. It is obvious that the contribution of the extraordinary index and the ordinary index to the measured phase shift vary with the incident angle according

to their respective functional forms. In this example, except in the neighborhood of incident angle of  $56^{\circ}$ , where  $w_s = w_p$ , the measured phase shift  $\Delta\Gamma$  given by Equation (15) is not proportional to the field-induced birefringence  $\Delta n_s - \Delta n_o$ .

The above example shows that the field-induced index changes may get amplified or reduced as a result of the multiple reflection. For samples of different thickness the relative contributions from  $\Delta n_s$  and  $\Delta n_o$  may also be different. The calculated  $w_s$  and  $w_p$  as functions of the thickness of the electrooptic layer is shown in Figure 4. The oscillations of  $w_s$  and  $w_p$  in the figure is again from the alternating phase relation between adjacent partial waves with the change of film thickness. The thickness change of the top electrode causes similar oscillations.

The fact that  $w_s$  and  $w_p$ , as functions of the incident angle, possess different functional forms greatly complicates the interpretation of the detected phase shift, however, it provides a means of determining both  $\Delta n_s$  and  $\Delta n_o$  from the experiments. A scheme of doing this is to measure the field-induced phase shift of electrooptic thin films at different incident angles while keeping the applied voltage constant. Using the present model, both  $w_s$  and  $w_p$  can be calculated as functions of the incident angle. Theoretically, the field-induced index changes,  $\Delta n_s$  and  $\Delta n_o$ , can be solved from the following set of equations:

$$\begin{aligned}\Delta\Gamma^I &= w_p^I \sin^2 \theta_2^I \Delta n_s - (w_s^I - w_p^I \cos^2 \theta_2^I) \Delta n_o \\ \Delta\Gamma^{II} &= w_p^{II} \sin^2 \theta_2^{II} \Delta n_s - (w_s^{II} - w_p^{II} \cos^2 \theta_2^{II}) \Delta n_o\end{aligned}, \quad (18)$$

where those superscripted by I and II are quantities associated with any two experimentally chosen incident angles,  $\theta_0^I$  and  $\theta_0^{II}$ , respectively. More accurate results may be obtained by using the calculated  $w_s$  and  $w_p$  to fit experimental data taken at many different incident angles.

### III. Detection Techniques and Applications

A schematic diagram of the reflection differential ellipsometer is shown in Figure 2. The light source is a He-Ne laser. The phase modulation of the laser beam is generated by a photo-elastic modulator which provides variable modulating depth at a frequency of 50 kHz, suitable for the lock-in amplification. As has been discussed in the previous section, it is preferred to adjust the optical compensator under zero applied field so that

$$\Gamma_c + \Gamma_p(0) + \Gamma_s(0) = 0 . \quad (19)$$

From Equation (10) we see that under the above condition, the waveform of the light intensity is predominantly  $2\Omega$  in frequency. Therefore the above condition, i.e. Equation (20), may be reached by observing the waveform of the light on a oscilloscope while adjusting the optical compensator. When an external electric field is applied to sample, an modulating component at frequency  $\Omega$  is created in the light intensity due to the field-induced phase shift. In order to pick out this phase shift, the reference signal of the lock-in amplifier must be set as  $\cos\Omega t$ . To obtain the best sensitivity of detection, the modulating amplitude  $M$  in Equation (11) should be adjusted to  $\pi/2$ .

To obtain the phase shift vs. applied voltage loops, a low frequency cyclic voltage is applied to the sample between the top and the bottom electrodes. The frequency of the applied voltage must be much lower than the modulation frequency of the light provided by the optical phase modulator (50kHz) in order for the lock-in amplifier to reach an steady output at any instantaneous voltage. During our experiments the cycling frequency of the applied voltage is typically around 0.5 Hz.

The present reflection differential ellipsometer has been used to characterize various electrooptic thin films. Figure 5 shows the birefringence vs. electric field curve for a 8/65/35 lead lanthanum zirconate titanate (PLZT) thin film sputter-deposited on a Pt/Ti-coated silicon substrate, measured by using this technique. The thickness of the PLZT film is 680 nm. The top electrode is a 360

nm thick indium-tin oxide (ITO) layer deposited by sputter deposition. The birefringence vs. electric field loop was measured at an incident angle of 47° for the probing laser beam.

To better evaluate the index changes of the sample, several field-induced phase shift vs. applied voltage curves were successively measured at different incident angles while keeping the cycling voltage constant. The phase shift of each curve at its maximum cycling voltage (8 volts) is plotted against the incident angles shown by the discrete points in Figure 6. With known thicknesses and indices of the PLZT thin film and the ITO electrode, Equation (15) was used to fit the experimental data by using  $\Delta n_r$  and  $\Delta n_o$  as two fitting variables in a least square fitting scheme. The resultant values are  $\Delta n_r = -1.3 \times 10^{-2}$  and  $\Delta n_o / \Delta n_r = -0.21$ . The solid line in Figure 7 is the theoretical curve of Equation (15) using the calculated  $w_r$  and  $w_s$ . The calculated curve from the single-reflection model, i.e. Equation (3), is also shown in the figure by the dashed line. It is clear that the phase shift peak in the incident angle dependence, shown in the Figure, stems from the interference of multiple reflection.

As been mentioned previously, the contributions of the index changes,  $\Delta n_r$  and  $\Delta n_o$ , to the measured field-induced phase shift are determined by  $w_r$  and  $w_s$ , through Equation (15). Correct field-induced birefringence vs. electric field curves can be only measured at incident angles where  $w_r = w_s$ . The  $w_r$  and  $w_s$  as functions of the incident angle of the PLZT sample is calculated using the multiple-reflection model and plotted in Figure 7. It is clear that for this PLZT sample, incident angles in the neighbourhood of 47° or 66° are preferred. This is the reason why an incident angle of 47° was chosen in measuring the electrooptic response shown in Figure 5.

Another example is the detection of the birefringent electrooptic effect of antiferroelectric lead zirconate thin films on Pt/Ti-coated silicon substrate. The films were deposited by using a dip-coating process. The thickness of the film is approximately 1  $\mu\text{m}$ . An incident angle of 67° was used during the measurement. A typical birefringence vs. electric field loop is presented in Figure 8. At this incident angle, the values of  $w_r$  and  $w_s$ , calculated from the model, are 22.9 and

17.1 respectively. In other words, according to the model, the detected field-induced phase shift contains larger contributions from the extraordinary index than from the ordinary index. In labeling the Y-axis of Figure 8 as the field-induced birefringence, therefore, some approximation is involved. The digital type of electrooptic response shown in Figure 8, as a result of the field-induced antiferroelectric-ferroelectric transition<sup>8</sup>, can only be observed in a reflection-mode electrooptic measurement where parallel electrodes create a very uniform electric field inside the thin film materials.

Because parallel electrodes are used in the reflection-mode differential ellipsometry, one can measure the field-induced birefringence and the electric polarization from the same sample. This enables us to directly measure the relationship between the field-induced birefringence and the electric polarization of thin film materials. Figure 9 shows the field-induced birefringence vs. polarization loop of a 8/65/35 PLZT thin film, obtained by simultaneously detecting the field-induced birefringence and the polarization of the thin film during a voltage cycle. This type of loop cannot be obtained in a transmission-mode electrooptic measurement because of the geometry of planar electrodes.

## VI. Conclusions

The principles of a reflection-mode differential ellipsometry for the electrooptic measurement of thin film materials is presented. The scheme of the measurement involves a phase-sensitive detection of the field-induced phase shift in a probing light beam reflected from the thin film samples. Neglecting the multiple reflections, the detected phase shift is proportional to the field-induced birefringence of the electrooptic thin film.

The occurrence of multiple reflection in the layered structure causes the "amplification" or "reduction" of the field-induced index changes in the measured signal due to the interference of the partial waves. A simplified multiple reflection model, which neglects the top electrode in considering the interference, is proposed to simulate the experimental situation. It is found from the model that the ordinary-index change and the extraordinary-index change contribute to the

measured phase shift in their respective manners. Therefore the measured field-induce phase shift is not in general proportion to the field-induce birefringence. The corrections to the measured indices changes calculated from the model prove to be semi-quantitatively consistent with the experiments.

The model demonstrates the usefulness of the multiple reflection in separating the extraordinary index change from the ordinary index change. Such separation may be achieved by measuring the field-induced change at different incident angles, where the respective contributions from the extraordinary index change and the ordinary index change are different.

The experiments demonstrate that the reflection-mode differential ellipsometry is a effective and convenient way of measuring the transverse electrooptic properties of thin films grown on opaque substrates. This measuring technique also provides a means of directly measuring the relationship between the field-induced birefringence and the polarization of thin film materials.

## **References**

1. C. E. Land, J. Am. Ceram. Soc. 72, 2059(1989)
2. Gene H. Haertling, Ferroelectrics, 75, 25(1987)
3. H. Adachi et al, J. Appl. Phys. 42, 867(1983)
4. K. Carl et al, Proc. of the IEEE, 61, 967(1973)
5. F. Wang et al, Proc. of the 4th International SAMPE Electronic Conf., Albuquerque, New Mexico, June 12-14, 1990
6. M. Ishida et al, Appl. Phys. Lett., 31, 433(1977)
7. D. Dimos, et al, "Electrooptic Effects and Photosensitivities of PZT Thin Films," Ferroelectric Films
8. F. Wang, et al, Optics Lett., in press
9. F. Wang et al, Appl. Phys. Lett., in press
10. B. G. Potter, Jr. et al, Appl. Phys. Lett. (to be published)
11. G. W. Farnell, et al, IEEE Trans. Sonics. Ultrasonics, SU-17, 188(1970)
12. Yariv et at, in Optical Waves in Crystals.
13. M. Born and E. Wolf, in Principlew of Optics, 4th Edition (Pergamon Press, 1970)
14. G. H. Haertling and C. E. Land, J. Am. Ceram. Soc. 54, 1(1971)

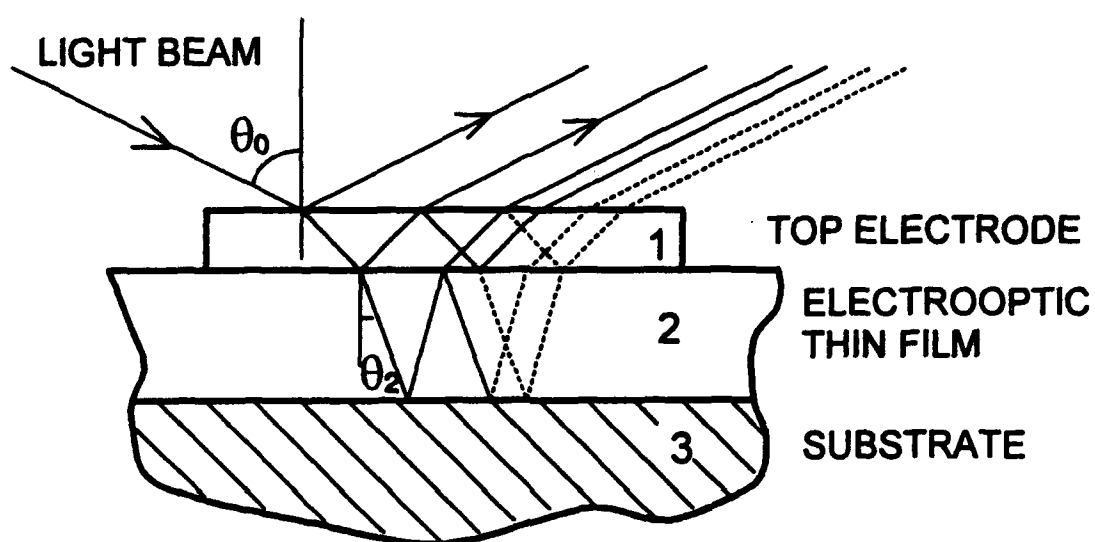


Figure 1. Schematic diagram of the arrangement of the electrodes. The probing light is obliquely incident on the sample with an incident angle of  $\theta_0$ .

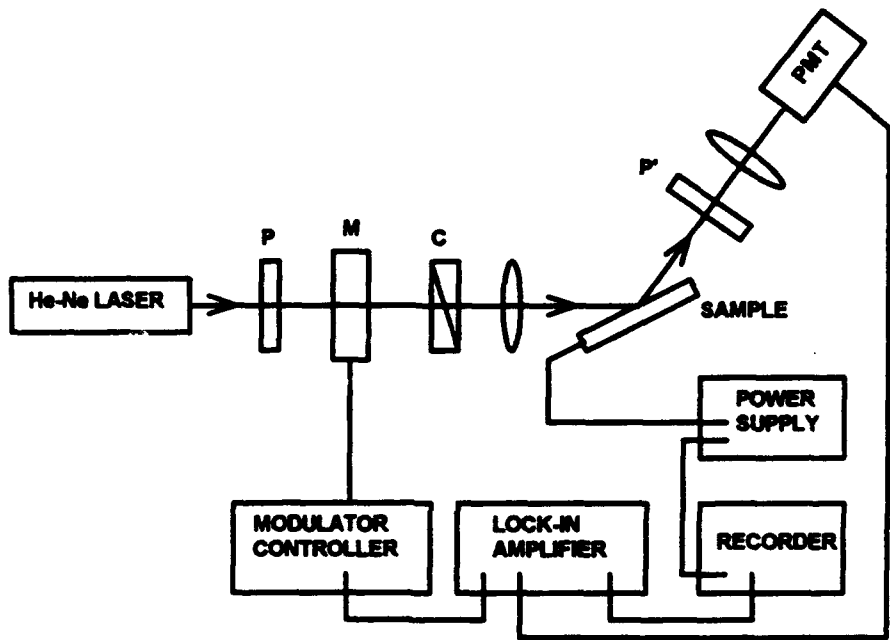


Figure 2. Schematic diagram of the reflection-mode differential ellipsometer.

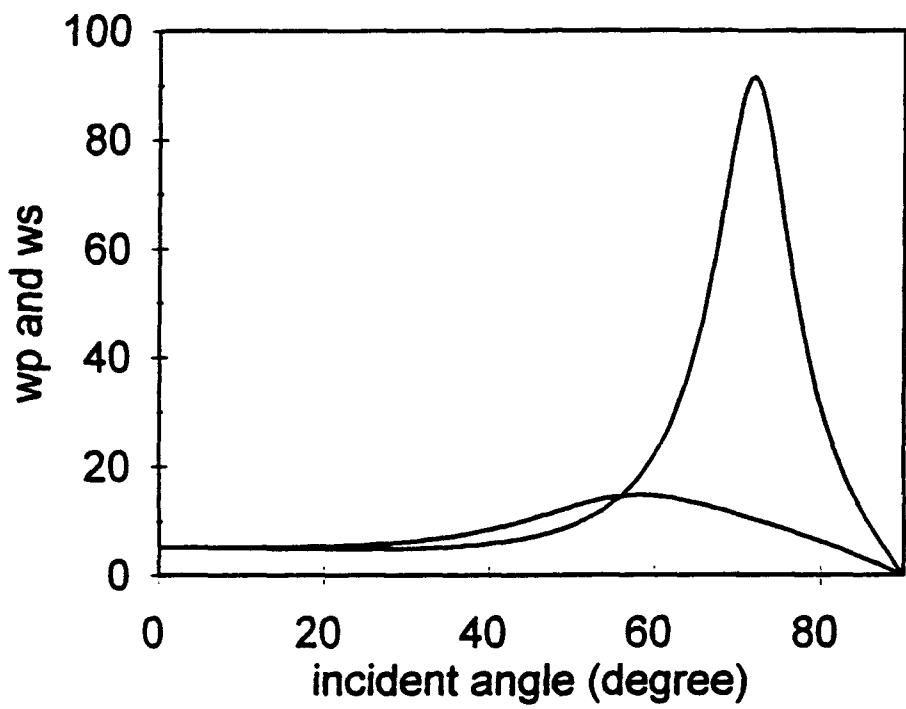


Figure 3. The calculated coefficients,  $w_p$  and  $w_s$ , for p- and s-component as functions of the incident angle. The thicknesses of the electrooptic layer and the top electrode are chosen to be unity wavelength and 0.2 wavelength of the probing light beam.

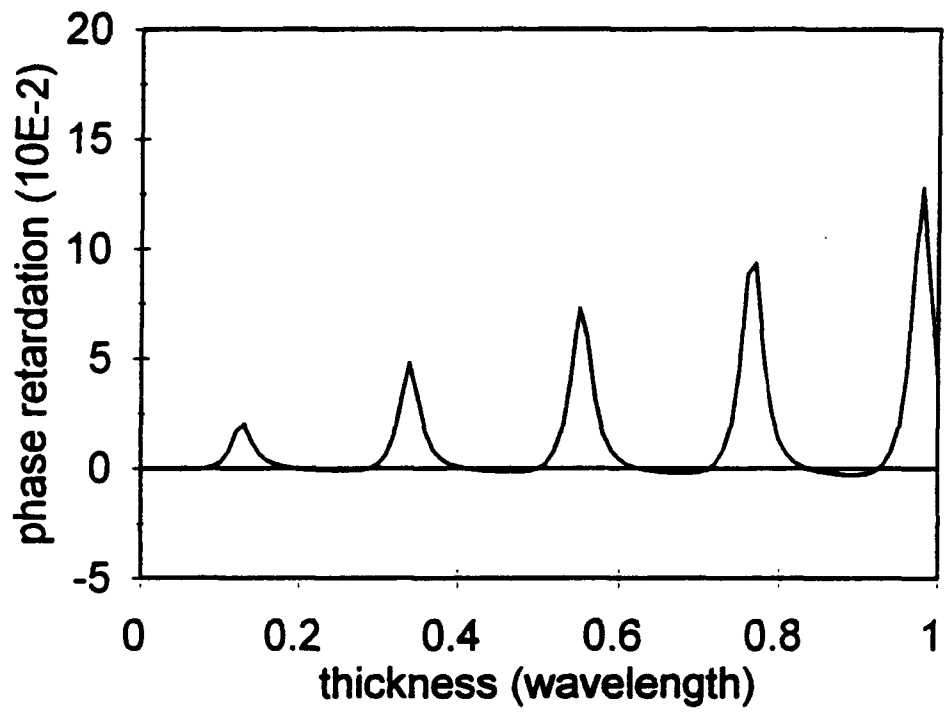
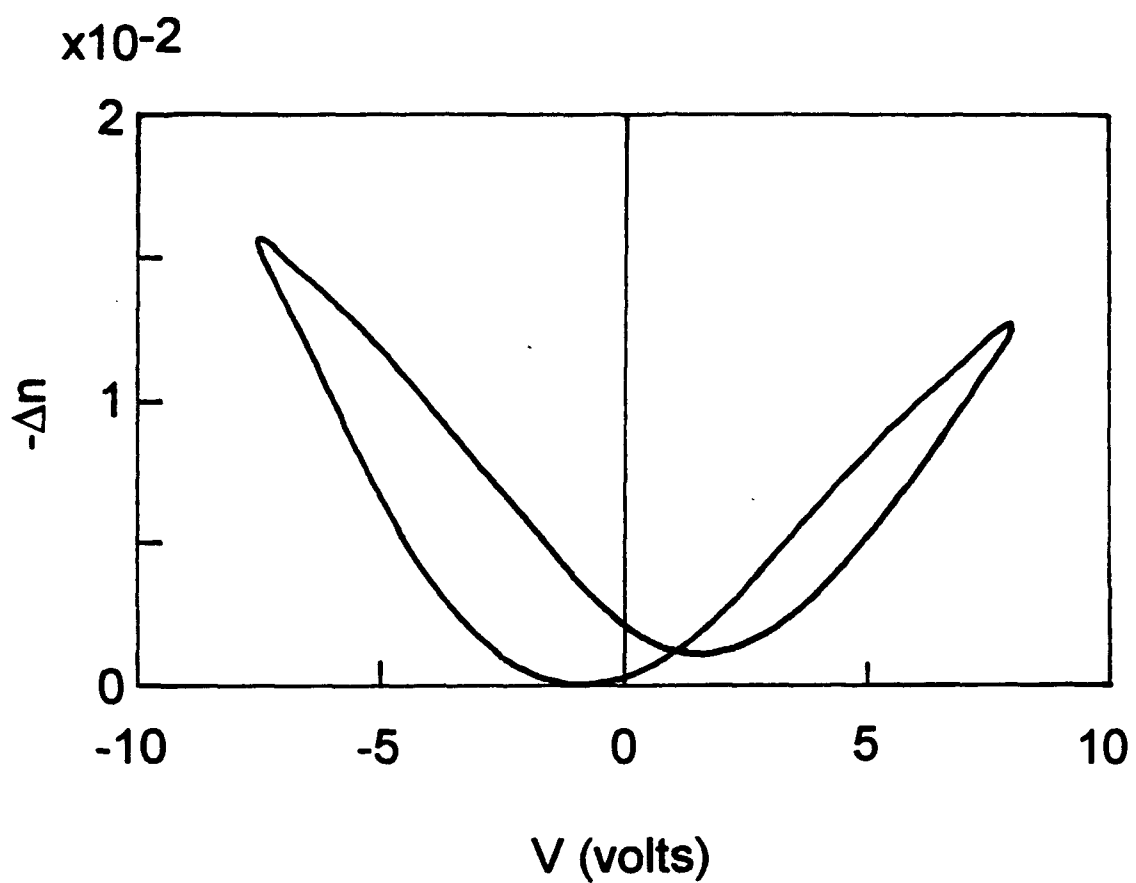


Figure 4. The calculated coefficient,  $w_1$ , and  $w_2$ , as functions of the thickness of the electrooptic layer. The thickness of the top electrode layer is chosen to be 0.2 wavelength of the light beam; the incident angle is chosen to be 60 degrees.



**Figure 5.** Field-induced birefringence vs. electric field loop for a 8/65/35 PLZT thin film sputter-deposited on a platinum-coated substrate.

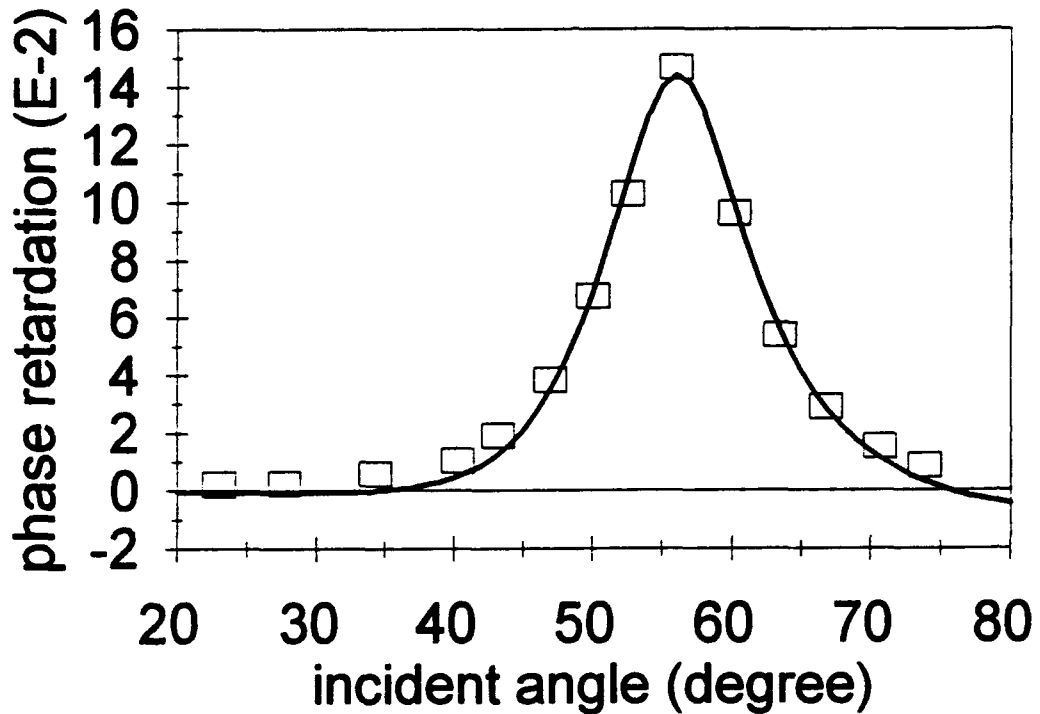


Figure 6. Incident angle dependence of the field-induced phase retardation for the PLZT thin film sample measured in Figure 5. The discrete points are experimental data. The solid line is the theoretical curve from least-square fitting Eq. 15 to the experimental data.

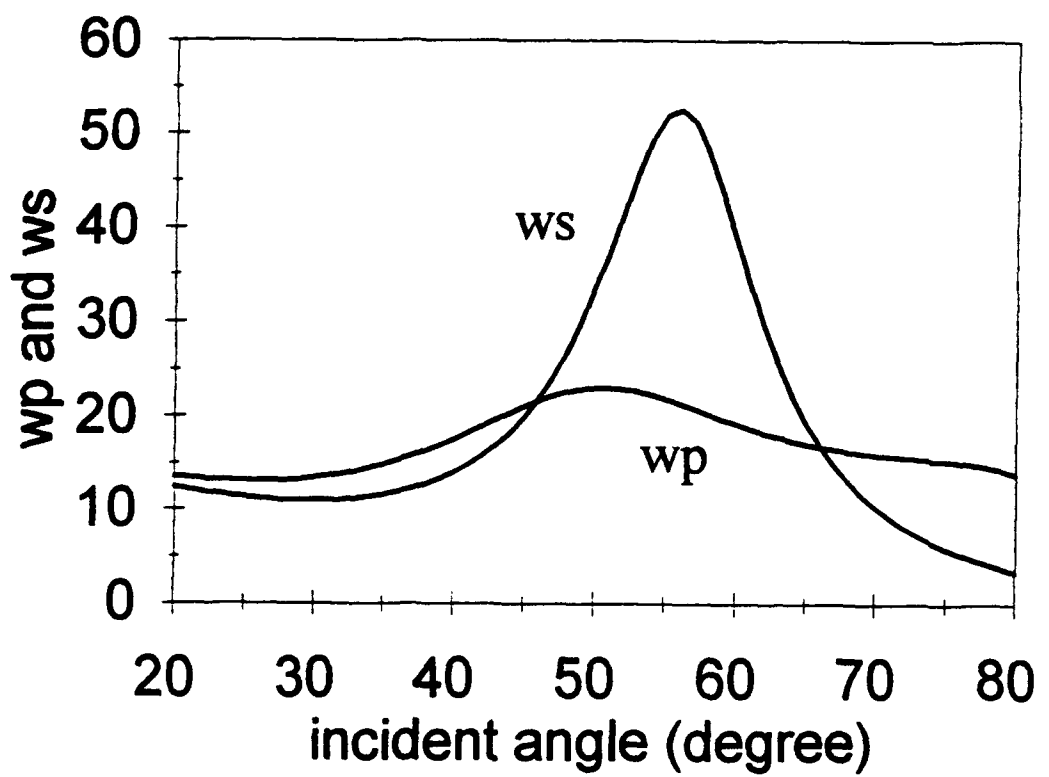


Figure 7. Calculated angular dependence of the coefficients,  $w_p$ , and  $w_s$ , for the thin film sample measured in Figure 5.

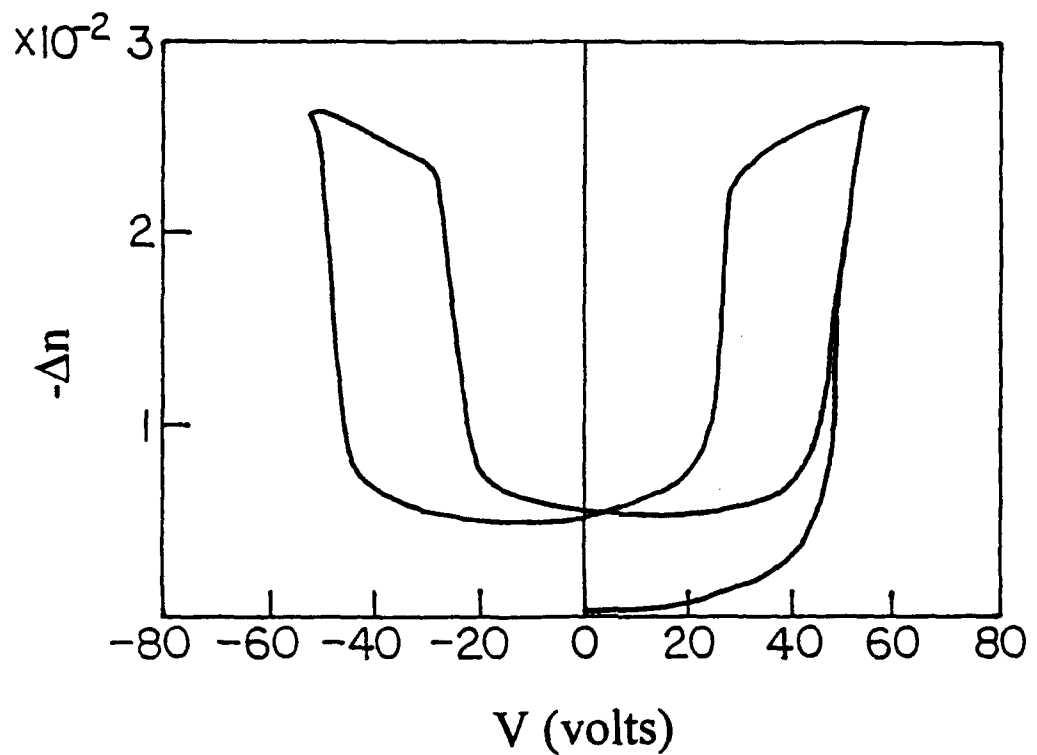


Figure 8. Field-induced birefringence vs. applied voltage loop for an antiferroelectric lead zirconate thin film grown on a platinum-coated substrate.

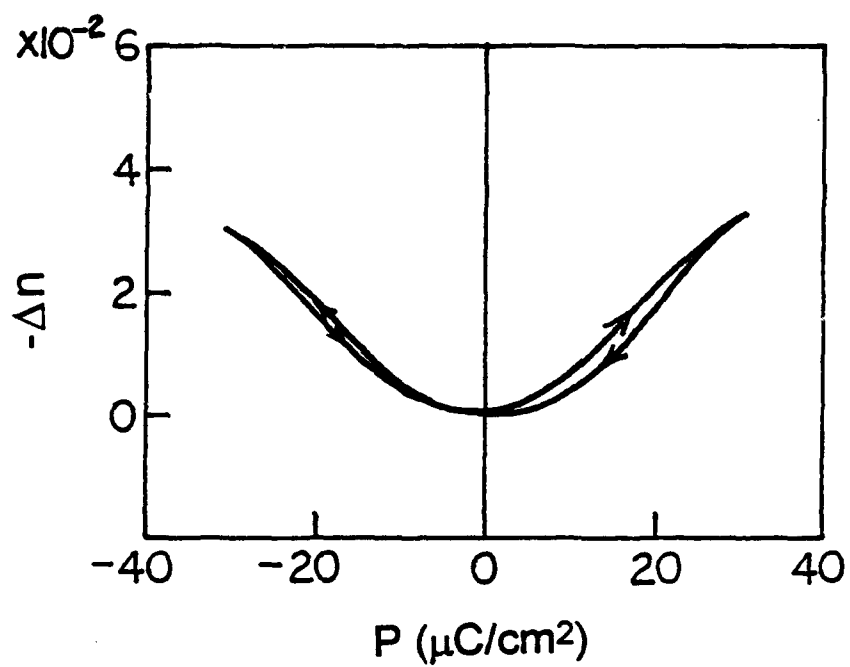


Figure 9. Field-induced birefringence vs. polarization loop measured from an 8/65/35 PLZT thin film grown on a platinum-coated substrate.

## **SECTION 3**

# Birefringent bistability in $(\text{Pb},\text{La})(\text{Zr},\text{Ti})\text{O}_3$ thin films with a ferroelectric-semiconductor interface

Feiling Wang and Gene H. Haertling

Department of Ceramic Engineering, Clemson University, Clemson, South Carolina 29634-0907

(Received 29 March 1993; accepted for publication 16 July 1993)

We report a birefringent bistability exhibited in ferroelectric thin films with a ferroelectric-semiconductor interface. Such birefringent bistability is observed in  $(\text{Pb},\text{La})(\text{Zr},\text{Ti})\text{O}_3$  (PLZT) thin films which are sandwiched between a platinum and a semiconducting indium-tin oxide (ITO) electrode. The magnitude of the birefringence between the two remanent states is approximately  $0.9 \times 10^{-3}$ . The Pt/PLZT/ITO structure features a nonvolatile electro-optic memory operation, i.e., the switching between the two remanent birefringent states with bipolar electric pulses.

Ferroelectric polarization reversal, which has facilitated a nonvolatile memory mechanism for electric signals,<sup>1,2</sup> has not proved to be able to perform a nonvolatile electro-optic memory function for optical signals due to the fact that the two remanent polarization states in normal ferroelectric materials are optically indistinguishable. The symmetry in the optical properties under polarization reversal may be broken if one of the polarization directions is made more favorable than the other under the influence of certain electrode combinations. The asymmetric polarization in ferroelectric thin films on semiconductor substrates has been observed,<sup>3</sup> however, its implications for the electro-optic properties of the thin films have not been studied. The purpose of this letter is to report the phenomenon of a birefringent bistability associated with the polarization reversal in ferroelectric  $(\text{Pb},\text{La})(\text{Zr},\text{Ti})\text{O}_3$  (PLZT)<sup>4</sup> thin films which are electroded with a metal and a semiconducting layer.

The birefringent bistability in PLZT thin films was observed to exist in a thin film metal/ferroelectric/semiconductor (MFS) structure shown in Fig. 1. Polycrystalline PLZT thin films of composition 8/65/35(La/Zr/Ti) were deposited on Pt-coated silicon substrates by means of magnetron sputtering. The thickness of the PLZT films was approximately 750 nm. Indium-tin oxide (ITO) films of about 350 nm in thickness were then deposited on the PLZT films also by sputtering. A post-deposition annealing process was used to obtain a perovskite crystalline structure of the PLZT material.

With dc voltage or electric pulses applied to the platinum and the ITO layers, a sandwiched PLZT film becomes birefringent with its c axis along the normal of the film surface as a result of the transverse electro-optic effect. A phase-detection scheme in the reflection mode, with the experimental setup shown in Fig. 2, was used to measure the field-induced birefringence,  $\Delta n = n_e - n_0$ , in the PLZT thin film. The modulation of the incident light was provided by a photoelastic modulator. At a finite incident angle, the reflected light polarized in the incident plane acquires a phase retardation with respect to the component polarized perpendicularly to the incident plane due to the birefringence of the PLZT thin films. Such phase retardation is associated with a modulating component of the light

received by the photodetector. With a proper setting of the reference signal, the output of the lock-in amplifier is proportional to the birefringence,  $\Delta n$ , of the PLZT thin films.

The birefringence in the PLZT films as a function of the slowly varying dc voltage exhibited severe asymmetry as revealed by a typical loop shown in the insert of Fig. 3. The voltage shown in the figure is measured with respect to the platinum electrode. An important feature of Fig. 3 is that there are two distinguishable remanent birefringent states dependent on the polarity of the voltage from which the zero voltage is reached. The occurrence of the two distinguishable remanent birefringent states is not a result of accidental poling of the material during the initial application of an electric field, since all samples reproduced the same features as in Fig. 3 regardless of the polarity of the initial electric field. To further verify the inherent nature of these two distinguishable birefringent states, a series of plots were successively taken from a small to a large field scan range. As shown in Fig. 3, with the increase of the scan range, the two remanent birefringent states approach their saturation values,  $\Delta n_A$  and  $\Delta n_B$ , respectively.

The interswitching of the two remanent birefringent states with electric signals was achieved by applying bipolar electric pulses to the MFS devices. With the detection system shown in Fig. 2, the output voltage of the lock-in amplifier (proportional to the birefringence of the thin film) was recorded versus time when bipolar electric pulses were fed to the device. Figure 4 represents the birefringent signal forms of the PLZT film responding to bipolar elec-

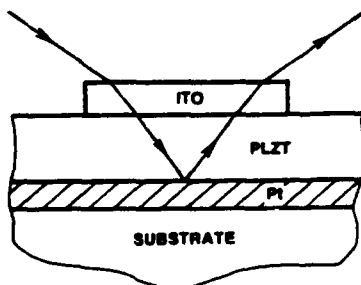


FIG. 1. Structure of the Pt/PLZT/ITO thin film device. The propagation of the light beam in the phase-detection measurement is shown by the line with arrows.

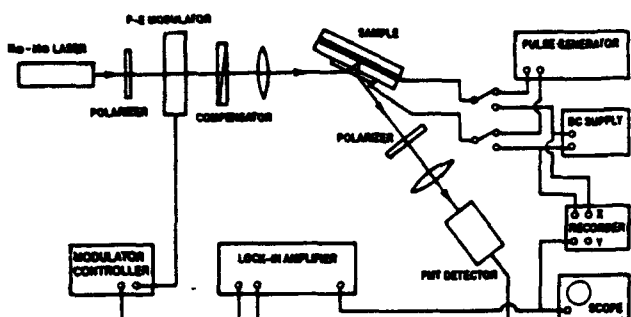


FIG. 2. Schematic diagram for the phase-detection scheme in the reflection mode.

tric pulses of 0.1 ms in pulse width and peak voltage ranging from 5 to 30 V. The interval between the pulses was 5 s. The dashed line schematically denotes the polarities and positions of the bipolar pulses.

It is shown in Fig. 4 that bipolar electric pulses switch the PLZT thin film between two distinguishable birefringent states, which correspond to the two remanent states for each dc cycle in Fig. 3. The magnitude of the birefringence between the two remanent states (birefringent spacing) substantially increases with increasing peak voltage of the pulse until saturation behavior takes place. The saturated birefringent spacing is approximately  $0.9 \times 10^{-3}$ . Such saturation is consistent with the dc response of the devices shown in Fig. 3. The nonvolatile nature of the birefringent switching is obvious in that after a positive pulse, the thin film remains in a low birefringent state until the following negative pulse switches the material to a high birefringent state. Because of the detection method, the response speed of the measuring system was determined by the integration time of the lock-in amplifier. The transient behavior of the switching, therefore, cannot be directly observed with this measurement.

Figure 5 shows the birefringent spacing of the device as a function of the pulse width while keeping the peak voltage constant. Although the intrinsic switching speed of the PLZT thin film is essentially determined by the domain switching process, the response time of the device, how-

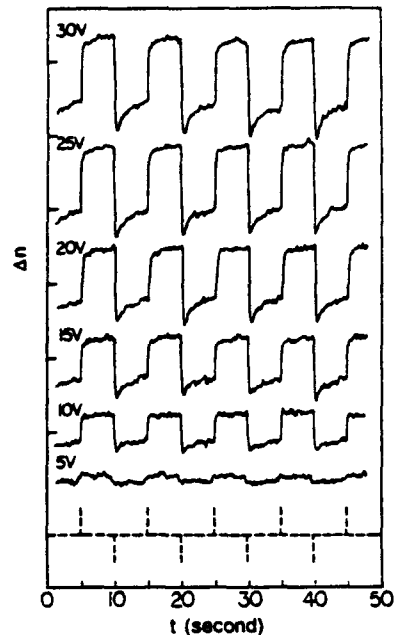


FIG. 4. Interswitching between the two remanent birefringent states with bipolar electric pulses. The peak voltage of the switching pulses are marked on each curve. The dashed line schematically denotes the positions and the polarities of the bipolar pulses. The vertical scale for the birefringence is  $10^{-3}$  per division.

ever, may be predominated by the *rc* constant of the device, which was approximately  $2.5 \mu\text{s}$ . It is shown in Fig. 5 that when the pulse width becomes comparable to the *rc* constant of the device, the birefringent spacing between the two states is significantly reduced, indicating an incomplete switching of the ferroelectric domains. When the pulse width becomes much larger than the *rc* constant, the birefringent spacing is no longer dependent on the pulse width.

The occurrence of the birefringent bistability in the device may be explained by the polarity sensitive polarization of the PLZT thin films with a ferroelectric-semiconductor interface. It was recognized that electrodes in contact with a ferroelectric material play an important role in sustaining polarizations in the ferroelectric material.<sup>5</sup> In particular, the compensation of surface charges by electrodes is sometimes crucial in determining the remanent polarization in thin film ferroelectrics. Experimental evidence has shown that the birefringent bistability in the

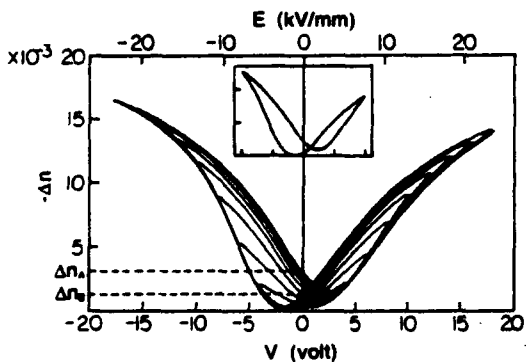


FIG. 3. Measured birefringence  $\Delta n$  in the PLZT thin film as a function of the slowly varying dc voltage, taken successively from a small to a large dc field scan range. A single cycle is shown in the insert. The horizontal and the vertical scales of the insert are  $5 \times 10^{-3}$  per division and 5 V per division, respectively.

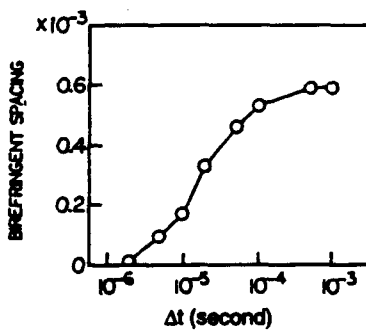


FIG. 5. Birefringent spacing between the two remanent states as a function of the pulse width with a fixed peak voltage of 15 V.

MFS structure was a result of the unequal remanent polarizations of opposite polarities caused by the PLZT/ITO interface. Being an *n*-type semiconductor,<sup>6</sup> an ITO film is expected to form a *p-n* junction with the PLZT thin film that usually exhibits *p*-type conduction properties.<sup>7</sup> Under the short-circuit condition, the band bending in the *p-n* junction creates a built-in bias (inside the PLZT film) that enhances the polarization in the direction of the ITO layer and suppresses the polarization in the direction of the Pt electrode. As a result, the PLZT thin films possess a higher remanent polarization when the zero voltage is reached from a negative polarity than a opposite polarity. A higher remanent polarization, in turn, produced a higher remanent birefringence in the PLZT thin films. It should be pointed out that the mechanism of the birefringent bistability is yet to be fully understood.

The birefringent bistability in the MFS structure is a potential mechanism for realizing a nonvolatile programmable spatial light modulator. It is also suitable for inte-

grated devices in waveguide architectures. The Pt/PLZT/ITO device presented here is actually a complete electrically addressable nonvolatile electro-optic memory unit.

The authors would like to thank E. Furman for many helpful discussions. This study was sponsored by the Office of Naval Research under Contract No. N00014-91-J508.

<sup>1</sup>J. T. Evans and R. Womack, IEEE J. Solid-State Circuits 23, 1171 (1988).

<sup>2</sup>G. H. Haertling, J. Vac. Sci. Technol. A 9, 414 (1991).

<sup>3</sup>Y. Xu, C. Chen, R. Xu, and J. D. Mackenzie, J. Appl. Phys. 67, 2985 (1990).

<sup>4</sup>G. H. Haertling and C. E. Land, J. Am. Ceram. Soc. 54, 1 (1971).

<sup>5</sup>D. Wurfel and I. P. Batra, Phys. Rev. B 8, 5126 (1973).

<sup>6</sup>K. S. Sree Harsha, K. J. Bachmann, P. H. Schmidt, E. G. Spencer, and F. A. Thiel, Appl. Phys. Lett. 30, 645 (1977).

<sup>7</sup>Z. Wu and M. Sayer, *Proceedings of the 1990 IEEE 7th International Symposium on the Applications of Ferroelectrics* (IEEE, Service Center, Piscataway, NJ, 1991), p. 677.

## **SECTION 4**

# A PLZT OPTICAL PHASE MODULATOR AND ITS APPLICATIONS

Feiling Wang and Gene H. Haertling  
Department of Ceramic Engineering  
Clemson University  
Clemson, South Carolina 29634-0907

An electrooptic phase modulator was designed and fabricated by using the quadratic electrooptic effect of PLZT ceramic of composition 10/65/35. The modulator can be operated at either the fundamental or double frequency of the AC signal driver. The modulator proved effective as a phase modulation device in a phase-detection measurement of small birefringent shift of thin film materials. The principles for such usage are discussed.

## Introduction

Relaxor ceramic materials in the  $(\text{Pb}, \text{La})(\text{Zr}, \text{Ti})\text{O}_3$  (PLZT) system are known to possess strong quadratic or slim-looped transverse electrooptic effects<sup>1</sup>. The applications of the materials in optical area have been found in light shutters, spatial light modulators, second harmonic generation as well as waveguide devices such as total internal reflection switches<sup>2,3</sup>. Although single crystal materials that possess linear electrooptic effects such as  $\text{LiNbO}_3$  and KDP have traditionally been the primary material group for optical phase modulation, polycrystalline PLZT ceramics which possess quadratic electrooptic effects can also be used as optical phase modulation media. In this report, an optical phase modulator made from a hot-pressed PLZT ceramic is presented. The application of the modulator in a phase-detection technique for the measurements of small optical phase retardation in thin film materials is discussed.

## Design and Operation

A bulk 10/65/35 PLZT wafer was chosen as the modulating medium. The material was made with a hot pressing process using stoichiometric powder derived from a water-soluble precursor. The material was transparent and showed typical dielectric properties for the material in this composition, i.e. high dielectric constant and very slim hysteresis loop. The electrooptic characterization showed that the dependence of the birefringence shift on the external electric field was primarily quadratic, as presented in Figure 1. The thickness of the PLZT wafer was 0.5 mm (20 mil) with both sides being optically polished. To accommodate the ac driving signal, copper planar electrodes were fabricated on one side of the material by a photolithography technique. The electrode gap width was 50  $\mu\text{m}$ , which allowed a light beam to pass the device without a special focusing effort. An ac electric signal of adjustable amplitude was fed to the electrode pair to drive the modulator. In addition, an adjustable dc bias was also applied to the modulator.

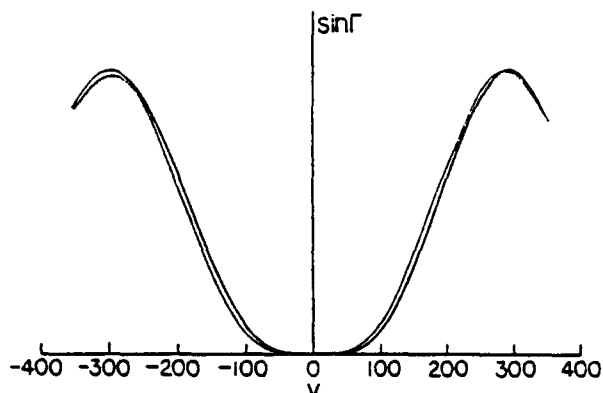


Figure 1 The electrooptic response of a 10/65/35 PLZT ceramic, measured by means of a phase-detection scheme. The Y axis is proportional to  $\sin\Gamma$  with  $\Gamma$  being the optical phase shift due to the birefringence of the material.

Under sufficiently small external field, the field-induced birefringent shift of the material can be expressed as a quadratic function of the applied field:

$$\Delta n = \text{constant} (E_b + E \sin\Omega t)^2, \quad (1)$$

where  $E_b$  is the field strength of the dc bias,  $\Omega$  is the frequency of the ac driving electric field. It is obvious that under a non-zero bias field, the phase shift generated by the modulator contains both  $\Omega$  and  $2\Omega$  components. By adjusting the bias field  $E_b$ , the relative amplitude of  $\Omega$  and  $2\Omega$  components can be altered. The function of the bias field in changing the primary modulating frequency is illustrated in Figure 2 where function  $\Gamma(t)$  is the phase retardation produced by the modulator.

To visualize the phase modulating function of the modulator and the interchange of the modulating frequency with the bias electric field, the modulator was sandwiched between two crossed polarizers with the modulation axis, the direction of the applied electric field, being oriented at 45 degree angle with respect to the polarization direction of the polarizer. With such a arrangement the polarization state of the originally linearly polarized light beam was periodically changed due to the phase shift  $\Gamma(t)$  imposed by the modulator. The intensity of the light output  $I(t)$  is given by:

$$I(t) = B \sin^2[\Gamma(t)/2] = B \sin^2[A(E_b + E \sin\Omega t)^2], \quad (2)$$

where A and B are two system constants. The waveform of the light intensity given by Equation (2) is graphically analyzed in Figure 2. As shown by the figure, the modulation is purely  $2\Omega$  in frequency at zero bias and gradually becomes dominated by the  $\Omega$  component with the increase of the bias electric field.

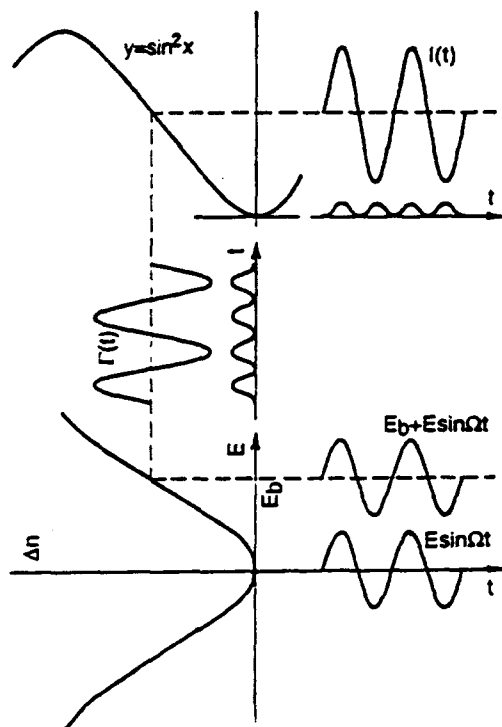


Figure 2 A graphic analysis of the operation modes of the PLZT phase modulator with and without dc bias field.

According to Equation (1), the modulation always contains a  $2\Omega$  component although its relative magnitude becomes very small compared to the  $\Omega$  component when a sufficient bias field is applied. A pure  $\Omega$  modulation mode can actually be achieved by using the saturation behavior in the electrooptic response of the material. The saturation behavior of the electrooptic response in PLZT materials have been observed<sup>4,5</sup>. In the presence of such saturation, the quadratic relation for the field-induced birefringence is no longer adequate; higher order terms or entirely new functional dependence needs to be used. In the electrooptic response curve that shows saturation behavior, there must be a point where the second derivative of the curve is zero. If a bias electric field is applied to this point, the modulation will be purely  $\Omega$  in frequency.

In practice, only a fairly low bias field is needed in order for the modulation at  $2\Omega$  frequency to become insignificant compared to the  $\Omega$  component. Figure 3 shows the waveforms of the light output, recorded by an

oscilloscope, from the second polarizer with the PLZT modulator driven by a 1kHz ac signal operating under various dc bias voltage. The square waves in the pictures are the trigger signal synchronized with the ac driving voltage. As expected, the modulation was purely  $2\Omega$  in frequency under zero bias and eventually became dominated by  $\Omega$  frequency components under a bias voltage of 150 volts. Components of both frequencies are clearly represented under an intermediate bias, as shown by Figure 3(b). The relative amplitude of modulation at both frequencies as functions of the dc bias was measured by a lock-in amplifier synchronized with the driving function generator. As shown in Figure 4, with the increase of the dc bias voltage, the amplitude of the  $2\Omega$  component decreased while the  $\Omega$  component increased. Under a bias voltage of approximately 120 volts the  $2\Omega$  component becomes zero while the  $\Omega$  component approaches a maximum. Under this bias voltage, the PLZT modulator provides

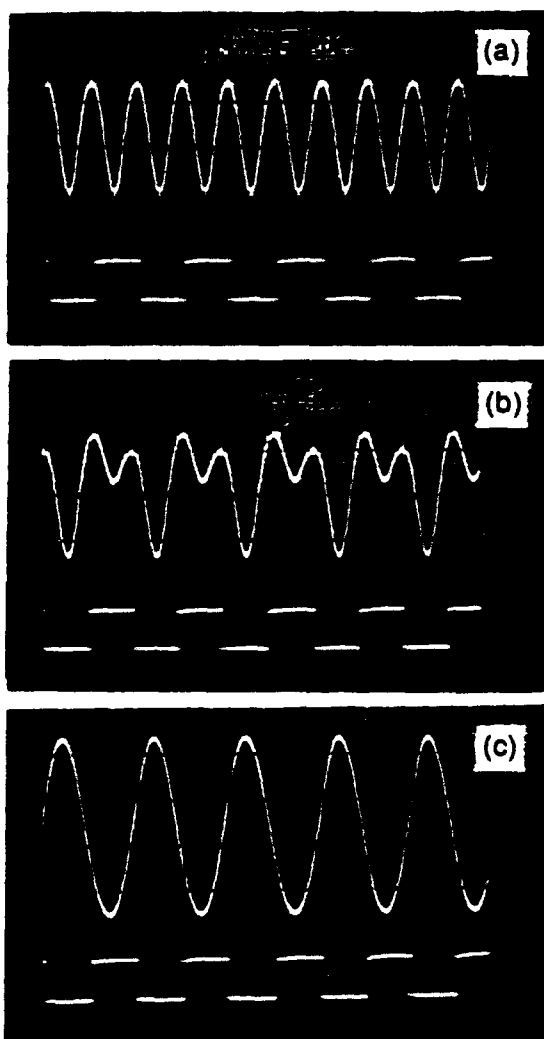


Figure 3 The waveforms of the output light modulated by the PLZT phase modulator operated under (a) bias=0V, (b) bias=20V and (c) bias=150V.

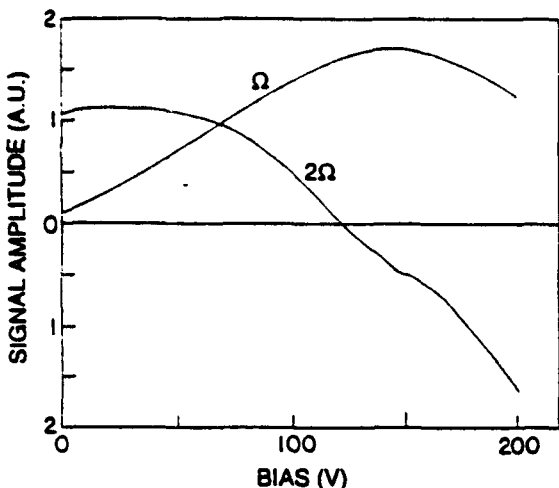


Figure 4 The  $\Omega$  and  $2\Omega$  frequency components in the light modulated by the PLZT phase modulator plotted as functions of the bias voltage.

the same modulation as that from a traditional modulator utilizing the linear electrooptic effect of single crystals, except that there is a constant phase shift. The constant phase shift can be compensated with an optical compensator in applications where it is not desirable. Much lower ac driving voltages are needed to achieve the same phase modulation depth for the PLZT modulator than for traditional modulators because of the strong quadratic electrooptic effect in the PLZT ceramic.

#### Applications

The PLZT phase modulator has been successfully used as a phase modulation device in a phase-detection scheme for the measurement of small birefringences of thin film materials. The optical arrangement for such application is shown in Figure 5. The PLZT compensator together with an optical compensator and the sample to be measured are sandwiched between two crossed polarizers. The modulating axis of the modulator is oriented 45 degrees with respect to the polarizer but parallel (or perpendicular) to the principle

optical axes of the sample determined by the direction of the external electric field. The purpose of the compensator is to compensate the constant phase shift generated by the modulator and to calibrate the system.

With the PLZT phase modulator being driven by an ac signal of frequency  $\Omega$  under zero bias, the total phase retardation for the light polarized along the modulating axis consists of contributions from all three components, namely, modulator, compensator and sample:

$$\Gamma = \Gamma_{\text{mod.}} + \Gamma_{\text{comp.}} + \Gamma_{\text{samp.}} \quad (3)$$

As been previously pointed out, the electrooptic effect of PLZT materials exhibits high order field dependence and saturation behavior in some circumstances. The phase modulation produced by the PLZT modulator, therefore, should be expressed by the following Fourier series:

$$\Gamma_{\text{mod.}}(t) = \text{constant} + \sum_{m=1}^{\infty} C_m \sin 2m\Omega t, \quad (4)$$

where coefficient  $C_1$  is proportional to the quadratic electrooptic coefficient of the PLZT modulating medium;  $C_2$  is proportional to the quartic electrooptic coefficient, etc. Although in most instances only  $C_1$  needs to be considered, the whole summation in Equation (4) is retained for the strictness of the following discussion.

By adjusting the compensator, the constant in Equation (4) can be eliminated; therefore we have

$$\Gamma(t) = \sum_{m=1}^{\infty} C_m \sin 2m\Omega t + \Gamma_{\text{samp.}} \quad (5)$$

The light intensity detected by the photomultiplier tube (PMT) is therefore given by

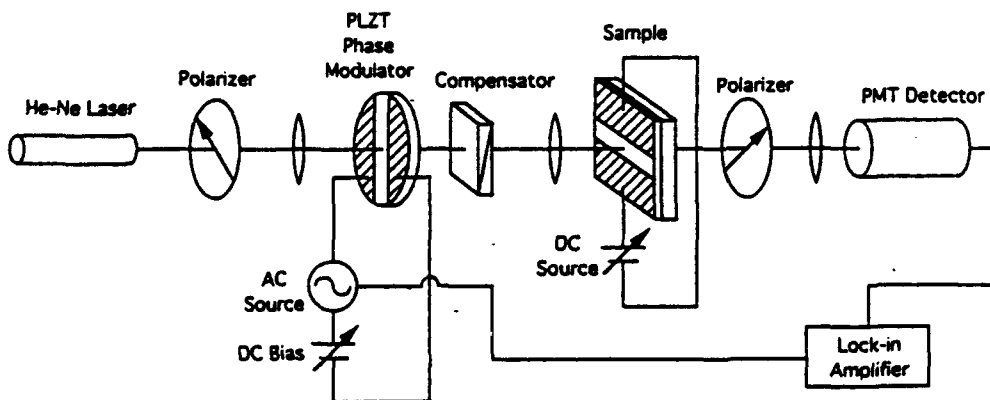


Figure 5 The optical arrangement in a phase-detection scheme using the PLZT modulator as a phase modulating device.

$$I(t) = I_0 \sin^2(\Gamma/2)$$

$$= (I_0/2)[1 + \cos(\sum_{m=1}^{\infty} C_m \sin 2m\Omega t + \Gamma_{\text{samp}})]. \quad (6)$$

If the reference signal of the lock-in amplifier is chosen as  $\sin 2\Omega t$ , the output signal of the lock-in amplifier,  $S$ , is proportional to the amplitude of the  $\sin 2\Omega t$  term in the Fourier expansion of Equation (6), that is

$$S = D \int_0^t I(t) \sin 2\Omega t dt$$

$$= D \int_0^t \cos(\sum_{m=1}^{\infty} C_m \sin 2m\Omega t + \Gamma_{\text{samp}}) \sin 2\Omega t dt \quad (7)$$

where  $D$  is a system constant. It can be shown that the above integration is approximately given by

$$S = D J_1(C_1) \sin \Gamma_{\text{samp}}. \quad (8)$$

where  $J_1$  is the Bessel function of the first order. With a fixed driving signal amplitude,  $C_1$  is a constant; the output signal from the lock-in amplifier therefore is proportional to the phase retardation generated by the sample, namely,  $\Gamma_{\text{samp}}$ . Moreover, in detecting the electrooptic effect of thin film materials, the phase retardation of the sample is usually very small so that the output from the lock-in amplifier becomes directly proportional  $\Gamma_{\text{samp}}$  while the proportional constant can be determined by the compensator.

With the PLZT phase modulator, the above scheme has proven an effective way of detecting very small phase retardations produced by electrooptic effects in thin film materials. As an example, Figure 6 shows the birefringence versus E-field curve of a 2/55/45 thin

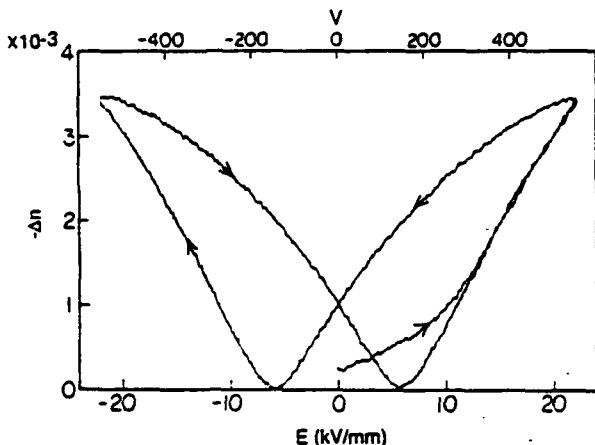


Figure 6 The birefringence versus E-field curve for a 2/55/45 PLZT thin film of  $0.5 \mu\text{m}$  thickness sputter-deposited on a fused silica substrate, measured with the phase-detection scheme using the PLZT phase modulator.

film of  $0.5 \mu\text{m}$  thick grown on a fused silica substrate, measured with the above phase-detection system under zero-bias mode.

When an appropriate bias field is applied, the modulation becomes predominated by the  $\Omega$  component. With the reference signal of the lock-in amplifier set at  $\sin 2\Omega t$ , the above measuring system functions similarly as in the zero-bias mode.

### Conclusions

An optical phase modulator was made by using the quadratic electrooptic effect of a hot-pressed PLZT ceramic. The device can be operated in a zero-bias mode which provides a modulation at double the frequency of the driving signal. When an appropriate bias is applied, the modulator provides a modulation dominated by the component at the frequency of the driving signal. Application of the PLZT modulator has been found in the phase-detection scheme for the measurement of very small birefringence in thin film materials.

### References

- [1] G.H. Haertling and C.E. Land, "Hot-pressed  $(\text{Pb},\text{La})(\text{Zr},\text{Ti})\text{O}_3$  Ferroelectric Ceramic for Electronic Applications," *J. Am. Ceram. Soc.* 54, 1(1971)
- [2] G.H. Haertling, "PLZT Electrooptic Materials and Applications-A Review," *Ferroelectrics*, 75, 25(1987)
- [3] H. Higashino, T. Kawaguchi, H. Adachi, T. Makino and O. Yamazaki, "High Speed Optical TIR Switches Using PLZT Thin Film Waveguides in Sapphire," *Japan. J. Appl. Phys.* 24 suppl., 284(1985)
- [4] F. Wang and A.Y. Wu, "Electro-optical and Nonlinear Optical Properties of Thin Film Materials Containing Oxygen-Octahedra under High DC Electric Field," *Proc. 7th Intern. Symposium on the Application of Ferroelectrics*, pp.131-134, Urbana, IL, June 6-8, 1990.
- [5] G.H. Haertling, unpublished results.

## **SECTION 5**

## **THIN FILM FERROELECTRIC REFLECTION SPATIAL LIGHT MODULATOR WITH FABRY-PEROT ETALON**

Feiling Wang and Gene H. Haertling

Gilbert C. Robinson Department of Ceramic Engineering

Clemson University

Clemson, SC 29634-0907

We report a reflection-mode thin film ferroelectric light modulator which has exhibited intensity modulation with signal-to-noise ratio of twenty and optical phase modulation as large as fifty degrees in a He-Ne laser beam. The large optical modulation was achieved by means of multiple reflection. A ferroelectric (FE) PLZT thin film material, sputter deposited on Pt-coated silicon substrate, was used as the electrooptic modulating medium. An indium-tin oxide (ITO) thin layer was deposited on the ferroelectric films as top electrodes. A He-Ne laser beam was obliquely incident on the ITO/FE/Pt structure. The light modulation was detected in the laser beam reflected from the thin film structure when a voltage signal was applied to the ITO and Pt electrodes. Unlike transmission-mode modulators, the sandwich of the ferroelectric films between the air-ITO and FE-Pt interfaces exhibited characteristics of a Fabry-Perot etalon. Near a Fabry-Perot peak, drastically enhanced light modulation than transmission devices was obtained. Design principles and the performance of the modulator are discussed.

## I. Introduction

A number of thin film ferroelectric materials, including lead lanthanum zirconate titanate (PLZT), barium titanate, lithium niobate, strontium barium niobate and lead magnesium niobate, have exhibited attractive birefringent electrooptic effect when deposited on suitable substrates<sup>1-4</sup>. Using these materials for optical modulation has been the focus of many studies. Integrated passive optical modulators using ferroelectric media may adopt three different designs, namely, transmission devices, waveguide devices and reflection devices. Transmission modulators are not compatible with opaque substrates; their usage are thus limited. They also suffer from shallow modulation depth because of the rather short optical path. Waveguide devices, such as total internal reflection (TIR) switch, using PLZT thin films grown on sapphire substrate have been successfully demonstrated<sup>5</sup>.

With the rapid advances in high-performance optoelectronic devices, it has become increasingly desirable to realize the integration of thin film optical modulators with semiconductor substrates to form monolithic hybrid devices<sup>6</sup>. Ferroelectric optical modulators in these devices may perform such functions as electrical-optical signal interface through spatial light modulation, intra- and inter-chip optical interconnections. The same ferroelectric media in these device may also perform all-optical operations, such as frequency doubling and optical logic, by using their outstanding optical nonlinearities. Combined with the more traditional task for ferroelectrics, namely, nonvolatile memory capability, ferroelectric thin films may become multifunctional media in various integrated optoelectronic devices. Using ferroelectric/electrooptic thin film for optical interconnection has been proposed by Lee and Ozguz<sup>7,8</sup>. A Fabry-Perot device using polymeric films as spacer for optical modulation has been reported by Eldering et al<sup>9</sup>. Enhanced phase retardation by means of interference has been observed in PZT films by Dimos *et al*<sup>10</sup>, however, incoherent light scattering has prevented a sufficient signal-to-noise ratio for intensity modulation.

In this paper we will report a reflection thin film ferroelectric spatial light modulator constructed on silicon substrates. By adopting a low finesse Fabry-Perot cavity, the modulator can achieve large phase modulation and high on/off signal ratio for intensity modulation. The device may be used as an implementation of free-space optical interconnections.

## II. Device Design and the Theory of Modulation

The thin film light modulator was constructed on oxidized and Pt/Ti-metallized silicon wafers. Fine grain ferroelectric PLZT thin films were deposited on the metallized silicon substrates by using magnetron sputtering. An indium-tin oxide layer was then sputter deposited on the ferroelectric thin films as top electrode. Figure 1 shows the schematic cross-section of the thin film modulator.

Linearly polarized light beam with equal amplitude for both p-polarization (parallel to the incident plane) and s-polarizations (perpendicular to the incident plane) was obliquely incident on the modulator as shown in Figure 1. Because of the polycrystalline nature of the ferroelectric thin films, the materials are optically uniaxial defined by the normal of the substrates. With an external electric field exerted through a voltage across the ITO and Pt layers, the extraordinary index  $n_e$  and ordinary index  $n_o$  experience field-induced changes,  $\Delta n_e$  and  $\Delta n_o$ , respectively. The corresponding changes in the indices for the p- and s-polarized light components are given by

$$\begin{aligned}\Delta n_p(\theta_2) &= \sin^2 \theta_2 \Delta n_e + \cos^2 \theta_2 \Delta n_o, \\ \Delta n_s &= \Delta n_o\end{aligned}\quad (1)$$

where  $\theta_2$  is the refraction angle of the light beam inside the thin film material. As the ferroelectric films are bounded by the Pt and ITO layers, the light beam experiences multiple reflections. Although all three interfaces, namely, air-ITO, ITO-FE and FE-Pt interfaces, cause light reflection, the air-ITO and FE-Pt boundaries dominates the characteristics of the reflected light beam because of the moderate difference between ITO and FE in refractive index. The device therefore can be characterized as a low finesse Fabry-Perot reflector. Under an external electric field, the optical length of the Fabry-Perot etalon becomes different for p- and s-polarized light components because of the field-induced birefringence in the ferroelectric thin films according to Equation (1). The polarization state of the reflected light, therefore, can be modulated with an voltage signal. As expected from any Fabry-Perot etalon, the modulation of the light can be greatly enhanced when a critical optical length of the etalon is satisfied. In the present devices, the critical optical length is determined by the thickness of the films and the incident angle of the light. Theoretical modeling has resulted in an accurate prediction for the light modulation as a function of the thickness of the films and incident angle<sup>11</sup>. The following

equation can be used to formally describe the phase difference  $\Delta\Gamma = \Delta\Gamma_p - \Delta\Gamma_s$ , between the field induced phase change in p-polarized light  $\Delta\Gamma_p$  and s-polarization light  $\Delta\Gamma_s$ :

$$\Delta\Gamma = \Delta\Gamma_p - \Delta\Gamma_s = w_p \sin^2 \theta_2 \Delta n_e - (w_s - w_p \cos^2 \theta_2) \Delta n_o . \quad (2)$$

where  $w_p$  and  $w_s$  are complicated functions of indices and thickness of all the layers involved as well as the incident angle. Figure 2 shows the calculated  $w_p$  and  $w_s$  as functions of the thickness of the ferroelectric layer with other parameters given. The oscillation of  $w_p$  and  $w_s$  is caused by the alternating phase relation between the neighboring reflected partial light beams with the thickness change. Consequently the total phase retardation of the device,  $\Delta\Gamma$ , exhibits similar oscillation. A phase retardation maximum occurs as neighboring reflected partial beams differ in optical phase by 180 degrees. Under this condition, partial light is forced to remain in the ferroelectric films for a much longer average path, experiencing accumulated phase retardation.

In order to characterize the ferroelectric thin film modulator, a reflection differential ellipsometer<sup>12</sup> was employed to measure the field-induced phase retardation of the reflected light. The intensity modulation of the light beam is detected with the optical set up shown in Figure 3. Linearly polarized He-Ne laser beam of 632.8 nm wavelength was obliquely incident on the thin film modulator, upon which electric signals were applied. A light sensor is located after a polarizer to detect the light reflected from the modulator.

### III. Experimental Results

Lead lanthanum zirconate titanate (PLZT) of composition 2/55/45 (La/Zr/Ti) was deposited on Pt/Ti-coated silicon substrate as the modulating medium. A post-deposition annealing process was employed to acquire the perovskite structure of the deposited thin films. Thickness of the PLZT films was approximately 480 nm. Indium-tin oxide layer of thickness approximately 350 nm was also sputter deposited on the PLZT films. The PLZT film exhibited well developed hysteresis loop as shown in Figure 4. The dielectric constant of the PLZT film was approximately 1500. Using a prism coupler (Meticon 2010), helium-neon laser light was successfully coupled into the PLZT thin film to form

guided waves, shown in Figure 5. It also permitted us to determine both the index of refraction and the thickness of the film simultaneously.

The phase shift of the reflected light beam as a function of the applied voltage, measured with the reflection differential ellipsometry, is shown in Figure 6. The measured phase shift in Figure 6 roughly represents the birefringence,  $\Delta n = \Delta n_s - \Delta n_o$ , of the film when a proper incident angle is chosen for the measurement. As shown by the figure, the field-induced birefringence of the PLZT film exhibits a slightly asymmetric butterfly-shaped loop, typical for ferroelectric thin films. Field-induced phase shift loops were taken at various incident angles. A phase-shift peak was located at approximately 57 degrees, where phase shift reaches approximately 50 degrees. This peak is consistent with the model calculation, from which the thickness of the films was designed.

The performance of the device as a light intensity modulator was examined using the measuring system shown in Figure 3. Electric pulses or sinusoid signals were applied to the devices with 2 mm diameter ITO dots as top electrodes. Light intensity modulations, sensed by a photo-multiplier tube, were recorded by an oscilloscope. Figure 7 shows a light intensity modulation responding to electric pulses of 10 volts in peak height and 5 ms in pulse width. An on/off ratio of 10 was achieved during the operation, as shown in the figure. The on/off ratio of the device as a function of the peak height of the pulses is shown by Figure 8. Light modulation remained substantial under pulses of peak height less than 5 volts, while modulation at 10 volts peak height was very visible.

The operation frequency of the a ferroelectric modulator may be limited by one of the following three processes: the inherent response speed of the electrooptic effect of the thin film material, rc constant of the device and response speed of the detector. Because of the large area of the electrodes and the high impedance of the wiring cable, the operation frequency of the present device is apparently rc constant limited, which is the slowest of these three processes, approximately  $50 \mu s$ . Under this limitation, the intensity modulation at a frequency of 100 kHz is still detectable, although with much shallower modulation depth. Figure 9 shows the 100 kHz modulation of the light intensity with a biased sinusoid voltage signal at the same frequency. The rc constant may be drastically reduced with reduced electrode area and wiring impedance, which will ultimately results in a material response limited operation bandwidth.

Because of the large field-induced birefringence in ferroelectric thin films,  $\Delta n_s - \Delta n_o \approx 0.02$  under a moderate external field, the modulator remained a substantial on/off signal ratio for intensity modulation even when the incident angle is a few degrees away from the Fabry-Perot peak. This property gives the ferroelectric modulator a great tolerance to the error of thickness control of the films, vital for practical fabrications.

#### IV. Conclusion

A thin film ferroelectric reflection spatial light modulator has been constructed on semiconductor substrates. The device consists of an ITO/PLZT/Pt thin film structure on oxidized silicon substrate. With the help of interference of multiple reflection, larger than 50 degrees phase shift in the reflected light from an obliquely incident light beam has been achieved. Using the device as an intensity light modulator, on/off signal ratio of twenty has been obtained with electric pulses of 10 peak voltage. With reduced rc constant, much wider modulation bandwidth can be achieved. This device may be used in various optoelectronic devices as an implementation of free-space optical interconnections.

#### Acknowledgments

The authors would like to thank E. Furman for his valuable comments on the subject. This work was sponsored by the Office of Naval Research under Contract No. N00014-91-J508.

#### References

1. K. D. Preston and G. H. Haertling, *Appl. Phys. Lett.* 60 (1992)2831
2. A. Wegner *et al*, *Ferroelectrics*, 116(1991)195
3. H. Adachi, *Appl. Phys. Lett.* 42(1983)867
4. F. Wang and G. Haertling, *Appl. Phys. Lett.* 63(1993)1730
5. H. Higashino *et al*, *Japan. J. Appl. Phys.* Vol. 24(1985), Suppl. 24-2, p. 284
6. C. H.-J. Huang and T. A. Rost, presented at the 6th International Symposium on Integrated Ferroelectrics, March 14-16, 1994, Monterey, California
7. S. Lee *et al*, *Optical Engineering*, 25(1986)250

8. V. H. Ozguz *et al*, manuscript
19. C. A. Eldering *et al*, J. Appl. Phys., 69(1991)3676
10. D. Dimos, *et al*, Ceramic Transactions, Vol. 25: Ferroelectric Film, (American Ceramic Society, Westerville, OH, 1992)
11. F. Wang *et al*, to be published.
12. F. Wang *et al*, Opt. Lett. 18(1993)1617

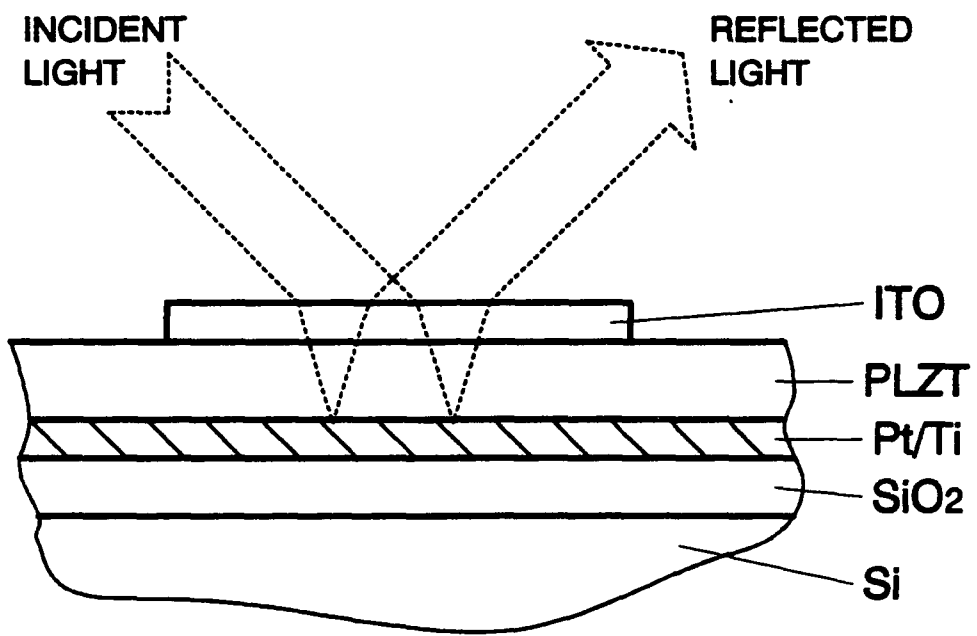


Figure 1. Schematic cross section of the ferroelectric thin film reflection light modulator.

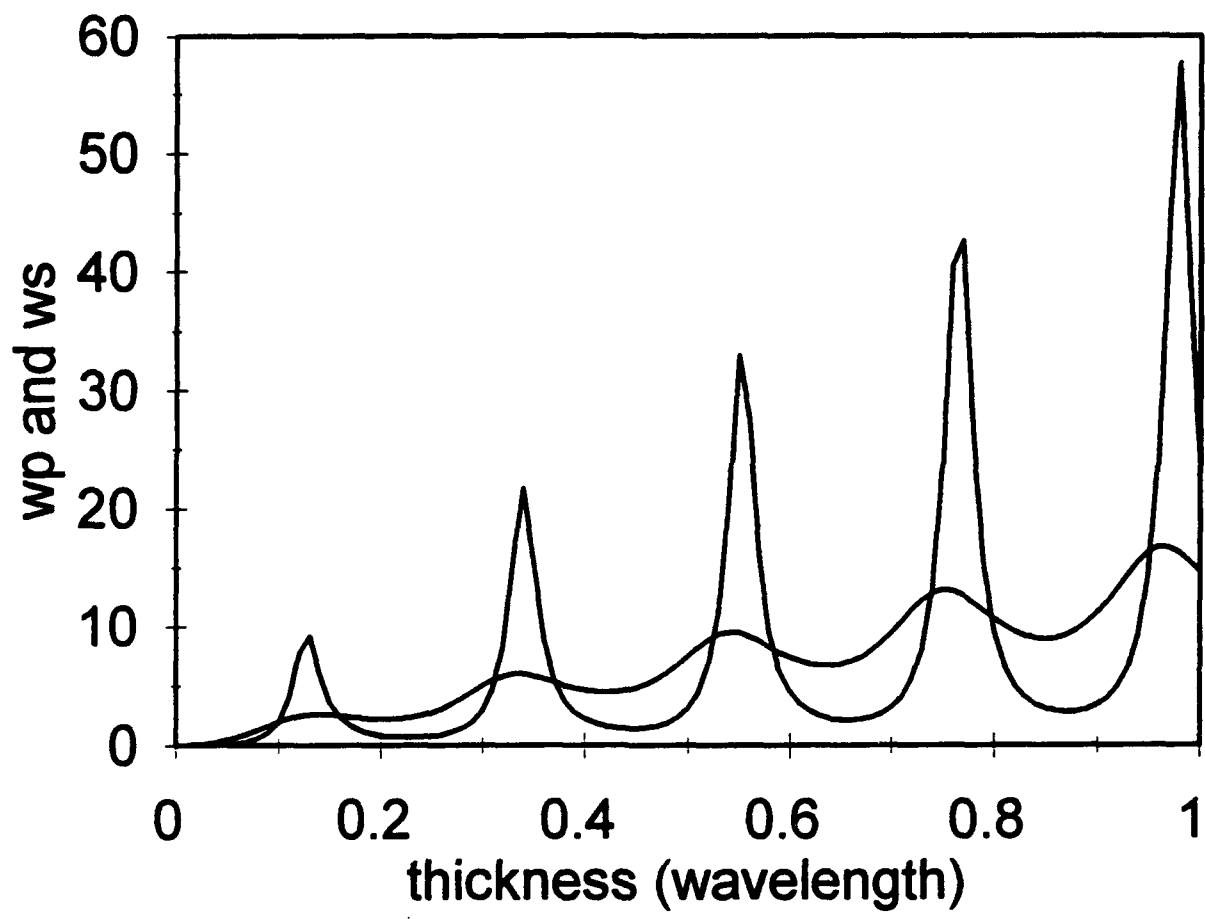


Figure 2. Calculated coefficients,  $w_p$ , and  $w_s$ , as functions of the thickness of the electrooptic layer.

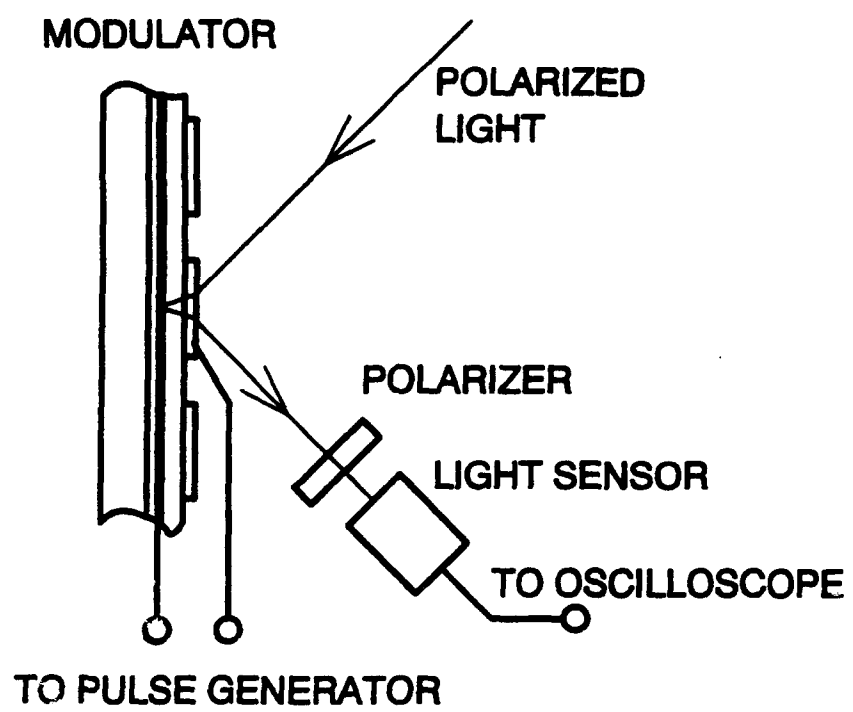
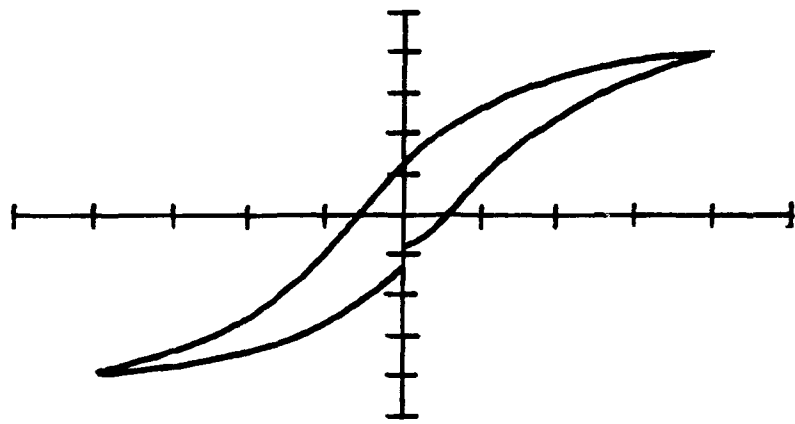


Figure 3. Light intensity modulation detecting system.



**Figure 4.** Dielectric hysteresis loop of the PLZT thin film used for light modulation.  
Thickness of the film is approximately  $0.48 \mu\text{m}$ . The horizontal and vertical scales are  $75 \text{ kV/cm}$  and  $\mu\text{C}/\text{cm}^2$  respectively.

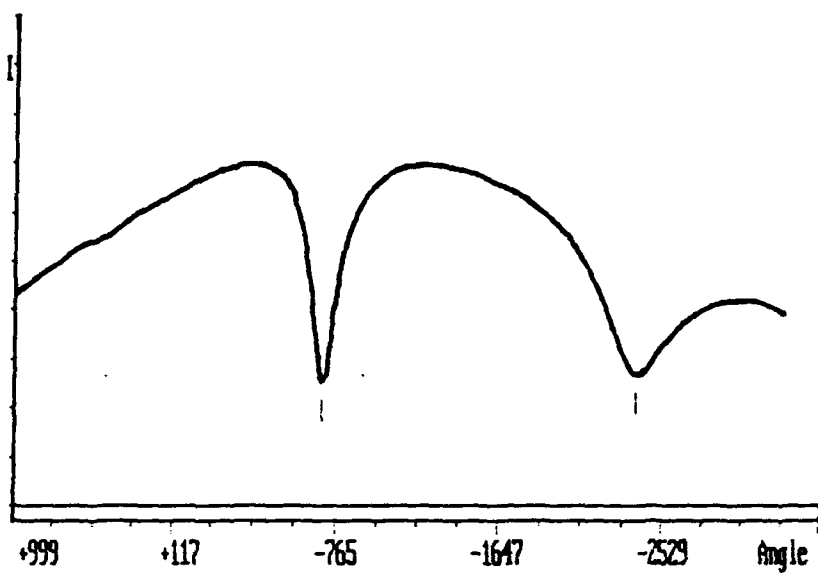


Figure 5. Light intensity profile from an incident angle scan of the prism coupler. The two dips indicate two waveguide modes created in the electrooptic thin film.

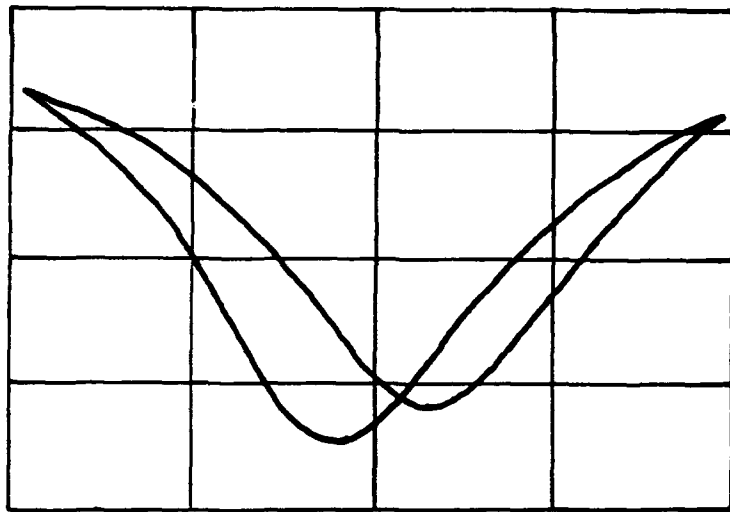
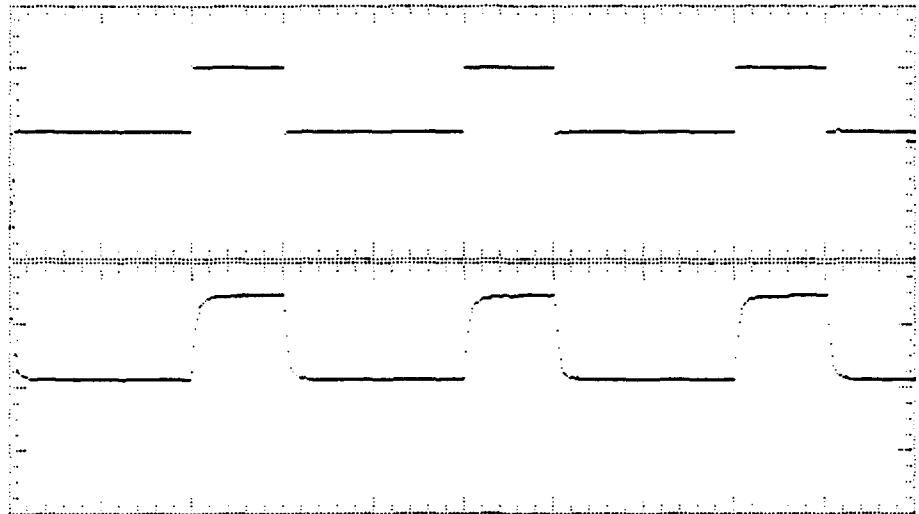


Figure 6. Field-induced relative phase shift (phase retardation) of the reflected light beam measured by using the reflection differential ellipsometer. The horizontal and vertical scales are 7.9 volts per division and 0.28 per division respectively.



**Figure 7.** Light intensity modulation with electric pulses. The upper trace is the voltage signal applied to the modulator. The lower trace is the recorded light intensity reflected from the modulator. The horizontal scale is 5 ms per division. The vertical scale for the upper trace is 10 volts per division.

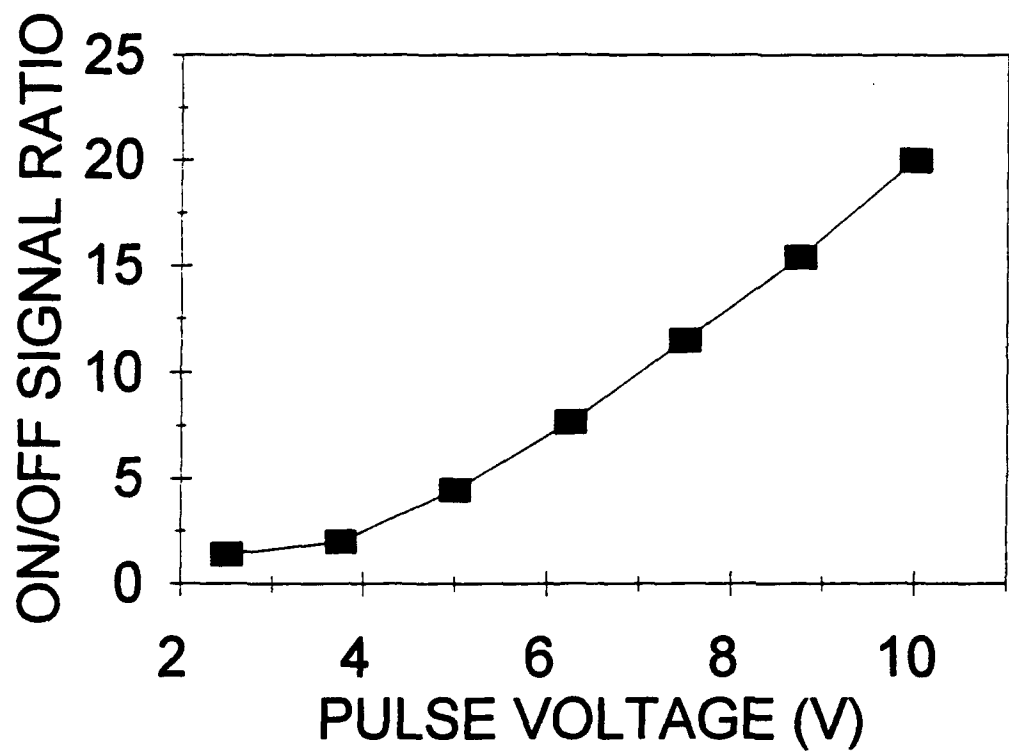


Figure 8. Light on/off ratio as a function of the pulse voltage.

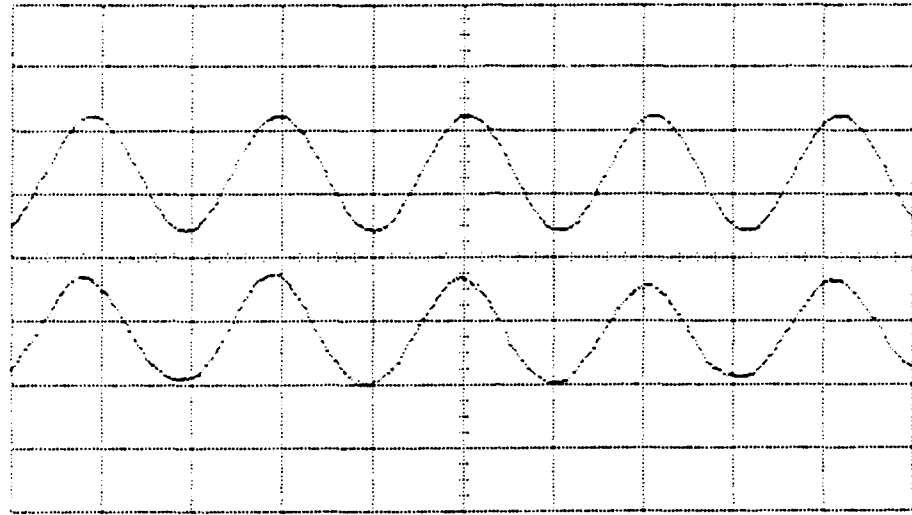


Figure 9. Light intensity modulation at a frequency of approximately 100 kHz. The upper trace is a biased sinusoid voltage signal (5 volts per division). The lower trace is the recorded light modulation.

## **SECTION 6**

# Transverse electro-optic effect of antiferroelectric lead zirconate thin films

Feiling Wang, Kewen K. Li, and Gene H. Haertling

Department of Ceramic Engineering, Clemson University, Clemson, South Carolina 29634-0907

Received March 16, 1992

The transverse electro-optic effect in antiferroelectric lead zirconate thin films grown on fused quartz is observed. The birefringence shift as a function of the external electric field exhibits a characteristic response that is related to the electric-field-induced antiferroelectric-to-ferroelectric structural transition.

Dielectric properties of lead zirconate ( $PbZrO_3$ ) ceramic have been extensively studied.<sup>1-6</sup> The appeal of lead zirconate is its antiferroelectric (AFE) crystal structure at room temperature. It is well known that a transition to a ferroelectric (FE) or paraelectric phase occurs in lead zirconate when it is subjected to a sufficiently high external electric field or elevated temperatures; however, the electro-optic properties of lead zirconate have not yet been explored in either bulk or thin-film form. The recent success in depositing lead zirconate thin films<sup>6</sup> has opened up the possibility of new integrated devices for utilizing its unique electro-optic response. This Letter is mainly concerned with the transverse electro-optic effect detected from lead zirconate thin films.

Lead zirconate thin films were deposited onto optically polished fused quartz by a dip-coating technique from an acetate precursor solution. Room-temperature x-ray diffraction patterns showed a peak at  $2\theta = 16.9$  deg, which is characteristic of the AFE double-cell crystal structure. Copper electrode pairs with a gap width of  $50 \mu m$  were fabricated on top of the films by a photolithography process. The transverse electro-optic properties were measured by means of a phase-detection technique<sup>8</sup> in the transmission mode. The light source was a He-Ne laser of 632.8-nm wavelength. The modulation of the laser beam was provided by a photoelastic modulator. Since in the phase-detection schemes the amplitude of the lock-in frequency is proportional to the phase retardation generated by the thin film, the possible electric-field-induced scattering effect<sup>9</sup> did not contribute to the output signal. The system was calibrated with an optical compensator.

A typical room-temperature birefringence shift of the lead zirconate thin film as a function of the applied dc electric field is shown in Fig. 1. The film thickness was  $0.65 \mu m$ . As seen from the figure, the hysteresis loop shows characteristic differences from the normal response of ferroelectric materials, e.g., lead lanthanum zirconate titanate (PLZT) of composition 8/65/35.<sup>10</sup> The most characteristic feature is represented by the enhanced hysteretic behavior in the high-electric-field region (10–20 kV/mm) and the

rapid increase of the slope when the increasing external electric field exceeds 17 kV/mm. The raggedness of the curve was caused by the system noise.

The observed birefringence curve can be related to the electric-field-induced AFE-FE phase transition in the lead zirconate thin films. It is known that an AFE-FE phase transition can be induced by an external electric field at temperatures slightly below the Curie point. The dielectric property corresponding to such a phase transition is the occurrence of the double hysteresis loop.<sup>1</sup> To demonstrate that such a field-induced phase transition can also occur in a lead zirconate thin film at room temperature, thin films were also deposited on silicon substrates coated with a conductive Pt/Ti metallization layer. Figure 2 shows typical room-temperature dielectric hysteresis of the films measured under dc and ac conditions. Compared with that of the double hysteresis loop obtained by Shirane *et al.*<sup>1</sup> at a temperature of  $228^\circ C$ , the critical electric field  $E_c$  for the AFE  $\rightarrow$  FE phase transition in the thin-film lead zirconate at room temperature is approximately an order of magnitude higher (at roughly 25 kV/mm). A possible reason for the large difference is that the farther the temperature is below the Curie point, the higher the external field that is required to cause the phase transition.

A model of the transverse electro-optic effect of polar materials shows that the change of refractive index along the polar direction can be in general described by a quadratic effect, whereas the linear electro-optic effect can be considered as a quadratic effect biased by an additional local electric field created by the spontaneous polarization.<sup>11,12</sup> If we assume that this view point applies when an AFE-FE phase transition occurs, the dependence of the field-induced birefringence shift  $\Delta n$  on the low-frequency external electric field  $E$  and the polarization  $P(E)$  should obey roughly the following relation:

$$\Delta n \propto \left[ E + \frac{4\pi}{3} P(E) \right]^2, \quad (1)$$

where the local electric field is approximated by the Lorentz formula for cubic materials. The solid

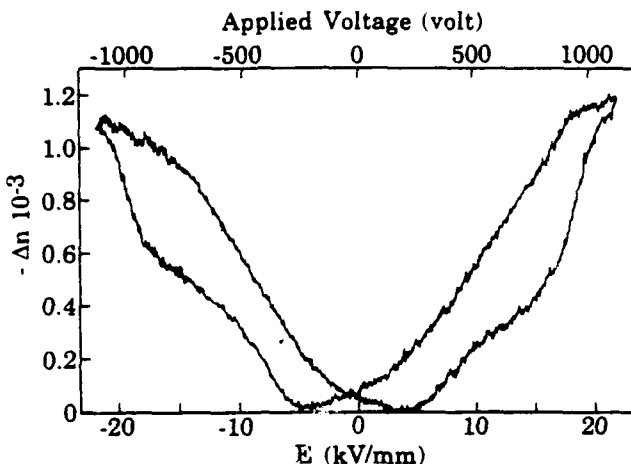


Fig. 1. Measured birefringence shift  $\Delta n$  as a function of the applied electric field  $E$  in a lead zirconate thin film on fused quartz.

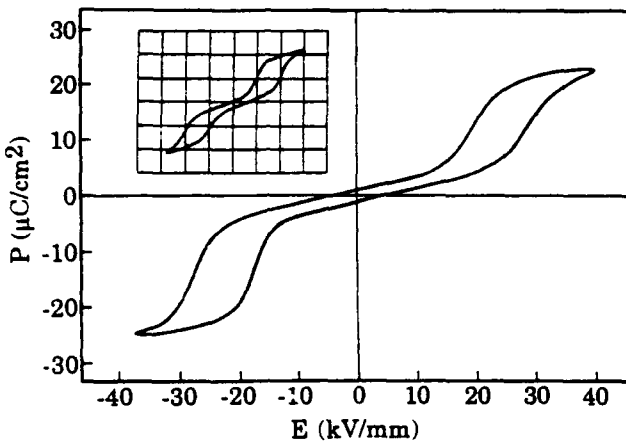


Fig. 2. Measured dc and ac (inset) dielectric property of a lead zirconate thin film on a Pt/Ti-coated silicon substrate. The direction of the electric field is perpendicular to the thin film. The horizontal and vertical scales for the ac loop are 15.4 kV/mm per division and 15.1  $\mu\text{C}/\text{cm}^2$  per division, respectively.

curve in Fig. 3 is a prediction of the birefringence curve calculated from a double hysteresis loop (dashed curve) by using relation (1). Although Fig. 1 indeed reveals some of the main features predicted by relation (1), a quantitative correlation between the dielectric hysteresis loop and the electro-optic hysteresis loop was not possible. As can be seen, the dielectric loop of Fig. 2 indicates that a rapid increase of the slope for the field-induced birefringence curve should occur near  $E = 25$  kV/mm when approached from below. The experimental result (Fig. 1) shows that this transition actually occurs at an external field of approximately 18 kV/mm for the film on fused silica. The discrepancy may be caused by the following three main reasons: (1) the measurements of the dielectric properties and electro-optic properties involved thin films deposited onto two different types of substrate, i.e., fused quartz and Pt/Ti-coated silicon, owing to the requirements of the experimental methods; (2) in the two measurements, the external fields were applied

in two different directions to the thin-film materials, which were generally anisotropic; and (3) in the electro-optic measurements, the distribution of the applied field in the film was nonuniform and possessed the general feature that the field strength at the edge of the electrodes was considerably higher than at the central region of the gap.<sup>13</sup> The electric-field strength as marked on the  $x$  axis in Fig. 1 is actually the average lateral field across the gap, which is given by  $E = V/g$ , where  $V$  is the applied voltage and  $g$  is the gap width. The distribution of the electric field implies that the AFE-FE phase transition does not occur simultaneously across the gap.

Both dielectric and electro-optic measurements suggest that the lead zirconate thin films possess a certain amount of FE crystal structure at room temperature in addition to the AFE phase. The FE phase is indicated by the hysteretic behavior in the low-electric-field region of the hysteresis loops. This mixed phase may be related to the stress and strain produced by the film-substrate interface.

Assuming that the lead zirconate thin film possesses the same nonlinear polarizability at optical frequencies as its isomorphs (as implied by Miller's rule<sup>14</sup>), e.g., PLZT thin films of composition 8/65/35, we estimate the birefringence shift in the polarization saturation region to be of the order of  $10^{-3}$ , which is consistent with the measured value at an electric-field strength near 20 kV/mm. As in other nonlinear-optical materials, the transverse electro-optic effect in the lead zirconate thin films consists of an electronic contribution and an ionic contribution. Although the ionic response is not essential for some applications, the characteristic electro-optic response in the lead zirconate thin films can be observed only when the electric-field-induced AFE-FE phase transition occurs. The response time for the AFE-FE phase transition in the lead

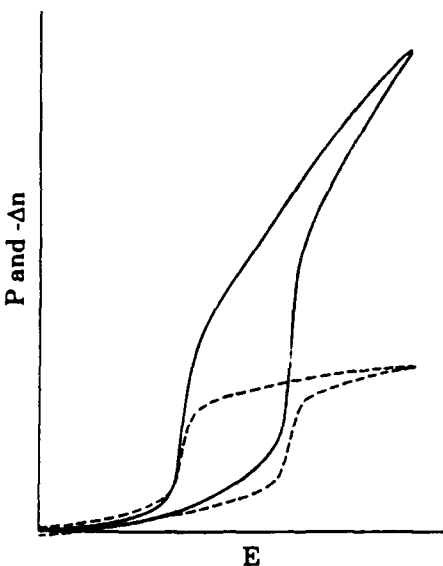


Fig. 3. Prediction of the transverse electro-optic property of a material under AFE-FE phase transition. The solid curve for  $\Delta n$  versus  $E$  is calculated from the dashed curve for  $P$  versus  $E$  by using relation (1).

zirconate thin films is still unknown; however, we may speculate that the time scale for such a process is a microsecond, as observed in related materials.<sup>15</sup>

The authors acknowledge the participation of R. Owens in this research.

## References

1. G. Shirane, E. Sawaguchi, and Y. Takagi, Phys. Rev. **84**, 476 (1951).
2. F. Jona, G. Shirane, F. Mazzi, and R. Pepinsky, Phys. Rev. **105**, 849 (1957).
3. B. A. Scott and G. Burns, J. Am. Ceram. Soc. **55**, 331 (1972).
4. O. E. Fesenko, R. V. Kdesova, and Yu G. Sindeev, Sov. Phys. Solid State **21**, 668 (1979).
5. M. T. Lanagan, J. H. Kim, S.-J. Jang, and R. E. Newnham, J. Am. Ceram. Soc. **71**, 311 (1988).
6. K. K. Li, F. Wang, and G. H. Haertling, "Antiferroelectric lead zirconate thin films derived from an acetate precursor system," J. Mater. Sci. (to be published).
7. G. H. Haertling, Ferroelectrics **116**, 51 (1991).
8. F. Wang, C. B. Juang, C. Bustamante, and A. Y. Wu, in *Proceedings of the 4th International SAMPE Electronics Conference* (Society for the Advancement of Material and Process Engineering, Covina, Calif., 1990), p. 712.
9. C. E. Land, IEEE Trans. Electron Devices **ED-26**, 1143 (1979).
10. G. H. Haertling and C. E. Land, J. Am. Ceram. Soc. **54**, 1 (1971).
11. S. K. Kurtz and F. N. H. Robinson, Appl. Phys. Lett. **10**, 62 (1967).
12. M. DiDomenico, Jr., and S. H. Wemple, J. Appl. Phys. **40**, 720 (1969).
13. G. W. Farnell, I. A. Cermak, P. Silvester, and S. K. Wong, IEEE Trans. Sonics Ultrason. **SU-17**, 188 (1970).
14. R. C. Miller, Appl. Phys. Lett. **5**, 17 (1964).
15. W. Pan, Q. Zhang, A. Bhalla, and L. E. Cross, J. Am. Ceram. Soc. **72**, 571 (1989).

## **SECTION 7**

**Antiferroelectric Lead Zirconate Thin Films**

**Derived from Acetate Precursors**

Kewen K. Li, Feiling Wang and Gene H. Haertling

Department of Ceramic Engineering

Clemson University, Clemson, SC 29634-0907

Antiferroelectric lead zirconate ( $PbZrO_3$ ) films derived from acetate precursors have been fabricated on Pt/Ti-coated silicon wafers and fused silica at  $700^\circ C$  with an automatic dip coating process. Films formed directly on the metallized silicon wafer showed the coexistence of perovskite and pyrochlore phases. A pre-coated titania layer of about  $100\text{\AA}$  facilitated the formation of the desired perovskite phase. Films deposited on fused silica exhibited interactions between lead and silica which inhibited the crystallization of the films. In this case, a pre-coated titania layer in the range of  $500\text{-}750\text{\AA}$  acted as a diffusion barrier layer, allowing the formation of the perovskite phase. Antiferroelectricity in the films was confirmed by x-ray superstructure, dielectric double hysteresis loops and dc bias behavior at room temperature. The corresponding transverse electrooptic properties were also measured for films deposited on fused silica.

## 1. Introduction

Lead zirconate (PZ) is a typical antiferroelectric (AFE) material at room temperature [1,2], from which the ferroelectric (FE) state can be induced when subjected to a sufficiently large electric field. However, this transition field usually exceeds the material breakdown strength, and consequently, the field-enforced AFE→FE transition is usually carried out at a few degrees centigrade below its Curie point (~230°C) [2]. Owing to the antiparallel arrangement of the spontaneous polarization directions, its unit cell is a superstructure of orthorhombic symmetry consisting of eight perovskite units [3,4]. Although lead zirconate has been well studied in the bulk form, its thin film properties have rarely been reported.

Preparation of the PZ films was first motivated by a mixed-phase problem encountered in the solution-derived FE lead zirconate titanate (PZT) or La-modified PZT (PLZT) thin films. The coexistence of the perovskite and the pyrochlore phases was commonly observed in these films [5-8] fabricated from different precursor systems, and the amount of the pyrochlore phase increased as the film composition approached the Zr-rich side [5,8]. Thus, PZ was expected to be the most difficult composition in the PZT family to obtain with the desired perovskite phase. Moreover, studying the formation of the PZ films benefits the overall knowledge about microstructure evolution mechanisms as well as providing a proper processing technique which could be applied to other PZT or PLZT compositions.

Remedies to the mixed-phase problem in the PLZT films have been proposed by forming a buffer layer of either lead titanate (PT) [9] or La-modified lead titanates (PLTs) [8] prior to the PLZT film deposition. These PT-based compositions were found to crystallize readily into the perovskite structure at lower temperatures, and PLZT films isostructurally grown on these buffer layers showed enhanced perovskite phase formation. Similar conclusions were noted for sol-gel LiNbO<sub>3</sub> films [10] in which the perovskite phase was formed at a much lower temperature when deposited on top of an existing perovskite layer.

AFE materials possess unique dielectric, piezoelectric [11,12] and electrooptic properties [13] which make them suitable for devices such as micro-displacement transducers. Since PZ is the base composition for some AFE compounds [14]; for example, Sn-modified PZT, preparation of the PZ films provided a starting point for other PZ-based AFE films. Further incentive to prepare PZ films on transparent substrates resulted from the theoretical interest in studying the electrooptic behavior associated with the field-induced AFE→FE phase transition [13].

The purpose of this paper is to overview the processing aspects of the PZ films prepared from the acetate precursor system and to study their microstructure evolution. Preliminary results on the electric/dielectric and electrooptic properties of the AFE PZ films are also discussed.

## **2. Experimental Procedure**

The specific precursors used in the preparation of the PZ films and the TiO<sub>2</sub> pre-coats were previously reported in a paper describing the acetate solution system for PLZTs [15]. For the PZ composition, lead subacetate powder, Pb(OOCCH<sub>3</sub>)<sub>2</sub>•2Pb(OH)<sub>2</sub>, and aqueous zirconium acetate solution (ZAA) were used. The oxide contents of the precursors were assayed beforehand. Lead subacetate was first dissolved into the ZAA and continuously stirred for 20 min. Methanol was then added into the mixture as a solvent and stirred for another 10 min. The final coating solutions contained 6 to 8.5wt.% oxide.

The TiO<sub>2</sub> pre-coats were derived from titanium diisopropoxide biacetylacetone (TIAA), 75wt.% in isopropanol. It was mixed with methanol at a weight ratio of 1 to 5 to form the coating solution containing about 3wt.% TiO<sub>2</sub>.

Films were deposited on Pt/Ti-coated Si wafers and optically polished fused SiO<sub>2</sub> for measuring their dielectric and electrooptic properties, respectively; however, Ag foils were also occasionally used as substrates. All films were formed by an automatic dip coating process which involved a multiple dipping and firing approach [16]. Substrates were withdrawn from the solutions at a speed of 18.7cm/min. The coating cycle was repeated 15 to 30 times which gave a final film thickness ranging from 0.6 to 1μ. Each coating layer was fired at 700°C for 2 minutes.

Pulverized solid samples obtained by drying the coating solution at 60°C were subjected to thermogravimetry analysis (TGA) and differential thermal analysis (DTA) in air. The dried samples were also heated in a furnace at various temperatures for 1 hour for x-ray diffraction (XRD) and other analyses.

Dielectric measurements were made at 1kHz. Hysteresis loops were measured with a modified Sawyer-Tower circuit. The transverse electrooptic properties were measured by means of a phase-detection technique in the transmission mode [17]. Evaporated Cu was used as the electrodes.

### 3. Results and Discussions

#### 3.1 Thermal Decomposition and Crystallization Behavior

XRD patterns of the pyrolyzed powder are shown in Fig. 1 as a function of the firing temperatures. Powders heated below 400°C (not shown) had a very broad amorphous peak centered around  $\sim 30^\circ 2\theta$  (CuK $\alpha$ ). Metallic Pb appeared at 400°C, and was subsequently oxidized at higher temperatures. A small amount of the perovskite PZ phase started to form at 600°C and became the only phase at 700°C. Formation of metallic Pb and PbO<sub>x</sub> during the thermal decomposition process was not uncommon for it has also been reported in sol-gel systems for PZT [18] and PZ [19]. The pyrochlore phase, however, was not appreciable in these XRD results.

Fig. 2 shows the TGA and DTA results of dried solid samples heated from room temperature to 800°C at a rate of 10°C/min. The sample lost about 30% of its weight during pyrolysis, and this corresponded to approximate 2 moles each of OAc<sup>-</sup> and OH<sup>-</sup>(or H<sub>2</sub>O) per mole of PZ. By comparing the results with Fig. 1 and other infrared spectra data, the dried solid first underwent dehydroxylation(or dehydration) at temperatures below 200°C. The endothermic peaks between 250 and 400°C were attributed to the decomposition of the acetate group and possibly the melting of Pb. The broad exothermic peak between 400 and 600°C accompanied by about 5% weight loss was the oxidation of residual carbonaceous material and Pb. The small exothermic peak at about 660°C corresponded to the crystallization of the perovskite PZ. From these results it was decided to set the processing temperature for the PZ films at 700°C.

### *3.2 Film Microstructure and Phase Formation*

*3.2.1 Pt/Ti-coated Si substrates.* Fig. 3 shows a scanning electron microscope (SEM) photograph of a 10-layer PZ film deposited on the Pt/Ti-coated Si substrate and treated afterwards with a dilute HF-HCl etching solution. The presence of two distinct phases in the film, also detected by XRD, was a phenomenon similar to that found in PLZT films [5-8]. The pyrochlore phase region appeared darker than the perovskite one owing to their differences in Pb content.

From Fig. 1 and 2, the appearance of metallic Pb during the decomposition process and the large temperature difference between the

formation of Pb (~375°C) and the crystallization of the perovskite phase (~660°C) suggests that: (1) the loss of Pb and (2) segregation of the Pb species during the firing process might be responsible for the observed microstructure. The absence of the pyrochlore phase in powdered samples indicated that the loss of Pb was more significant in thin films. These arguments are also supported by the fact that a faster heating rate, which would shorten the time to reach the crystallization temperature, improves the film microstructure [5].

Using PT or PLT buffer layers proved to be as effective in modifying the microstructure of the PZ film as those of the PLZT films. However, a TiO<sub>2</sub> layer was also found to be capable of improving the perovskite phase formation. Results from XRD and TG/DTA experiments on composition PT indicated that Pb had a much greater tendency to combine with Ti; i.e. no Pb was detected by XRD and perovskite PT could be formed at ~470°C which was almost 200°C lower than that of PZ. A relatively thin TiO<sub>2</sub> layer, dip-coated onto the Pt/Ti-coated Si substrate and fired at 700°C for 30sec, was estimated [16] to be in the range of 100Å and possessed a rutile structure. The etched microstructure of a PZ film processed at the same conditions as in Fig. 3 but with a pre-coated TiO<sub>2</sub> layer is shown in Fig. 4. The pyrochlore phase was not discernible in this picture and the film morphology has been improved dramatically with the TiO<sub>2</sub> pre-coat. The reasons for the improved microstructure of the PZ films deposited with a TiO<sub>2</sub> pre-coat are presently under study.

For Pt/Ti-coated Si substrates, growing films on PT or PLT layers was more easily controlled than on a TiO<sub>2</sub> layer. However, TiO<sub>2</sub> has proved to be very useful for films deposited on fused SiO<sub>2</sub> substrates. On both types of sublayers, however, the PZ films were found to retain a small amount of the pyrochlore phase when examined by XRD, therefore, excess Pb (as much as 20at.%) has been added in the preparation of subsequent films in order to compensate for the loss of Pb.

*3.2.2 Fused silica substrates.* PZ films deposited directly onto fused SiO<sub>2</sub> substrates and fired at 600-700°C were colorless and showed no crystallinity under XRD. Large cracks were present throughout the films and also the substrate surfaces, suggesting a film-substrate interaction. Films could be crystallized into the perovskite structure with the PT or PLT buffer layers but regions of imperfections still could be found. This indicated that in these Pb-containing layers, Pb was responsible for the film-substrate interactions. This effect was not unexpected since it was well known that PbO reacts easily with SiO<sub>2</sub> to form low melting silicates. The TiO<sub>2</sub> sublayer was found to be the better choice in this case, yet it required a layer thickness of 500-750Å to inhibit such interactions. Similar uses of TiO<sub>2</sub> layers have been reported for PLZT films deposited on glass substrates [20] and in CMOS devices integrated with PLZT ferroelectrics [21].

The crystallized PZ films were transparent, light yellow in color and suitable for transmission electrooptic properties measurements. Fig. 5

shows the morphology of a  $1\mu\text{m}$  PZ film deposited on a fused  $\text{SiO}_2$  substrate pre-coated with a  $\text{TiO}_2$  layer. As can be seen in Fig. 6 its XRD pattern that this film was highly crystallized into a single perovskite phase. The superstructure orthorhombic {110} peak at about  $16.9^\circ 2\theta$  confirmed the multiple cell structure of this film.

**3.2.3 Microcracks.** All PZ films deposited on the above two types of substrates had a certain degree of microcracks as can be seen in Fig. 3 to 5. While this phenomenon was not observed in other FE PLZT films deposited on the same substrates under similar processing conditions, their formation was attributed particularly to the extra volume shinkage which occurred at the phase transition from the higher temperature paraelectric state to the lower temperature AFE state [14] during the film cooling stage. On the other hand, microcracks were not seen in PZ films deposited on substrates such as Ag, which possessed a higher thermal expansion coefficient ( $22 \times 10^{-6}^\circ\text{C}^{-1}$ ) than those of the Pt-coated Si ( $2.6 \times 10^{-6}^\circ\text{C}^{-1}$ ) and fused  $\text{SiO}_2$  ( $0.5 \times 10^{-6}^\circ\text{C}^{-1}$ ). Since the general PLZT films were in a compressive state when deposited on Ag foils [22], it suggested that the microcracks could be avoided by a residual compressive stress. These microcracks, however, did not prevent the measurements of the electrical and optical properties, yet they affected somewhat the optical quality of the films on fused  $\text{SiO}_2$ .

### *3.3 Dielectric and Electrooptic Properties*

All the PZ films had a dielectric constant at 1kHz in the range of 200 to 250. Dissipation factors were 0.02 to 0.03 and dc resistivities were greater than  $10^{10}\Omega\text{-cm}$ . A typical polarization versus electric field (P-E) double hysteresis loop measured at room temperature was shown in Fig. 7 for a  $0.8\mu\text{m}$  PZ film deposited on a Pt/Ti-coated Si substrate with a  $\text{TiO}_2$  sublayer. The  $\text{AFE} \rightarrow \text{FE}$  transition field was about  $40\text{kV/mm}$  and the reverse  $\text{FE} \rightarrow \text{AFE}$  was about  $20\text{kV/mm}$ . The FE phase saturated at about  $60\text{kV/mm}$  with a polarization between  $0.3$  to  $0.4\mu\text{C/mm}^2$ .

The success in observing the double hysteresis loop of PZ film at room temperature was attributed to the superior dielectric strength usually found for thin film materials. For example, the  $\text{AFE} \rightarrow \text{FE}$  transition field found for these PZ films was an order of magnitude greater than the reported values for bulk materials [2]. Such a large field would certainly cause breakdown in bulk PZ.

Inasmuch as the slope of the P-E hysteresis loop indicates the permittivity of the sample, this parameter would be expected to increase sharply as the sample passed through the  $\text{AFE} \rightarrow \text{FE}$  and  $\text{FE} \rightarrow \text{AFE}$  phase transitions. Fig. 8 shows the variation of the permittivity of a virgin PZ film recorded as a function of a slowly varying dc bias applied first in the positive direction. The permittivity sharply increased by 40 to 60% of its original value at the  $\text{AFE} \rightarrow \text{FE}$  transition field and dropped as the loop

saturated. The increase in permittivity at the FE $\rightarrow$ AFE transition was slightly smaller than at the AFE $\rightarrow$ FE transition.

Weak ferroelectricity was usually observed in these PZ films and was best illustrated in Fig. 8. As the varying dc field just completed one half cycle and switched to the negative direction, the permittivity started to increase slightly and then dropped before the AFE $\rightarrow$ FE transition. A possible ferroelectric interface between the Ti-containing layer and the PZ film might explain this phenomenon, however, earlier results on pure PZ films also showed some ferroelectric behavior at low fields. This effect will require further detailed study.

Fig. 9 demonstrates the dc bias-induced hysteresis behavior obtained in the antiferroelectric films. As expected, this film behaved like a linear capacitor when the alternating field ( $\pm 24.6\text{kV/mm}$ ) was below the AFE $\rightarrow$ FE transition field ( $\sim 32.3\text{kV/mm}$ ). When biased with a dc voltage at 16V (24.6kV/mm), the P-E hysteresis loop behaved like a normal ferroelectric material with two polarization states. This was originated from the hysteresis in the AFE $\leftrightarrow$ FE phase transitions.

The films deposited on fused  $\text{SiO}_2$  substrate were electroded with an interdigital pattern having a gap width of 10  $\mu\text{m}$ . The birefringence curve shown in Fig. 10 again showed the ferroelectric behavior at small fields. The AFE $\rightarrow$ FE transition was accompanied by a steep increase in the birefringence. A detailed description of this transverse electrooptic behavior has been given elsewhere [13].

#### **4. Summary**

AFE PbZrO<sub>3</sub> films derived from acetate precursors were deposited on several substrates by an automatic dip coating process. The phase inhomogeneity observed in these films was attributed to the volatility of the Pb species formed during the precursor decomposition process. A thin TiO<sub>2</sub> layer was able to facilitate the formation of the perovskite PbZrO<sub>3</sub> and also inhibit the interactions between Pb and SiO<sub>2</sub> at the processing temperature. X-ray diffraction revealed the superstructure characteristic of the antiferroelectric phase in these films. The antiferroelectric properties, along with the dc bias behavior, were measured for PbZrO<sub>3</sub> films at room temperature.

## References

1. E. Sawaguchi, G. Shirane and Y. Takagi, *J. Phys. Soc. Japan* **6** (1951) 333.
2. G. Shirane, E. Sawaguchi and Y. Takagi, *Phys. Rev.* **84** (1951) 476.
3. E. Sawaguchi, H. Maniwa and H. Hoshina, *Phys. Rev.* **83** (1951) 1078.
4. H. Fujishita, Y. Shiozaki, N. Achiwa and E. Sawaguchi, *J. Phys. Soc. Japan* **51** (1982) 3583.
5. L.N. Chapin and S.A. Myers, *Mater. Res. Soc. Symp. Proc.* **200** (1990) 153.
6. C.-C. Hsueh and M.L. Mecartney, *ibid*, p. 219.
7. A.H. Carim, B.A. Tuttle, D.H. Doughty and S.L. Martinez, *J. Am. Ceram. Soc.* **74** (1991) 1455.
8. K.D. Preston and G.H. Haertling, *Integrated Ferroelectrics* **1** (1992) 89.
9. S.L. Swartz, S.J. Bright, P.J. Melling and T.R. Shrout, *Ferroelectrics* **108** (1990) 71.
10. S. Hirano and K. Kato, *J. Non-Cryst. Solids* **100** (1988) 538.
11. B. Jaffe, *Proc. Inst. Radio Engrs.* **49** (1961) 1264.
12. K. Uchino and S. Nomura, *Ferroelectrics* **50** (1983) 191.
13. F. Wang, K.K. Li and G.H. Haertling, *Opt. Lett.* **17** (1992) 1122.
14. D. Berlincourt, H.H.A. Krueger and B. Jaffe, *J. Phys. Chem. Solids* **25** (1964) 659.
15. G. H. Haertling, *Ferroelectrics* **116**, 51 (1991).

16. K.K. Li, G.H. Haertling and W.-Y. Howng, *Integrated Ferroelectrics.* 3 (1992) to be published.
17. F. Wang, C.B. Juang, C. Bustamante and A.Y. Wu, in Proc. of the 4th Intern. SAMPE Electronic Conf., Albuquerque, New Mexico, June, 1990 (Soc. Advancement of Mater. & Process Engr., Covina, Calif.) p.712.
18. Y. Takahashi, Y. Matsuoka, K. Yamaguchi, M. Matsuki and K. Kobayashi, *J. Mater. Sci.* 25 (1990) 3960.
19. K.D. Budd, S.K. Dey and D.A. Payne, *Brit. Ceram. Proc.* 36 (1985) 107.
20. Y. Takahashi and K. Yamaguchi, *J. Mater. Sci.* 25 (1990) 3950.
21. B.A. Tuttle, private communication.
22. K.K. Li, G.H. Haertling and W.-Y. Hwong, presented at the Am. Ceram. Soc. 94th Ann. Meeting, Minneapolis, MN, April 1992. (Abstr.45-E-92)

## Figure Captions

- Fig. 1. XRD patterns of dried powder pyrolyzed at different temperatures. (#: Pb,  $\circ$ : oxidized Pb, \*: perovskite  $\text{PbZrO}_3$ .)
- Fig. 2. TGA and DTA curves of dried  $\text{PbZrO}_3$  powder heated in air at a rate of  $10^\circ\text{C}/\text{min}$ .
- Fig. 3. SEM photograph of a 10-layer  $\text{PbZrO}_3$  film deposited on a Pt/Ti-coated Si substrate.
- Fig. 4. SEM photograph of a 10-layer  $\text{PbZrO}_3$  film formed on a Pt/Ti-coated Si substrate with a thin  $\text{TiO}_2$  pre-coat.
- Fig. 5. A  $1\mu\text{m}$   $\text{PbZrO}_3$  film formed on fused  $\text{SiO}_2$  pre-coated with a  $\text{TiO}_2$  layer.
- Fig. 6. XRD pattern of the  $\text{PbZrO}_3$  film shown in Fig. 5 and its superstructure peak characterizing the antiferroelectricity.
- Fig. 7. A typical dielectric double hysteresis loop of  $\text{PbZrO}_3$  film deposited on Pt/Ti-coated Si substrate with a  $\text{TiO}_2$  layer.
- Fig. 8. Variation of the  $\text{PbZrO}_3$  film permittivity as a function of the dc bias.
- Fig. 9. P-E hysteresis loop of a  $\text{PbZrO}_3$  film with and without a dc bias when the alternating field is lower than the  $\text{AFE} \rightarrow \text{FE}$  transition field.
- Fig. 10. Birefringence shift,  $\Delta n$ , versus electric field, E, plot of an anti-ferroelectric  $\text{PbZrO}_3$  film on fused  $\text{SiO}_2$ .

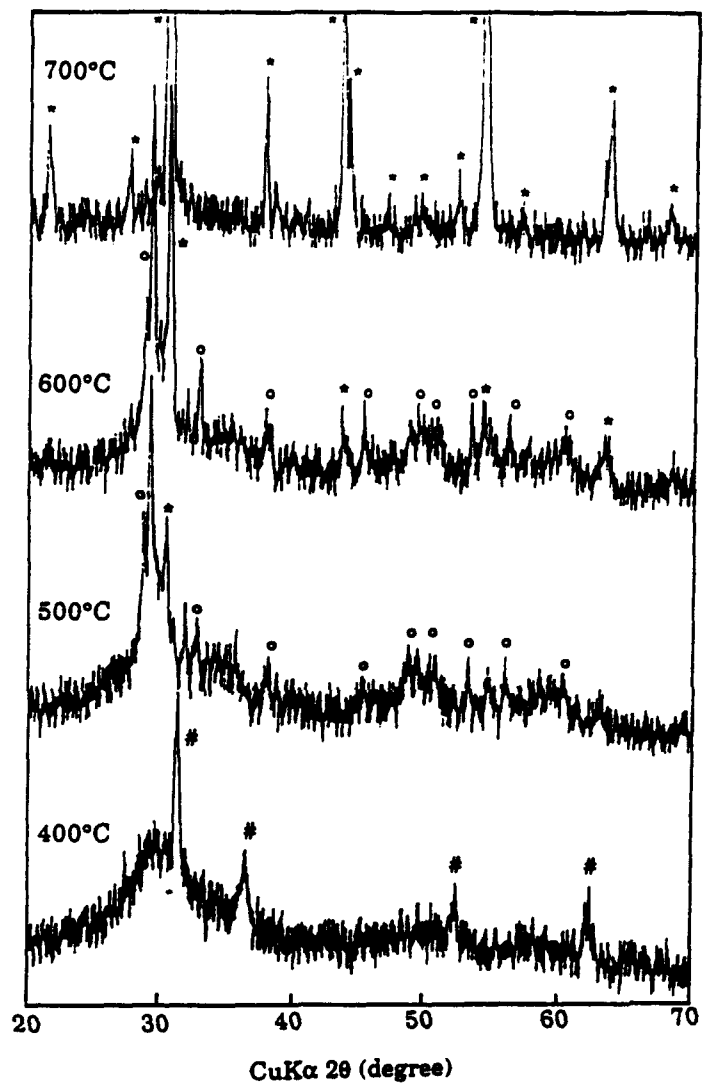


Fig. 1. XRD patterns of dried powder pyrolyzed at different temperatures. (#: Pb, o: oxidized Pb, \*: perovskite  $\text{PbZrO}_3$ .)

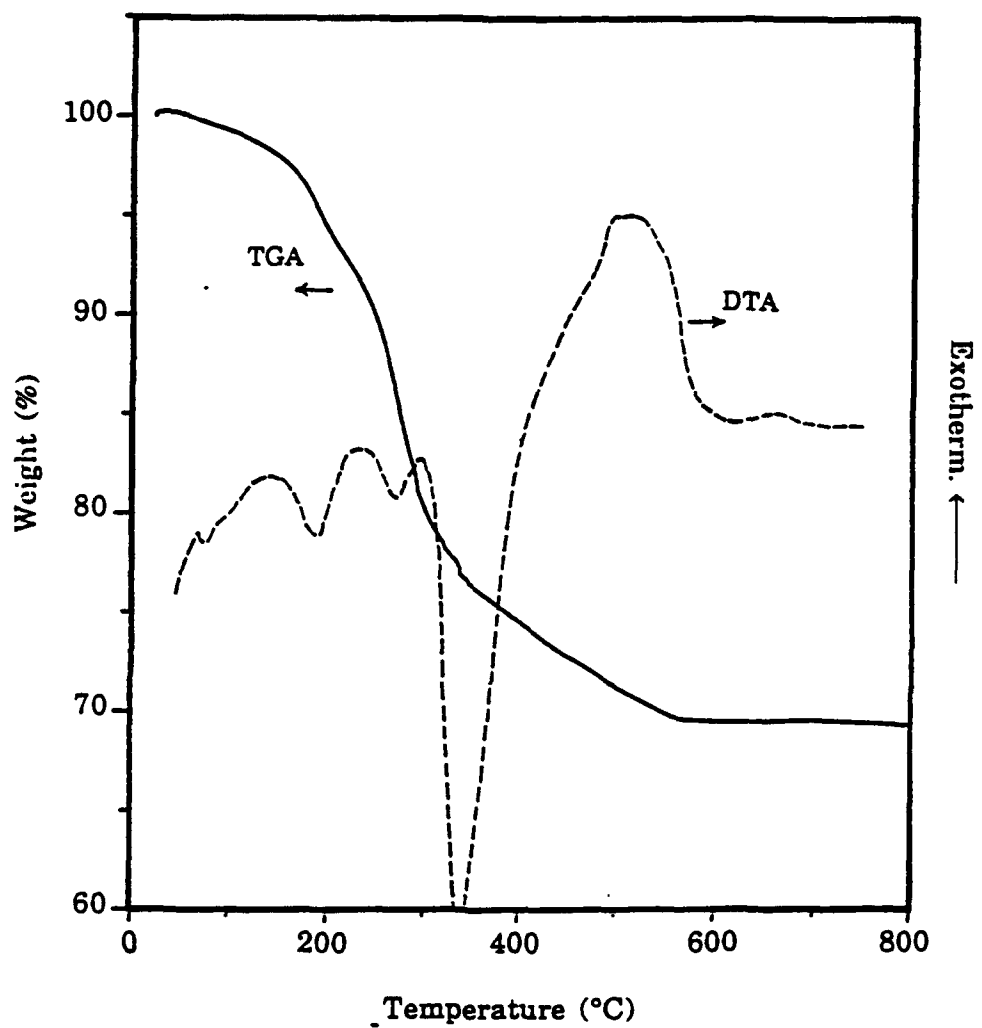
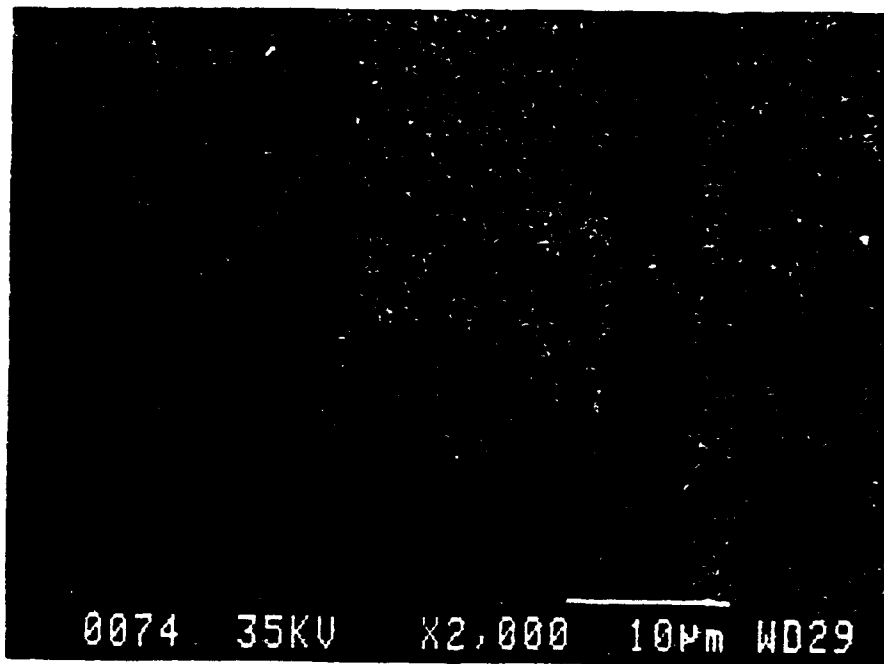


Fig. 2. TGA and DTA curves of dried  $\text{PbZrO}_3$  powder heated in air at a rate of  $10^\circ\text{C}/\text{min}$ .

**Figure 3.**

(K.K. Li, F. Wang and G.H. Haertling)



**Fig. 3.** SEM photograph of a 10-layer PbZrO<sub>3</sub> film deposited on a Pt/Ti-coated Si substrate.

**Figure 4.**

(K.K. Li, F. Wang and G.H. Haertling)

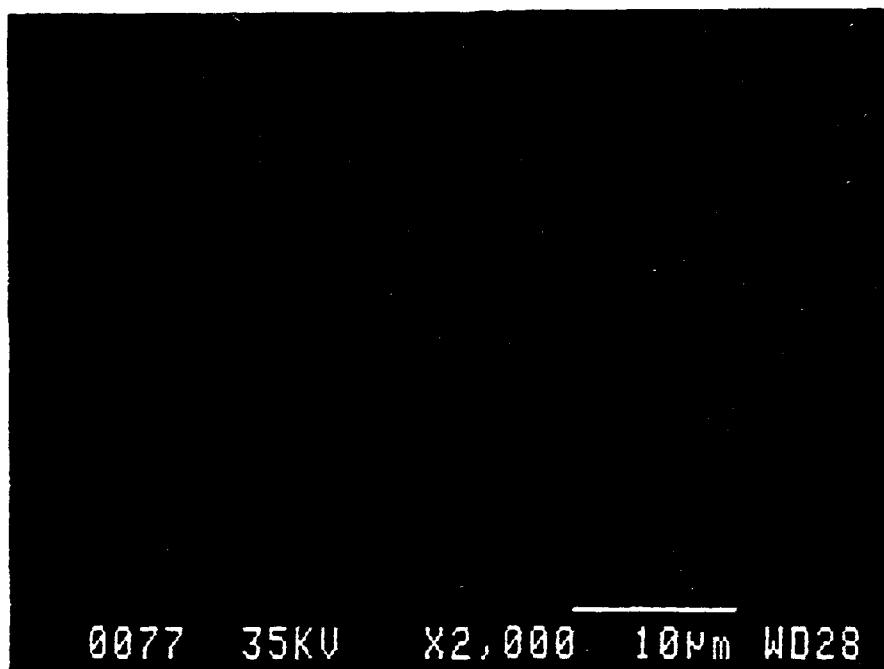


**Fig. 4.** SEM photograph of a 10-layer PbZrO<sub>3</sub> film formed on a Pt/Ti-coated Si substrate with a thin TiO<sub>2</sub> pre-coat.

**Figure 5.**

(K.K. Li, F. Wang and G.H. Haertling)

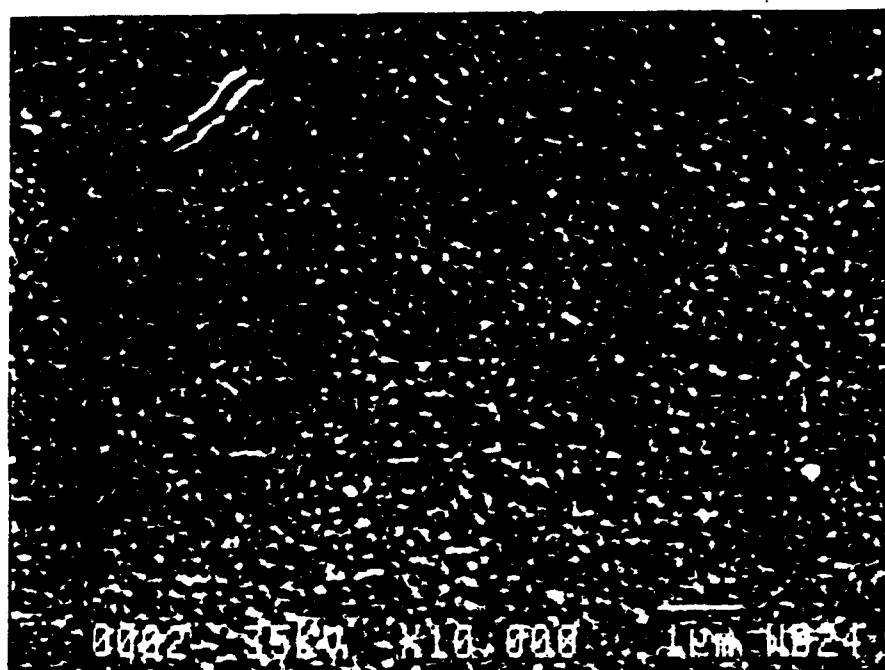


**Fig. 5.** A  $1\mu\text{m}$   $\text{PbZrO}_3$  film formed on fused  $\text{SiO}_2$  pre-coated with a  $\text{TiO}_2$  layer.

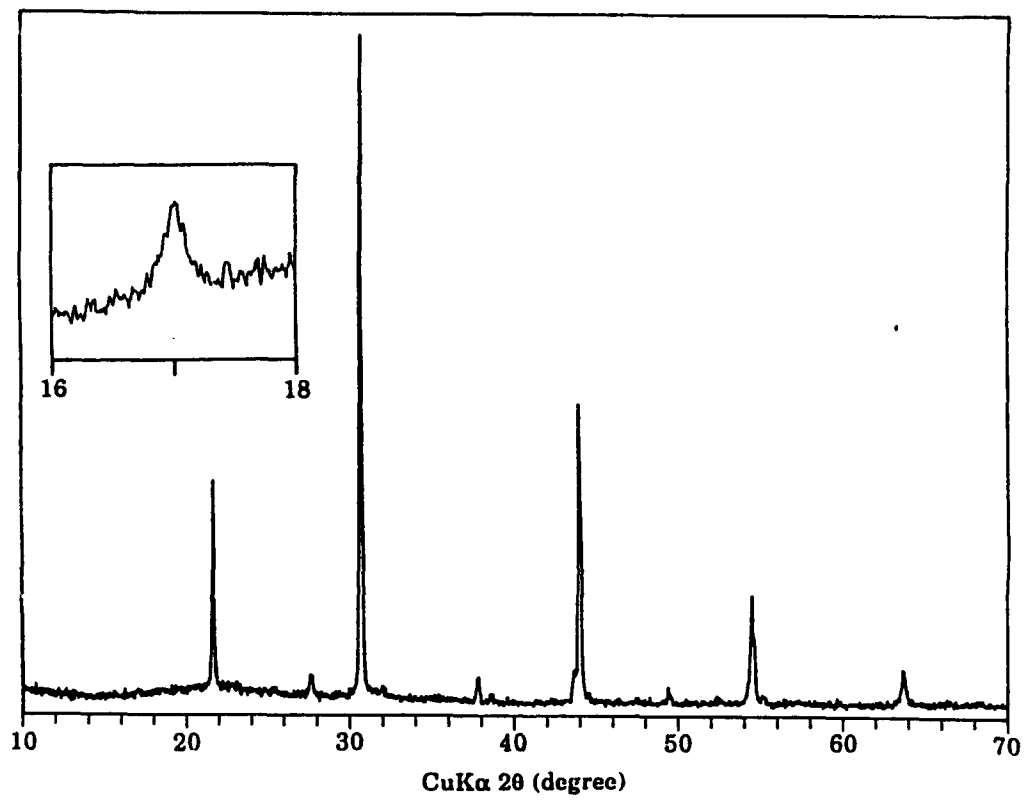
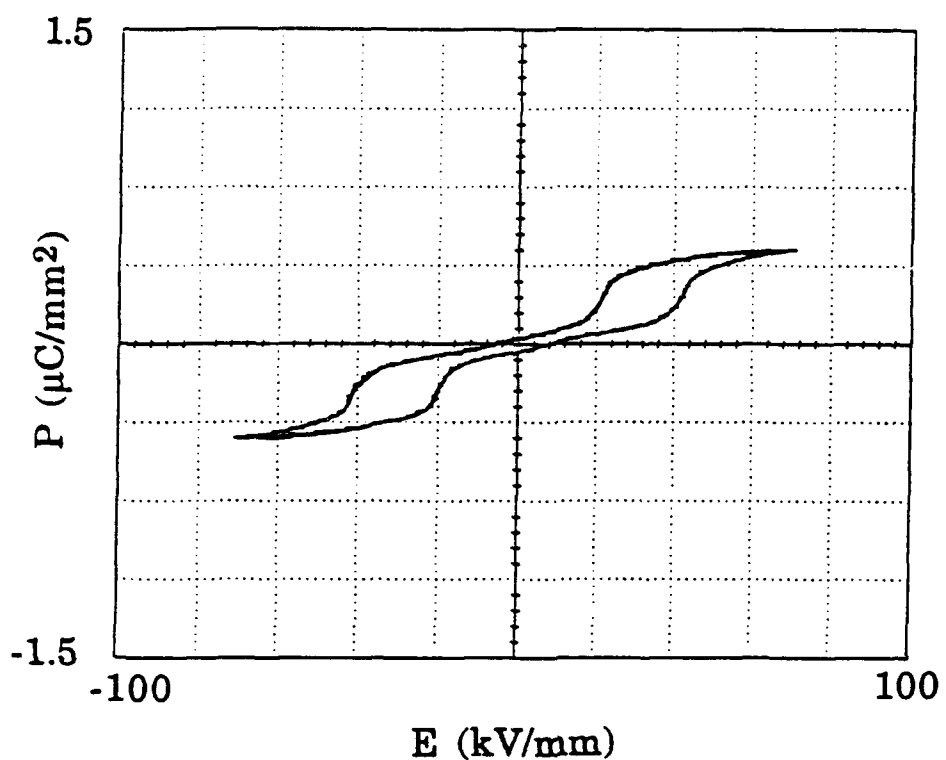


Fig. 6. XRD pattern of the  $\text{PbZrO}_3$  film shown in Fig. 5 and its superstructure peak characterizing the antiferroelectricity.

**Figure 7.**

(K.K. Li, F. Wang and G.H. Haertling)



**Fig. 7.** A typical dielectric double hysteresis loop of  $\text{PbZrO}_3$  film  
deposited on Pt/Ti-coated Si substrate with a  $\text{TiO}_2$  layer.

**Figure 8.**

(K.K. Li, F. Wang and G.H. Haertling)

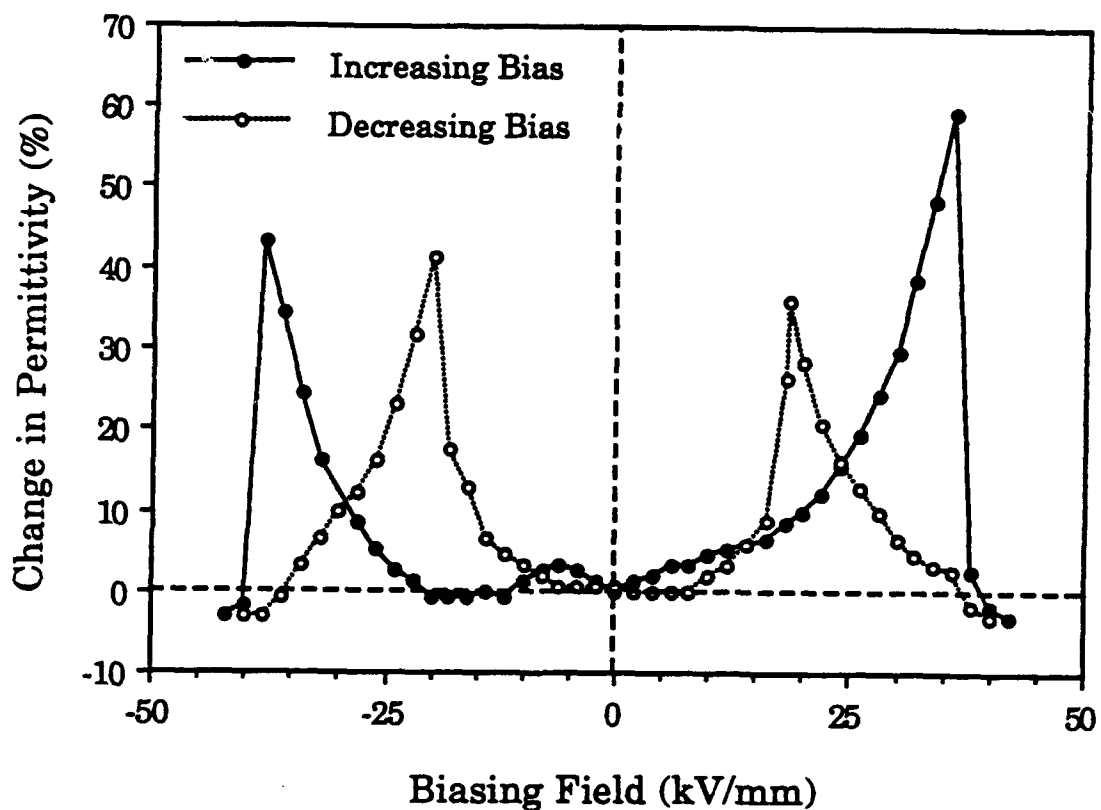


**Fig. 8.** Variation of the  $\text{PbZrO}_3$  film permittivity as a function of the dc bias.

**Figure 9.**

(K.K. Li, F. Wang and G.H. Haertling)

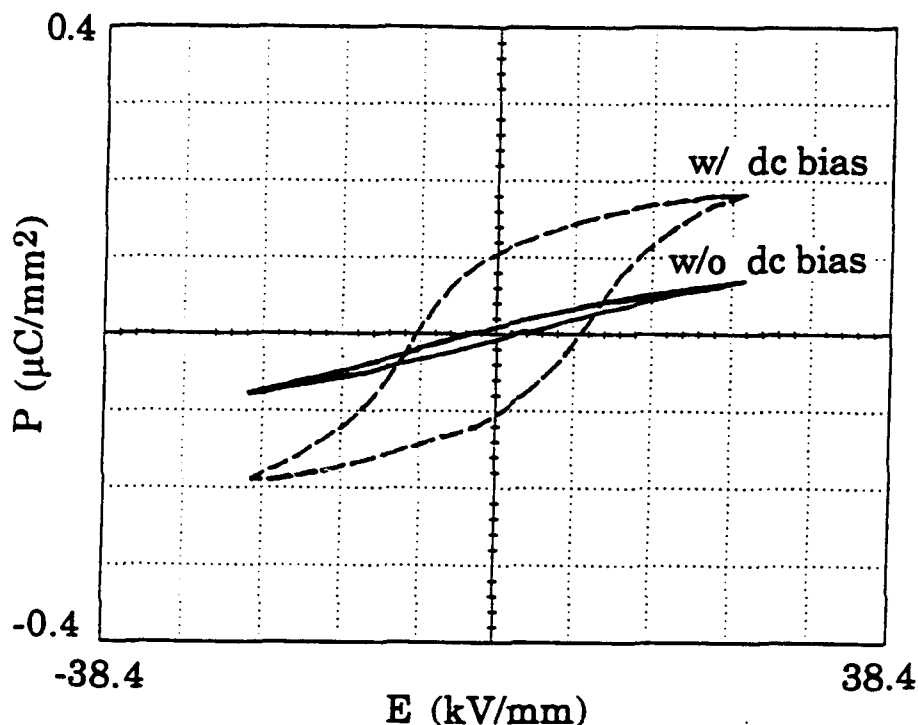


**Fig. 9.** P-E hysteresis loop of a  $\text{PbZrO}_3$  film with and without a dc bias when the alternating field is lower than the AFE $\rightarrow$ FE transition field.

**Figure 10.**

(K.K. Li, F. Wang and G.H. Haertling)

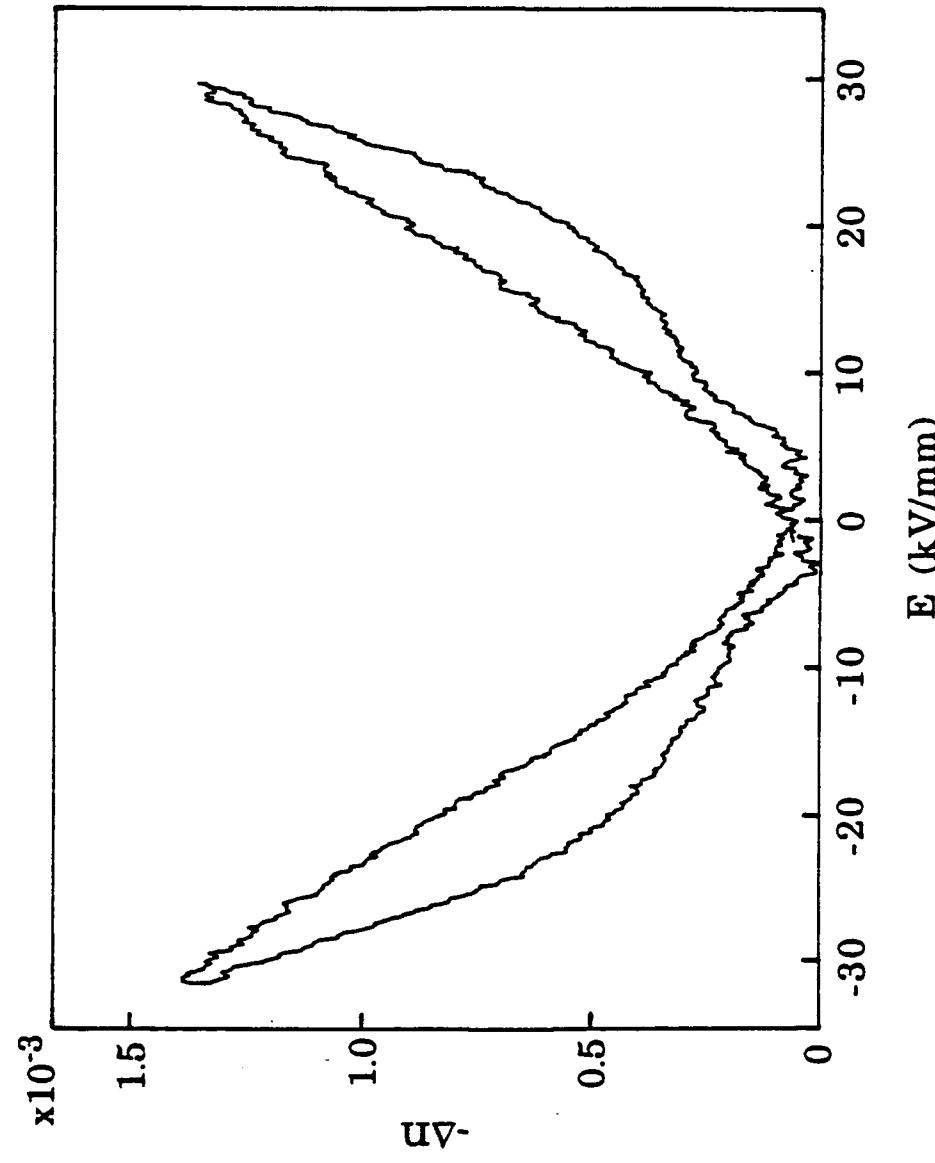


**Fig. 10.** Birefringence shift,  $\Delta n$ , versus electric field,  $E$ , plot of an antiferroelectric  $PbZrO_3$  film on fused  $SiO_2$ .

## **SECTION 8**

# TRANSVERSE ELECTROOPTIC PROPERTIES OF ANTIFERROELECTRIC LEAD CONTAINING THIN FILMS

Feiling Wang, Kewen K. Li and Gene H. Haertling  
Department of Ceramic Engineering  
Clemson University  
Clemson, South Carolina 29634-0907

The transverse electrooptic effect was observed in solution coated lead zirconate thin films. The electric-field-induced birefringent shift exhibited a characteristic response which differed from the normal butterfly-like loops for ferroelectric materials. The observed unique response in lead zirconate thin films was related to their antiferroelectric nature and the electric-field-induced antiferroelectric-ferroelectric phase transition. The possible applications of the materials for optical memory are discussed.

## Introduction

Ferroelectric (FE) thin films, owing to their high dielectric constant and two electrically switchable remanent states, have attracted great interest for the development of nonvolatile memory devices and other applications<sup>1,2</sup>. A variety of ferroelectric materials are also known to possess transverse electrooptic properties, i.e. the electric-field-controlled birefringence; however, ferroelectric switching (polarization reversal with an electric field) has not proved equally useful in integrated optical and/or optoelectronic devices. To facilitate an optical memory function in optoelectronic devices, it is desirable for the waveguide materials to possess two electrically switchable birefringent states. However, the two remanent polarization states are not distinguishable for the index ellipsoid in ferroelectric materials. Therefore, it is not feasible to realize optical memory in ferroelectric materials by switching between the two remanent polarization states.

Recently the transverse electrooptic effects in antiferroelectric (AFE) lead zirconate ( $PbZrO_3$ ) thin films were observed<sup>3</sup>. The electric-field-induced birefringent shift in the lead zirconate thin films showed a characteristic response not exhibited in ferroelectric materials. The unique electrooptic response in the antiferroelectric thin films was found to stem from the electric-field-induced antiferroelectric-ferroelectric phase transition. Besides its importance as a fundamental material property, the transverse electrooptic effect in the antiferroelectric thin films may also furnish a mechanism for optical memory in optoelectronic devices. In this report the latest measurements of the transverse electrooptic properties in antiferroelectric lead zirconate thin films are presented.

## Experimental Method

Lead zirconate thin films were deposited onto fused silica and Pt/Ti coated silicon substrates by a solution coating technique from an acetate precursor<sup>4,5</sup>. The antiferroelectric crystal structure of the resultant thin films was confirmed by the appearance of the X-ray diffraction peak at  $2\theta = 16.9^\circ$ , characterizing the antiferroelectric double cell structure. For the measurement of the dielectric properties of the materials, copper dots were evaporated onto the thin films deposited on the Pt/Ti-coated silicon substrate. For the detection of the transverse electrooptic properties, copper interdigitated electrodes with gap widths ranging from 5 to 40  $\mu m$  were deposited on top of the thin films grown on the fused silica substrates.

The electric-field-induced birefringent shift of the thin film was measured by means of a phase-detection technique<sup>6</sup>, using a He-Ne laser of wavelength of 632.8 nm as the light source. The phase modulation of the incident light was provided by means of a modulator. The measurements were performed with a transmission mode. In the phase detection scheme, the amplitude of the output signal (from a lock-in amplifier) at the modulating frequency was directly proportional to the phase retardation of the sample, provided that the total phase retardation of the sample was sufficiently small. A slow varying dc voltage was applied to the interdigitated electrodes during the measurement. An optical compensator was used to calibrate the measuring system.

## Results and Discussion

A typical electrooptic response of the lead zirconate thin film is shown in Figure 1 where the birefringent shift of the thin film is plotted as a function of the slow varying dc electric field. The thickness of the film was 1  $\mu m$ . Interdigital electrodes with a gap width of 10  $\mu m$  was used in the measurement. As shown in the figure, the electrooptic response of the antiferroelectric thin film exhibits a number of features different from that of ferroelectric materials. For the purpose of comparison, a typical birefringence versus E-field curve for a ferroelectric thin film, i.e. PLZT<sup>7</sup> of composition 2/55/45, is shown in Figure 2. The birefringence versus E-field curve for the lead zirconate thin film is characterized by (1) enhanced hysteretic

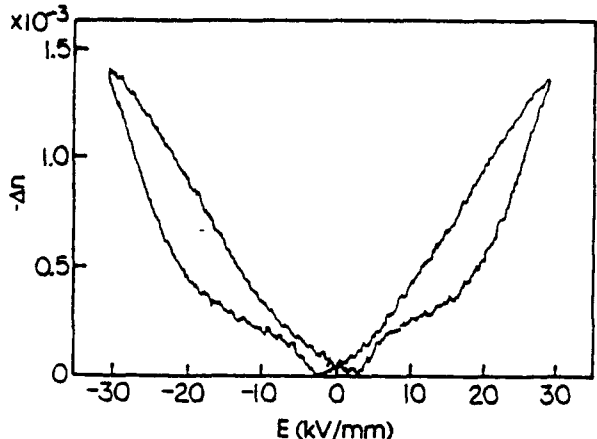


Figure 1 Measured birefringent shift as a function of the external dc electric field for a lead zirconate thin film deposited on a fused silica substrate.

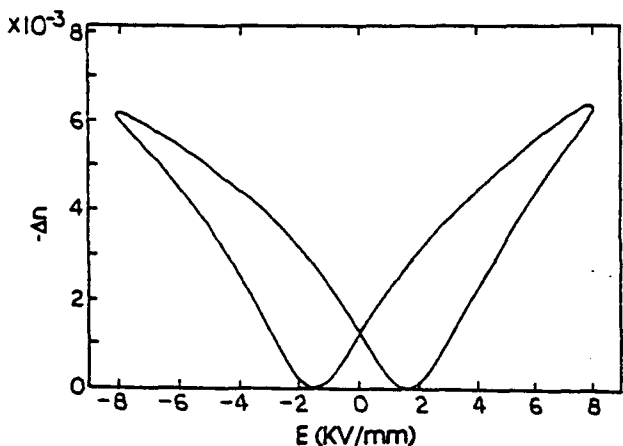


Figure 2 Measured birefringent shift as a function of the external dc electric field for a ferroelectric PLZT thin film deposited on a sapphire substrate.

behavior in the region of field strength above 10 kV/mm, (2) diminished hysteretic behavior in the region of field strength below 5 kV/mm and (3) rapid increase of the slope when the increasing electric field exceeds 20 kV/mm. It was found that the characteristic response of the lead zirconate thin films was attributed to the electric-field-induced AFE-FE structural transition<sup>3</sup>.

With the help of a phenomenological model, the correlation between the field-induced birefringent shift of a material and electric polarization P(E) can be described by the following relation:

$$\Delta n = [E + \beta P(E)]^2, \quad (1)$$

where  $\beta$  is a constant dependent on the crystal structure of the material ( $4\pi/3$  for cubic structure). The main features for the electrooptic response of the lead zirconate thin films shown in Figure 1 are consistent with those predicted from the dielectric properties (double hysteresis loop) by using relation (1).

To better understand the nature of the antiferroelectric lead zirconate thin films, a static bias electric field was applied to the thin film material in both the dielectric and electrooptic measurements. Thin films deposited on the Pt/Ti coated silicon substrates were used for the measurement of the dielectric behavior. With the increase of the dc bias, the polarization versus E field curve of the lead zirconate thin film gradually evolves from a double hysteresis loop to a single hysteresis loop. As shown in Figure 3, under an appropriate bias field, the shape of the biased single hysteresis loop very much resembles the normal hysteresis loop for ferroelectric materials. Unlike the ferroelectric materials, however, the two remanent states in the biased single hysteresis loop (denoted by  $P_A$  and  $P_B$  in Fig.3) possess polarizations of different magnitude, which produce two distinct birefringent states in the thin films. These birefringent states are clearly represented in the biased birefringence versus E-field curve, as shown in Fig.4, measured from a lead zirconate thin film grown on a fused silica substrate. A static bias field of approximately 17 kV/mm was applied during the measurement. It is obvious that the two distinguished remanent birefringent states  $\Delta n_A$  and  $\Delta n_B$  are associated with the two remanent polarization states  $P_A$  and  $P_B$  in the biased single hysteresis loop shown in Figure 3. It should be noted, however, that to avoid the breakdown of the electrodes through the air, the bias electric field and the scan range are lower in the measurement of the electrooptic properties than in the measurement of the dielectric property. In addition, because these two measurements involve thin films deposited on two different types of substrates with different directions of applied electric field, quantitative correlation between these two measurements is not possible.

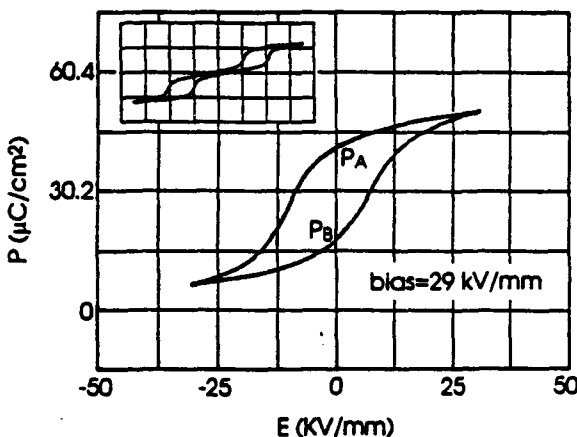


Figure 3 Dielectric properties of a lead zirconate thin film grown on a Pt/Ti-coated silicon substrate, taken under a static bias field of 29 kV/mm. The insert is a hysteresis loop of the same sample taken with zero bias field. The horizontal and vertical scales for the insert plot are 25 kV/mm per division and 30.2  $\mu\text{C}/\text{cm}^2$  per division, respectively.

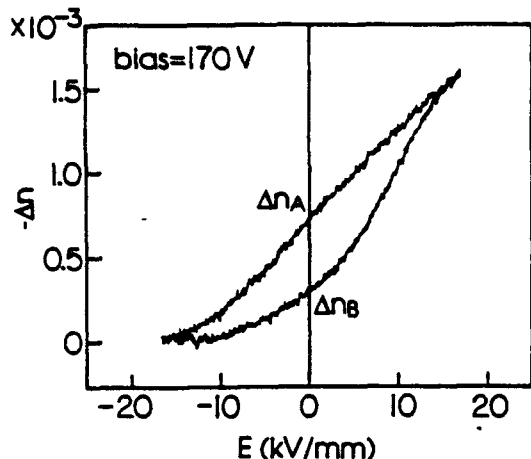


Figure 4 Birefringent shift as a function of the slow varying external field measured with a dc bias field of 17 kV/mm for a lead zirconate thin film on a fused silica substrate.

It was found that the lead zirconate thin films acquired a permanent birefringence once an initial electric field of sufficient magnitude was applied. Shown in Figure 5 is the birefringent shift of a lead zirconate thin film as a function of the slow varying external electric field recorded during the first few cycles of the field scan. In the first half cycle of the field scan, the birefringence of the material drastically increased when the increasing electric field exceeded approximately 16 kV/mm. When the external electric field was reduced to zero, the material retained a significant remanent birefringent shift. During the next few scan cycles, this remanent birefringence kept increasing yet the increment was smaller and smaller after each cycle. A stable remanent birefringence (permanent birefringence) was finally reached as shown previously in the birefringence versus E-field curve of Figure 1. The stable remanent birefringent state, under zero external electric field, was chosen as the zero-

birefringence point in plotting both Figure 1 and Figure 4. After testing a few lead zirconate thin film samples, it was found that this initiating process of the material was reproducible.

The observed permanent birefringence in the antiferroelectric thin films mentioned above may be related to other types of memory behavior previously observed in antiferroelectric lead zirconate materials<sup>8</sup>. A possible explanation for this birefringence memory is that when the AFE-FE phase transition occurred under a sufficiently high electric field the ferroelectric domains are forced to align along the direction of the E-field; although the structure of antiparallel dipoles was restored after the withdrawal of the external E-field, the antiferroelectric dipoles remained preferentially aligned in the direction along which the E-field was previously applied. Such an explanation for the birefringence memory is supported by an optical study of the lead zirconate crystal which showed that the index of refraction is the smallest for the light polarized along the  $a$  axis of the antiferroelectric unit cell<sup>9</sup>. This mechanism of birefringence memory is distinguished from that of ferroelectric materials where birefringence memory is mainly caused by the remanent polarization.

The characteristic electrooptic response of the lead zirconate thin films may furnish a means of realizing optical memory in optoelectronic devices. Two different mechanisms may be utilized in optical memory devices. In the first type of memory, the information may be stored in a virgin material by applying a sufficiently high electric field. After the withdrawal of the electric field, as shown in Figure 5, the thin film material becomes permanently oriented and possesses a permanent birefringence of approximately  $1.3 \times 10^{-3}$ . The second type of memory is associated with the two distinguished birefringent states of the thin film materials in the presence of a bias electric field as shown in Figure 4. Because these two birefringent states,  $\Delta n_A$  and  $\Delta n_B$ , are produced by the two remanent states of polarization,  $P_A$  and  $P_B$ , of the material, they are stable under the bias field. The merit of the second type of memory is that the two birefringent states are electrically switchable. For example, a TIR switch<sup>10</sup> made of the antiferroelectric thin film would allow the inter-switching of the light between the two waveguide channels by electric pulses of opposite polarities, operated under a static bias field. Such a switch is not possible with ferroelectric materials in which the two remanent polarization states are optically equivalent.

### Conclusions

The transverse electrooptic property of the solution coated lead zirconate thin film exhibits a characteristic response which is attributed to the electric-field-induced antiferroelectric-ferroelectric phase transition. Under an appropriate static bias electric field, the material possess two distinguishable birefringent states

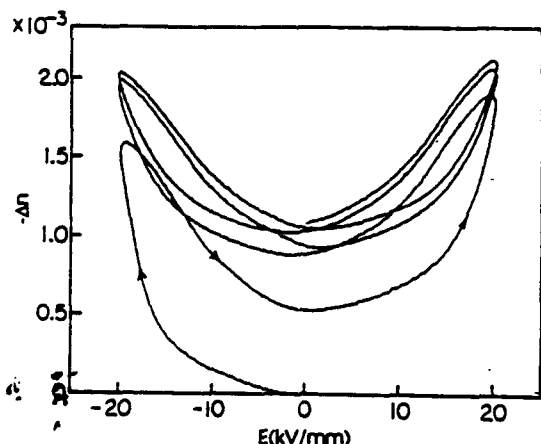


Figure 5 The evolution of the electrooptic response of a lead zirconate thin film on a fused silica substrate during the first few cycles of the electric field scan.

associated with the two remanent polarization states of the material. The thin films were also found to acquire a permanent birefringence once a sufficiently high electric field was applied to the virgin materials.

Two types of mechanisms are proposed for utilizing the antiferroelectric thin films for optical memory in optoelectronic devices. The first type of memory makes use of the permanent orientation of the material induced by an initial electric field. The second type of memory involves the inter-switching between the two distinguishable birefringent states of the material under a bias field with electric pulses.

#### Acknowledgment

This study was partially sponsored by the Office of Naval Research under contract No. N00014-91-J-508.

#### References

- [1] G.H. Haertling, "Ferroelectric Thin Film for Electronic Applications," *J. Vac. Sci. Technol. A*, 9, 414(1991)
- [2] D. Bonsurant and F. Gnadinger, "Ferroelectrics for Nonvolatile RAMs," *IEEE Spectrum*, July 1989, p.30
- [3] F. Wang, K.K. Li, and G.H. Haertling, "Transverse Electro-Optic Effect of Antiferroelectric Lead Zirconate Thin Films," *Optics Lett.* 17, 1122(1992)
- [4] K.K. Li, F. Wang, and G.H. Haertling, "Antiferroelectric Lead Zirconate Thin Films Derived from an Acetate Precursor System," *J. Mater. Sci.* (to be published)
- [5] G.H. Haertling, "PLZT Thin Film Prepared from Acetate Precursors," *Ferroelectrics*, 116, 51(1991)
- [6] F. Wang, C.B. Juang, C. Bustamante, and A.Y. Wu, "Electro-optic Properties of  $(Pb, La)(Zr, Ti)O_3$ ,  $BaTiO_3$ ,  $(Sb, Ba)Nb_2O_6$  and  $BaNaNb_5O_{15}$  Thin Films," in *Proc. of 4th International SAMPE Electronic Conference*, p.712
- [7] G. H. Haertling and C.E. Land, "Hot-pressed  $(Pb, La)(Zr, Ti)O_3$  Ferroelectric Ceramic for Electronic Applications," *J. Am. Ceram. Soc.* 54, 1(1971)
- [8] K. Uchino, "Digital Displacement Transducer Using Antiferroelectrics," *Japan. J. Appl. Phys.* 24, suppl., 24(1985)
- [9] F. Jona, G. Shirane, and R. Pepinsky, "Optical Study of  $PbZrO_3$  and  $NaNbO_3$  Single Crystals," *Phys. Rev.* 97, 1585(1955)
- [10] H. Higashino, T. Kawaguchi, H. Adachi, T. Makino and O. Yamazaki, "High Speed Optical TIR Switches Using PLZT Thin Film Waveguides on Sapphire," *Jpn. J. Appl. Phys.* 24, suppl., 284(1985)

## **SECTION 9**

# Discrete electro-optic response in lead zirconate thin films from a field-induced phase transition

Feiling Wang, Kewen K. Li, Eugene Furman, and Gene H. Haertling

Department of Ceramic Engineering, Clemson University, Clemson, South Carolina 29634

Received May 4, 1993

A discrete transverse electro-optic response associated with a field-induced antiferroelectric-ferroelectric phase transition has been observed to exist in lead zirconate thin films grown on Pt/Ti-coated silicon substrates. The magnitude of the birefringence jump from the antiferroelectric to the ferroelectric state is approximately  $2.5 \times 10^{-2}$ . Quantitative correlation between the field-induced birefringence and the polarization was also experimentally studied. The discrete birefringent change in the thin films may be a desirable property for applications in optical switches or other integrated-optical devices.

The field-induced antiferroelectric (AFE)-ferroelectric (FE) phase transition has been utilized to produce discrete strain for applications in actuators and shape memory.<sup>1,2</sup> To exploit optical usefulness of AFE materials, one can ask questions as to whether a field-induced AFE-FE phase transition is accompanied by a discrete change in optical properties of the materials. In a recent Letter the transverse electro-optic effect in AFE lead zirconate (PZ) thin films was reported.<sup>3</sup> It was found that the field-induced birefringence in the PZ films exhibited a characteristic response different from that of ferroelectric materials; this response was attributed to the field-induced AFE-FE structural transition. However, because of the field nonuniformity created by the planar electrodes, the measured birefringence did not clearly show the discrete change under the field-induced AFE-FE phase transition predicted by a phenomenological model. The electro-optic measurement in the transmission mode also made it unfeasible to study experimentally the correlation between the birefringence of the thin film materials and their polarization because (1) the electro-optic properties and the dielectric properties had to be measured from thin films deposited onto two different types of substrate, and (2) the direction of the external electric field was different for the two types of measurement owing to the requirements of the measuring methods.

With a newly developed measuring method that uses a phase-detection scheme in the reflection mode, it has become possible to measure the electro-optic effect of thin films deposited onto opaque substrates. Both dielectric and electro-optic properties of the thin films therefore can be measured from the same sample with the same configuration of electrodes. The purpose of this Letter is to report what is to our knowledge the first observation of the discrete birefringent change in PZ thin films under field-induced AFE-FE phase transitions and the direct measurement of the correlation between the field-induced birefringence and the polarization of the materials.

Polycrystalline PZ films were deposited onto Pt/Ti-coated silicon wafers by using an automated dip-

coating technique from an acetate precursor.<sup>4,5</sup> Indium tin oxide (ITO) layers were deposited onto the films as top electrodes by means of magnetron sputtering for both dielectric and electro-optic measurements. The dielectric properties of the films were measured by means of a Sawyer-Tower circuit. When a voltage is applied to the ITO and the Pt electrodes, a sandwiched PZ thin film becomes birefringent, with its *c* axis along the normal of the film surface as a result of the transverse electro-optic effect. A reflection-mode phase-detection technique,<sup>6</sup> was used to measure the field-induced birefringence,  $\Delta n = n_s - n_0$ , in the PZ thin films. The arrangement of the optics and the electrodes is illustrated in Fig. 1. A He-Ne laser of 632.8-nm wavelength was utilized as the light source. The polarizers, P and P', are inclined 45° with respect to the incident plane and mutually crossed. The polarization state of the light beam was modulated in a periodic manner by means of a photoelastic modulator, M. At a finite incident

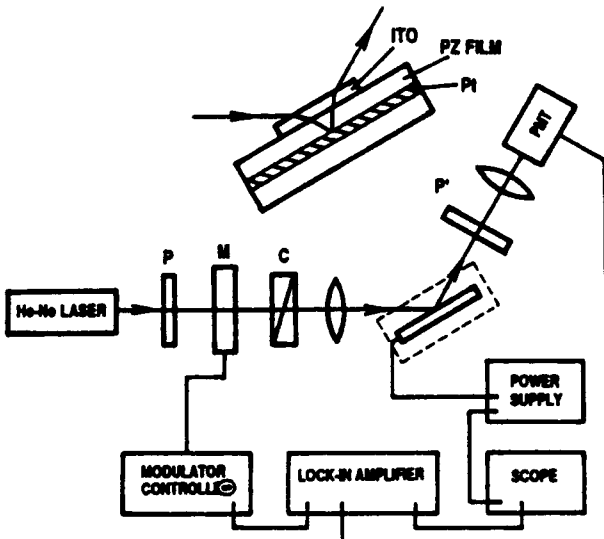


Fig. 1. Measuring system for the field-induced birefringence of the PZ films. Also shown is the arrangement of the electrodes. PMT, photomultiplier tube.

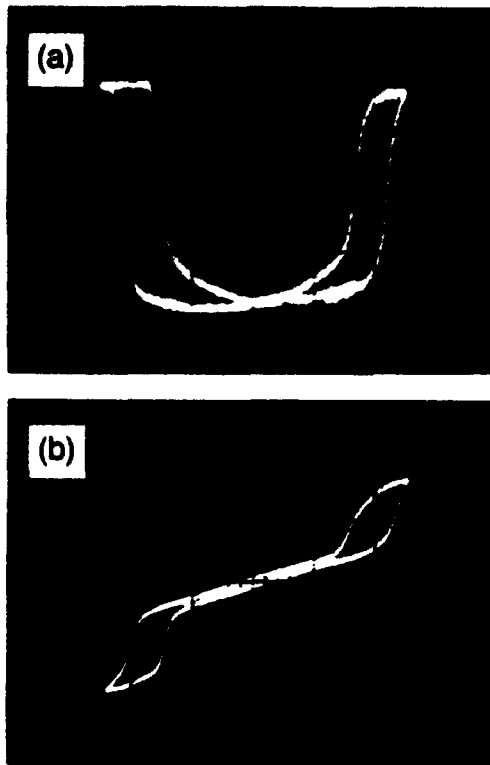


Fig. 2. (a) Field-induced birefringence as a function of the applied low-frequency voltage, (b) polarization as a function of the applied low-frequency voltage. The horizontal scale is 20 volts per division. The vertical scales are  $-0.7 \times 10^{-2}$  and  $20 \mu\text{C}/\text{cm}^2$  for (a) and (b), respectively.

angle, the reflected light polarized in the incident plane acquires a phase retardation with respect to the component polarized perpendicularly to the incident plane as a result of the birefringence of the PZ thin film. Under a properly chosen reference signal in the lock-in amplifier at the modulation frequency (synchronized with the photoelastic modulator), the output signal of the lock-in amplifier is proportional to the phase retardation generated by the thin film. The proportional constant was calibrated by using the adjustable optical compensator, C.

A typical response of the birefringence in the PZ films versus low-frequency ( $\sim 0.2$ -Hz) voltage is shown in Fig. 2(a). The voltage was measured with respect to the bottom electrode, i.e., platinum coating. The thickness of the PZ film was approximately  $1 \mu\text{m}$ . A clear transition is manifested with an abrupt increase of the birefringence as the increasing external field reaches approximately  $40 \text{ kV/mm}$  (40 V). The enhanced birefringence is sustained until the field is reduced below approximately  $30 \text{ kV/mm}$  (30 V). In order to relate the observed electro-optic response of the PZ thin film with its dielectric properties, we measured a polarization-versus-voltage loop, shown in Fig. 2(b), from the same sample. Figure 2(b) exhibits a typical double-hysteresis loop for AFE materials under a field-induced AFE-FE structural transition. Comparing Figs. 2(a) and 2(b), it is clear that the transition behavior in the electro-optic response occurs precisely at the electric field where

the field-induced AFE-FE transition occurs. Such an electro-optic response is consistent with an earlier prediction.<sup>3</sup> The reason for the discrete change in the birefringence to be observed in this measurement was that the electric field in the thin-film material during the reflection-mode phase-detection measurement was uniform. The magnitude of the birefringent difference between the AFE state ( $\Delta n_A$ ) and the FE state ( $\Delta n_F$ ) is approximately  $\Delta n_A - \Delta n_F = 2.5 \times 10^{-2}$ , which is similar to that of perovskite thin film in ferroelectric phase, i.e., 8/65/35 lead lanthanum zirconate titanate, under polarization saturation.<sup>7</sup>

Although the main features of the electro-optic response shown in Fig. 2 are consistent with the theoretical prediction, the quantitative correlation between the birefringence  $\Delta n$  and the polarization of the thin-film materials possesses a more complicated behavior. In Fig. 3, the field-induced birefringence is plotted as a function of the polarization by detecting both quantities simultaneously in a low-frequency voltage cycle. Portion A of the curve corresponds to the AFE state of the material; portions F and F' correspond to the field-induced FE state, while portions B and B' of the curve correspond to the phase transition, which occupies a small portion of the time duration in the voltage cycle. In the field-induced FE state the birefringence exhibits a different polarization dependence from that in the AFE state. Detailed measurements showed that within the AFE region the birefringence of the thin films can be described by a quadratic function of the polarization as expected by using a phenomenological model similar to that for FE materials. In the field-induced FE region, however, the birefringence exhibits a saturation behavior that is not fully understood at present. The splitting of the curve in the phase-transition region indicates that a single order parameter, namely polarization, is not sufficient for determining the birefringence of the material during the phase transition. The asymmetry shown in both Figs. 2 and 3 may be attributed to a ferroelectric-semiconductor contact behavior in the presence of ITO electrodes.<sup>7</sup>



Fig. 3. Birefringence as a function of the polarization. The horizontal and vertical scales are  $10 \mu\text{C}/\text{cm}^2$  per division and  $-0.7 \times 10^{-2}$ , respectively.



Fig. 4. Birefringence-versus-applied-voltage curve under a bias of -20 V. The horizontal and vertical scales are 10 volts per division and  $-0.7 \times 10^{-2}$  per division, respectively.

The quadratic electro-optic  $R$  coefficient for the PZ thin film in the AFE phase is evaluated from the experimental data to be approximately  $3 \times 10^{-19} (\text{m/V})^2$ , which is 2 orders of magnitude smaller than that of a typical FE perovskite thin-film material. Because the low-frequency linear susceptibility of the PZ films is an order of magnitude smaller than that of FE perovskite materials, the quadratic polarization-optical  $g$  coefficient defined by

$$\Delta n = -\frac{1}{2} n^3 g P^2, \quad (1)$$

where  $P$  is the polarization of the material, yields  $g = 0.05 \text{ m}^4 \text{ C}^{-2}$ , which is close to the typical value for perovskite materials in the FE phase.<sup>8</sup> This result seems to extend the boundary of Miller's rule<sup>9</sup> into AFE materials. An explanation of the constancy of the polarization-optical  $g$  coefficient is that the field-induced birefringence in a perovskite material is determined by the (low-frequency) local bias field that is dominated by the linear susceptibility of the materials at the low frequency, provided that the nonlinear

polarizability at optical frequencies is similar for all perovskite materials, including AFE materials. The nonlinear polarizability of the materials at optical frequencies is known to be dominated by the electronic polarization determined by a structure common to all perovskites, namely, oxygen octahedra.<sup>10,11</sup>

The observed discrete change of the field-induced birefringence at the AFE-FE phase transition field may be utilized in optical switches or spatial light modulators. With a bias field, the thin-film materials exhibits a birefringent bistability, as shown by the biased  $\Delta n$ -versus-voltage loop in Fig. 4. Such bistability may be used to realize programmable spatial light modulators, in which on/off status of a pixel can be interswitched by bipolar electric pulses.

This study was sponsored by the U.S. Office of Naval Research under contract N00014-19-J-508.

## References

1. K. Uchino, Jpn. J. Appl. Phys. **24** (Suppl. 2), 460 (1985).
2. W. Pan, C. Q. Dam, Q. Zhang, and L. E. Cross, J. Appl. Phys. **66**, 6014 (1989).
3. F. Wang, K. K. Li, and G. H. Haertling, Opt. Lett. **17**, 1122 (1992).
4. K. K. Li, F. Wang, and G. H. Haertling, "Antiferroelectric lead zirconate thin films derived from an acetate precursor system," J. Mater. Sci. (to be published).
5. G. H. Haertling, Ferroelectrics **116**, 51 (1991).
6. F. Wang, "Electro-optic properties of  $(\text{Pb},\text{La})(\text{Zr},\text{Ti})\text{O}_3$  thin film and related materials," Ph.D. dissertation (University of New Mexico, Albuquerque, N.M., 1991), p. 12.
7. F. Wang and G. H. Haertling, "Birefringent bistability in  $(\text{Pb},\text{La})(\text{Zr},\text{Ti})\text{O}_3$  thin films with a ferroelectric-semiconductor interface," Appl. Phys. Lett. (to be published).
8. P. D. Thacher, J. Appl. Phys. **41**, 4790 (1970).
9. R. C. Miller, Appl. Phys. Lett. **5**, 17 (1964).
10. M. DiDomenico, Jr., and S. H. Wemple, J. Appl. Phys. **40**, 720 (1969).
11. F. Wang and A. Y. Wu, Phys. Rev. B **46**, 3709 (1992).

## **SECTION 10**

## **PHOTO-ACTIVATED BIREFRINGENCE IN ANTIFERROELECTRIC THIN FILMS VIA A STRUCTURAL PHASE TRANSITION**

Feiling Wang, Gene H. Haertling and Kewen K. Li

Gilbert C. Robinson Department of Ceramic Engineering

Clemson University

Clemson, SC 29634-0907

It is known that an electric field induced antiferroelectric (AFE)-to-ferroelectric (FE) phase transition in lead zirconate thin films produces a digital birefringence change. When antiferroelectric thin films are bounded by certain semiconductor electrodes, however, the AFE-to-FE phase transition may be suppressed by the heterojunction formed between the antiferroelectric thin films and the electrodes. Such effect has been observed in lead zirconate titanate PZT (4% titanate) thin films grown on Pt/Ti-coated silicon substrates and capped with a semiconducting indium-tin oxide (ITO) thin film. In the dark, the field-induced AFE-to-FE phase transition was suppressed by the heterojunction formed between PZT and ITO films. It has been found that the illumination of the thin film structure with a low intensity soft-ultraviolet light effectively lifted the interfacial suppression; the PZT thin films experienced a pronounced AFE-to-FE phase transition. This UV light-activated phase transition was accompanied by a significant change in the birefringence of the PZT thin films. With the help of proper interference condition of multiple reflections, an obliquely incident visible laser beam experienced a phase retardation of approximately 30 degrees between the UV addressed and non-addressed states in the PZT films. This phenomenon may possess significant value in such applications as optical switching at low light intensity levels.

The use of ferroelectric materials for all-optical information processing are mainly based on two distinct properties, i.e., optical nonlinearity and photorefractive effect. The photorefractive effect, resulting from electrooptic effects under photo-induced charge migration, requires much lower light intensity than processes relying solely on optical nonlinear susceptibilities. The pursuit of low light intensity and fast response media is apparently a vital issue to the advance of all-optical processes. Recently, an antiferroelectric thin film material has shown unique electrooptic properties, i.e., a digital electrooptic response, which may be valued in electrooptic switching and modulation<sup>1,2</sup>. The purpose of this paper is to report a newly observed photo-induced birefringence in an antiferroelectric thin film material. The photo-induced birefringence is associated with a photo-activated antiferroelectric (AFE)-to-ferroelectric (FE) structural transition.

Antiferroelectric thin films of lead zirconate titanate (PZT) with four percent lead titanate were deposited on Pt/Ti-coated silicon substrates by using an automatic dip-coating technique<sup>3</sup>. The thickness of the films was approximately 690 nm. An indium-tin oxide layer of approximately 240 nm thick was deposited on the PZT films by means of sputtering. With the introduction of lead titanate, the required electric field for antiferroelectric-to-ferroelectric transition was reduced from 50 kV/mm for lead zirconate to approximately 20 kV/mm for the PZT composition while maintaining their antiferroelectric structure under naught external field. The PZT thin films also showed improved transparency than lead zirconate films. Helium-neon laser light was successfully coupled into the PZT films to form propagating modes as shown by the outcoupling intensity plot, Figure 1, recorded by using a prism coupler in an angle scan.

A reflection differential ellipsometer was employed to characterized the field-induced birefringence in the thin films<sup>2</sup>. A helium-neon laser beam of 543.5 nm was obliquely incident on the thin film sample. The phase-sensitive detection scheme allowed the direct measurement of the relative phase shift of the p-polarized light (component parallel to the incident plane) light with respect to s-polarized light (component perpendicular to the incident plane) as a function of a low frequency voltage signal. It was found that, in the dark, the phase-shift vs. voltage loop was severely asymmetric about the polarity of the applied voltage. As the material exhibited a digital electrooptic response in a negative half cycle of the voltage (the potential of the ITO electrode was lower than that of Pt bottom electrode), the expected digital electrooptic response was absent in the positive half cycle of the voltage, as shown in Figure 2(a).

It appeared that the absence of the digital electrooptic response in the positive half voltage cycle was caused by the ITO-PZT boundary, which suppressed the field-induced AFE-to-FE phase transition. The suppression of the phase transition in the positive half voltage cycle was confirmed by the dielectric characterization of the thin film material in the dark, presented in Figure 2(b), taken by using a Sawyer-Tower circuit. The same PZT thin films with copper top electrodes showed normal double hysteresis loop, typical for antiferroelectric materials under field-induced phase transition.

The photo-activated birefringence change in the PZT thin films was observed when the films were illuminated with a low intensity soft ultraviolet (UV) light source. The arrangement of the experiment was schematically shown in Figure 3. The light source was a short arc mercury vapor lamp. Filtered radiation from the lamp, peaked at 365 nm wavelength, was brought to the thin film samples through a fluid filled UV light guide. The intensity of the UV radiation at the sample was estimated as less than 100 mW/cm<sup>2</sup>. Under the UV illumination, the electrooptic response of the PZT thin films manifested a characteristic change. As shown in Figure 4(a), a phase-shift vs. voltage loop recorded by a digital oscilloscope, the electrooptic response of the material became characteristically symmetric. Withdrawal of the UV illumination restored the asymmetric electrooptic response of the material shown in Figure 2(a). A corresponding change in the hysteresis loop of the materials with the UV illumination was also observed, shown by Figure 4(b). Comparing Figure 2 and 4, it was clear that the UV illumination lifted the ITO-PZT interfacial suppression to the field-induced AFE-to-FE phase transition in the positive half voltage cycle.

The amplitude of the photo-induced birefringence was estimated as 0.024, similar to that of lead zirconate thin films. The thin film structure shown in Figure 1 behaved like a Fabry-Perot etalon, where the air-ITO and PZT-Pt interfaces were the primary reflection surfaces. The large field-induced phase-shift measured in the reflected light beam, shown in Figure 2(a) and 4(a), was obtained by taking advantage of the Fabry-Perot peak. At a Fabry-Perot peak, greatly enhanced phase modulation can be achieved; approximately 30 degrees was obtained in this experiment. Because the experimentally convenient incident angles were close to the Brewster angle for p-polarized light incident on the ITO layer, the Fabry-Perot etalon possessed higher finesse for the s-polarized light component than the p-polarized light. Therefore, near a Fabry-Perot peak, the measured relative phase retardation contained more contribution from the phase shift of the s-polarized light component. The modeling work of such process is to be published elsewhere.

The effects of an ITO-FE heterojunction in the electrooptic response of ferroelectric lead lanthanum zirconate titanate (PLZT) thin films were previously observed<sup>4</sup>. It was assumed that a polarization in the direction of the ITO layer is unfavorable for minimizing the free energy of the thin film structure in the presence of the ITO-FE junction, where substantial energy was stored when under a reversed bias. This junction arose from the semiconductor nature of the ITO and PLZT materials. Such effect resulted in a higher remanent polarization after a negative half voltage cycle than the positive half cycle in the PLZT thin films. It seemed that a more severe alteration in the free energy distribution occurred when the ITO layer formed a junction with the antiferroelectric PZT thin film material. In the positive voltage half cycle, the energy stored in the ITO-AFE junction may have prevented the field-induced AFE-to-FE phase transition. With an UV illumination, the migrations of the photo-excited charge carries may have released the energy stored in the junction, that in turn set in the AFE-to-FE phase transition. A theoretical analysis of this kind is in progress.

Although much of the details of the photo-activated phase transition are to be revealed both experimentally and theoretically, this effect has been quite attractive because of the large birefringence change acquired under a rather low input UV light level. This birefringence change is currently unparalleled by any nonlinear optical or photorefractive processes. It may hold significant promise for applications in optical switching and storage. As shown in the experiments, thirty degrees of phase shift in the reflected light beam was obtained as a result of the low-intensity UV illumination. This effect may facilitates an all-optical switching at low light intensity levels and a new way of generating holograms.

This study was sponsored by the U.S. Office of Naval Research under contract N00014-19-J-508.

## References

1. F. Wang, K. K. Li, and G. H. Haertling, Opt. Lett. 17, 1122 (1992)
2. F. Wang, K. K. Li, E. Furman, and G. H. Haertling, Opt. Lett. 18, 1615(1993)
3. K. K. Li, F. Wang, and G. H. Haertling, "Antiferroelectric lead zirconate thin films derived from an acetate precursor system," J. Mater. Sci., in press.
4. F. Wang and G. H. Haertling, Appl. Phys. Lett. 63, 1730(1993)

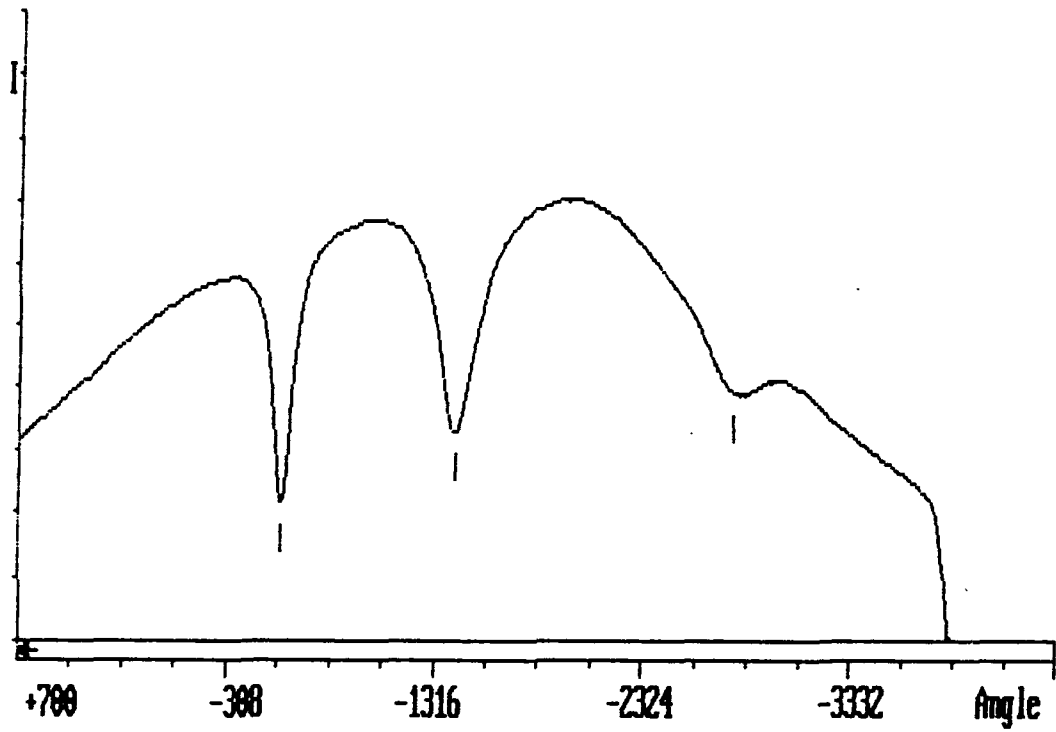


**Figure 1.** Light intensity profile from an incident angle scan of a prism coupler (Meticon 2010). The dips indicate the guided waves created in the antiferroelectric thin film material.

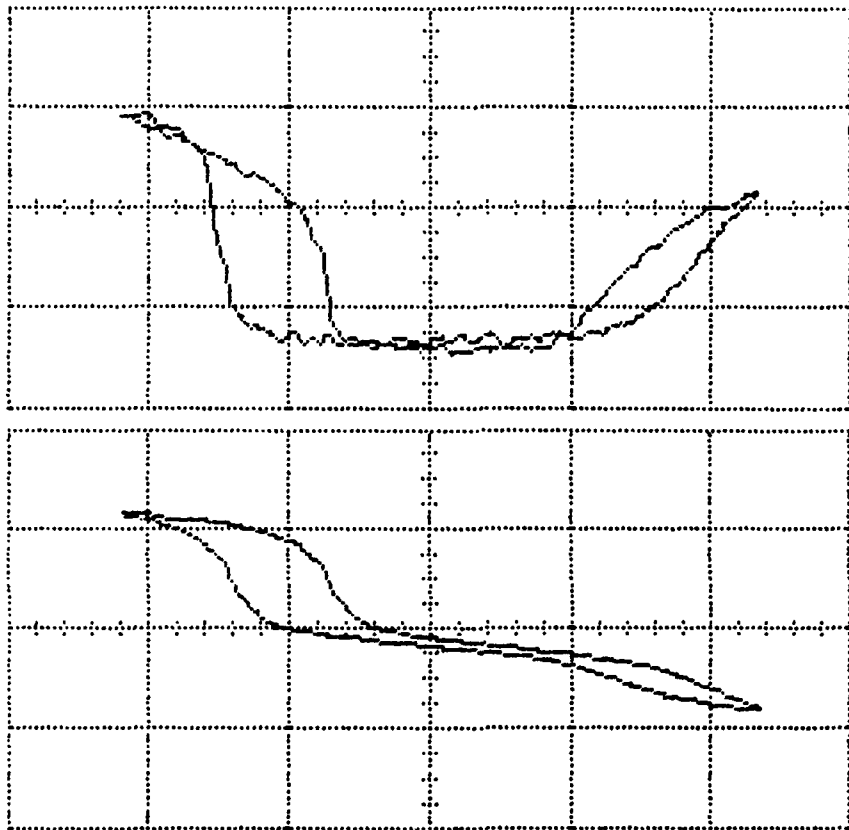


**Figure 2. (a):** Phase retardation of the reflected light beam as a functions of a low frequency voltage signal taken in the dark. **(b):** Polarization of the thin film material as a function of the low frequency voltage signal taken in the dark. The horizontal scale is 7.5 volts per division. The vertical scales for (a) and (b) are 0.21 per division and  $27 \mu\text{C}/\text{cm}^2$  per division respectively.

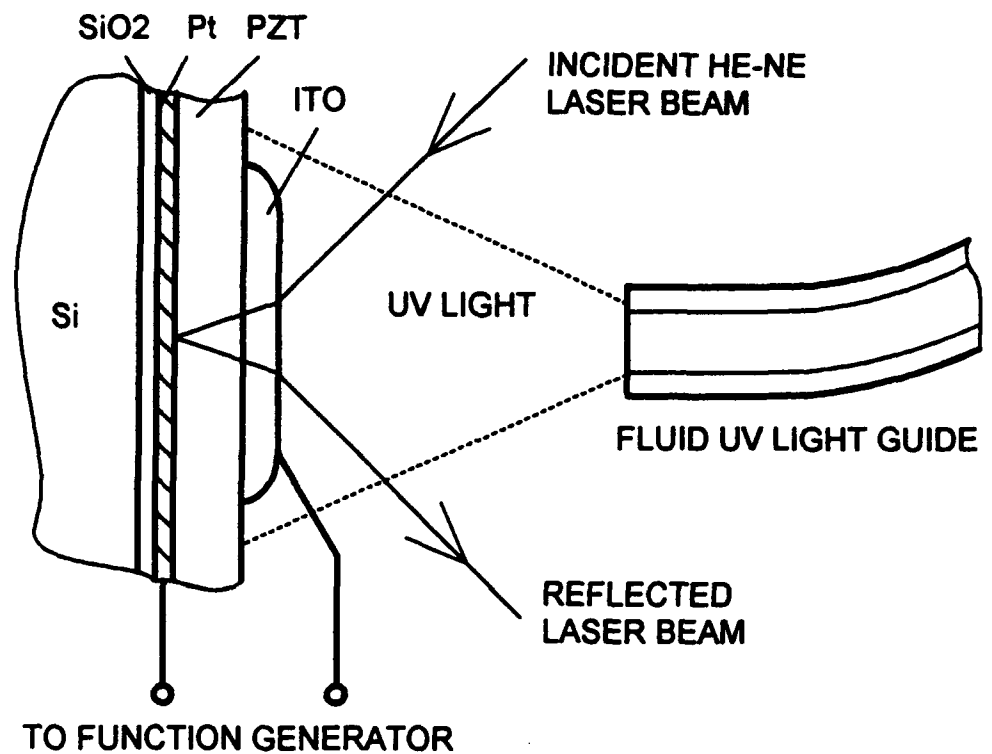
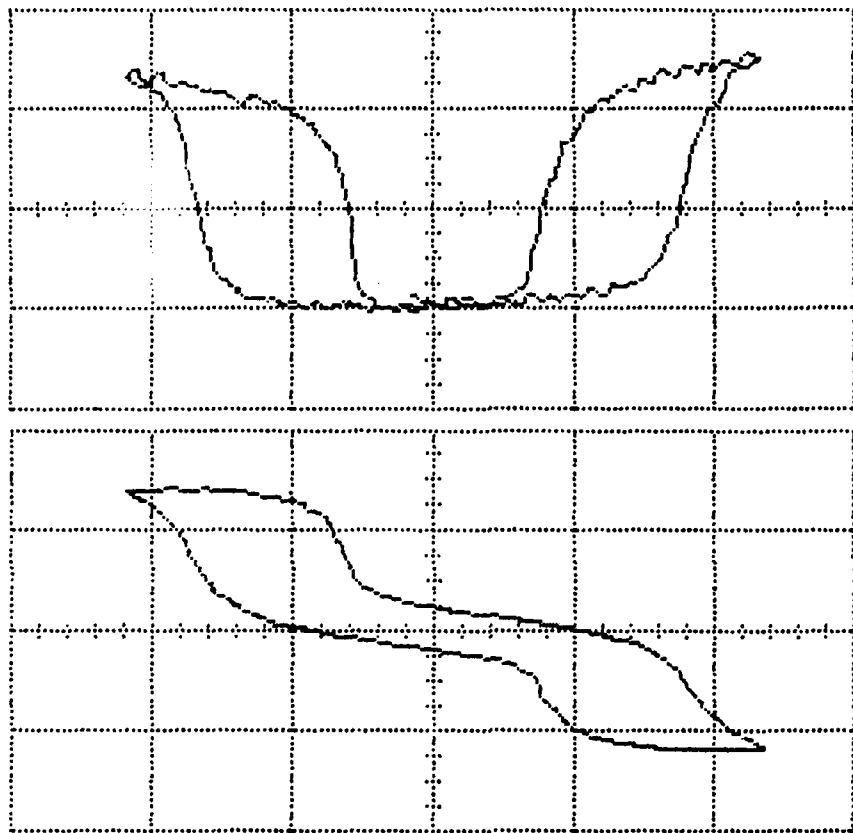


Figure 3. Arrangement of the light sources in detecting the electrooptic and dielectric properties of the thin film material with UV illumination.



**Figure 4.** (a): Phase retardation of the reflected light beam as a function of a low frequency voltage signal taken with UV illumination. (b): Polarization of the thin film material as a function of the low frequency voltage signal taken with UV illumination. The horizontal scale is 7.5 volts per division. The vertical scales for (a) and (b) are 0.21 per division and  $27 \mu\text{C}/\text{cm}^2$  per division respectively.

## **SECTION 11**

## REFLECTIVE PLZT THIN FILM LIGHT MODULATOR — A PROTOTYPE DEVICE

(This device was constructed as one of the requirements for concluding the Office of Naval Research project "Intelligent Processing of Ferroelectric Thin Films" carried out at Clemson University, completed in March, 1994.)

The device adopts an ITO/PLZT/Pt thin film structure on a silicon substrate. The modulating medium is a ferroelectric/electrooptic PLZT thin film. A transparent indium-tin oxide (ITO) layer was deposited on the PLZT film as the top electrode. A reflected light of finite reflection angle is modulated in its polarization state by means of an voltage signal exerted to the ITO and Pt layers. The largest modulation depth is obtained near a Fabry-Perot interference peak located at an incident angle of approximately 57 degrees.

The packed assembly, shown in the photograph, consists of a wired ITO/PLZT/Pt thin film modulator, a polarizer and a photo-transistor. The orientation of the modulator and the photo-detector is arranged in specific angles to obtain a large modulation depth when a light beam of 633 nm wavelength (from a He-Ne laser) is incident through the input aperture. When desired, the photo-transistor may be removed to let the reflected light exit from the output aperture for external detection or visual monitoring. Driving voltage signal is applied to the modulator through a BNC connector. The photo-transistor is wired to an output jack.

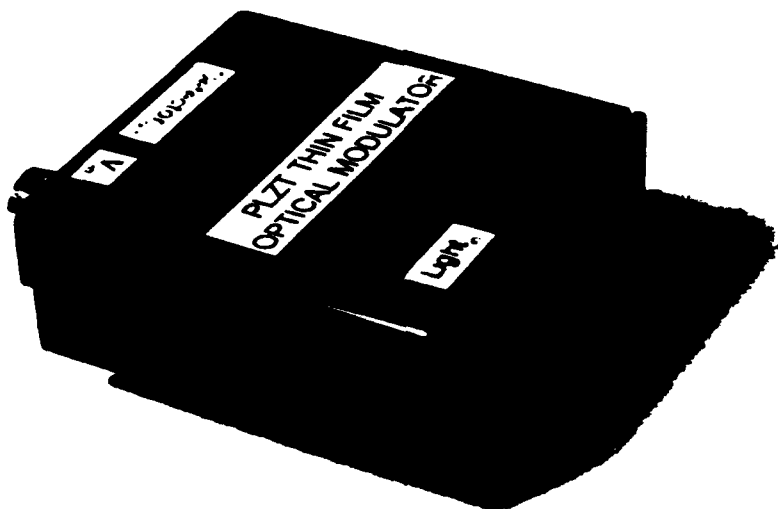
The performance of the device as a light intensity modulator or a phase modulator is described in Section 5. The following summarizes the main features and advantages of the device:

1. Integrated form.
2. Compatible with silicon or other semiconductor substrates
3. Reflection-mode — preferred for free-space optical interconnections.
4. Modulating visible and infrared light.
5. Operated at or near a Fabry-Perot peak.
6. High on/off signal ratio for intensity modulation — 20 at 10 volts pulses.
7. Large optical phase modulation — above 50 degrees at 10 volts pulses.
8. Capable of digital and analog modulations.

9. High-frequency modulation\*.
10. Simple design; easy to fabricate.
11. Large tolerance to the error of thickness and incident angle control.
12. Low cost.

\*The bandwidth of the prototype is limited by the large  $rc$  constant that can be drastically reduced. The PLZT thin film material has proved to be able to modulate light at GHz frequencies.

The above listed features are favorable for the device to be incorporated in monolithic optoelectronic devices for light modulations, particularly for the implementation of free-space optical interconnections.



**PLZT Thin Film Optical Modulator**

**Part VII.**

**Chemical Vapor Deposited Thin Films**

# **INTELLIGENT PROCESSING OF FERROELECTRIC THIN FILMS**

## **Annual Report**

### **Part VII.**

#### **Chemical Vapor Deposited Thin Films**

**Submitted by:** Jaideep Mavoori  
Raj Singh

**The Gilbert C. Robinson Department of Ceramic Engineering  
Clemson University**

# **RAPID ISOTHERMAL PROCESSING ASSISTED METAL ORGANIC CHEMICAL VAPOR DEPOSITION OF PLZT FILMS**

April 25, 1994

## **Introduction**

Chemical Vapor Deposition (CVD) finds numerous applications in depositing various materials like semiconductors, dielectrics, ceramics and metals. Some of the advantages of CVD over other kinds of thin film processing techniques are : (1) better step coverage and (2) compatibility with in-situ processing techniques. One of the more popular types of CVD is metal-organic chemical vapor deposition (MOCVD), a part of its popularity being due to the versatility of the technique. It offers a range of material growth possibilities because of the large number of metalorganic precursors available and the chemical similarity between those precursors (an essential property for good quality growth). This technique has the advantage of depositing films layer by layer as in case of atomic layer epitaxy and also for certain applications MOCVD can provide very high growth rates. As compared to any other type. (e.g. thermal, plasma enhanced, radio frequency heating etc.) RIP assisted MOCVD (RIP-MOCVD) offers best prospects of inventing new materials and developing emerging optical and electronic materials. Some of the features of RIP-MOCVD like (1) use of lamps as the source of optical and thermal energy, (2) high heating and cooling rates and (3) capability of low temperature processing, prove advantageous. As an example, for the deposition of high temperature superconducting thin films, RIP assisted MOCVD

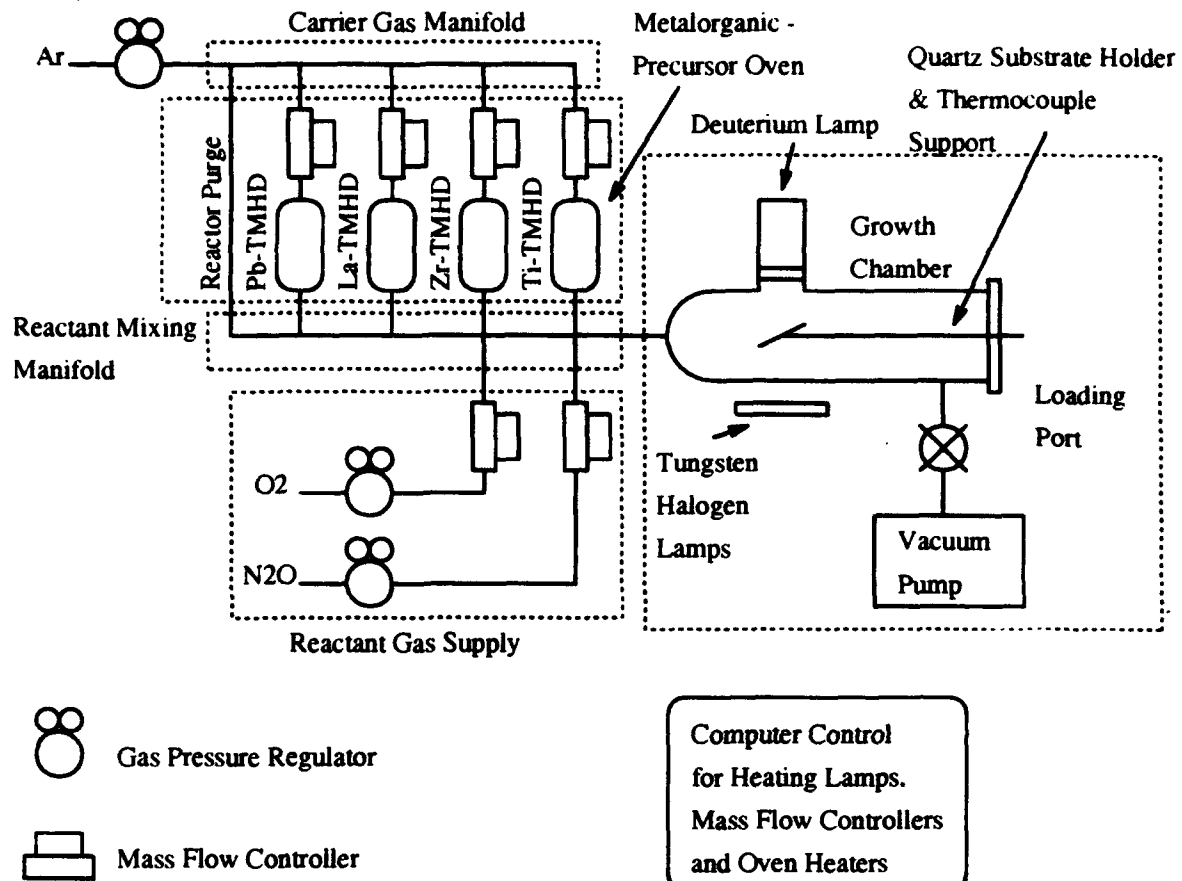


Figure 1: The main sub-systems of the RIP set up.

has provided the best low processing temperature results [1] reported by anyone. This report summarizes the research done in collaboration with Dr. Singh, over the past 6 months in RIP-MOCVD of PLZT thin films.

## Experimental Procedure

A schematic of the RIP-MOCVD system is presented in figure 1. The deuterium lamp used is a VUV lamp that aids in the photoexcitation of the organic precursors used. A suitable precursor should have a high enough vapor

pressure at the deposition pressure, for transport and should not decompose spontaneously at the operating temperature (of the source oven) losing its volatility. The precursors used in this study were metal  $\beta$ -diketonates, viz., 2,2,6,6-tetramethyl- 3,5-heptanedione compounds (TMHDs) of Pb, La, Zr, Ti. For the oxidation, a mixture of  $N_2O$  and  $O_2$  was utilized. Initially the transport properties and deposition characteristics and process conditions of each of the precursors were studied followed by their combined deposition. Experiments were done with and without the deuterium lamp for each of the above TMHDs to determine the phases deposited on Si and yttrium stabilized zirconia (YSZ) substrates. There were marked differences in the deposition characteristics of  $La_2O_3$  on Si (111) and YSZ substrates with and without irradiation by the deuterium lamp (cf. figures 2 and 3). With irradiation by the  $D_2$  lamp, films on the Si substrate had (222), (400) and (440) orientations of cubic  $La_2O_3$ , while without the  $D_2$  lamp, the films had very weak peaks and none of which matched any of the five  $La_2O_3$  peaks. Similar results were observed in case of  $Pb_2O_3$ ,  $ZrO_2$  and  $TiO_2$ . Once the precursors were tested separately, they were deposited simultaneously, with the carrier flow rates adjusted to obtain films of a particular composition. For the deposition of PLZT, experiments were performed by varying different process parameters like the deposition temperature, precursor flow rates and  $N_2O$ : $O_2$  flow rates. The XRD pattern of one of the PLZT films deposited is presented in figure 4. The XRD pattern shows the presence of the perovskite phase, proving the feasibility of the technique for deposition of PLZT.

## Conclusion

Preliminary results of this research are quite encouraging. Further experimentation with the heating rates, in-situ substrate pre-clean prior to deposition and post-deposition anneal recipes can provide optimized PLZT films with good electro-optic and dielectric properties.

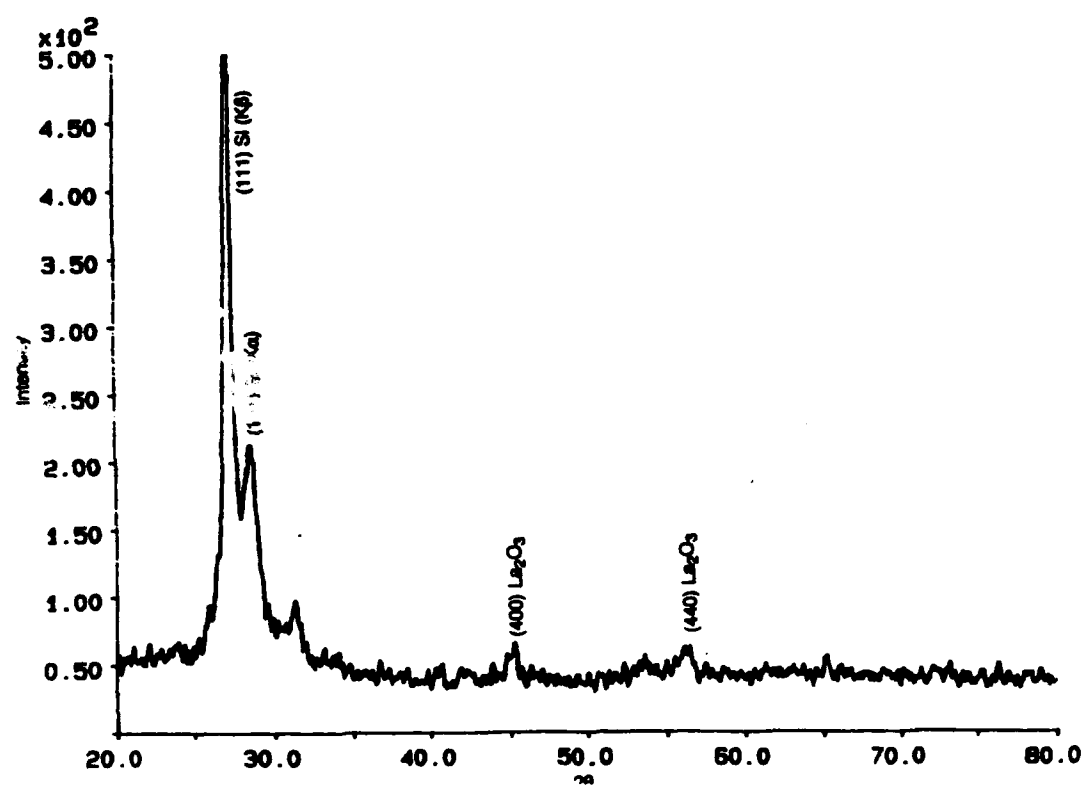


Figure 2: X-ray diffraction pattern for the MOCVD lanthanum oxide films deposited without UV irradiation.

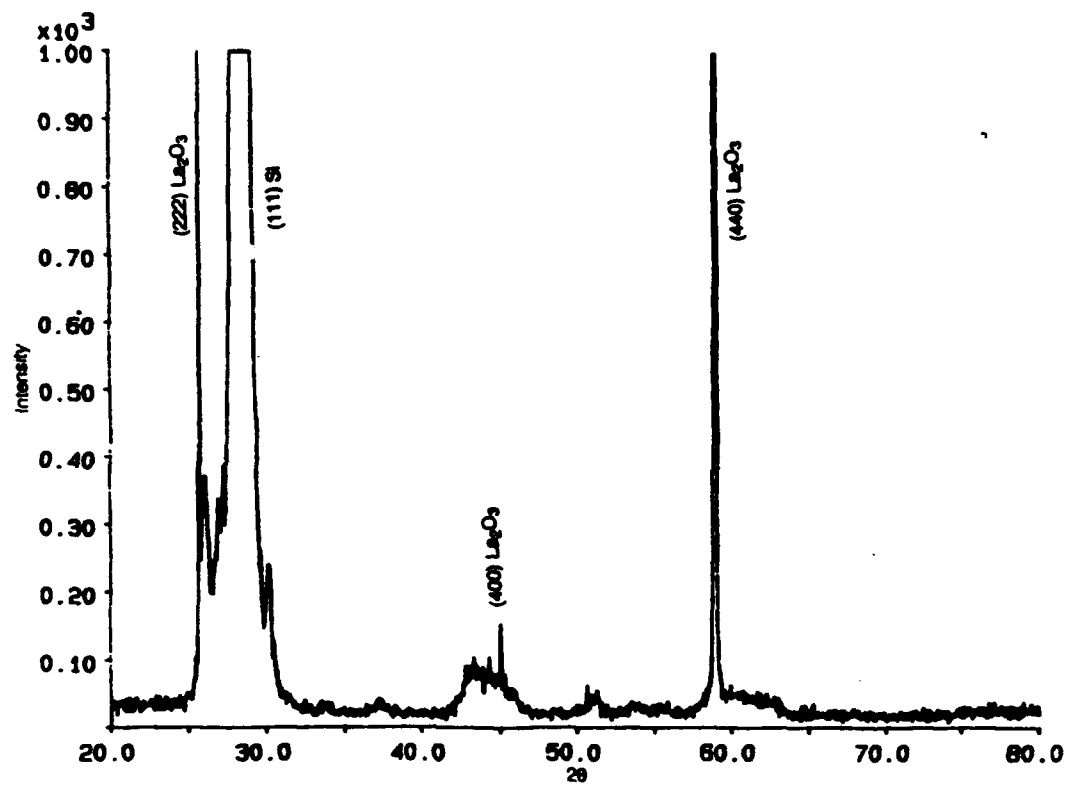


Figure 3: X-ray diffraction pattern for the MOCVD  $\text{La}_2\text{O}_3$  films deposited with UV irradiation from a  $\text{D}_2$  lamp.

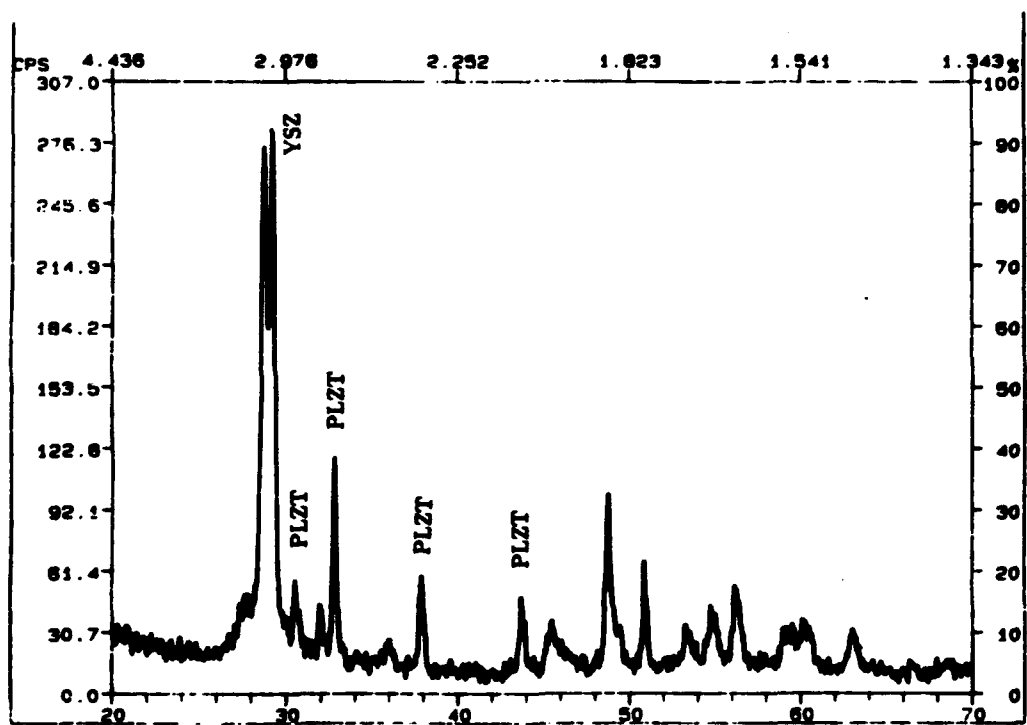


Figure 4: X-ray diffraction pattern of the PLZT film on YSZ.

## **References**

- [1] R. Singh, Current trends in rapid isothermal processing (RIP), in *Proceedings of the international conference on Beam Processing of Advanced Materials*, edited by J. Singh and S. M. Copley, pages 619–688, TMS, 1992.

**Part VIII.**

**Publications**

## DIELECTRIC AND ELECTROOPTIC PROPERTIES OF ACETATE DERIVED PLZT X/65/35 THIN FILMS

GENE H. HAERTLING

*Clemson University, Clemson, South Carolina, U.S.A.*

(Received May 31, 1993)

PLZT solutions were prepared from the as-received acetate precursors by means of a simple mixing procedure which produced a stock solution of approximately 10% oxide solids. Films were fabricated via dip coating and heat treating at 700°C for two minutes per layer. As many as 150 layers were deposited with an automatic dip coating system. All of the resulting films were optically transparent and well crystallized in the perovskite phase. The films were evaluated with respect to dielectric and electrooptic properties. Shutter contrast ratios as high as 1000 to 1 were measured.

**Keywords:** *thin films, PLZT films, electrooptics*

### INTRODUCTION

Thin films of ferroelectric (FE) compositions in the PLZT system are promising candidates for future devices involving memory and non-memory dielectrics, piezoelectric resonators, pyroelectric detectors and electrooptic modulators. A number of these applications necessitate films with thicknesses greater than those presently being designed for low voltage (1-3V) random access memories; i.e., 0.1-0.4 microns. A typical example of such an application is that of a transverse-mode spatial light modulator (SLM) which generally requires a film of several microns thick in order to generate the necessary optical retardation for sufficient optical contrast. Although much of the needed retardation can be produced via the direct electrooptic effect by simply increasing the electric field, there is a limit to this process since saturation of polarization or dielectric breakdown eventually occur. Consequently, for a given material composition, further gains in total retardation must be achieved by increasing the optical path length; i.e., the film thickness.

This investigation reports on work involved in the study of thicker films (0.5-6.5  $\mu\text{m}$  of PLZT compositions composed of varying concentration of La (0-12 atom percent) at a constant Zr/Ti ratio of 65/35.

### EXPERIMENTAL

The precursor materials used in the fabrication of the PLZT films consisted of lead subacetate ( $\text{PbsubAc}$ ) powder with a  $\text{PbO}$  concentration of 78.6 wt.%, lanthanum acetate ( $\text{LaAc}$ ) aqueous solution with an  $\text{La}_2\text{O}_3$  content of 6.7 wt.%, zirconium acetate ( $\text{ZrAc}$ ) aqueous solution containing 22.22 wt.%  $\text{ZrO}_2$  and titanium acetylacetone ( $\text{TiAAc}$ ) chelated solution consisting of 16.96 wt.%  $\text{TiO}_2$ .

The various steps involved in the processing and fabrication of the films are

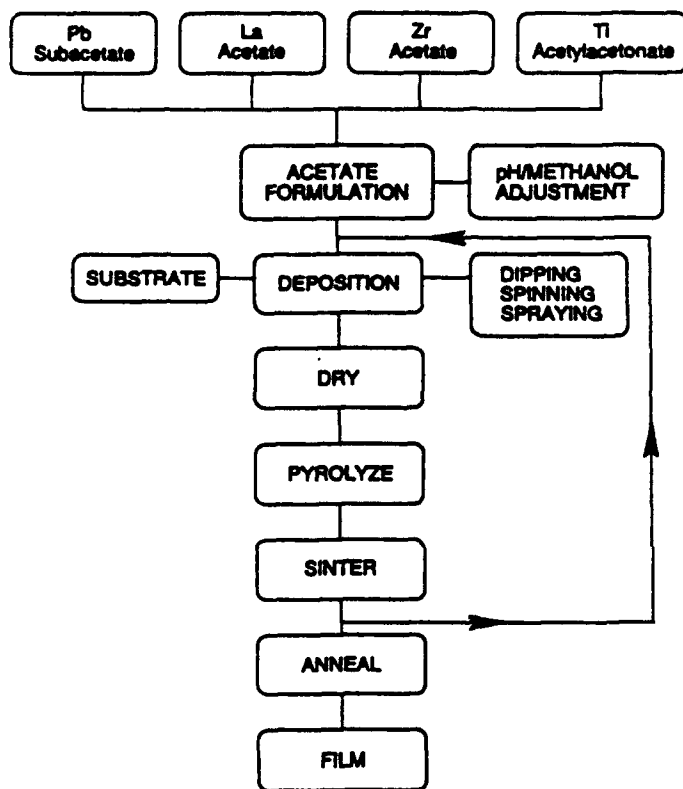


FIGURE 1 Flowsheet of the acetate process.

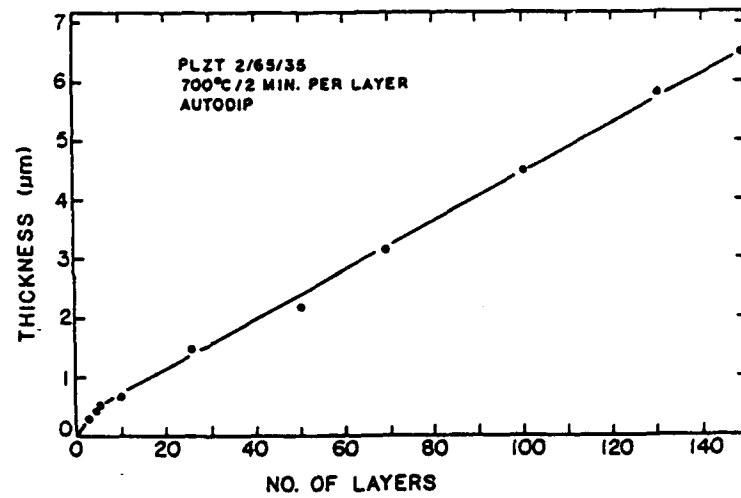


FIGURE 2 Relationship of film thickness to the number of layers.

shown in Figure 1. Compositions of various PLZT formulations ranging in La content from 0 to 12 atom % at a constant 65/35 Zr/Ti ratio were prepared by mixing the precursor ingredients in the proper proportions as they were received from the vendors. The solutions were then deposited via a dip coating process onto substrates consisting of either electrically conductive tin oxide coated (30 nm) PLZT (0.375 mm thick), randomly oriented sapphire (1.25 cm diameter  $\times$  0.5 mm thick) or Ag foil (0.127 mm thick). After drying for several seconds, the films were moved directly into the heating chamber and sintered at 700°C for two minutes per layer. An automatic, computer-controlled, dip coating apparatus was used to deposit and sinter the films.<sup>1</sup> As many as 150 layers were deposited, thus producing a total sintered thickness of 6.5  $\mu\text{m}$  for the thickest films. A plot of the sintered film thickness as a function of the number of layers is given in Figure 2. As can be seen, the sintered film thickness is linearly related to the number of layers throughout the major portion of the deposition process. The slope of the plot in the linear region was calculated to be 415 angstroms (0.0415  $\mu\text{m}$ ) per layer; however, this value was less than half of the slope for the first few layers which was approximately 1000 angstroms (0.1  $\mu\text{m}$ ) per layer. The deposition behavior exhibited in this portion of the curve is believed to be due to the influence of the substrate surface.

A final anneal of the film, when performed, was carried out at 100°C below the sintering temperature for a period of 30 minutes with a slow cool in the furnace to room temperature; however, most of the films were not given an anneal in this study since the benefits of stress relief for these PLZT films on a PLZT substrate were considered to be marginal.

For the dielectric and hysteresis loop measurements, top copper electrodes, one mm diameter were deposited on the films through a mask via vacuum evaporation. Small signal dielectric measurements were carried out on a digital LCR meter at 1 kHz. Hysteresis loops ( $P$  vs.  $E$ ) were measured on the films at frequencies of 1 kHz and near dc ( $\frac{1}{2}$  Hz) at a driving voltage of <20 volts. Since PLZT substrates were inappropriate for use when determining the electrooptic characteristics of PLZT films, sapphire was chosen as an alternate substrate. Sapphire is highly transparent and readily available, however, it should be kept in mind that a thermal expansion mismatch between the film and substrate (i.e., 5.4 vs.  $9 \times 10^{-6}/\text{C}$ , respectively) could lead to stresses in the film which may alter their properties.

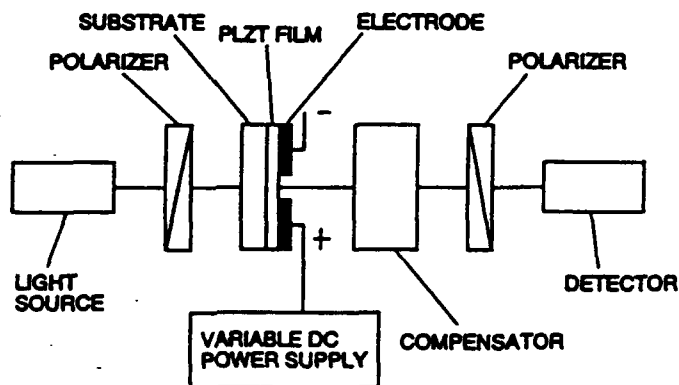


FIGURE 3 The setup for electrooptic measurements.

While it was felt that this could be the case with the films of less than one micron thickness, such a mismatch was not considered to be a significant factor in the measurements on the thicker films.

Electrooptic measurements were made on films dip coated on sapphire and elecroded with thermally evaporated aluminum. Several 50  $\mu\text{m}$  gaps for producing the transverse electric field were photolithographically generated in the electrodes using a commercial aluminum etch which did not attack the PLZT film. The setup for the measurements is shown in Figure 3. An incandescent white light source along with a Babinet-Soleil compensator, crossed polarizers, a variable dc power supply and a United Detector Technology, Model S370, detector were used to make the birefringence measurements.

## RESULTS AND DISCUSSION

### Materials

Examples of the transparency of PLZT 2/65/35 films of various thicknesses ranging from 0.5  $\mu\text{m}$  (5 layers) to 4.5  $\mu\text{m}$  (100 layers) are shown in Figure 4. These specimens were autodip coated on PLZT substrates with a full sintering cycle for each layer. It was observed that all of the films were optically transparent and crack free, having a smooth, highly polished appearance. The grain sizes of these films ranged from 0.5–2 microns.

A typical optical transmission curve for a 5.5  $\mu\text{m}$  thick PLZT film on sapphire is given in Figure 5. Overall, it may be observed that the transmittance of this film is very similar to that of the bulk material.<sup>2</sup> Additionally, it should be noted that the total transmission of the film is approximately the same as that of the bulk, i.e., 64% at 800 nm wavelength vs. approximately 67% for the bulk at the same wavelength. The onset of transparency was found to take place at approximately 360 nm, which is slightly lower than the 370 nm of the bulk.

An optical photomicrograph of a polished cross section and an SEM micrograph of a fractured surface are given in Figure 6. This figure shows the excellent thickness uniformity of the films after sintering as well as revealing the intimate growth between the many deposited layers. It also points out the fact that the thicker films are actually single, monolithic entities with bulk-like characteristics. X-ray diffraction patterns taken on several of the films indicated that the films possessed well developed, perovskite structures with little evidence for preferred orientation.

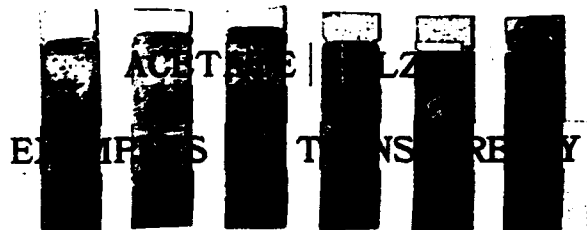


FIGURE 4 PLZT dip coated (2/65/35) on  $\text{SnO}_2/\text{PLZT}$  substrates illustrating optical transparency of the 5, 10, 25, 50, 69 and 100 layer samples (left to right).

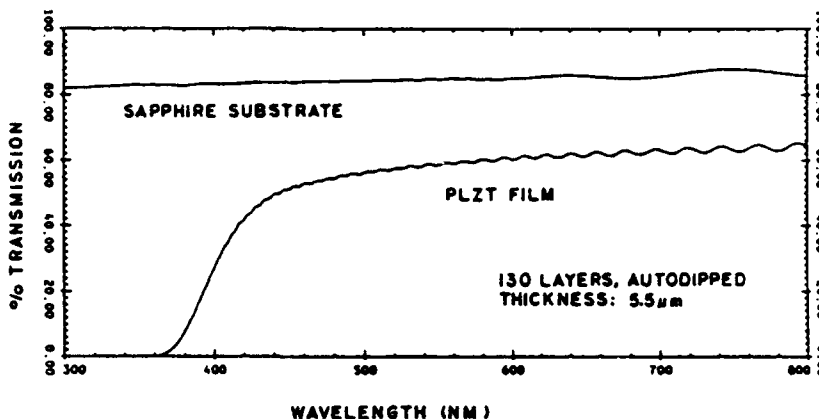


FIGURE 5 Optical transmittance of a 5.5  $\mu\text{m}$  thick PLZT film on sapphire and the sapphire substrate without the film.

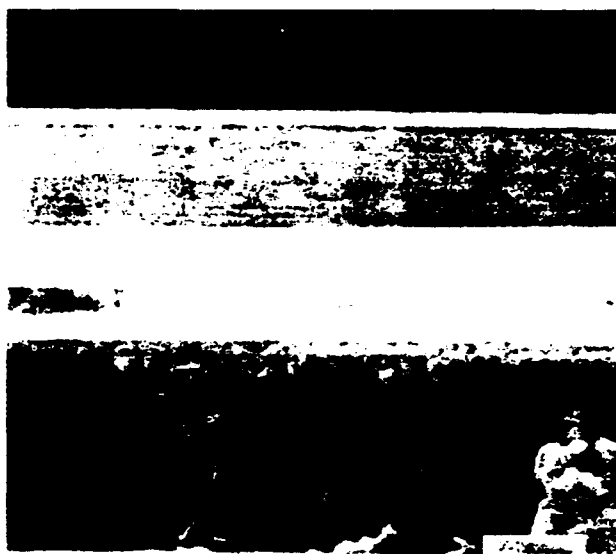


FIGURE 6 Cross section photomicrographs of 2.2  $\mu\text{m}$  (50 layers) thick PLZT 2/65/35 film on PLZT substrate at  $\times 1250$  magnification (top) and 3.2  $\mu\text{m}$  (69 layers) thick PLZT film at  $\times 11.000$  (bottom).

#### DIELECTRIC PROPERTIES

The dielectric properties of several of the PLZT films are listed in Table I as a function of thickness and in Table II as a function of composition. In Table I, it can be noted that the small signal relative dielectric constants (avg. = 702) and dissipation factors (avg. = 0.108) did not change significantly with increasing film thickness, however, this was not the case with the large signal properties taken from the hysteresis loops. Remanent polarization ( $P_R$ ) increased with increasing

TABLE I  
Electrical properties of PLZT 2/65/35 films of varying thickness

No. layer	Film thickness ( $\mu\text{m}$ )	Dielectric constant	Dissipation factor	$P_R$ ( $\mu\text{C}/\text{cm}^2$ )	$E_c$ ( $\text{kV}/\text{cm}$ )
5	0.5	664	0.124	26	67
10	0.8	714	0.135	28	45
25	1.5	776	0.109	29	51
50	2.1	708	0.103	33	51
69	3.2	712	0.095	36	46
100	4.5	638	0.081	37	43

TABLE II  
Dielectric properties of 0.6  $\mu\text{m}$  thick PLZT films dip coated on Ag foil: ( $r_c$  values were obtained on sapphire substrates)

Comp.	$T_c$	Dielectric constant	Tangent delta-%	$P_R$ $\mu\text{C}/\text{cm}^2$	$E_c$ $\text{kV}/\text{cm}$	$\times 10^{-10}\text{m/V}$
0/65/35	235	455	0.095	43	96	1.08
2/65/35	205	500	0.110	41	95	—
6/65/35	145	685	0.104	29	80	0.79
8/65/35	125	790	0.092	19	62	0.53
9/65/35	120	875	0.095	10	40	0.44
9.5/65/35	—	860	0.090	—	—	0.37
10/65/35	118	845	0.080	8	35	—
11/65/35	115	730	0.063	5	25	—
12/65/35	—	700	0.056	4	20	—

thickness, and coercive field ( $E_c$ ) decreased with increasing thickness. These results again point out that the thicker films generally possessed properties more closely associated with bulk materials.

Dielectric data on compositions with La concentrations ranging from 0 to 12 atom % at a constant Zr/Ti ratio of 65/35 are given in Table II. The trends noted in these results generally follow those of the bulk materials; however, their absolute values, in some cases, were significantly different. For example, (1) the Curie temperatures ( $T_c$ ) for all of the films were lower than the bulk by 50 to 80°C; (2) the dielectric constants were also lower, but the deviation from the bulk only became significant at La contents greater than 6%; (3)  $P_R$ s were higher (more remanence) than the bulk for La contents of 9% or higher and (4)  $E_c$ s were substantially higher than the bulk for all compositions. The curves showing the temperature dependence of dielectric constant and the hysteresis loops for this series of compositions are given in Figures 7 and 8, respectively.

### ELECTROOPTIC PROPERTIES

Using the setup shown in Figure 3, birefringence measurements were made on several of the films (5.5  $\mu\text{m}$  thickness) deposited on sapphire. These data are given in Figure 9. It can be seen that the PLZT composition 0/65/35 at the top of the

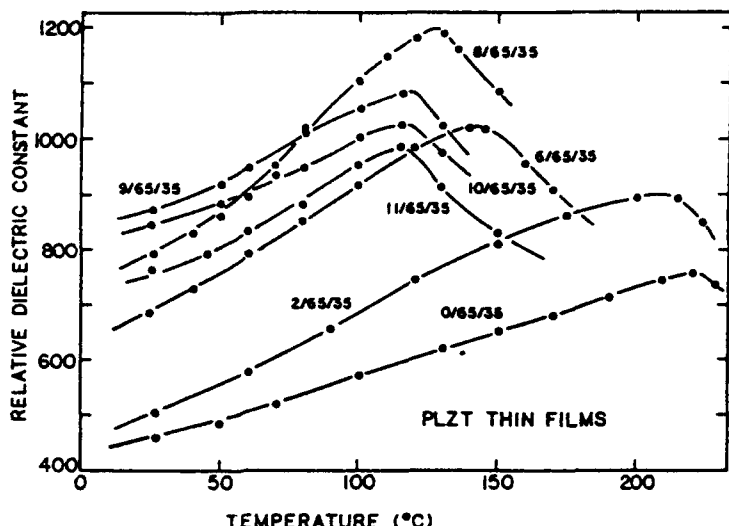


FIGURE 7 Temperature dependence of dielectric constant for various PLZT compositions.

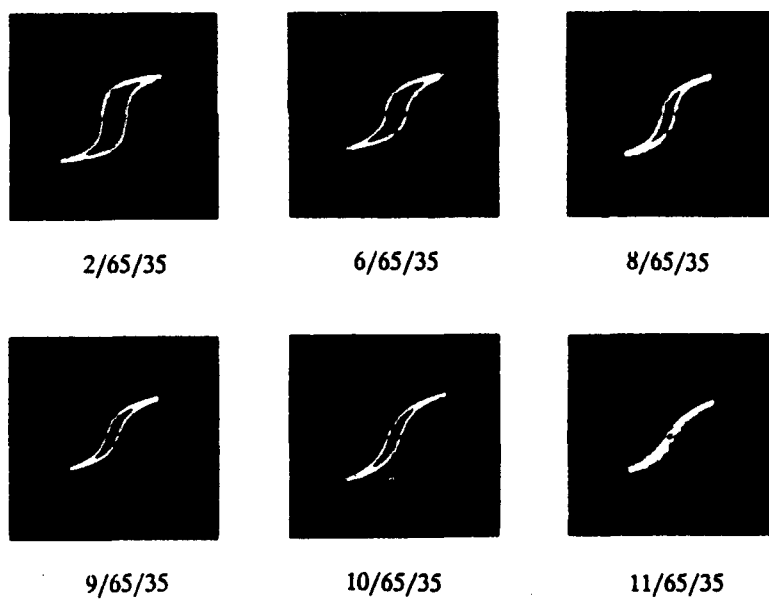


FIGURE 8 Hysteresis loops of selected films (0.6  $\mu\text{m}$  thick) of PLZT dip coated on Ag foil.

figure is ferroelectric with definite remanent birefringence and switching characteristics, whereas, all of the other compositions (6, 8 and 9% La) appear to have very little remanent birefringence. The birefringences in these latter compositions appear to be primarily of the electrically-induced, quadratic nature which is similar to that of the bulk PLZT relaxor materials but only within the range from 9 to 12% La. The reason for the lack of remanence in compositions 6/65/35 and 8/65/35 is not understood at this time; but it is believed to be due, at least in part, to

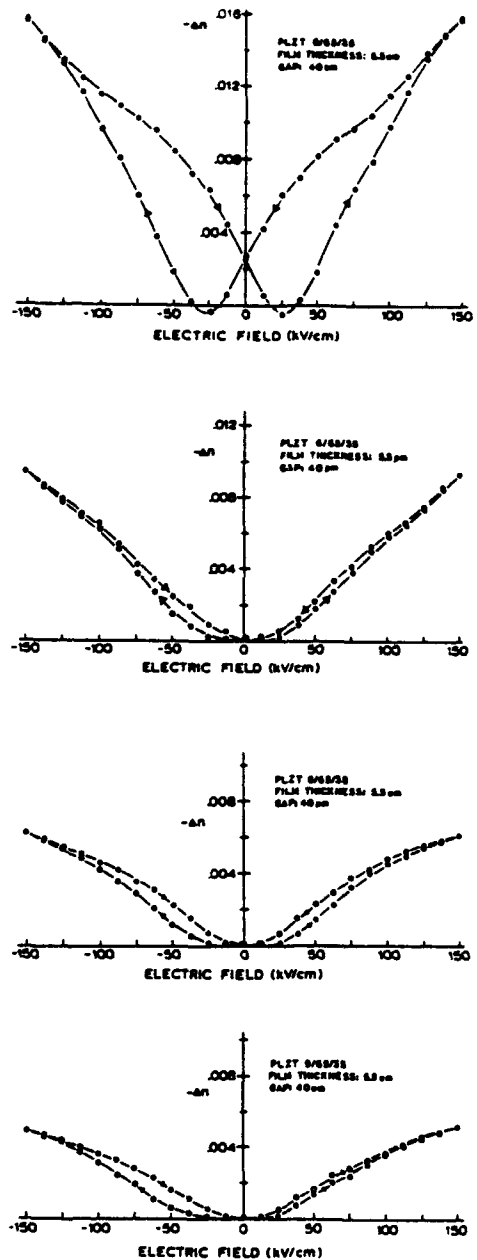


FIGURE 9 Electrooptic transverse-mode birefringence data on films of selected PLZT compositions. stresses in the film from thermal mismatches or substrate clamping during activation when the film is constrained from moving piezoelectrically.

A closer examination of the non-remanent birefringence curves of Figure 9 reveals that at lower electric fields ( $< 50$  kV/cm) the dependence is quadratic, however, "saturation effects" at higher fields causes the overall curve to be approximately linear. The saturation effect is, in all likelihood, the normal approach

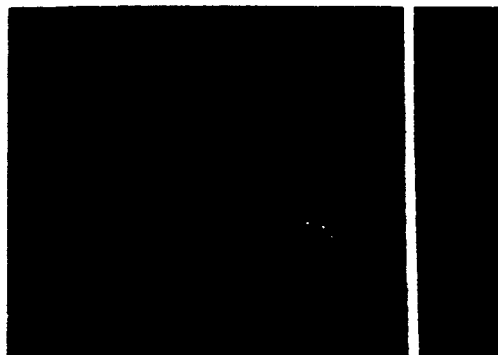


FIGURE 10 Transverse-mode PLZT thin film device with one gap activated (right) and one gap inactive; (thickness = 5.5  $\mu\text{m}$  and gap = 40  $\mu\text{m}$ ).

toward the half-wave retardation condition as experienced in bulk material, but spread out over much higher values of electric field. It was not possible in any of the films to actually achieve half-wave retardation, and this again, is believed to be due to the clamping effects of the substrate. Such effects were similarly noted by Wang *et al.* for compositions in the PLZT system.<sup>3</sup>

Although the required electrical fields for the films were substantially higher than the bulk materials (15 kV/cm vs. 150 kV/cm), it should also be noted that the birefringence values achieved were quite competitive with the bulk; i.e., -0.004 to -0.016 at 150 Kv/cm for a 5.5  $\mu\text{m}$  thick film. The electrooptic  $r_c$  coefficients, calculated as a linear coefficient across the useable range of electric fields from 0 to 150 Kv/cm, were determined for the various compositions and are given in Table II. As seen, the values range from  $1.08 \times 10^{-10}$  m/V for 0/65/35 to  $0.37 \times 10^{-10}$  m/V for 9.5/65/35. A comparison of these values with similar ones for bulk material shows that the films at the 5  $\mu\text{m}$  thick level possess bulk-like electrooptic properties.

Further evidence for the bulk-like character of these films is given in Figure 10. This figure is a photograph of one of the measured films (0/65/35) with one of the gaps activated while the other gap was held in the inactive state. To date, contrast ratios of up to 1000 to 1 have been obtained.

#### ACKNOWLEDGEMENTS

The author wishes to gratefully acknowledge the assistance of Kewen K. Li and Kimberly D. Preston for the preparation of some of the PLZT thin and thick film samples. This work was supported by the Office of Naval Research under contract No. N0014-91-J-1508.

#### REFERENCES

1. K. K. Li, G. H. Haertling and W. Y. Howng, *Integrated Ferroelectrics* (to be published).
2. G. H. Haertling, *Ferroelectrics*, 75, 1 (1987).
3. F. Wang and A. Y. Wu, *Proceedings of 1990 Int'l. Sym. Appl. Ferroelectrics*, Urbana, 131 (1992).